A Demand-Controlled Application of Deep Brain Stimulation with a Portable Neurostimulator

Inaugural Dissertation

zur

Erlangung des Doktorgrades
Dr. nat. med.

der Medizinischen Fakultät
und
der Mathematisch-Naturwissenschaftlichen Fakultät
der Universität zu Köln

vorgelegt von

Safwan Al-Qadhi

aus Sana'a, Jemen

Prost Druck GmbH, Jülich

2021

Betreuer (supervisor): PD Dr. Christian Hauptmann

Referenten (referees): PD Dr. Mohammad Maarouf
Prof. Dr. Wolfgang Walkowiak

Datum der mündlichen Prüfung: 22.03.2021

Acknowledgments

The research work in connection with this thesis has involved a great number of people, whom I am indebted to and I wish to thank them all for their help and support.

First and foremost, I would like to express my gratitude to ***Prof. Dr. Dr. Peter A. Tass*** *for letting me be part of his research group at the* ***Forschungszentrum Jülich (FZJ)****. I am grateful for the opportunities I have been given during my PhD to develop as a researcher in such a stimulating and supportive environment.*

A special thanks and appreciation to my supervisors ***Prof. Dr. Wolfgang Walkowiak*** *and* ***Priv.-Doz. Dr. Mohammed Maarouf*** *at the University of Cologne for their scientific support in my educational journey throughout the whole PhD-study.*

I am thankful to my supervisor ***Priv.-Doz. Dr. Christian Hauptmann*** *at the FZJ. I thank him for his encouragement, guidance as well as for revising the thesis.*

The mentorship my supervisors have all provided me, together with the knowledge and skills I have gained throughout my PhD, will be invaluable in my future career.

I would like to acknowledge the friendship and support of all my colleagues in the ***Neuromodulation group (INM-7)*** *at the* ***Institute of Neuroscience and Medicine*** *who have contributed to both my personal and professional development at Jülich over the last three years.*

Special thanks to my colleagues Dr. Giovanna Castillo and Dr. Martin Ebert for their enthusiasm in revising the thesis. I thank PD Dr. Oleksandr Popovych, Dr. Borys Lysyansky and Dr. Alexander Silchenko for the discussions about signal processing, and Norbert Pawelczyk for the technical support.

I thank my colleagues Natalie Schlothauer, Dr. Timea Toth, Dr. Magteld Zeitler, Ilya Adamchic, Julia Buhlmann, and Dr. Areh Mikulic for the kind and collegial atmosphere. In addition, I want to thank Sarah Harzheim and Nina Klein for the administrative support and the organization of my visits to Switzerland and China.

I would be remiss if I do not acknowledge the support of past group members Dr. Eylem Kirlangic, M.Sc. Munir Bhatti, Dr. Sacha van Albada, Veronika Kriebel, and Judith Coenen.

It is important for me to thank Jan Heßler, Stefan Demary, Wolfgang Rieger, Jens Kirchhoff and the other members of the IT team for their support with computer and software.

Special thanks for Alexander Wegener from ANM GmbH in Cologne for his guidance and instructions during my experiments in China and for the technical support.

I also thank the administration of the IPMM program at the ***University of Cologne*** *especially Dr. Debora Grosskopf-Kroiher and Dr. Daniela Mutschler for the numerous workshops and for the support at the later stages of my PhD.*

I would like to acknowledge the financial support provided by the ***Deutsche Forschungsgemeinschaft (DFG)*** *and the* ***Bundesministerium für Bildung und Forschung (BMBF)****.*

Last but not least, I owe a special thanks to all my friends who were there for me through thick and thin, to give advice on life and research. I offer my regards and blessings to all of those who supported me in any respect during the completion of this thesis.

To my family;

Mother & Father

Wife & Sons

Sisters & Brothers

Die in dieser Dissertation vorgestellte Forschung entstand in der Zeit vom Januar 2010 bis Dezember 2013 am Forschungszentrum Jülich, Institut für Neurowissenschaften und Medizin, Neuromodulation Gruppe, in Jülich, Deutschland

The research presented in this thesis was carried out from January 2010 until December 2013 at the Research Center Jülich, Institute of Neuroscience and Medicine, Neuromodulation group, in Jülich, Germany.

Abstract

Deep brain stimulation (DBS) is an electrical therapy for several advanced neurological disorders such as Parkinson's disease (PD). The improvement of current DBS technique has gained more importance in order to increase the therapeutic benefits and reduce the side effects. The electrical stimulation of the deep brain is administered at standard high-frequency (HF) or by using dedicated patterns intending the modulation of pathological neuronal activity. Apart from the development of new stimulation protocols such as the desynchronizing coordinated reset (CR) DBS protocol, a continuous and appropriate adjustment of the stimulation parameters might increase the efficacy of DBS. Therapeutic benefits could be maximized by a system that automatically detects the demand for further stimulation and continuously modifies the stimulation parameters. For instance, such a system can help the clinician to find the optimal parameters easily, without lengthy test procedures. In this thesis, the technical realization of a demand-controlled application of CR DBS for Parkinson's disease (PD) with a portable neurostimulator is investigated. The applicability of such an autonomic system is studied retrospectively using local field potential (LFP) and resting tremor recordings from PD patients, as well as LFP recordings from parkinsonian non-human primates were used. A demand-controlled application of DBS requires a real-time analysis of the on-going pathological activity. LFP recordings during DBS are normally contaminated by strong artifacts that are caused by technical drawbacks. The artifacts inhibit the examination of the presence of pathological activity. Therefore, software-based technical solutions for artifact reduction were developed and implemented to obtain clean feedback signals from the recordings. Additional tests were performed on LFP recordings in saline solution to evaluate the performance of the implemented algorithms. Results obtained from these tests indicated the efficacy of the algorithms in removing most of the artifacts. Furthermore, the biological recordings were analyzed to find biomarkers of the pathological activity that can be used as a criterion to quantify the demand for tuning the stimulation parameters. The proposed approach aims to analyze and monitor the variation in the strength of such pathological activities. A demonstration of the tuning of several HF and CR DBS parameters was performed in real-time with a digital signal processor (DSP) board using tremor-like recordings collected from a healthy subject. This thesis explores and demonstrates the design and implementation of a demand-controlled application of DBS that is adapted according to the pathological fluctuations of patients and can be more efficacious than standard continuous DBS technique.

Kurzfassung

Die tiefe Hirnstimulation ist eine elektrische Therapie für verschiedene fortgeschrittene neurologische Erkrankungen wie die Parkinson-Krankheit (PD). Die Verbesserung der tiefen Hirnstimulation hat mehr an Bedeutung gewonnen, um den klinischen Nutzen zu erhöhen und die potenziellen Nebenwirkungen zu verringern. Die elektrische Stimulation des tiefen Gehirns kann mittels Standard-Hochfrequenz (HF) oder mit dedizierten, speziellen Mustern, die auf die Modulation der pathologischen neuronalen Aktivität abzielen, durchgeführt werden. Neben der Entwicklung von neuen Stimulations-protokollen, wie des Protokolls der de-synchronisierenden „Coordinated Reset“ (CR), könnte eine kontinuierliche und gezielte Anpassung der Stimulationsparameter die Wirksamkeit der tiefen Hirnstimulation erhöhen. Der therapeutische Nutzen könnte somit durch ein System, das den Bedarf für eine weitere Stimulation automatisch erkennt und ständig die Stimulationsparameter modifiziert, maximiert werden. Darüber hinaus kann ein solches System den Ärzten helfen, die optimalen Stimulationsparameter ohne langwierige Einstellungsprozeduren leicht zu finden. In der vorliegenden Arbeit wird die technische Realisierung einer bedarfsgesteuerten Anwendung der CR Stimulation für Parkinson-Patienten mit einem tragbaren Neurostimulator vorgestellt. Die Anwendbarkeit eines solchen autonomen Systems wird retrospektiv erforscht. Zu diesem Zweck wurden bereits vorhandene Aufnahmen der lokalen Feldpotentiale (LFP) und des Ruhetremors von Parkinson-Patienten, sowie LFP Messungen von nicht-menschlichen Primaten, die unter Parkinson-Symptomen leiden, verwendet. Die bedarfsgesteuerte Anwendung der tiefen Hirnstimulation erfordert eine Echtzeit-Analyse der pathologischen Aktivität. LFP Aufnahmen während der tiefen Hirnstimulation sind in der Regel von starken Artefakten kontaminiert. Diese Artefakte verhindern die einfache Analyse der erfassten Daten zur Feststellung des Vorhandenseins einer pathologischen Aktivität. Deshalb wurden software-basierte technische Lösungen für die Unterdrückung von Artefakten entwickelt und implementiert. Weitere Tests wurden mit LFP Aufnahmen vorgenommen, die im Rahmen von Messungen in Salzlösung gewonnen wurden. Diese Messungen helfen, die Leistung der implementierten Algorithmen zu beurteilen. Die Ergebnisse aus diesen Tests zeigten, dass die entwickelten Algorithmen die meisten Artefakte hochwirksam entfernen können. Weiterhin wurden die biologischen Aufnahmen analysiert, um Biomarker für die pathologische Aktivität zu finden. Diese Biomarker können als Kriterium verwendet werden, um den Bedarf zur Anpassung der Stimulationsparameter zu quantifizieren. Somit können entsprechend des vorgeschlagenen Ansatzes die Veränderungen in der Stärke der pathologischen Aktivität analysiert und überwacht werden. Die Anpassung von unterschiedlichen HF und CR Stimulationsparametern wurde in Echtzeit mit einem

digitalen Signalprozessor (DSP), anhand von Parkinson-zitterten-ähnlicher Messdaten eines gesunden Probanden, präsentiert. Somit kann diese Arbeit die Konzeption und Umsetzung einer bedarfsgesteuerten Anwendung der tiefen Hirnstimulation demonstrieren und zeigt, wie die pathologischen Schwankungen der Patienten für die Anpassung der Stimulationsparameter verwendet werden können. Es ist zu hoffen, dass solche Verfahren die Wirksamkeit der tiefen Hirnstimulation – englisch: Deep Brain Stimulation (DBS) - verbessern können.

ملخص الأطروحة

التحفيز العميق للدماغ Deep Brain Stimulation (DBS) هو تقنية علاجية كهربائية لعدة امراض عصبية متقدمة مثل مرض الباركنسون Parkinson's Disease (PD). تكتسب فكرة تطوير هذه التقنية أهمية أكبر مع الوقت من أجل زيادة الفوائد العلاجية وتقليل الآثار الجانبية المحتملة. تتم عملية التحفيز الدماغي عن طريق إرسال ذبذبات كهربائية عالية التردد High Frequency (HF) اما مستمرة أو باستخدام أنماط مخصصة من هذه الذبذبات الى المناطق الدماغية المستهدفة لغرض التأثير على ألنشاط المرضي للخلايا العصبية. بالإضافة إلى فكرة تطوير بروتوكولات تحفيز كهربائي جديدة مثل بروتوكول الإعادة الموجهة Coordinated Reset (CR) DBS والذي يهدف الى إعادة النشاط العصبي المرضي الى حالة أقرب للطبيعية، تعتبر فكرة التقويم الدائم والمناسب لمعاملات التحفيز واعدة أكثر لزيادة فعالية تقنية ال DBS, مثلا عن طريق تطوير نظام أوتوماتيكي قادر على اكتشاف وتحليل النشاط العصبي المرضي وتقييم الحاجة الى استمرارية التحفيز الكهربائي للدماغ او تغيير معاملات التحفيز المستخدمة بشكل دائم. في هذه الأطروحة قمنا بدراسة إمكانية إنشاء تطبيق اوتوماتيكي لتقنية التحفيز الكهربائي العميق للدماغ لمرضى الشلل الرعاش مع جهاز محمول يستعمل للتحفيز العصبي. يهدف هذا التطبيق الى تعديل معاملات التحفيز الكهربائي عند الحاجة فقط بعكس التقنيات ألحالية التي تحفز الدماغ بشكل مستمر. لقد تم عمل دراسة استرجاعية retrospective study لإمكانية تحقيق هكذا تطبيق باستخدام نوعين من البيانات المسجلة مسبقا: النوع الأول هو النشاطات العصبية الدماغية Local Field Potential (LFP) المسجلة عن طريق قطب كهربائي مزروع في المنطقة المستهدفة في الدماغ تم الحصول عليها من مرضى الباركنسون ومن ثديات عليا غير بشرية تم اصابتها بالباركنسون (قرود المكاكا - Macaque monkeys) والنوع الثاني هو قياسات الرعاش Resting Tremor في مرضى الباركنسون عن طريق حساسات لقياس الاهتزازات في الأطراف المصابة. إن إنشاء تطبيق لتقييم الحاجة لإعادة ضبط معاملات التحفيز يتطلب تحليلاً في الوقت الحقيقي للنشاط المرضي. تسجيلات النشاط العصبي في الدماغ تكون عادة مشوشة نتيجة لبعض العيوب التقنية التي تمنع دراسة وتحليل الإشارات العصبية المسجلة من المرضى. لذلك، تم تطوير حلول تقنية برمجية (خوارزميات) لتقليل التشويش وللحصول على إشارات أكثر نقاءً. تم اختبار الخوارزميات على تسجيلات LFP من تجارب مخبرية في محلول ملحي. أظهرت النتائج فعالية الخوارزميات في إزالة التشويش. كما تم برمجة خوارزميات اخرى لتحليل البيانات ولحساب المؤشرات الحيوية على وجود النشاطات المرضية عن طريق رصد وتحليل التغيرات في قوة ألنشاط العصبي المرضي. هذه المؤشرات الحيوية يتم استخدامها كمعيار لتقييم الحاجة لإعادة ضبط المعاملات المستخدمة للتحفيز. لعرض كيفية تعديل معاملات التحفيز الكهربائي للدماغ في الوقت الفعلي تم تجريب مبدئي للتطبيق مع تقنية الاعادة الموجهة بواسطة معالج إشارات رقمي Digital Signal Processor (DPS) على تسجيلات مشابهة لرعاش الباركنسون تم اخذها من شخص سليم. هذه الأطروحة تستكشف تصميم وتنفيذ تطبيق لتقنية أوتوماتيكية للتحفيز الكهربائي لعمق الدماغ تكون قادرة على التكيف مع التقلبات المرضية ويمكن ان تكون أكثر فاعلية من تقنيات التحفيز المستمر التقليدية.

Contents

List of Figures

Abbreviations and Symbols

ACC	Resting tremor recording using accelerometers
BRS	Breathing sensor
CMRR	Common mode rejection ratio
CR	Coordinated reset
DBS	Deep brain stimulation
DC	Direct current
DFT	Digital Fourier transform
DSP	Digital signal processor
ECG	Electrocardiogram
EEG	Electroencephalogram
EMG	Electromyograms
FFT	Fast Fourier transform
GPe	Globus pallidus externus
GPi	Globus pallidus internus
GUI	Graphical user interface
HF	High frequency
IPG	Implantable pulse generator
LAN	Local area network
LFP	Local field potential
McBSP	Multichannel buffered serial ports
NaCl	Sodium Chloride
PD	Parkinson’s disease
PLI	Power line interference
PSD	Power spectral density
Pt/Ir	Platinum/Iridium
SNc	Substantia nigra pars compacta
SNR	Signal to noise ratio
SNr	Substantia nigra pars reticulata
STN	Subthalamic nucleus
USB	Universal serial bus
VIM	Ventral intermediate
WLAN	Wireless local area network

Chapter 1

Introduction

Deep brain stimulation (DBS) is an effective and approved[1] electrical therapy for advanced Parkinson's disease (PD) with medically refractory symptoms and for several other neurological disorders (Coffey, 2009, Hariz, 2012, Benabid et al., 1991). For electric DBS, depth electrodes are chronically implanted in target areas in the brain and connected subcutaneously to an implantable pulse generator (IPG). The IPG is battery-powered and implanted under the patient's collarbone. Via the depth electrodes, the IPG is used to administer a continuous high-frequency (HF) periodic pulse train (Coffey, 2009). HF (>100 Hz) is the standard DBS protocol and has been empirically developed relying on intra-operative observations. Despite therapeutic success for involuntary movement disorders, HF DBS still has some limitations. For instance, its therapeutic effects may wear off over time and undesired stimulation of neighboring areas might cause side effects (Kumar et al., 2003, Volkmann, 2004, Rodriguez-Oroz et al., 2005).

Strong neuronal synchronization of brain activity has become one of the characteristics of PD (Lenz et al., 1994, Nini et al., 1995, Brown, 2003). The mechanism of HF DBS on the abnormal neuronal activity is still a matter of ongoing debate (Miocinovic et al., 2013, Carron et al., 2012). In order to improve the therapeutic effects of DBS, new stimulation protocols have been developed. Among them, coordinated reset (CR) has been introduced as a robust desynchronizing stimulation technique based on timely coordinated phase resets of synchronized neuronal populations (Tass, 2003b, 2003a). The objective of the CR protocol is to selectively counteract the pathological neuronal synchronization process (Tass, 2003b). CR protocol splits the entire synchronized neuronal population into several sub-populations in a timely coordinated manner that are phase-shifted with respect to each other ultimately leading to desynchronization (Tass, 2003b, 2003a).

The further enhancement and detailed understanding of the DBS mechanism might have the potential to maximize therapeutic benefits, minimize power consumption and to extend the field of DBS application to other areas. Stimulation parameters of DBS are adjusted intermittently every few months to cope with the dynamic nature of PD (Deuschl et al., 2006a). This shows that a closed-loop technique that continuously adjusts the

[1] By the US Food and Drug Administration (FDA)

stimulation parameters according to the current pathological neuronal activity could be more effective than classical open-loop DBS (Rosin et al., 2011, Little et al., 2013). In this regard, the optimization of the stimulation strategy, through a demand-controlled application of desynchronizing CR DBS, is expected to have a strong impact on the reduction of side effects. This is because the stimulation amplitude and duration can be reduced considerably (Feng et al., 2007, Grant & Lowery, 2013). The demand-controlled application aims to optimize the stimulation effects by quantifying and detecting the need for further stimulation and appropriately adapting the stimulation parameters.

A demand-controlled application requires a real-time analysis of the pathologic neuronal activity. The implanted electrodes for DBS offer a unique opportunity to record the pathological activity from the target area during CR stimulation. The electrical field in the vicinity of the implanted electrode, known as the local field potential (LFP), can provide relevant information about the pathological activity of large neuronal populations (Tass et al., 2010). LFP activity is believed to be modulated by DBS and that it correlates with motor and non-motor impairments (Priori et al., 2013, Little & Brown, 2012). LFP activity is characterized by multiple rhythms which operate at distinct frequencies (Brown, 2003, Cassidy et al., 2002, Levy et al., 2002, Foffani et al., 2005a). Furthermore, the analysis of the LFP activity could provide an insight into the mechanisms of action underlying DBS. Therefore, LFP recordings are still the most suitable candidate feedback signal for such a demand-controlled application of DBS (Priori et al., 2013). In addition, motoric symptoms of PD, particularly resting tremor, can be analysed to uncover their relationship to the pathological synchronization in the brain (Tass et al., 2010).

1.1 Aim of the thesis

In this project, we investigate the technical realization of a demand-controlled application of CR DBS for Parkinson's disease (PD) with a portable neurostimulator. The main objective is to develop and implement technical solutions for real-time artifact reduction and data analysis. The applicability of such an autonomic system is studied retrospectively using two kinds of existing electrophysiological recordings:

(i) Internal LFP recordings from PD patients and from non-human primates rendered parkinsonian. These include: (a) LFP recordings during desynchronizing CR DBS and (b) Spontaneous LFP recordings after CR stimulation sessions.

(ii) External recordings of parkinsonian resting tremor especially of the hands. The tremor signal was recorded by means of accelerometers simultaneously with the LFP signals during and after the CR stimulation sessions.

LFP recordings during active DBS are normally contaminated by strong artifacts that can be one million times greater than the LFP activity (Giannicola et al., 2012, Rossi et al., 2007, Abosch et al., 2012). These artifacts hindered the investigation of the pathological neuronal activity. LFP recordings during CR DBS are contaminated by some artifacts such as stimulus artifacts, exponential decay/growth after stimuli, power line interference (PLI), and electrical background noise. To obtain a reasonable feedback signal during CR DBS for the demand-controlled application, we developed and implemented software-based technical solutions for real-time artifact reduction. An efficient solution for that was the software implementation of the Nelder-Mead algorithm which is an optimization technique based on the least squares method (Nelder & Mead, 1965). The aim of implementing the Nelder-Mead algorithm was to remove artifacts from short epochs of LFP recordings (i.e., up to 500 ms). In order to give a proof-of-principle and to optimize the flexibility and accuracy of the implemented technical solutions, off-line simulations and in-vitro tests (i.e., in saline solution) were performed. Results obtained from these tests showed a high efficacy of the implemented algorithms in removing most of the artifacts. For spontaneous LFP activity and tremor recordings after CR DBS, different techniques based on digital filtering and wavelet transform were used for artifact reduction.

Analysis techniques of LFP recordings are typically performed in the frequency domain. In our application, the real-time spectral analysis of neuronal activity during CR DBS resulted to be more challenging because of the short data segments included in the CR stimulation protocol but are free of strong artifacts, e.g., the stimulus artifact. The short data segments were collected on a regular basis to analyze the pathological neuronal activity. We implemented several technical solutions for data analysis in order to calculate biomarkers-values of the pathological activity in the LFP recordings. During CR DBS, two analysis techniques were used: averaging of data segments and modified spectral analysis. The spectral power of the collected short data segments was scaled by a factor that was calculated from the selected CR stimulation parameters. In order to investigate the spontaneous LFP and tremor recordings, the spectral analysis was the main analysis tool. The variation in the spectral power of the LFP and tremor recordings was monitored over time to determine the demand value. Finally, tremor-like recordings from a control subject were used to test and demonstrate the real-time adjustment of CR DBS parameters.

Off-line tests and simulations of the implemented technical solutions for the artifact reduction and data analysis were performed in MATLAB before being implemented and tested for real-time processing in Simulink. Afterward, the Simulink modules were converted into C files for hardware applications. The C files were compiled by a C compiler to generate a machine code that was finally tested on a digital signal processor (DSP) board. The latter is placed in a portable neurostimulator and is used for the implementation of new stimulation strategies. The portable neurostimulator is an external trial DBS device which was developed to apply HF and CR DBS protocols to patients (Hauptmann et al., 2009).

The portable neurostimulator is used for both stimulation and data acquisition and has the capability to simultaneously record LFP, tremor and other biological signals during stimulation (Hauptmann et al., 2009). The DSP board can instantaneously access the data acquired by the portable neurostimulator which is necessary for a closed-loop application. In this work, the LFP and tremor recordings used to investigate the realization of the demand-controlled application of desynchronizing CR DBS were recorded by the portable neurostimulator.

1.2 Structure of the thesis

The thesis is organized as follows:

Chapter 2 gives medical background about Parkinson's disease and its pathophysiology and some of its symptoms (Section 2.1). A technical description of the surgical technique DBS for Parkinson's disease is given in Section 2.2. DBS protocols such as the standard stimulation technique HF DBS and the newly developed technique CR DBS are presented in Section 2.2.1 and Section 2.2.2, respectively. In these sections, stimulation parameters and patterns of CR DBS are explained in more detail since most of the implemented technical solutions are dedicated to this DBS protocol.

In **Chapter 3** the technical setup and data used to test the demand-controlled application are introduced. The portable neurostimulator is presented in Section 3.1 and a brief description of the DSP used for real-time data processing is given in Section 3.1.1. Information about LFP recordings from PD patients, from non-human primates and in saline solution is given in Section 3.2.1 and Section 3.2.2. The tremor recordings from PD patients are described in Section 3.2.3. The software and program flow used to generate the machine code for our hardware applications are described in Section 3.3.

Chapter 4 presents the technical solutions for artifact reduction. This chapter describes the implemented algorithms to remove the principal artifacts in the LFP recordings during active CR DBS (Section 4.1). These artifacts include: the stimulus artifact (Section 4.1.1), exponential decay/growth (Section 4.1.2), PLI (Section 4.1.3) and electrical background noise (Section 4.1.4). Further movement and technical artifacts are shown in Section 4.1.5. The optimal artifact reduction sequence during CR DBS is presented in Section 4.1.6. Technical solutions for artifact reduction of spontaneous LFP and tremor recordings are introduced in Section 4.2.

Chapter 5 presents the technical solutions for data analysis and estimation of demand as well as the way how to tune the stimulation parameters. The implemented algorithms to analyse (i) LFP recordings during active CR DBS and (ii) the spontaneous LFP and tremor recordings are introduced in Section 5.1 and Section 5.3, respectively. The implemented algorithms to determine the demand from (i) the LFP recordings during active CR DBS

and (ii) from the spontaneous LFP and tremor recordings are introduced in Section 5.2 and Section 5.4, respectively. Examples for testing the technical solutions on simulated data, LFP recordings from non-human primates, as well as on LFP and tremor recordings from PD patients are shown in this chapter. The real-time tuning of CR stimulation parameters using tremor-like recordings from a control subject is demonstrated in Section 5.5.

In **Chapter 6** the results are summarized and discussed. Real-time artifact reduction and data analysis with the portable neurostimulator are discussed in Section 6.1 and Section 6.2, respectively. The proposed approach for calculating the demand-value from LFP and tremor recordings during and after CR DBS is summarized in Section 6.3. Limitations and future directions are mentioned in Section 6.4.

Appendix A gives information about the implementation of the Nelder-Mead algorithm in Simulink. The algorithm was the main technique used for the removal of exponential and PLI artifacts from the short data segments during active CR DBS.

Appendix B represents the Simulink modules constructed for the demand-controlled application of DBS. All Simulink modules presented in this appendix were converted by the Embedded Coder of MATLAB into C source files and tested with the DSP board within the portable neurostimulator.

Chapter 2

Parkinson's Disease and Deep Brain Stimulation Protocols

2.1 Parkinson's disease

Parkinson's disease (PD) is caused by an alteration of physiological activity of the basal ganglia; a group of nuclei in the brain that play a major role in the control of human movements, association and emotion (Brown, 2003, Bevan et al., 2002, Wichmann & DeLong, 1996). The main components included in the basal ganglia are the striatum, substantia nigra, globus pallidus and the subthalamic nucleus (STN) (Bevan et al., 2002). The substantia nigra is composed of the substantia nigra pars compacta (SNc) and the substantia nigra pars reticulata (SNr), while the globus pallidus consists of the globus pallidus externus (GPe) and the globus pallidus internus (GPi) (Bevan et al., 2002). A simplified diagram of the basal ganglia and its connections to other brain structures is shown in Figure 2.1. The dopaminergic neurons in the SNc produce the chemical neurotransmitter dopamine which is important for the functionality of the basal ganglia system (Alexander & Crutcher, 1990). The output nuclei of the basal ganglia (i.e. the GPi and the SNr) is connected with the striatum through two different pathways: direct and indirect (Obeso et al., 2000). These two pathways are antagonists in their function for motor control. The projection from the striatum to the GPi and the SNr forms the direct pathway, which decreases the inhibition of the thalamus and thus facilitates voluntary movements. The indirect pathway connects the striatum with the GPi and the SNr through the GPe and STN. The excitatory projection from the STN to the GPi and SNr increases the inhibition of the thalamus and thus reduces the muscle activity (Obeso et al., 2000). The balance between both pathways is maintained and modulated by the dopaminergic connections from the SNc to each nucleus (Bevan et al., 2002). Therefore, dopamine is associated with the balance and smoothness of muscle movements (Albin et al., 1989). Chronic and progressive degeneration of dopaminergic cells, especially in the SNc, reduces the level of dopamine (Priebe et al., 2012). This dopamine depletion can be associated with changes in the neuronal firing patterns (Magill et al., 2001).

Parkinson's disease is characterized by abnormal neuronal synchronization (Lenz et al., 1994, Brown, 2003) where neuronal populations e.g. in the thalamus or basal ganglia form a pacemaker that fires in a periodical manner (Deuschl et al., 2000). Under healthy conditions, these neuronal populations fire in an uncorrelated manner (Brown et al., 2001). Pathological oscillations in the local field potentials (LFP) recorded in the basal ganglia are divided into different bands: < 8 Hz ("theta" band), 8 – 13 Hz ("alpha" band) and 14 – 30 Hz ("beta" band) and > 60 Hz ("high gamma" band) (Brown & Williams, 2005). The tremor frequency is classified in the range of 3 – 10 Hz (Bergman & Deuschl, 2002, Brown & Williams, 2005). The limits of each band range are defined in different ways in order to detect the variations along different frequency regions and gain deeper understanding about the disease.

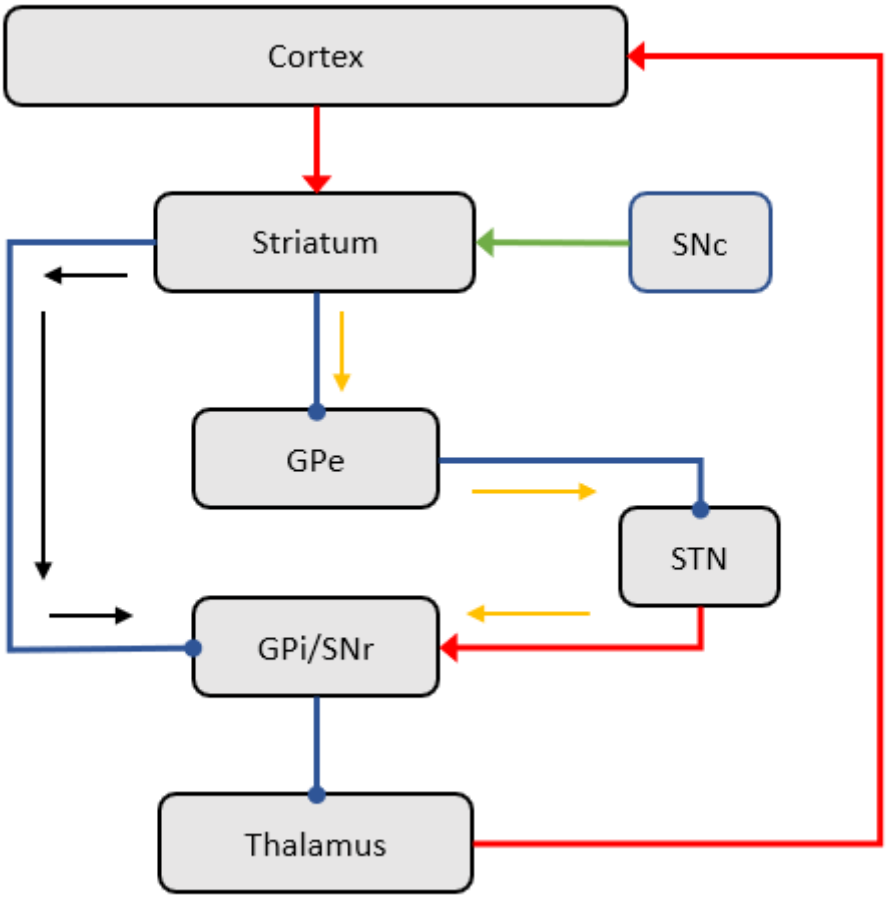

Figure 2.1. A simplified diagram of the pathways in the basal ganglia. The main components included in the basal ganglia are the striatum, substantia nigra, globus pallidus (pars externus and internus) and the subthalamic nucleus. The direct pathway (indicated by the black arrows) goes from the striatum directly to the GPi/SNr and then to the thalamus. The indirect pathway (yellow arrows) goes from the striatum through the GPe and the STN and back to the GPi, then to the thalamus. The dopaminergic connections from the SNc are shown in green, excitatory connections (Glutamatergic) in red, and inhibitory connections (GABAergic) are in blue. This figure is modified from the figures presented in (Bevan et al., 2002).

Symptoms of PD are motoric and non-motoric. Non-motoric symptoms are such as depression, pain and sleep disorders (Chaudhuri & Schapira, 2009). Potential motoric symptoms include bradykinesia (slowing of physical movements), akinesia (complete loss of physical movements), rigidity, postural instability, and resting tremor (Bergman & Deuschl, 2002). Several studies have reported the efficacy of DBS in suppression of parkinsonian tremor (Volkmann, 2007, Nishio et al., 2009, Rodriguez-Oroz et al., 2005). In this thesis, we focus on resting tremor, since it can be externally recorded by means of accelerometers (Van Someren et al., 2006). Tremor-like recordings from a control subject were used to test the demand-controlled application of DBS; in particular, the real-time adjustment of the CR DBS parameters.

Currently, there is no cure for PD; nevertheless, therapies with medications can alleviate the symptoms. A widely used drug for PD is L-Dopa; however, only a small portion of the drug reaches the dopaminergic neurons where it is transformed into dopamine (Latteri et al., 2011). The rest of the L-dopa is often metabolized to dopamine elsewhere, causing a variety of side effects (Wolf et al., 2006). Although the development of L-dopa has dramatically reduced the need for neurosurgical treatment for movement disorders, patients may become resistant to this drug treatment with time (Rodriguez-Oroz et al., 2005).

2.2 Deep brain stimulation (DBS)

DBS has become an effective treatment for advanced PD patients with medically refractory symptoms (Limousin et al., 1995, Benabid et al., 1991). The development of DBS for the treatment of neurological disorders is based on clinical observations and experimental results (Volkmann, 2007). In 1987, Benabid observed that permanent brain stimulation leads to therapeutic benefits like those achieved with surgical lesioning (Benabid et al., 1987, Benabid et al., 1991). By mapping the brain to find the best location to remove tremor, Benabid noticed that acute stimulation of the ventral intermediate (VIM) nucleus at frequencies above 100 Hz suppressed tremor (Benabid et al., 1987, Benabid et al., 2011). Later, DBS was approved in 1997 by the US Food and Drug Administration (FDA) as a treatment for Parkinson's tremor (Coffey, 2009). The list of indications has steadily grown since then and DBS has been approved for psychiatric disorders such as obsessive-compulsive disorders (OCD) and has been tested as a therapy for many other disorders such as Gilles de la Tourette syndrome, epilepsy, and treatment-resistant depression (Coffey, 2009, Hariz, 2012, Miocinovic et al., 2013). DBS is reversible, adaptable, and can be performed bilaterally without making a destructive lesion in the brain (Volkmann, 2007, Benabid et al., 2011).

In the neurosurgical technique DBS, a medical device called brain pacemaker is implanted into patients. The DBS device mainly consists of an implantable pulse generator (IPG), a multi-contact macro-electrode, and connection cables (see Figure 2.2). Macro-electrodes are chronically implanted into target structures according to the type of symptoms to be addressed (Benabid, 2007). The usual targets for the implantation of DBS electrodes for PD patients are either the STN, the globus pallidus internus (GPi) or the ventral intermediate (VIM) nucleus (Brown & Williams, 2005, Benabid et al., 1993). The IPG is implanted under the patient's collarbone and connected to the DBS electrodes through subcutaneous cables. The IPG is battery-powered and can be programmed telemetrically.

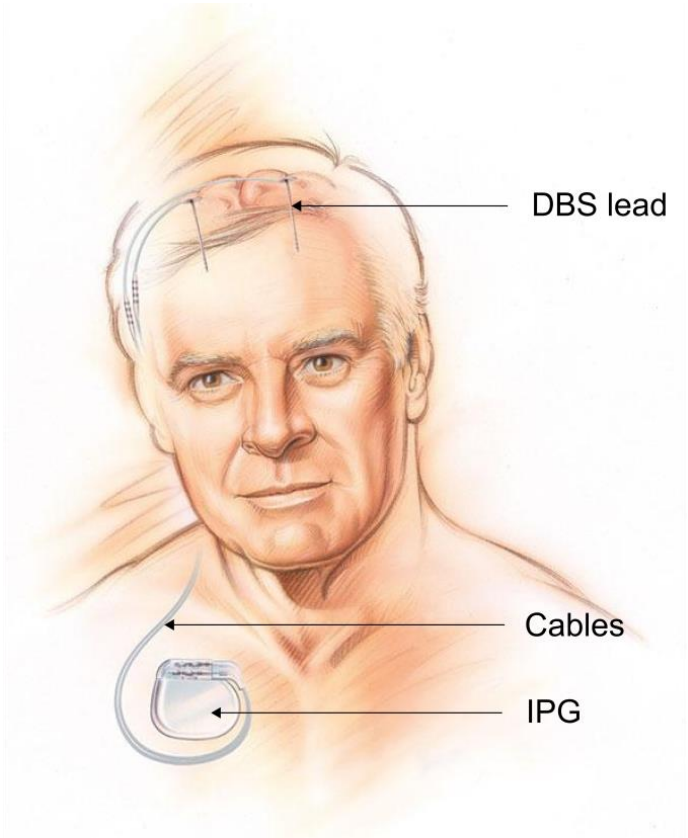

Figure 2.2. Main components of DBS device. The DBS leads implanted in the brain are connected through subcutaneous cables to the implantable pulse generator (IPG) implanted under the patient's collarbone. (Source: courtesy of Medtronic GmbH).

Implantable components of DBS devices are made of materials with long history of use in medical products (Coffey, 2009). Nowadays, Medtronic[2] produces the only US approved DBS device. Medtronic DBS leads have cylindrical shape with four annular platinum/iridium (Pt/Ir) electrode contacts near the tip (Coffey, 2009). The leads are 28 or 40 cm long with a diameter of 1.27 mm, and a 80A urethane outer jacket (Coffey, 2009). The conductor wires within the outer jacket are made of Pt/Ir alloy with fluoro-polymer

[2] Minneapolis, Minn., USA

insulation (Coffey, 2009). The two most used lead-models for DBS are Medtronic lead 3387 and Medtronic lead 3389. Target areas in the brain for lead 3387 are Thalamus, GPi and STN, whereas the target area of lead 3389 is STN (Coffey, 2009). These two leads have a contact length of 1.5 mm and differ in the spacing between the annular contacts where 3387 and 3389 have 1.5 mm and 0.5 mm spacing, respectively (Coffey, 2009). A model of the Medtronic lead 3389 and its electrical field during stimulation are shown in Figure 2.3.

Scaled-down versions of the human DBS macro-electrode, e.g., with a diameter of 0.635 mm, 0.50 mm contact length, and 0.50 mm space between contacts [3], are used to stimulate the brain of non-human primates (Tass et al., 2012). Other producers of DBS devices, who received Conformité Européenne (CE) approval, are St. Jude Medical[4] and Boston Scientific Corporation[5] (Lucht, 2013, Weigelt, 2013). The latter has produced DBS leads with eight cylindrical shape electrode contacts.

Apart from providing therapeutic stimulation, the implanted electrodes for DBS offer a unique opportunity to record pathological neuronal oscillations in the target area. The DBS leads can be connected to external devices such as the portable neurostimulator (see Section 3.1), before being connected to the IPG, to enable intra-operative stimulation or externalized macro-recordings (Hauptmann et al., 2009). LFP activity is recorded intra-operatively, during lead implantation, by micro- and macro-electrodes (Brown & Williams, 2005). LFP activity is typically recorded bipolarly through two of the four contacts of the implanted electrode (Rossi et al., 2007).

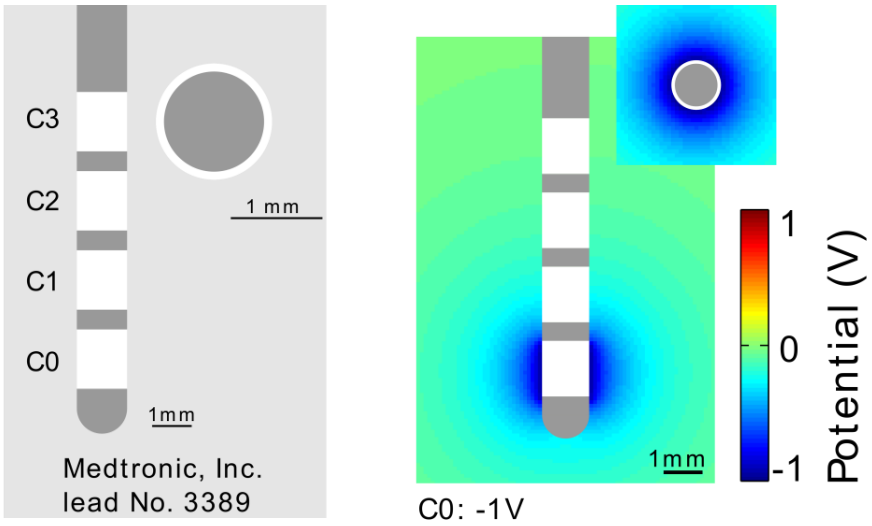

Figure 2.3. A model of an electrode implanted for DBS. Left: Medtronic lead No. 3389. Right: Electrical potential field distribution during stimulation. **(**Source: courtesy of Julia Buhlmann (Buhlmann et al., 2011)).

[3] Numed Inc, Hopkinton, NY
[4] Abbott Inc. (St. Jude Medical), Missesota USA
[5] Boston Scientific - Fremont, California, USA

2.2.1 High-frequency (HF) stimulation protocol

Currently, electrical DBS is performed by administering a permanent HF (> 100 Hz) periodic pulse train applied by the IPG via the depth electrode (Benabid et al., 2009, Little & Brown, 2012). Depending on the patient's clinical status, the IPG delivers a constant voltage pulse train that can be tuned over a wide range of parameters such as amplitude 0 – 10.5 V in 0.1 V steps (assuming a 1 kΩ load, i.e., 0 – 10.5 mA), frequency 3 – 250 Hz with 33 steps, and pulse width (PW) 60 – 450 µs in 30 µs steps increments (Coffey, 2009).

It is well known from experimental studies that irreversible electrochemical reactions may be caused by an unbalanced charge (Harnack et al., 2004), which can lead to tissue destruction (Scheiner et al., 1990) in patient's brain. High charge-densities can be observed, when a pulse train or single pulses are administered (Hauptmann et al., 2009). The charge can be influenced by the duration and amplitude of the pulse, as well as by the resistance and the electrode contact surface (Harnack et al., 2004, Kuncel & Grill, 2004). Therefore, existing brain pacemakers use active or passive charge-balancing techniques (Ortmanns, 2007) to deliver charge-balanced biphasic pulses (Lilly, 1961). No current is delivered into the brain during the intervals between pulses (Coffey, 2009).

DBS devices typically implement biphasic and asymmetric rectangular stimulus waveforms that are charge-balanced (Foutz & McIntyre, 2010). The portable neurostimulator applies charge-balanced and rectangular waveforms consisting of a high

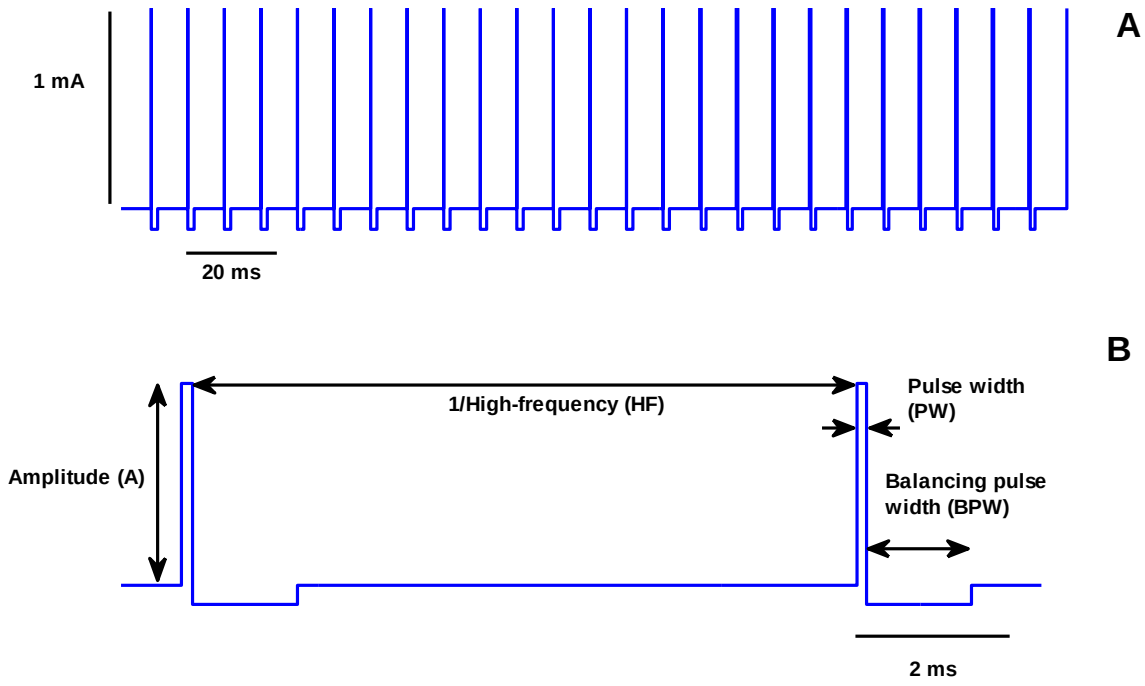

Figure 2.4. Stimulation parameters of HF DBS protocol. A: HF DBS biphasic pulse train at 130 Hz. B: Two HF pulses (magnified plot of signal represented in A) are shown to illustrate the stimulation parameters.

amplitude and short duration phase followed by a low amplitude and long duration phase (Hauptmann et al., 2009) as shown in Figure 2.4. The electrical DBS pulses can be applied with cathodic or anodic polarity. Nevertheless; other different stimulation waveforms could be more effective in terms of, e.g., therapeutic stimulation or energy consumption than rectangular waveforms (Foutz & McIntyre, 2010).

Stimulation parameters such as frequency, pulse width, and amplitude are modified intermittently every 3-12 months and patients normally attend checkups at neurology clinics for this update (Rosin et al., 2011). Between clinical modifications, the stimulation parameters remain unadjusted. The optimal choice of stimulation parameters is crucial for maximal clinical improvement (Lysyansky et al., 2011). It is also possible that the patient can modify some parameters through a dedicated device that communicates in a wireless mode with the IPG. This modification only can affect a limited range of parameter values determined by the clinicians.

Despite many clinical improvements in some patients, HF DBS causes side effects such as cerebellar ataxia (inability to coordinate balance), dysesthesia (abnormal sensation), dysarthria (difficulty saying words), memory decline and depression (Deuschl et al., 2006b, Rodriguez-Oroz et al., 2005, Volkmann, 2004, Tasker, 1998). The causes for the occurrence of side effects are still not fully understood. Possible reasons might be the improper placement of the electrodes or excessive current delivery (Lumsden et al., 2013, Starr et al., 2004). Furthermore, pathological neuronal synchronization reappears within seconds once HF DBS is turned off (Meissner et al., 2005). Therefore, more efficient stimulation techniques are required to increase the therapeutic benefits and to reduce unpleasant side effects.

2.2.2 Coordinated reset (CR) stimulation protocol

Coordinated reset is introduced as a robust desynchronizing stimulation technique (Tass, 2003b, 2003a). It is primarily developed for electrical DBS to enable effective desynchronization and unlearning of pathological synchrony and connectivity (Tass, 2003b, 2003a). CR is based on the fact that the brain is an adaptive system that is capable to learn. Therefore, CR aims at long-lasting effects by forcing the brain to unlearn the pathological activity through external perturbation, i.e. through electrical CR stimulation. In the CR DBS protocol, short sequences of high-frequency pulse trains are delivered to the brain in a coordinated manner, i.e. at different times at different contacts of the stimulation electrode (Tass, 2003b, 2003a) as illustrated in Figure 2.5.B and Figure 2.6. Consequently, the synchronized neuronal population is divided into several sub-populations, i.e. a cluster state, where the sub-populations are phase-shifted with respect to each other. Subsequently, the sub-populations go from the cluster state to network desynchronization (Tass, 2003b) as shown in Figure 2.5.D. In order to maintain

and prolong the desynchronization state, CR is applied in an *m:n* ON-OFF mode, where *m* cycles with CR stimulation pulses are followed by *n* cycles without stimulation (Tass, 2003b, Lysyansky et al., 2011).

The long-lasting desynchronizing effects of CR stimulation have been investigated in detail in several theoretical studies (Tass & Majtanik, 2006, Hauptmann & Tass, 2007, Tass & Hauptmann, 2007, Hauptmann & Tass, 2009). In addition, CR stimulation of the subthalamic nucleus shows both acute and sustained long-lasting after-effects on motor function in parkinsonian non-human primates (Tass et al., 2012). CR stimulation in non-human primates indicates a possible mechanism of CR DBS; the decrease in synaptic connectivity which reduces the pathological oscillatory activity within the motor circuitry (Tass et al., 2012).

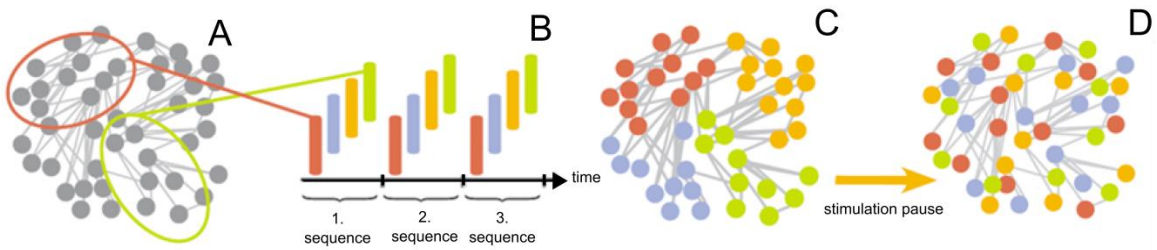

Figure 2.5. Illustration of the neuronal desynchronization due to CR DBS. A: Synchronized neuronal population. B: Brief and mild resetting stimuli administered at different sites at subsequent times. C: Cluster state. D: Transient desynchronization. **(**Source: ANM GmbH, courtesy of Dr. C. Hauptmann).

CR stimulation parameters

Besides the stimulation parameters used in standard HF DBS, some additional parameters (illustrated in Figure 2.6.) are included in the CR stimulation protocol:

CR frequency (F_R): The frequency at which the CR stimulation pattern is repeated.

On-cycle (C_{on}): One period of F_R in which the CR stimulation bursts are delivered via the selected contacts of the electrode.

Number of on-cycles (N_{on}): The number of C_{on} that are delivered in succession.

Off-cycle (C_{off}): One period of F_R in which no CR stimulation bursts are delivered to the target area in the brain.

Number of off-cycles (N_{off}): The number of C_{off} that are delivered in succession.

Number of pulses (N): The number of pulses included in each burst delivered through one contact of the electrode. An overlap between two stimulation bursts of two contacts is not allowed.

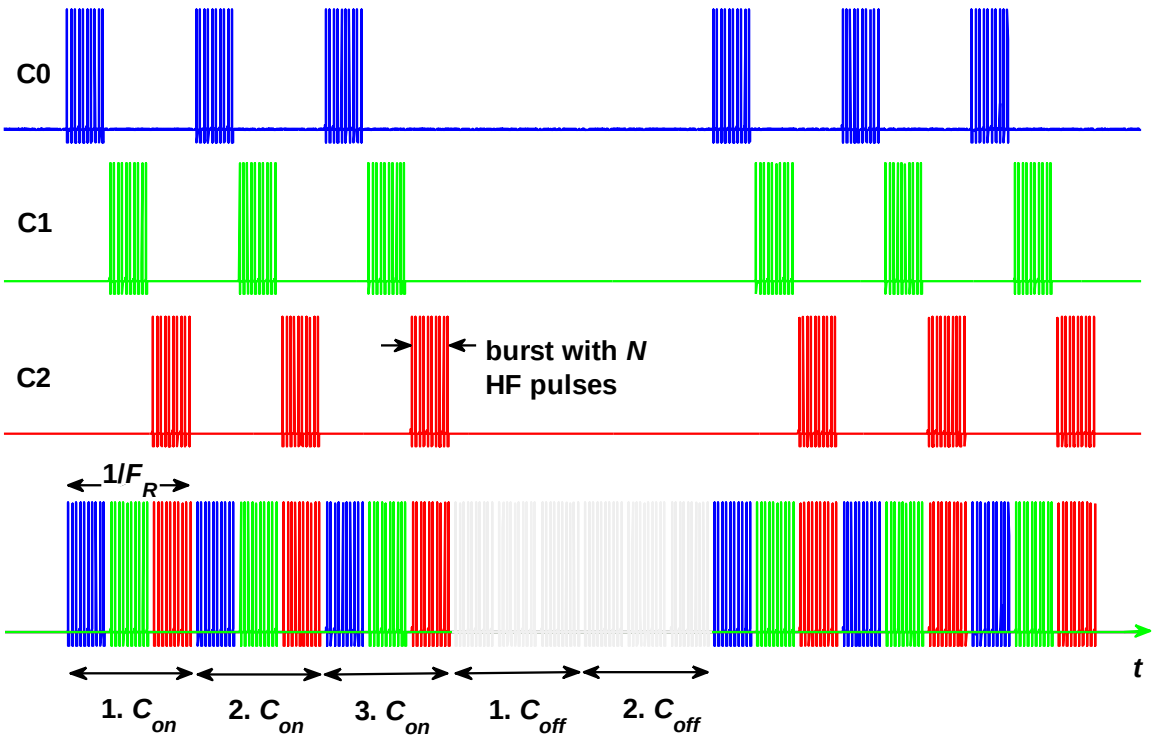

Figure 2.6. Stimulation parameters of CR DBS protocol. The three stimulation signals (blue, green, and red) are delivered to the brain in a coordinated manner, i.e., at different times through the three contacts (C0, C1 and C2) of the electrode. The fourth contact is used as a reference. The signal at the bottom represents the sum of all pulses to illustrate the parameters of CR DBS protocol. In this figure, three successive C_{on} are followed by two successive C_{off}. The CR parameter values used in this case are: HF 130 Hz, F_R 5 Hz, N_{on} 3, N_{off} 2, N 10, PW 120 µs, and BPW 1200 µs.

CR stimulation patterns

The CR stimulation technique enables the application of different stimulation patterns by changing the activation sequence of the three contacts of the implanted electrode (Hauptmann et al., 2009). For instance, the stimulation bursts of the three contacts can have a fixed sequence during stimulation as illustrated in Figure 2.7.A. The fourth contact is used as reference (more details can be found later in Section 3.2.1). In order to reduce the risk of inducing a cyclic activation of the pathological neuronal population, the sequential activation of the stimulation contacts can be randomized (Hauptmann et al., 2009) as shown in Figure 2.7.B. In addition, the number of pulses in each burst and the delay between bursts allow the portable neurostimulator to apply a variety of CR stimulation patterns. Further variations of the CR stimulation pattern were discussed deeply in a modeling study (Tass & Hauptmann, 2009).

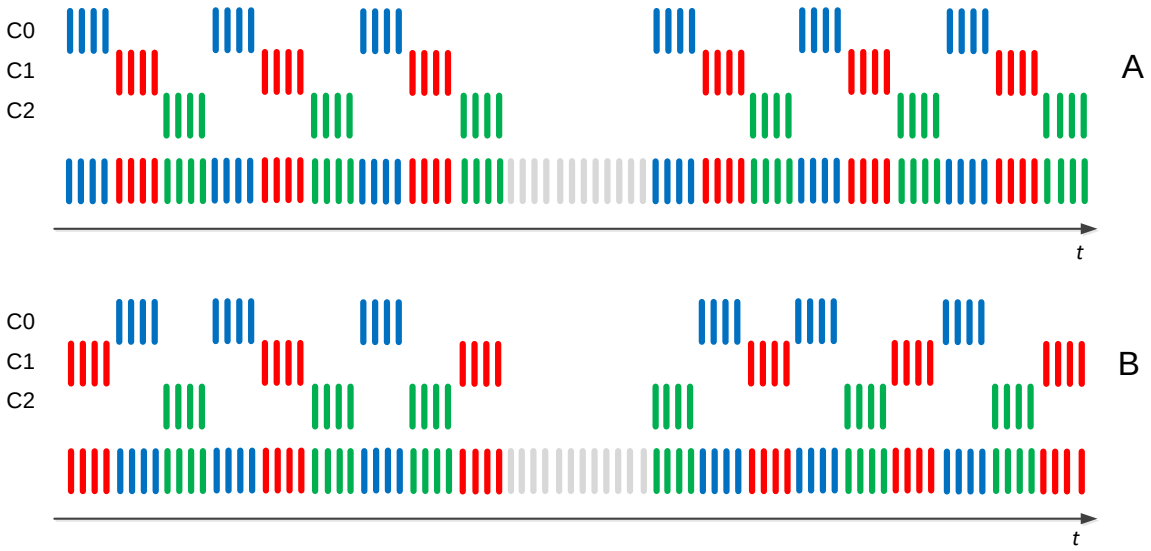

Figure 2.7. Schematic illustration of CR DBS patterns. A: Sequential CR stimulation; the stimulation bursts have fixed sequence. B: Random CR stimulation; the stimulation bursts of the three contacts follow a random sequence. This figure is modified from the figures presented in (Hauptmann et al., 2009).

Chapter 3

Technical Setup and Data Acquisition

3.1 The portable neurostimulator

The portable neurostimulator[6] is a medical device used for both data acquisition and stimulation. It is mainly used as an external trial deep brain stimulation (DBS) device for the application of desynchronizing stimulation techniques (Hauptmann et al., 2009). Several stimulation strategies can be applied to patients. Among them, one can mention high-frequency (HF) and coordinated reset (CR) DBS as well as visual and acoustic stimulation protocols. In terms of data acquisition capabilities, the portable neurostimulator enables the recording of local field potentials (LFP) through sixteen channels, electro-encephalograms (EEG) through twelve channels, electromyograms (EMG) through ten channels, and heart rate and breathing activity. In addition, six accelerometers and two strength sensors can be connected to the portable neurostimulator. The device is powered either by internal rechargeable batteries or by a peripheral power supply.

Mainly, three components (shown in Figure 3.1.) were involved in the development of the demand-controlled application of CR DBS:

(i) The portable neurostimulator used as a stimulation and data acquisition unit.
(ii) A laptop associated to the portable neurostimulator used as a unit visual inspection of data and modification of the stimulation process.
(iii) An additional laptop used as a programming unit.

The stimulation is controlled using a software on laptop (ii). In order to create a better interface experience for the physician, this software had implemented a graphical user interface (GUI) that allows the selection of stimulation parameters, stimulation mode, and the stimulation electrode (see Figure 3.2). Stimulation parameters pass through a plausibility check before being transferred from the laptop to the portable neurostimulator establishing whether they are within the predefined interval (Hauptmann et al., 2009). The

[6] The portable neurostimulator was developed by the Institute of Neuroscience and Medicine at the research center Juelich, Germany.

portable neurostimulator establishes wired or radio communication with the laptop. The GUI is divided into several functional areas. The one used to modify the stimulation parameters (blue frame in Figure 3.2) is more relevant for the demand-controlled application of DBS. Additionally, the GUI enables data visualization and video streaming of patients in real-time.

The recorded data is converted from analog to digital signal and stored as a binary file on the hard disk of the laptop. The sampling rate used for data acquisition is 1 kHz with an amplitude resolution of 24 bits. An additional log file (ASCII format) documents the on- and offset of stimulation, initiation of the data and video file. Each modification of the stimulation mode or parameters is also registered in this file. We refer to (Hauptmann et al., 2009) for more details regarding the portable neurostimulator system.

The programming laptop (iii) is mainly used to implement the technical solutions for artifact reduction and data analysis as well as for programing new stimulation protocols. The programming laptop can be connected to laptop (ii) via LAN to enable data analysis in real-time. This analysis is performed without influencing critical tasks on laptop (ii) such as control of stimulation protocol and data storage. The transfer of the implemented algorithms between the digital signal processor (DSP) board placed in the portable neurostimulator and the programming laptop was handled via a universal serial bus (USB) cable.

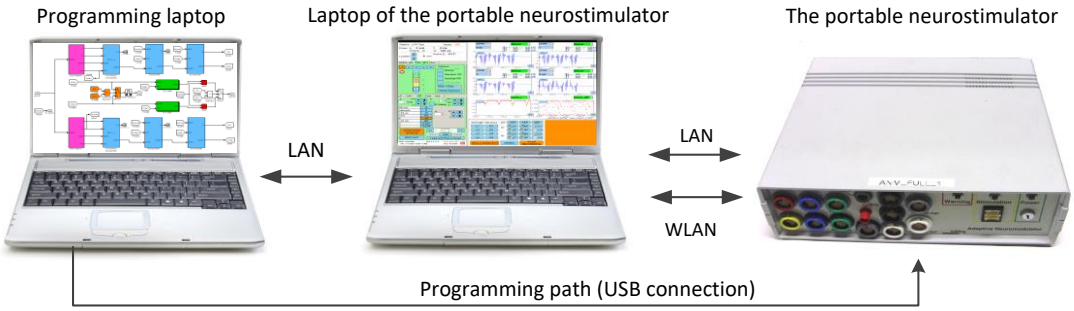

Figure 3.1. Main hardware components used for the demand-controlled application of desynchronizing CR DBS. Right: Portable neurostimulator device used for both data acquisition and stimulation. Middle: Laptop of the portable neurostimulator used for data visualization and modification of the stimulation process. Left: Programming laptop for the implementation of the demand-controlled algorithms. Connections between the portable neurostimulator and its paired laptop are set via LAN and WLAN. The additional programming laptop is connected via a USB cable.

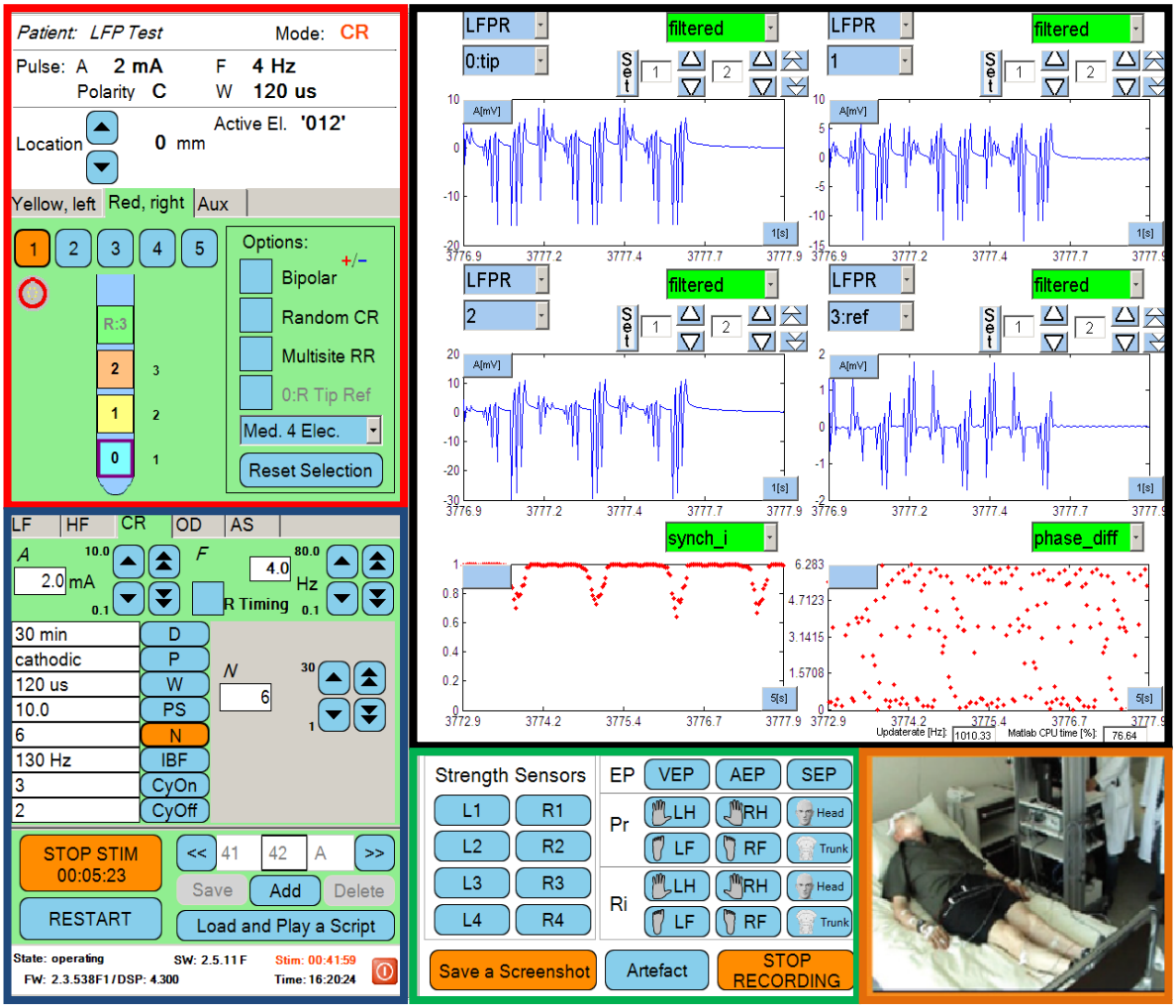

Figure 3.2. Graphical interface of the portable neurostimulator. The functional areas are indicated by different colored frames. Red frame presents patient data, stimulation mode, and selection of stimulation contacts. Blue frame shows stimulation patterns and parameters. Black frame help us to visualize in real-time the stimulation signals and recorded data. Green frame: Indicators of the patient status in order to register movement artifacts and manage the data storage. Orange frame: A video display of the patient.

3.1.1 Digital signal processor board

The demand-controlled application of DBS was tested with the TMS320C6713 DSP board[7] shown in Figure 3.3. The main advantage of such a processor is its versatility, which enables designing, testing, and implementing algorithms for real-time applications (Spectrum Digital, 2006). For more details about the key features of the DSP board (i.e., central processing unit (CPU), memory and peripherals) we refer to (Kuo & Gan, 2004, Rulph, 2004).

[7] The DSP resides on a board from Texas Instruments (Spectrum Digital, EBV Electronik, CH).

The DSP board has instantaneous access to the data recorded by the portable neurostimulator which is necessary for the DBS autonomic system. The implemented technical solutions for artifact reduction and data analysis were optimized iteratively in order to meet the requirements of the DSP board. Parts of the implemented algorithms and the recorded data were stored on the external memory of the DSP in order to overcome the internal memory limitations. However, splitting the implemented algorithms between internal and external memories affected the DSP performance. The limited bus width (32-bit), between CPU and external memory has limited fetching capability for the required data in the short clock cycle; particularly, when the iteration loops of the algorithms were processed.

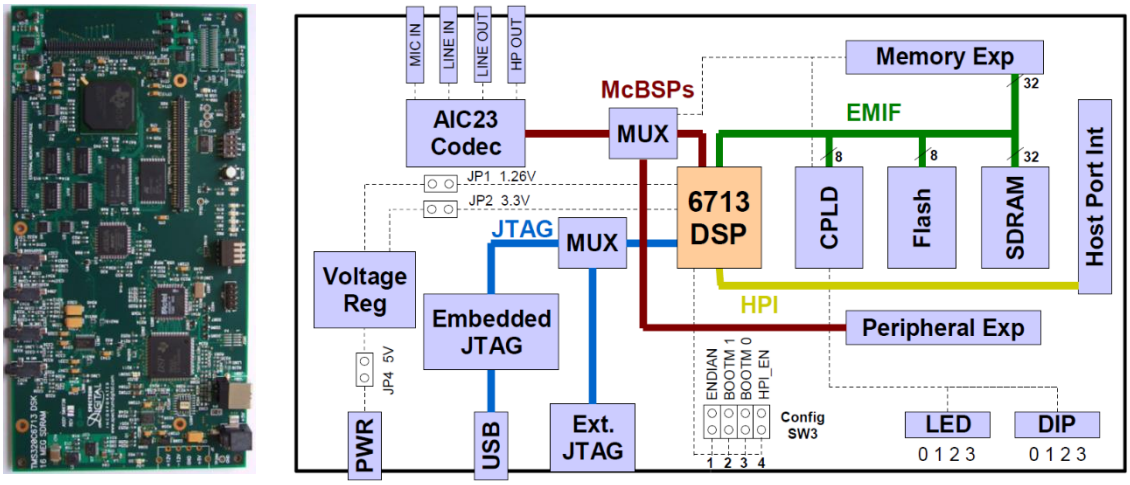

Figure 3.3. The TMS320C6713 DSP board. Left: The DSP board placed in the portable neurostimulator and used to test the demand-controlled application of DBS. Right: Main hardware components of the DSP board.

3.2 Data acquisition

The implemented technical solutions for the demand-controlled application of desynchronizing CR DBS are tested retrospectively. We used existing LFP and tremor recordings collected from Parkinson's disease (PD) patients, from parkinsonian non-human primates and in *in–vitro* (i.e., in saline solution). The data of PD patients was used in accordance with European and German data protection provisions. The patients approved the usage of data for scientific research projects and participated with informed written consent and with the permission of the local ethics committee. Additionally, all the animals, whose data are used in this thesis, were handled according to the guidelines for the care and use of laboratory animals established by the Beijing Association for Laboratory Animal Science.

3.2.1 LFP recordings

The human LFP activity was recorded from the target area intra-operatively, i.e. during the implantation of the DBS electrode, and post-operatively, i.e. before connecting the electrode to the implantable pulse generator (IPG). LFP activity was recorded from the subthalamic nucleus (STN) or the ventral intermediate (VIM) nucleus from four patients with unilateral (one side, e.g. hand) or bilateral (both sides) predominant resting tremor (Tass et al., 2010). Taking into account the fact that recording of neuronal activity generated at a distance and picked up by two contacts increases the likelihood that only local potentials are recorded, LFP activity was measured bipolarly among each of these three contacts (0, 1 and 2) and the contact number 3 which is used as a reference (Brown et al., 2001). In other words, the data was collected between three contact pairs 0-3, 1-3, and 2-3. Mostly, one or two contacts are located in the target area in the brain. For more details regarding tremor patients and the data acquisition procedure we refer to (Tass et al., 2010).

Non-human LFP recordings were collected from three parkinsonian Macaque monkeys (Xierxin, China). These monkeys were rendered parkinsonian by injecting 1-methyl-4-pheny1-1,2,3,6-tetrahydropyridine (MPTP). Animals were hosted under controlled conditions of humidity, temperature and light, in individual cages. After achieving a stable parkinsonism, a scaled-down version of the human DBS macro-electrode (described in Section 2.2) was implanted bilaterally under stereotactic guidance into the STN (Tass et al., 2012). Spontaneous LFP recordings were performed by the portable neurostimulator for at least 2 minutes after stimulation sessions. More than 20 recordings from each side of the brain were made over 4 months.

3.2.2 Tests in saline solution

As a proof-of-concept, the implemented algorithms for artifact reduction and data analysis were tested with LFP recordings collected in saline solution. The experimental configuration, shown in Figure 3.4, aimed at generating stimulation/recording conditions in absence of neuronal activity to study and optimize the accuracy of the implemented algorithms. The tests were carried out at different time stamps and locations using two types of electrodes: a Medtronic DBS electrode model 3389 used for humans and a scaled-down version used for non-human primates (see Section 2.2 for more details). The electrodes were immersed in glass container filled with saline solution[8] at room temperature and connected to the portable neurostimulator. One contact was used as reference and the other three contacts were dedicated for performing the stimulation and LFP recording. The CR

[8] 8.6g of NaCl per liter of water, Berlin Chemie AG, Germany

stimulation parameters were set to HF 130 Hz, F_R 4 Hz, A 2 mA, N_{on} 3, N_{off} 2, N 6, PW 120 µs, polarity cathodic (for more details on the DBS parameters see Section 2.2.1 and Section 2.2.2).

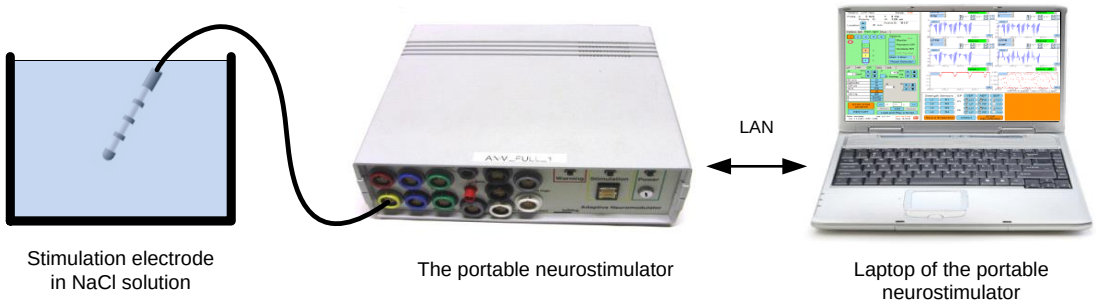

Figure 3.4. Experimental setup for LFP recordings in saline solution. Left: Medtronic stimulation electrode model 3389 is placed in saline solution. Middle: Portable neurostimulator is used for stimulation and data acquisition. Right: Laptop associated to the portable neurostimulator is used to control and monitor the stimulation/recording process.

3.2.3 Tremor recordings

Parkinsonian tremor recordings were collected from patients using accelerometers during and after CR DBS sessions (Tass et al., 2010). A maximum of six DC-response accelerometers (FGP FA108-A1 S/N6081) were fixed to the limbs of PD patients, specifically to the hands and lower legs. The accelerometers are used for measuring very low vibrations in one axis. In this work, the data of four PD patients with predominant resting tremor were used to test the demand-controlled application of DBS. The tremor signals, recorded at time epochs in which patients developed evident tremor, were correlated with the video stream of patients. In this thesis, whenever the word “tremor” is used, it refers to the parkinsonian resting tremor. We also use the abbreviation ACC for tremor recordings in some figures.

Additionally, the tremor signals were used to demonstrate the tuning of the stimulation parameters in real-time during CR DBS. These tests were performed with tremor-like signals generated by a healthy subject and recorded using the portable neurostimulator. An accelerometer was placed on the right hand of the subject who imitated tremor with different frequencies and amplitudes. Several tests were performed to adjust stimulation parameters during sequential and random CR stimulation, as well as during HF DBS. Each test lasts 80 s and, in every case, only one stimulation parameter was adjusted (see Section 5.5 for more details).

3.3 Software applications

Three software environments were used for the development of the demand-controlled application of CR DBS: MATLAB[9], Simulink[10], and Code Composer Studio (CCS)[11]. MATLAB is technical computing software that performs numerical computation, acquisition and visualization of data. Simulink is an extension of MATLAB used for modeling, simulating, and analyzing dynamical systems (Angermann et al., 2007). CCS is a C compiler used for the compilation of code with respect to dedicated target hardware such as DSPs.

Off-line tests were performed in MATLAB in order to characterize the dynamics of the LFP and tremor recordings and to test the performance of the implemented algorithms for artifact reduction and data analysis. After off-line, these algorithms were transferred to Simulink which was the main platform used for the real-time implementation. Different algorithms for artifact reduction and data analysis were implemented and optimized to meet the DSP board requirements. The program flow for generating the machine code is shown in Figure 3.5. All implemented Simulink modules for the demand-controlled application of DBS are described in Appendix B.

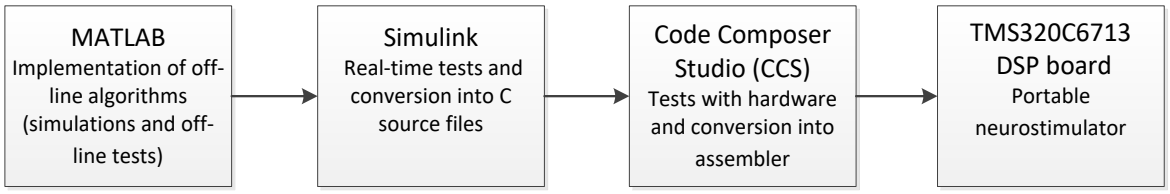

Figure 3.5. Flow diagram of the machine code for the demand-controlled application of DBS. Algorithms for artifact reduction and data analysis were tested off-line in MATLAB before being implemented in Simulink for real-time processing. Then, the Embedded Coder of MATLAB converts the Simulink modules into C source files. Finally, these C source files are compiled using CCS and implemented on the memory of the DSP board.

[9] MathWorks, Inc., USA, version 2007a and 2006b
[10] MathWorks, Inc., USA, version 2006b
[11] Texas Instruments, USA, version 3.1. CCS is software provided by the Texas Instruments to support its DSPs platforms.

Chapter 4

Software-based Solutions for Artifact Reduction

The implanted electrodes for DBS can be connected intra- and post-operatively to external devices such as the portable neurostimulator before being connected to the implantable pulse generator (IPG), i.e. while the connection cables are still accessible. Apart from providing therapeutic stimulation, the implanted electrodes offer a unique opportunity to record pathological neuronal activity from the target area in the brain. These electrodes record the electrical activity, i.e. the local field potential (LFP) in the vicinity of its contacts and this enables to study the pathological neuronal dynamics.

LFP recordings during DBS are normally contaminated by strong artifacts that are caused by technical drawbacks. Several techniques have been proposed for artifact removal during DBS, especially for high-frequency (HF) DBS. However, these techniques cannot compensate the effect of several factors like stimulation and recording systems, ambient environment etc. Artifact-reduced LFP recordings can be used as feedback signal for the demand-controlled application of DBS and support the rational selection of stimulation parameters (Kent & Grill, 2012, Rossi et al., 2007).

The LFP recordings during desynchronizing coordinated reset (CR) DBS are also contaminated by artifacts caused by hardware, patients' movement and the background. The artifacts found in the LFP recordings during active CR DBS differ from those detected in the spontaneous signals recorded after stimulation. In this chapter, we discuss each type of artifact along with its developed and implemented reduction techniques which were tested off-line before being implemented for real-time processing. These tests were performed with data collected from PD patients, non-human primates, and in saline solution.

4.1 Artifact reduction during CR DBS

To effectively reduce artifacts during CR DBS, some information on their characteristics were required, such as their source, form and regularity. The principal artifacts found in LFP recordings during CR DBS are:

1. Stimulus artifact
2. Saturation artifact (exponential decay after stimuli)
3. Power line interference (PLI)
4. Electrical background noise

4.1.1 Stimulus artifact

The stimulus artifact is a technical problem created by the electrical stimulation pulses. Simultaneous stimulation and LFP recording via the implanted electrode often prevent the neuronal activity from being recorded properly. The typical graphical description of stimulus artifact shows a spike followed by an exponential decay curve (McGill et al., 1982). Several techniques have been introduced for the removal of the stimulus artifact. An overview of these techniques and their applicability to the LFP recordings during CR DBS is presented in this section.

Several researchers have written about the usage of analogue and digital filters for the removal of the stimulus artifact (Wichmann, 2000, Rossi et al., 2007). Although digital filters are successful in eliminating high-frequency components of this artifact, they may not be able to restrict its low frequency components (Al-ani et al., 2011). Moreover, it is difficult to remove the stimulus artifact in the frequency domain by means of filters, since filtering is inadequate for eliminating artifacts with a frequency content close to that of the neuronal structure (Wichmann, 2000, Hashimoto et al., 2002).

Furthermore, the LFP recordings during CR DBS indicate that the stimulation pulses are followed by exponential decays as shown in Figure 4.1. This figure presents LFP recording in saline solution with stimulation periods (i.e., on-cycles) and large pauses (i.e., off-cycles). The figure also illustrates the variability of the stimulus artifact in terms of: (i) amplitude and (ii) exponential decays after stimuli (i.e. during the on-cycles) and between stimulation periods (i.e. during the off-cycles). The application of filters to these decays caused low frequencies which overlapped the spectral components of the neuronal activity. Additionally, the removal of the stimulus artifact by means of filters has affected the short off-cycles (i.e., < 500 ms), which are included in the CR stimulation protocol and which are, by construction, free of stimulus artifact (see Section 2.2.2).

Another approach has been the subtraction of a template of the artifact from the LFP recording (Hashimoto et al., 2002, Wichmann, 2000, Blogg & Reid, 1990). Such a template can be built by averaging a large number of artifact-containing segments of LFP recordings, which are triggered by their onset. The artifact is expected to be removed by subtracting the template from the individual and subsequent segments. This approach could help in revealing neuronal responses with short latency to stimulation (Hashimoto et al., 2002); however, this method presents some limitations. For instance, if a neuronal response occurs with a fixed latency to the stimulus artifact, it might appear in the artifact template; thus,

getting eliminated from the subsequent segments. In addition, building a template without neuronal activity is not well-suited for real-time processing, though it might be better suited for off-line procedures.

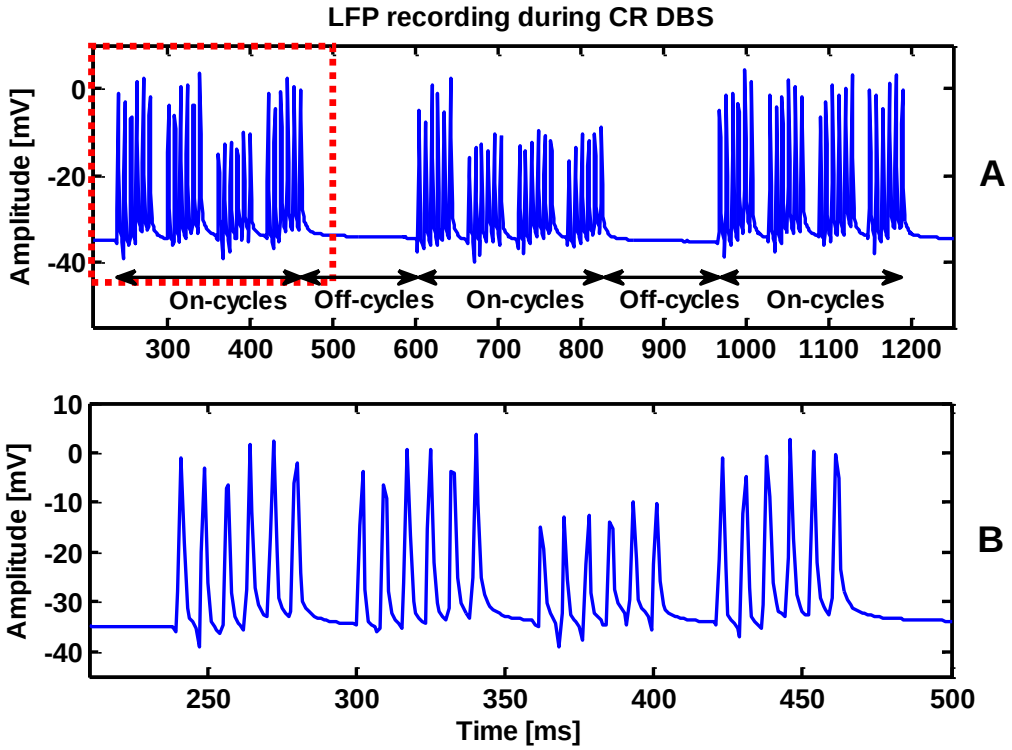

Figure 4.1. Stimulus artifact in the LFP recordings during CR DBS. A: LFP recording in saline solution during CR DBS. B: Magnified plot of the dashed red frame in graph A shows the stimulus artifact during the on-cycles. The graphs illustrate the variability of the stimulus artifact in terms of: (i) amplitude and (ii) exponential decays after stimuli (i.e. during the on-cycles) and between stimulation bursts (i.e. during the off-cycles).

Some authors have also come up with the implementation of hardware and software blanking for removal of the stimulus artifact (Knaflitz & Merletti, 1988, Roby & Lettich, 1975, Black et al., 1983). In this approach, an electrical circuit switch is turned on to sample the input signal and turned off to hold-mode during the artifact (Freeman, 1971, Babb et al., 1978). The circuit is usually triggered either by an external pulse or by the stimulation pulse itself (Minzly et al., 1993). A disadvantage of the hardware blanking method is that it involves the usage of analogue electronics which are not that stable, and could blank out some useful information as well (O'Keeffe et al., 2001). Specifically, if the trigger signal mismatches the targeted segment of the input signal, a part of the stimulus artifact could persist and get recorded along with the neuronal activity.

Another practiced method is the ‘down-sampling and interpolation’ of LFP recordings. Under this method, the signal is down-sampled in such a way that only the time intervals between stimuli are sampled (Waddell et al., 2009). However, this method requires a high sampling rate (e.g. > 10 kHz), whereas the LFP recordings of the portable neurostimulator

are sampled at 1 kHz to support the real-time processing. In addition, it demands that the stimulus artifact should have a clear shape. This is because the interaction between the new samples in the presence of unclear stimulus artifact might affect the spectral content of the recorded data. The stimulus artifact, recorded through the LFP recordings during CR DBS, is irregular in shape, and is followed by irregular exponential decays as shown in Figure 4.1.

Due to the variability of the stimulus artifact, and the subsequent exponential artifact after each stimulus, the fore-mentioned techniques are unable to adapt to the artifact dynamic. Consequently, residuals of the stimulus artifact could still exist. In order to remove the exponential artifact during CR DBS (i.e. during the on-cycles), fitting functions should be calculated for each exponential artifact in real-time. This procedure results to be computationally expensive, affecting the performance of the digital signal processor (DSP) board. Consequently, the total removal of the LFP recordings within the on-cycles was necessary for the accurate interpretation of the recorded neuronal activity.

The technical solutions for artifact reduction and data analysis during CR DBS were executed such that only the off-cycles were considered. The CR stimulation protocols contain larger pauses (off-cycles) of up to 500 ms where no stimulation is applied. Collecting this stimulus artifact-free data can be useful for analyzing the pathological neuronal activity on a regular basis (Hauptmann et al., 2009). Therefore, we implemented two methods to delimit the off-cycles from the LFP recordings in real-time: *candidate segment of data* and *sawtooth wave*. The latter is calculated based on the CR stimulation parameters used.

Candidate segment of data

This method involves the following steps:

***Detection of off-cycles*:** during the on-cycles, the amplitude of the stimulus artifact is much larger than the biological signal; whereas, during the off-cycles, the signal decreases exponentially and approximately by a factor of ten. This difference in amplitude was used to set a user-defined threshold for detection of the off-cycles. The output of this step consists of only logical values (1/0), where ones and zeros are assigned to values above and below the threshold respectively, as illustrated in Figure 4.2.A. Although a threshold can be manually set on the laptop paired with the portable neurostimulator (for more details see Section 3.1), a fixed threshold was mostly used for a large number of PD patients.

***Segmentation*:** the aim of this step is to identify whether the binary output of the previous step corresponds to the on- or off-cycles. This is because for exponential decay segments, even the on-cycles may have values low enough after stimuli to cross the threshold set for detecting the off-cycle values, resulting in zeros in the binary output. Fortunately, the duration of the off-cycles is much longer than the time between two stimuli in the on-cycles,

and the amplitude of the signal during the off-cycles is always below the threshold. Hence, it was possible to eliminate the problem of zeros of the on- cycles by setting the following condition: the logical values after the threshold should include a specific and long enough chain of successive zeros. These successive zeros correspond to signal values that are considered a valid candidate to be included in the data to be analyzed; also known as a *candidate segment of data*, as shown in Figure 4.2.B.

***Comparison*:** The aim of this step is to determine the onset and end of the off-cycles. A window of comparators is used to examine the values of the *candidate segment of data*. The length of the window (typically 10 – 80 values in 10 steps) should be given before the detection step is performed. The *candidate segment of data* should include a vector of successive zeros of the window of comparators' length. If all values of the *candidate segment of data* match the values set for the window of comparators (zeros), one-flag is

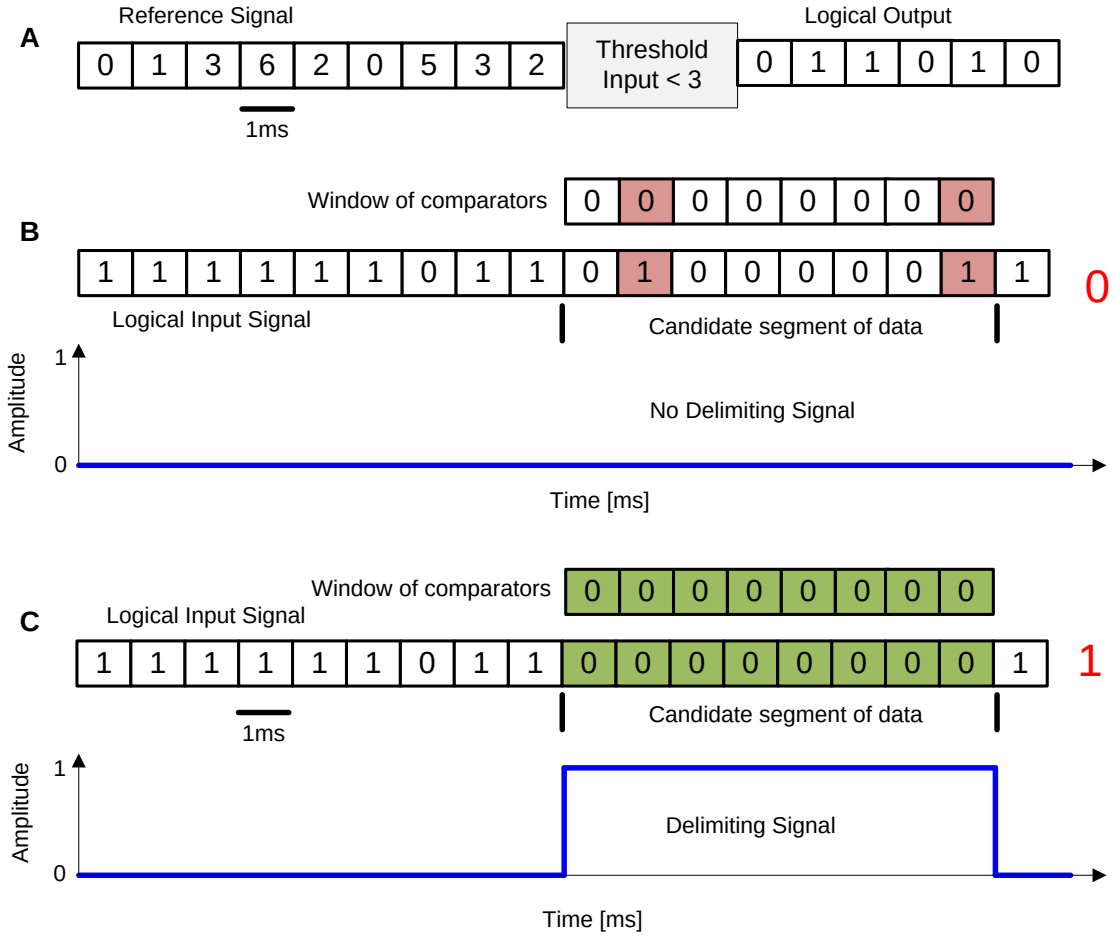

Figure 4.2. Illustration of the concept of the *candidate segment of data* method for delimiting the off-cycles in real-time. A: Samples of LFP recording, for which a threshold (input>3) is set, which translates the input signal in binary (1/0). B and C demonstrate the two different cases of matching results in binary, which are matched by window of comparators containing the same number of zeros. B: Mismatch of signal (red background). C: Match of signal (green background). The zero- and one-flags (colored red) to the right indicate whether the next step is enabled or not to form the delimiting signal.

given by all comparators to indicate that the next step is enabled, as shown in Figure 4.2.C. However, in case of mismatch, a zero-flag is given, i.e. the current segment is omitted and the next one is processed, and simultaneously, the input signal is shifted by one sample.

***Delimitation*:** If the previous step results in a one-flag, a delimiting signal is generated, which is automatically synchronized with the LFP recording. By multiplying both signals, only the off-cycles appear in the output for further processing, as illustrated in Figure 4.3 Subplots D and E.

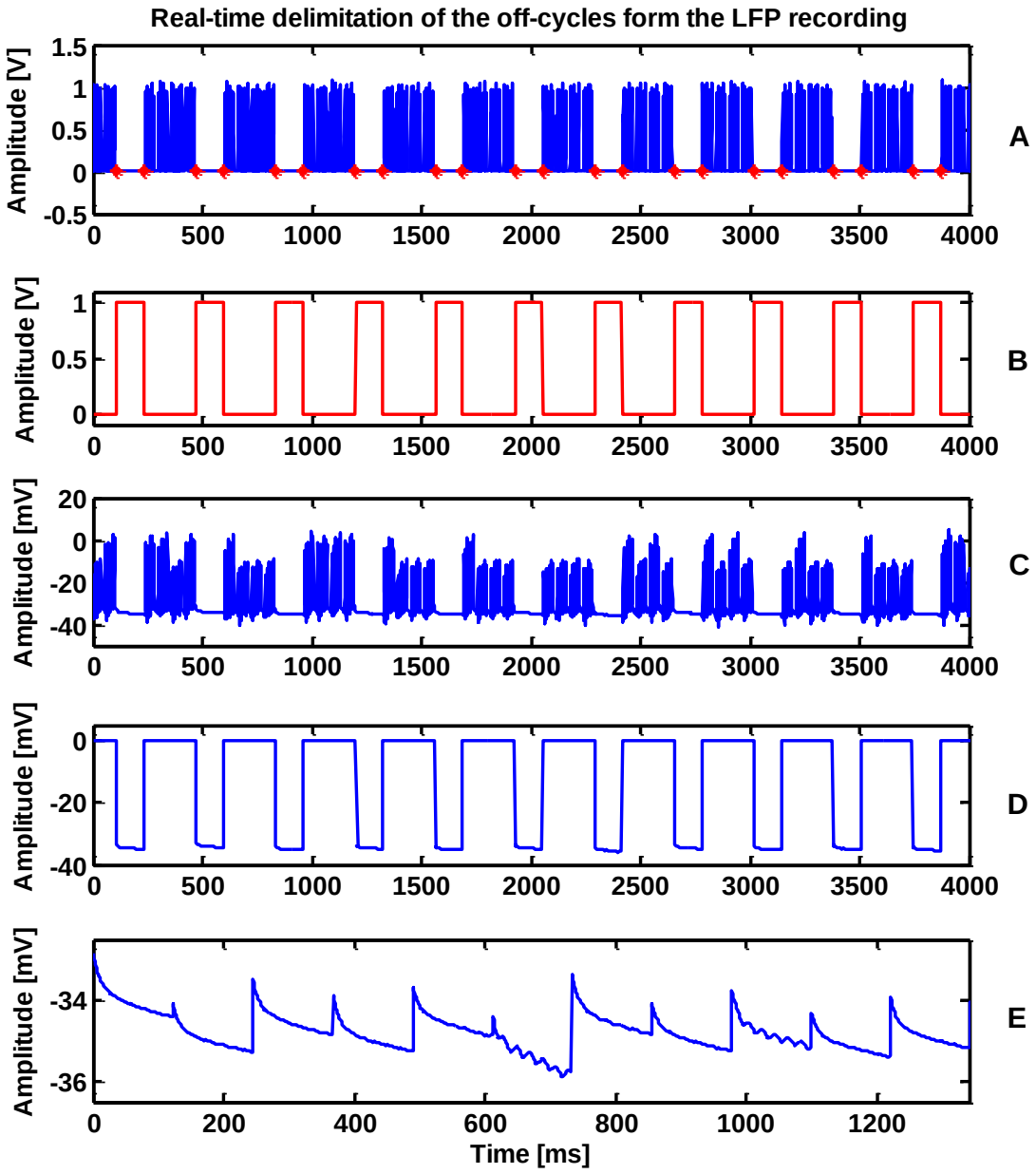

Figure 4.3. Real-time delimitation of the off-cycles from the LFP recordings. A: The absolute value of the reference signal (red asterisks depict the onset and end of the off-cycles). B: The delimiting signal formed in real-time. C: LFP recording from a PD patient. D: The result of multiplying the delimiting signal by the LFP recording; only the off-cycles are delimited. E: Concatenation of the off-cycles. In this example, we get 1.4 s off-cycles out of a 4 s LFP recording.

For the *candidate segment of data* method, the reference signal generated by the portable neurostimulator was optimal for the detection of the off-cycles, as shown in Figure 4.3. This reference signal is, by construction, synchronized with the LFP recordings and consists of clear stimulation pulses. In case the reference signal is distorted and inappropriate for the detection step, one of the LFP recording channels can be used. The length of the window of comparators is adjustable during stimulation according to the selected CR stimulation parameters; in particular, the CR frequency F_R, the number of on-cycles N_{on}, and the number of off-cycles N_{off} (The CR stimulation parameters are explained in Section 2.2.2).

The objective of using a long enough chain of successive zeros is to avoid detecting the time intervals between the stimuli within the on-cycles. In addition, the segment length determines the number of samples that are discarded directly after the on-cycles. This shortcoming of the *candidate segment of data* method, i.e. discarding some milliseconds of data after stimulation, might result in loss of neuronal activity with short latency to stimulation. The required inputs for this method are the threshold value and the length of the window of comparators. An additional parameter can be used to determine the number of samples to be discarded at the end of the off-cycles. Figure 4.3 demonstrates a typical real-time application of this method of discarding the on-cycles, including the stimulus artifact, from an LFP recording during CR DBS.

Sawtooth wave with CR stimulation parameters

The second solution to delimit the off-cycles in real-time is implemented by using a *sawtooth wave*, as illustrated in Figure 4.4.A. The CR stimulation parameters F_R, N_{on}, and N_{off} are used to build the *sawtooth wave* S_{sw} which is sampled at 1 kHz as the LFP recordings. The parameters that define the *sawtooth wave* are: (i) the duration of one cycle D_{cy} of F_R, (ii) the duration D_n of one set of successive on- and off-cycles, and (iii) the frequency F_{sw} of the *sawtooth wave*. The calculation of these values is described in Equation 4.1, Equation 4.2 and Equation 4.3, respectively.

$$\boldsymbol{D_{cy} = \frac{1}{F_R}}, \tag{4.1}$$

$$\boldsymbol{D_n = \left(N_{on} + N_{off}\right) \cdot D_{cy}}, \tag{4.2}$$

$$\boldsymbol{F_{sw} = \frac{1}{D_n}}. \tag{4.3}$$

Subsequently, the initial *sawtooth wave* S_{sw_0} is calculated and its amplitude is scaled by D_n as shown in Equation 4.4.

$$\boldsymbol{S_{sw_0} = mod\,(t_i \cdot F_{sw}\,, 1) \cdot D_n,} \tag{4.4}$$

where *i* is a time index and *mod* is the modulus after division. The duration of the on-cycles, $N_{on} \cdot D_{cy}$ in Equation 4.5, is then subtracted from S_{sw_0}, i.e. the wave is vertically shifted below the zero line, as shown in Figure 4.4.B. An additional parameter *q* is introduced in order to discard some samples at the onset of the off-cycles.

$$\boldsymbol{S_{sw} = S_{sw_0} - N_{on} \cdot D_{cy} + q.} \tag{4.5}$$

Afterwards, the signum function (*sign*) sorts the values of the *sawtooth wave*. The *sign* function assigns -1, 1, and 0 to samples below, above, and at the zero line, respectively. As negative values are generated by the *sign* function, the *sawtooth wave* is offset by 1 and subsequently scaled by 0.5, such that the amplitude is restricted between 0 and 1, as shown in Figure 4.4.C. So, it is noteworthy that the amplitude of the LFP recording should not be scaled. The end *sawtooth wave* S_{dl} is then multiplied with the LFP recording to delimit the off-cycles.

$$\boldsymbol{S_{dl} = 0.5 \cdot (sign(S_{sw}) + 1).} \tag{4.6}$$

The use of the *sawtooth wave* method to delimit the off-cycles requires that the LFP data should be shifted along the time axis, so that it gets synchronized with the delimiting signal. For the real-time implementation, this is performed once at the beginning of the recording process and as long as the stimulation parameters (i.e., F_R, N_{off} and N_{on}) remain unchanged. This method has an advantage over the *candidate segment of data* method, in that discarding some samples after the on-cycles is optional. This method can also be used to remove the stimulus artifact if the duration of the stimuli and their onset during the on-cycles are known. Both the *candidate segment of data* and the *sawtooth wave* methods are implemented in the Simulink module which is represented in Appendix B.

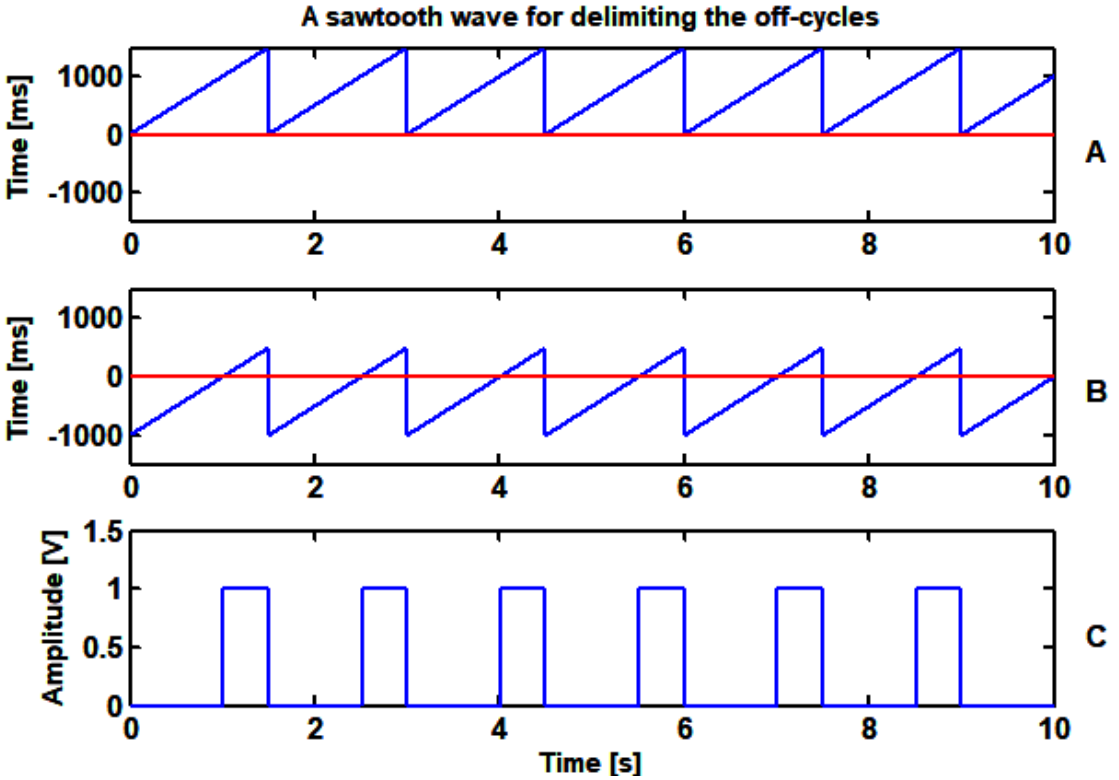

Figure 4.4. Illustration of the concept of building a *sawtooth wave* based on the CR stimulation parameters for delimiting the off-cycles in real-time. A: Initial *sawtooth wave* $\boldsymbol{S_{sw_0}}$. B: The wave is shifted vertically below the zero line by subtracting the duration (in milliseconds) of the on-cycles from the *sawtooth wave*. C: The sign function is used to build the delimiting signal. The CR stimulation parameters used here are F_R 4 Hz, N_{on} 4, and N_{off} 2.

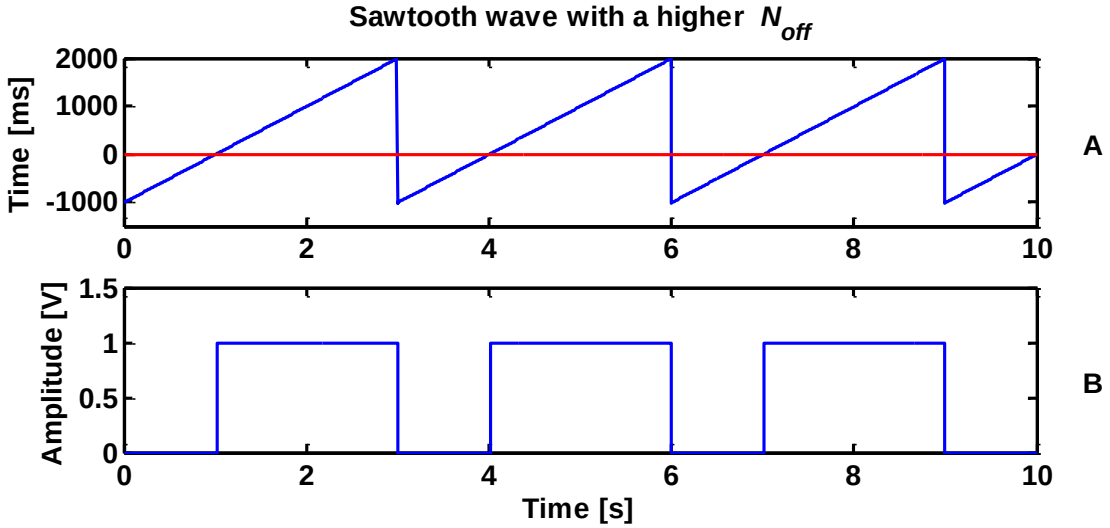

Figure 4.5. *Sawtooth wave* with a higher number of off-cycles. This figure is identical to Figure 4.4, except for the number of off-cycles. This increase in number of off-cycles resulted in increased proportion of time for amplitude value 1, as compared to that for value 0. The CR stimulation parameters used here are F_R 4 Hz, N_{on} 4, and N_{off} 8. The purpose of the figure is to explain the effect of increasing the number of off-cycles

4.1.2 Saturation artifact after stimuli

After the removal of the stimulus artifact, we focused on the artifacts that contaminate the off-cycles. The principal artifact in the off-cycles resulted from an exponential decay/growth after the on-cycles. In order to select appropriate artifact removal techniques, it was crucial to define the exact source of the artifact. The application of an inappropriate technique could misrepresent the results or generate new artifacts that could be wrongly interpreted as a neuronal activity. As mentioned in Section 2.2.1, balanced and biphasic DBS pulses are used by the portable neurostimulator. A mismatch of the biphasic pulses can occur due to the imperfection of the fabrication of the electrical circuitry used in neurostimulators (Sooksood et al., 2009). This mismatch can be avoided by the implementation of some active or passive techniques that support the charge-balancing. One of the active techniques involves the use of non-integrated and large direct current (DC) blocking capacitors in series with the stimulation electrode (Ortmanns, 2007). These capacitors ensure that no DC currents are delivered to the stimulation electrode over time. However, it is important to discharge these capacitors frequently to avoid the saturation caused by DC integration, and to prevent reduction of the output voltage of the stimulator (Sooksood et al., 2009). The portable neurostimulator uses the active pulse balancing technique with the capacitors and the exponential discharge process takes place between stimuli.

Additionally, the stimulation pulses can saturate the amplification system of the recording device (Nguyen et al., 2013, Kent & Grill, 2012). At the end of the stimulation periods (i.e., the on-cycles), the preamplifier should return to baseline creating a long discharging tail (i.e., the exponential artifact) that can be seen along the off-cycles. In the LFP recordings during CR DBS, a considerable variability was noticed in the exponential artifact shapes among electrode channels. Moreover, such variability was observed even in individual channels among trails of the same stimulus as indicated in Figure 4.6. This figure shows a number of delimited and concatenated off-cycles of LFP recording from a PD patient before the removal of the exponential artifact.

The variability in the artifact shapes among off-cycles can be caused due to, e.g., the application of random sequence of CR stimulation through the different contacts. Another reason behind this variability is that an exponential decay rides on the falling tail of the previous artifact due to different decay times. Thus, the assumption of the regularity of artifact shape can no longer be considered as holding true. Due to the variability of the exponential artifact, it was the main artifact in the off-cycles which caused a major challenge for the removal process in real-time. The optimal solution in this case was to fit independent functions for each individual exponential artifact in the off-cycles.

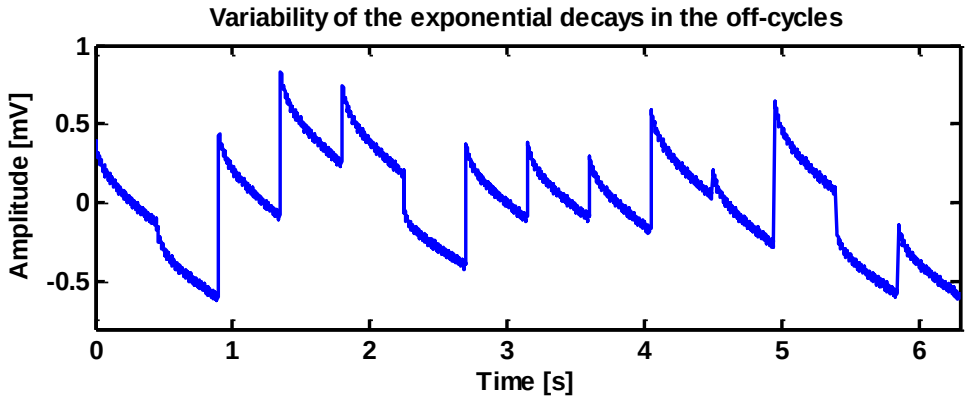

Figure 4.6. Variability of the exponential decays in the off-cycles. The figure shows (i) a number of merged off-cycles of LFP recording from PD patient, (ii) the variability in steepness, and (iii) variability in the off-set of the artifact. This variability makes the task of separation of artifact more challenging.

Polynomial fitting

Several techniques, which are based on the subtraction of a fitting curve from the recorded data, are used for the removal of signal decays after stimuli. A polynomial curve is usually preferred to fit such decays (Wagenaar & Potter, 2002). On one hand, polynomial fitting is easy to implement and requires less computational effort to calculate the fitting curve. This approach is based on matrix multiplications and additions and does not require a large memory to buffer intermediate results. On the other hand, the frequency content of the desired signal, in some applications, lies outside the frequency content of the polynomial curve. For instance, if the frequency of interest is above 20 Hz and the frequency of the fitting curve is below 10 Hz then the frequency content of the desired signal is not affected.

By polynomial fitting of the decays of the off-cycles in the LFP recordings during CR DBS, we found that the frequency content of the fitting curves was in the frequency range of the parkinsonian resting tremor, i.e. between 3 – 10 Hz. Therefore, it was difficult to interpret these results. An example of how polynomial fitting can misrepresent the results is given in Figure 4.7. In this example, a polynomial curve, which was used to fit the off-cycles, is fitted by an exponential curve. Subtracting both fitting curves from each other has revealed low frequencies in the fit residuals. These low frequencies were caused by the polynomial fitting and were found to be exactly in the frequency range of resting tremor.

Generally, a higher order polynomial is desirable because fitting curves created by low order polynomials (e.g. cubic polynomial) may not be able to accurately fit the portion of the exponential curve. Furthermore, the use of polynomials of higher orders, such as ten or higher, could not overcome this shortcoming for two reasons: First, the polynomial order is given as a static variable before the processing starts, and cannot be changed during the course of the recording. So, a polynomial with order higher than that effectively required for fitting the given curve may even deteriorate the quality of fit because some undesirable

contributions may appear. Second, a polynomial of very high- order (e.g. order >15) may end up fitting the recorded neuronal activity itself. While removing the artifact from the off-cycles, the recorded neuronal activity will also get removed. Due to these limitations, a more sophisticated technique was required. Nevertheless, polynomial fitting was not completely excluded, and it was used in some optimization stages and off-line tests.

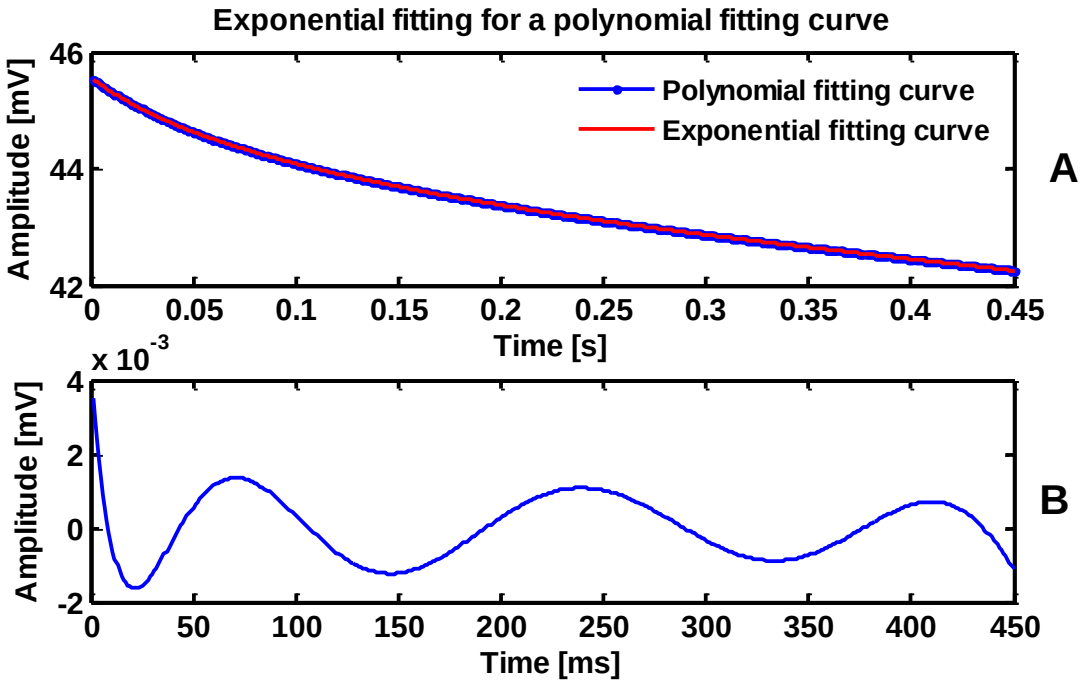

Figure 4.7. Exponential fitting of a polynomial fitting curve. A: Both fitting curves seem similar on absolute scale. However, (B) shows that it is better to directly take the difference and compare (relative scale). The residual of such a difference results in a low frequency in the range of the neuronal activity, approximately at 7 Hz.

Exponential fitting

An exponential fitting curve can accurately describe the exponential decay in the off-cycles and assures that the frequency content of the recorded neuronal activity is not affected. Therefore, a non-linear fitting technique is required. The most well-known algorithms used for non-linear fitting are Gauss-Newton (Hartley, 1960, Fletcher & Powell, 1963), Levenberg-Marquardt (Marquardt, 1963) and the Nelder-Mead algorithm (Nelder & Mead, 1965). The two former algorithms are based on derivatives of the objective function, whereas the latter is a direct search method that fits data without derivatives.

Non-linear fitting algorithms use the least squares method, as shown in Equation 4.7. Basically, they search for the global minimum, i.e. the optimal solution is found by minimizing the sum of the squares of the residuals r_j among the data points y_j and the estimated points x_j of the fitting curve $f(x_j, \sigma)$, as shown in Equation 4.7 and Equation 4.8.

Many iterations are required to search for the optimal combination of parameters σ in order to fit the data points the closest.

$$\min_{\sigma} \sum_{i=0}^{n} r_j^2(\sigma), \tag{4.7}$$

$$\mathbf{s.t.} \quad r_j = y_j - f(x_j, \sigma), \qquad \mathbf{for\ j = 1, \cdots, n} \tag{4.8}$$

where n is the total number of data points. For the real-time removal of the exponential artifact during CR DBS, the Nelder-Mead algorithm was implemented by using of Simulink blocks (routines) that can be converted into C source files. The concept of the Nelder-Mead algorithm is explained, and the results obtained from its implementation in Simulink are shown in Appendix A.

Double exponential fitting

In order to remove the exponential artifact from the off-cycles, we found that at least a double exponential fitting curve is required. Furthermore, it has been seen that LFP recordings during CR DBS show that the artifact includes both exponential decays and growths. The use of an exponential fitting curve with adequate exponents (positive or negative) increases the probability of reaching the best fit within the given number of iterations. Thus, we implemented both exponential fitting functions in Simulink for real-time processing, as described in Equation 4.9 and Equation 4.10. In both equations, the term $f(x_j, \sigma)$ in Equation 4.8 is replaced by the double exponential curves as follows:

$$\min_{\sigma} \sum_{j=0}^{n} \left[y_j - \left(a_1 \cdot e^{-b_1 \cdot t_j} + a_2 \cdot e^{-b_2 \cdot t_j} \right) \right], \tag{4.9}$$

$$\min_{\sigma} \sum_{j=0}^{n} \left[y_j - \left(a_1 \cdot e^{b_1 \cdot t_j} + a_2 \cdot e^{b_2 \cdot t_j} \right) \right], \tag{4.10}$$

where $\mathrm{j} = 1, \cdots, n$ and the parameter vector is defined as $\sigma = [a_1, a_2, b_1, b_2]$.

At the end, the control unit in the Simulink module automatically selects which fitting curve describes the decay of the off-cycles the closest. The choice is made based on the minimal sum of squares of residuals between the fitting curves and the off-cycles. Therefore, the implemented Nelder-Mead module in Simulink for exponential fitting

provides more flexibility to cope with the variability of the artifact in terms of decay/growth and in terms of the steepness of the artifact. An example for fitting the off-cycles of LFP recording, taken from a PD patient during CR DBS, by a double exponential curve, is shown in Figure 4.8.A. After the removal of the PLI, low frequencies (artifacts) in the frequency range of resting tremor were found in the fit residuals, as shown in Figure 4.8.B. We found that these low frequencies have multiple causes. For instance, the double exponential curve could not fit some off-cycles accurately due to the large amplitude of the PLI, as explained later in Section 4.1.6.

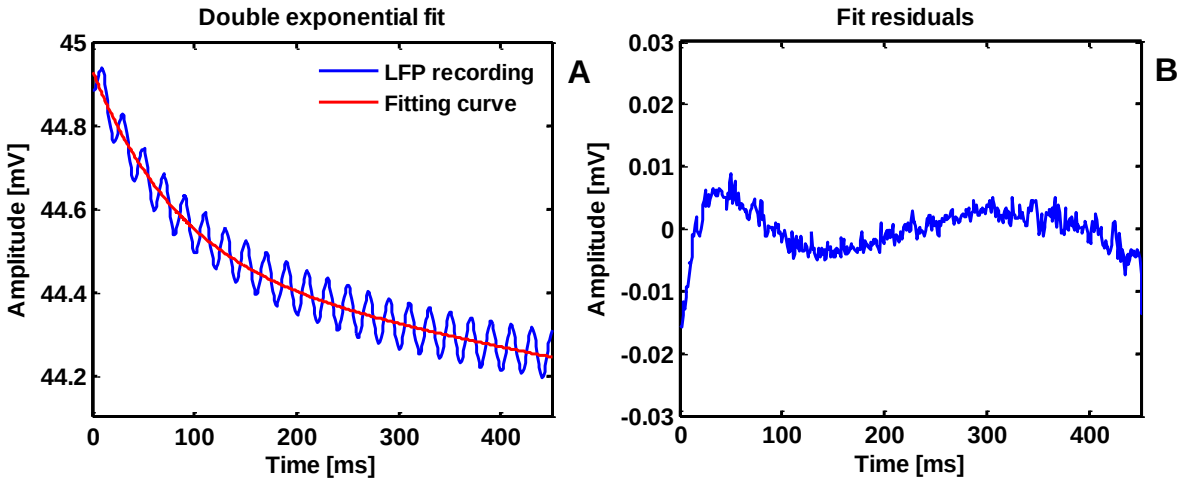

Figure 4.8. Double exponential fitting of the off-cycles. A: The off-cycles (blue), which are still contaminated by PLI, are fitted with a double exponential curve (red). B: Residuals after the removal of the artifacts result in a low frequency curve.

High-order exponential fitting

Apart from the reasons mentioned so far, another reason responsible for the additive low frequencies in the fit residuals is described next. In some CR stimulation sessions, high F_R and low N_{off} values are used. This creates short and steep exponential decays/growths in the off-cycles, especially directly after the on-cycles. As a result, the double exponential fitting curve may not describe the decay of the off-cycles accurately. One possibility to increase the accuracy of the fitting process is by using a high-order exponential fitting, e.g. of 5^{th} order. A high-order exponential can follow the trend of the off-cycles better than that of the double exponential fitting.

In Simulink, we modified the Nelder-Mead module to be able to fit a 5^{th} order exponential curve to the off-cycles. The reduction of the exponential artifact by high-order fitting curves was effective, since low frequencies were completely removed, as illustrated in Figure 4.9. However, it was relatively more demanding from computational perspective, since conversion of the module into C source files resulted in a large source code which cannot be processed in real-time. Therefore, the performance of the DSP was affected.

Nevertheless, this module was used for numerous off-line artifact reduction tests. For the 5th order exponential fitting the term $f(x_j, \sigma)$ in Equation 4.8 is replaced here by the 5th order exponential curves, Equation 4.11 and Equation 4.12, and the parameter vector is defined here as $\sigma = [c_1, \dots, c_5, d_1, \dots, d_5]$.

$$\min_{\sigma} \sum_{j=0}^{n} \left[y_j - (c_1 \cdot e^{-d_1 \cdot t_j} + c_2 \cdot e^{-d_2 \cdot t_j} + \cdots + c_5 \cdot e^{-d_5 \cdot t_j}) \right], \tag{4.11}$$

$$\min_{\sigma} \sum_{j=0}^{n} \left[y_j - (c_1 \cdot e^{d_1 \cdot t_j} + c_2 \cdot e^{d_2 \cdot t_j} + \cdots + c_5 \cdot e^{d_5 \cdot t_j}) \right]. \tag{4.12}$$

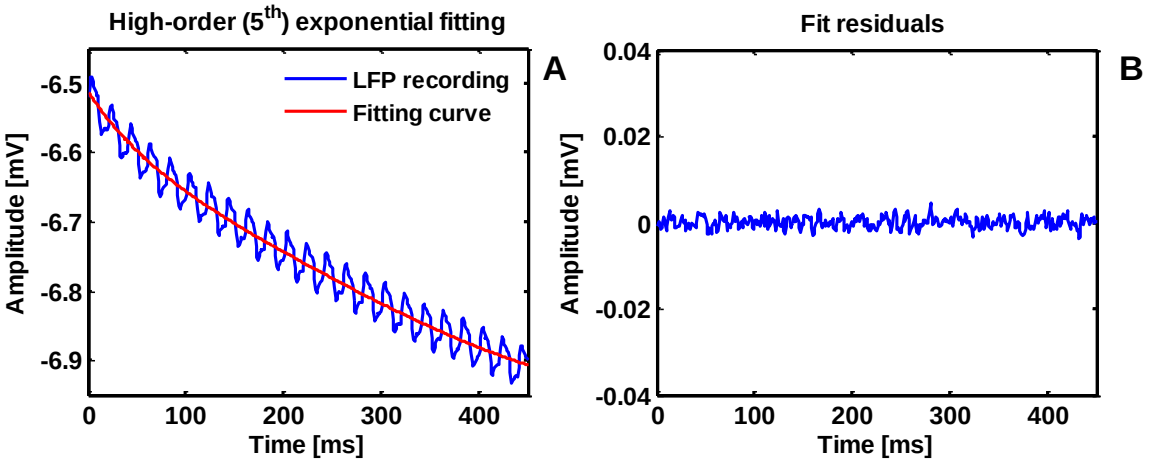

Figure 4.9. High-order (5th) exponential fitting. A: The off-cycles (blue) are fitted with 5th order exponential curve (red). B: The corresponding residuals after the removal of PLI contain no low frequencies.

Segmentation of off-cycles

As high-order exponential fitting was computationally demanding, another solution was required to overcome the limitations created by the hardware and by the steepness of the exponential artifact. This solution was to divide the off-cycles into smaller segments. For instance, off-cycles which last 450 ms are divided, e.g., into three segments, each of 150 ms length. These segments were then fitted separately with double exponential curves. The off-cycles were divided maximally into three segments. After subtracting the fitting curves from the segments and removing the PLI, the segments were concatenated. This method was implemented in Simulink and tested in real-time on the LFP recordings in saline solution (see Figure 4.10 and Figure 4.11), as well as on short off-cycles (120 ms) of LFP recordings from PD patients (see Figure 4.12).

The LFP recordings in saline solution include no neuronal activity. Therefore, the artifact-reduced off-cycles of these recordings should include neither low frequencies in the time domain nor dominant peaks in the frequency domain. Application of the segmentation approach on LFP recordings in saline solution and from PD patient have shown that the additive low frequencies caused by exponential fitting are eliminated, as shown in Figure 4.10.C, Figure 4.11.B, and Figure 4.12.C. However, the concatenation of the segments caused discontinuities in the signal which in turn affected the spectral analysis. We found that the removal of PLI before the exponential artifact further reduced the drawback of the concatenation process, as explained in Section 4.1.3 and discussed in detail in Section 4.1.6. The removal of the exponential artifact from the off-cycles was the most critical stage in artifact reduction during CR DBS, since the frequency response of the remaining artifact lies exactly in the frequency range of interest.

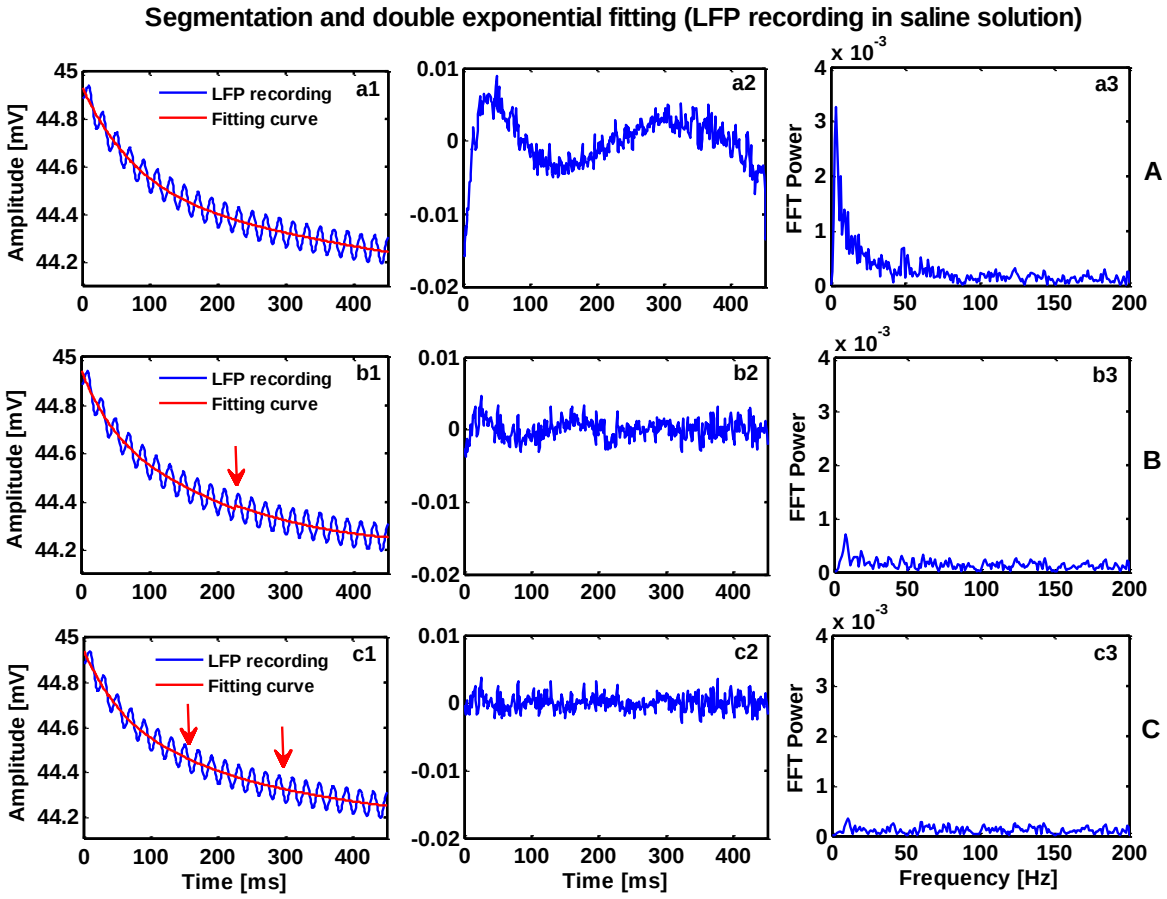

Figure 4.10. Segmentation of off-cycles and double exponential fitting (LFP recording in saline solution). A: Non-segmented off-cycles are shown in (a1). Low frequencies, which are caused by an inaccurate fitting, appear in the fit residuals after the removal of the exponential artifact and PLI (a2) and in the power spectrum (a3). B: The off-cycles are divided into two segments (indicated by a red arrow). The low frequencies are reduced in (b2) and (b3). C: The off-cycles are divided into three segments (c1). The low frequencies are further reduced in (c2) and (3).

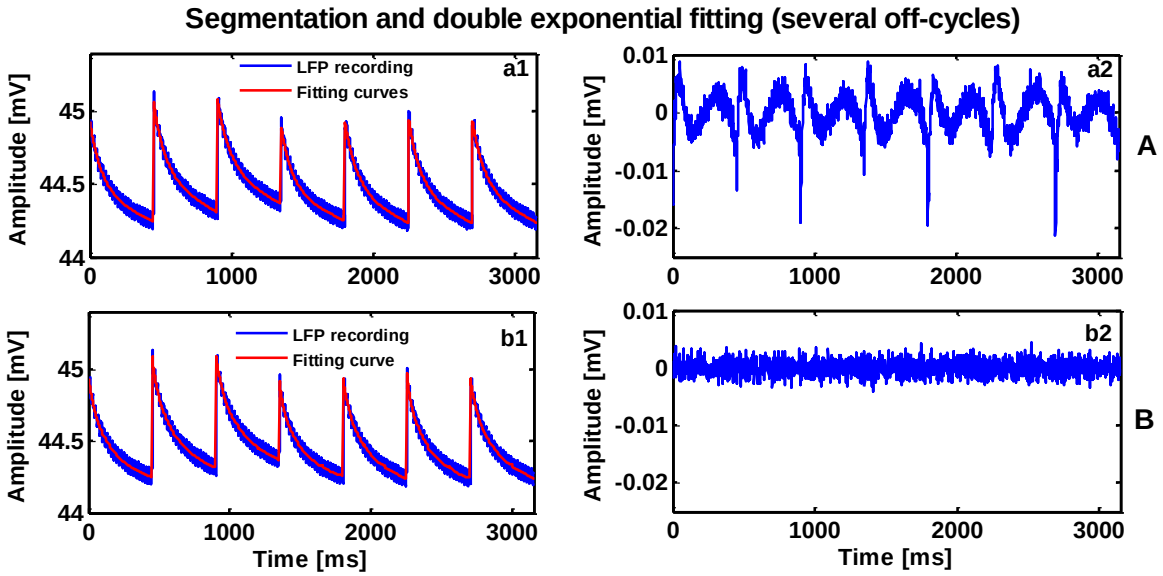

Figure 4.11. A comparison for a single segment and 3-segment fitting of several concatenated off-cycles (LFP recording in saline solution). A: The off-cycles (a1) are exponentially fitted without segmentation; thus, low frequencies are seen in fit residuals (a2). B: The off-cycles are divided into three segments (b1); thus, the low frequencies are strongly reduced (b2).

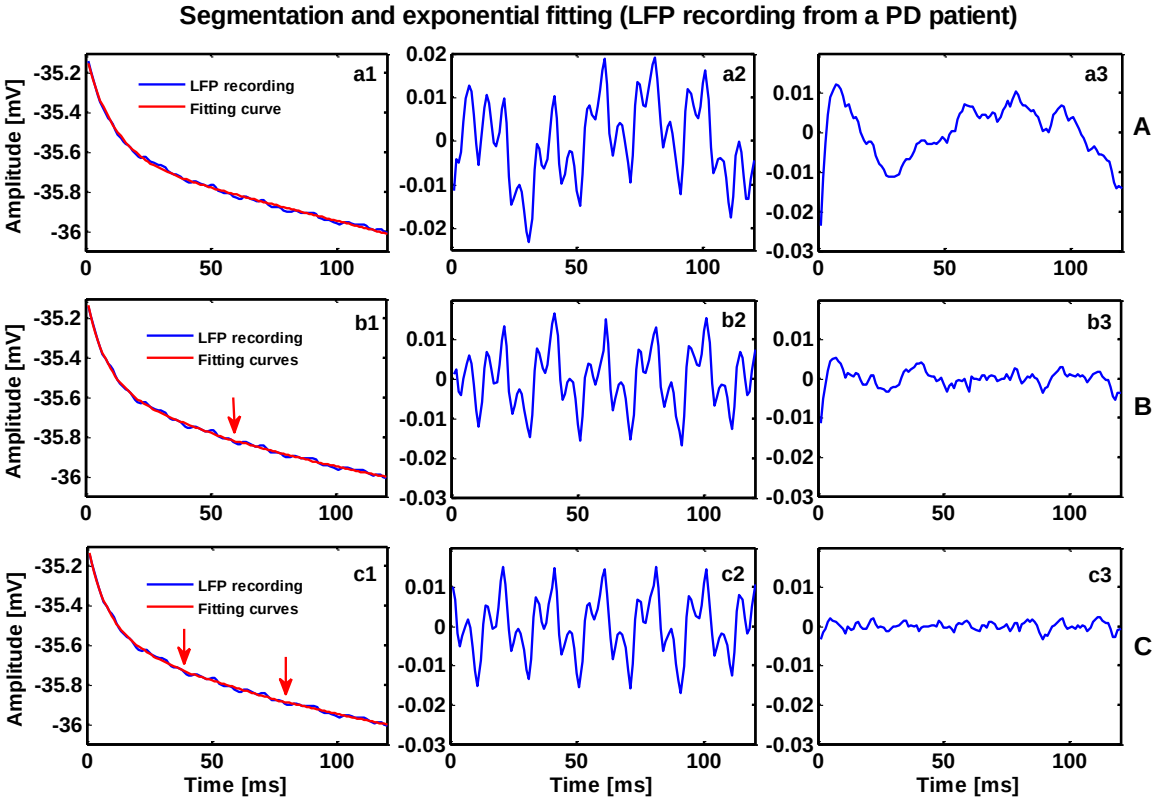

Figure 4.12. Segmentation and double exponential fitting of short off-cycles, i.e., 120 ms (LFP recording from a PD patient). A: Non-segmented off-cycles (a1). Low frequencies appear before (a2) and after (a3) the removal of PLI. B: The off-cycles are divided into two segments (red arrow). The low frequencies are reduced in (b2) and (b3), as compared to (a2) and (a3), though still not removed completely. C: The off-cycles are divided into three segments (c1). The low frequencies before (c2) and after (c3) the removal of PLI are strongly reduced.

4.1.3 Power line interference

The PLI artifact arises from the environmental electric power sources such as turning machines (Yacoup & Raoof, 2008). PLI is characterized by fixed frequency sinusoid with random amplitude and phase, and also higher harmonics (Costa & Tavares, 2009). LFP recordings are contaminated by PLI due to stray currents flowing through the patient and the cables (Levkov et al., 2005). In such environments, the patients' body behaves like an antenna which attracts the electromagnetic interference signals. Thus, the PLI gets transformed into a virtual differential signal (Huhta & Webster, 1973, Thakor & Webster, 1980) that cannot be suppressed even by an infinitely high common mode rejection ration (CMRR) (Levkov et al., 2005). The PLI in the LFP recordings during CR DBS consists of the fundamental 50 Hz and mostly its odd harmonics (i.e. 150 Hz, 250 Hz and 350 Hz). Even harmonics (i.e. 100 Hz and 200 Hz) do exist, but are rare.

Preliminary measures, (e.g. a good isolation of the electric device and cables), remained inefficient in the case of a highly contaminated and weak neuronal activity. Although biomedical amplifiers have a very high common mode rejection ratio, biological signals are often contaminated by residual PLI (Levkov et al., 2005). PLI is generally removed by conventional analogue and digital filters. For the short off-cycles of the CR stimulation protocol, the main limitation to use filters is that they require continuous data. Therefore, filtering was not an efficient approach since there is a phase distortion of PLI caused by delimiting the off-cycles. Additionally, the exponential artifact in the off-cycles added low frequencies to the data when digital filters were used to remove the PLI before delimiting the off-cycles.

An additional challenge of removing the PLI was the considerable variability of the PLI amplitude in consecutive off-cycles. For instance, for some off-cycles, the amplitude of PLI was three times larger than the previous or subsequent off-cycles, as shown in Figure 4.13. In this figure, off-cycles of LFP recording from a PD patient are delimited and concatenated after the removal of exponential artifacts. The amplitude fluctuations is impulsive, and only during the off-cycles. Besides the digital filters, we tested some additional techniques for the removal of PLI from the off-cycles in real-time such as:

Difference between two LFP channels

A sufficient approach to remove the PLI could be by using the LFP channels themselves. Here, we tried to make use of the synchrony of the LFP recordings and assumed that the same PLI artifact should be found in the data recorded by the active contacts of the implanted electrode (see Section 2.2). This artifact should be removed by taking the difference of two LFP signals before the delimitation of the off-cycles. However, the results have shown that the PLI was reduced but not eliminated, as shown in Figure 4.14. This

shows that PLI has different amplitudes in each channel. Possible reasons for such differences are, for example, the variation in the impedances of the electrode contacts or the different lengths of connection cables.

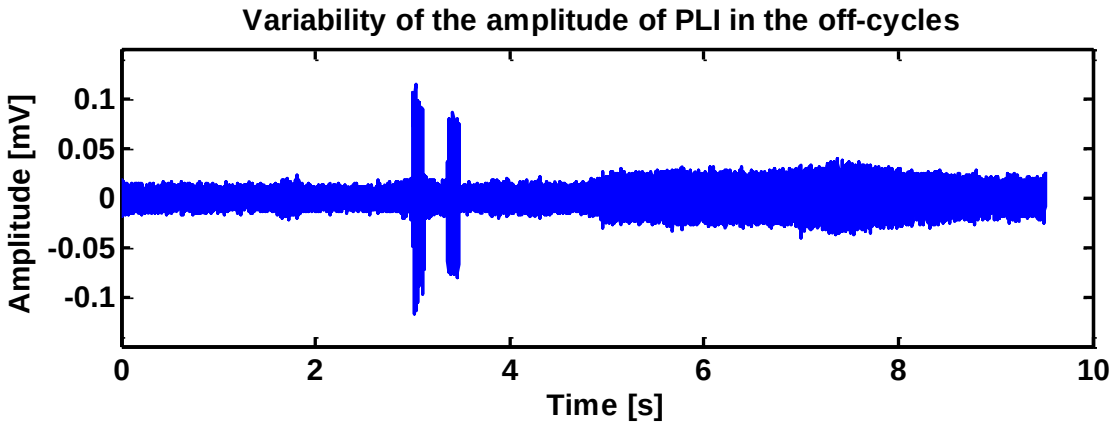

Figure 4.13. Variability of PLI amplitude in the off-cycles. The successive off-cycles last 120 ms. The amplitude of two off-cycles (between the third and fourth seconds) is three times larger than the previous and subsequent off-cycles.

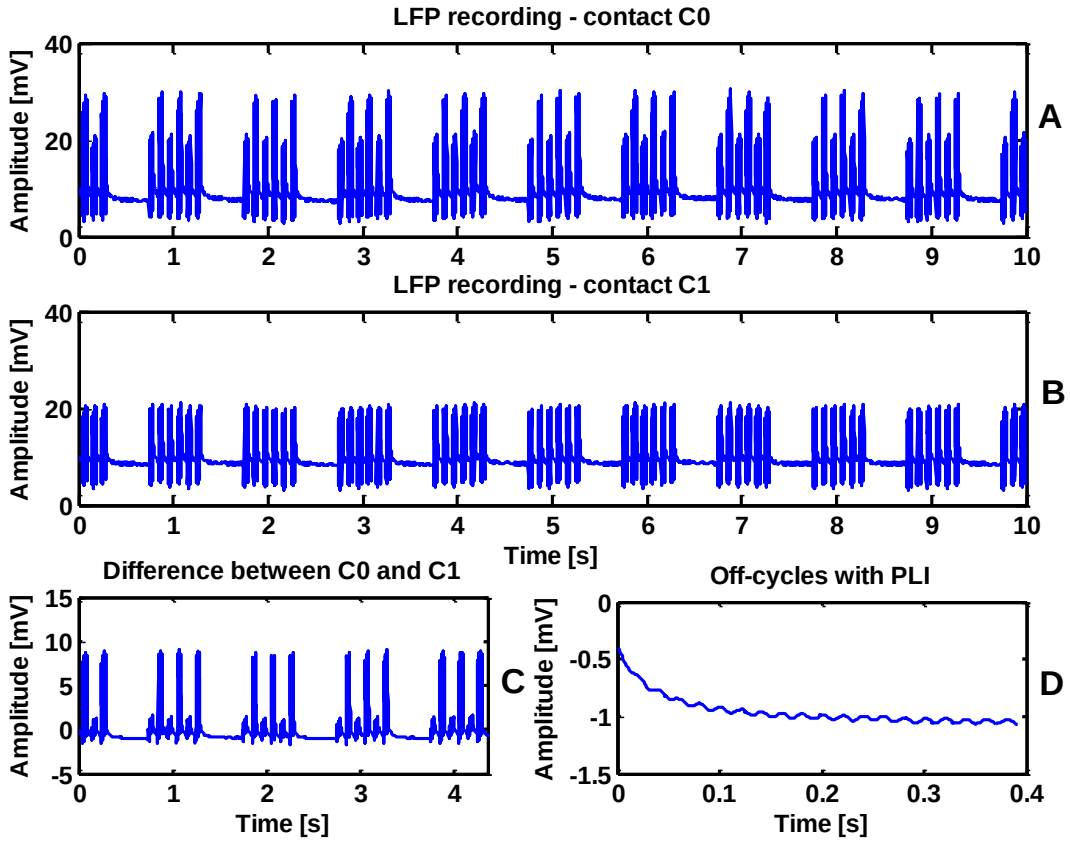

Figure 4.14. Difference between two LFP channels for PLI removal. A and B: Two LFP signals recorded by two contacts of the implanted electrode. C: A segment of the difference between amplitudes of both signals. D: Off-cycles of the difference are still contaminated by PLI artifact.

Off-cycles averaging

Another attempt to remove the PLI was to average many off-cycles in real-time once the off-cycles have been delimitated. This approach worked only partially, since there is a phase distortion of the PLI signal caused by the delimitation of the off-cycles. During averaging, the amplitude of PLI was reduced to a small extent or even sometimes amplified as well but was never eliminated completely. The process of averaging a large number of off-cycles over time is shown in Figure 4.15.A. Although the amplitude of PLI was reduced, a remaining PLI can be clearly seen at the end of this averaging process (see Figure 4.15.C).

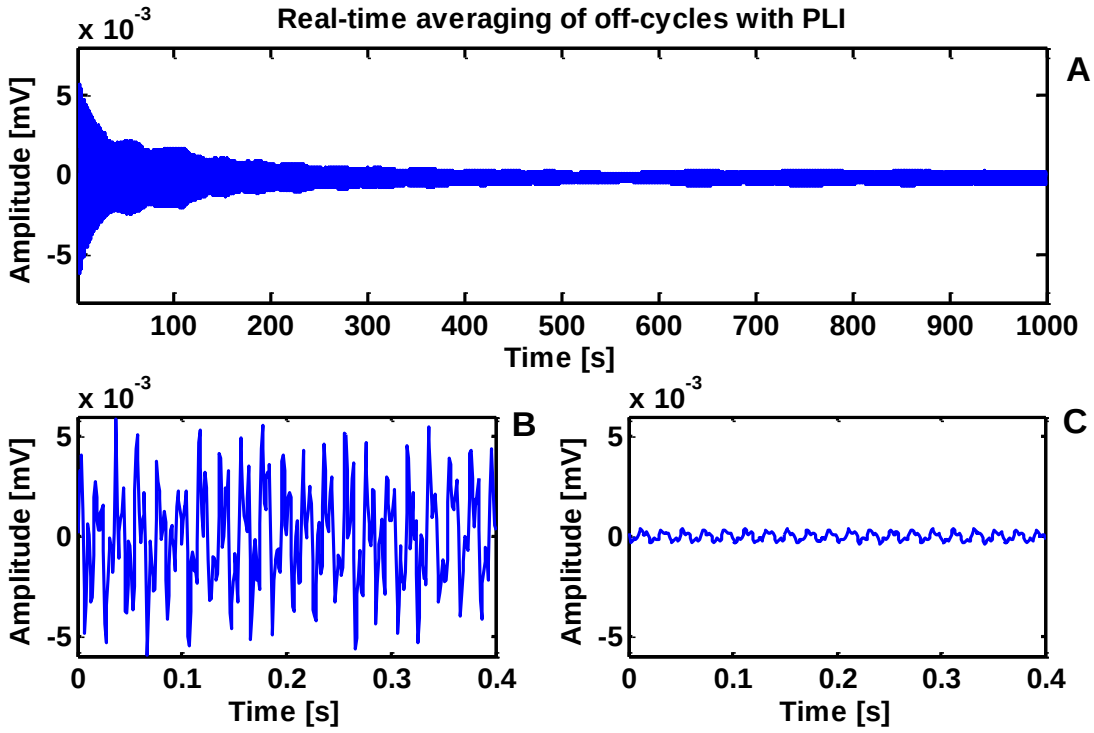

Figure 4.15. PLI removal by averaging of off-cycles. A: A large number of off-cycles contaminated by PLI are averaged over time. B: The first off-cycles contaminated by large PLI. C: The result of averaging the off-cycles (after 1000s). Although the amplitude of PLI was reduced, a remaining PLI can be clearly seen at the end of this averaging process.

Due to the variability in PLI amplitude and the shortness of the off-cycles, subtracting an independent reference signal of PLI from each off-cycles period seemed to be a more efficient approach. In our tests, we found that making a copy of the PLI signal and subtracting it from the biological signal eliminates this artifact without affecting the frequency components of the neuronal activity. In order to generate an independent reference signal of the PLI for the off-cycles, the amplitude and phase of this signal should be determined in real-time. This was possible through the implemented Nelder-Mead algorithm. The implementation of this algorithm was twofold since it was used to remove both the PLI and the exponential artifact (see Section 4.1.2). The steps of removing the PLI and harmonics from the LFP recordings during CR DBS are described as follows:

(i) Transformation of the off-cycles from the exponential form to a linear form by first removing the exponential artifact, as shown in Figure 4.16.

(ii) Calculation of the amplitude and phase of the reference signal for the basic PLI, i.e., the 50 Hz, using the Nelder-Mead module.

(iii) Deduction of the reference signal from the off-cycles period in the linear form.

(iv) Re-processing of the result obtained in step (iii) using the steps (ii) and (iii) for the odd harmonics of PLI, as shown in Figure 4.17.

The algorithm copes successfully with changes in amplitude and phase of the PLI and harmonics. The objective of removing the PLI and its harmonics was to reveal any neuronal activity with fixed latency to stimulation. The end result included off-cycles without PLI that can be analyzed for pathological neuronal activity. The saline solution was used here to test the Nelder-Mead module, and the results are shown in Figure 4.16 and Figure 4.17.

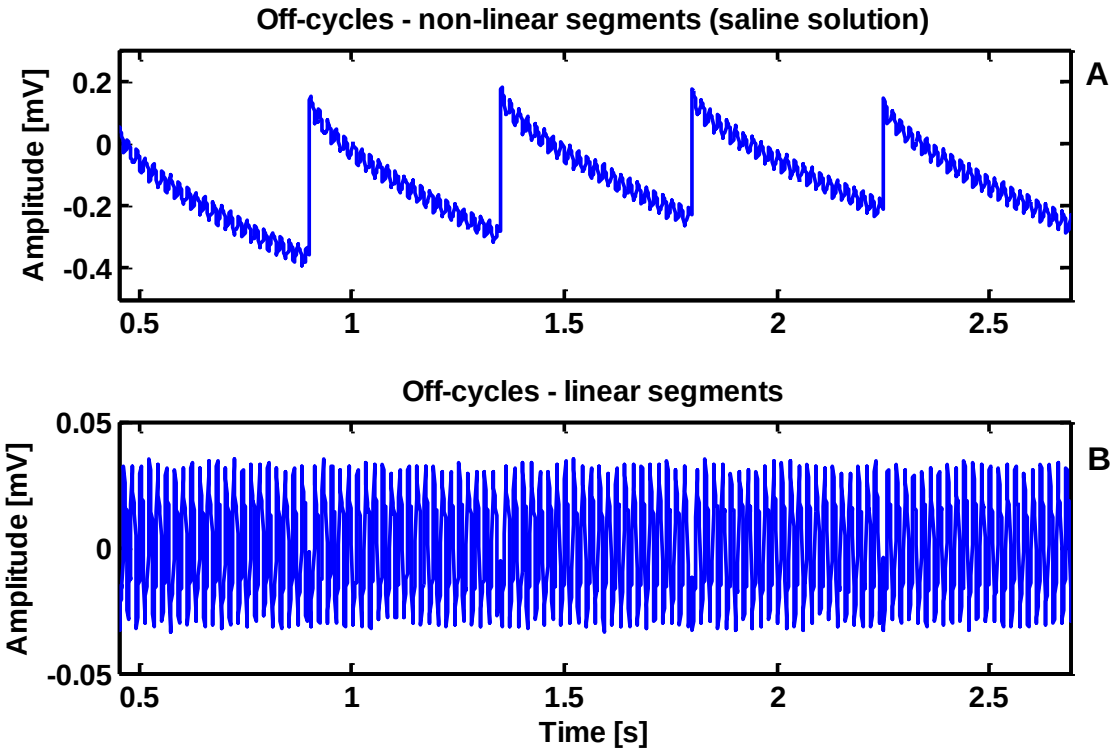

Figure 4.16. Transformation of the off-cycles from a non-linear form to a linear form. A: Concatenated off-cycles in a non-linear form. B: Off-cycles transformed into a linear form. The transformation enables the accurate estimation of amplitude and phase of the PLI artifact.

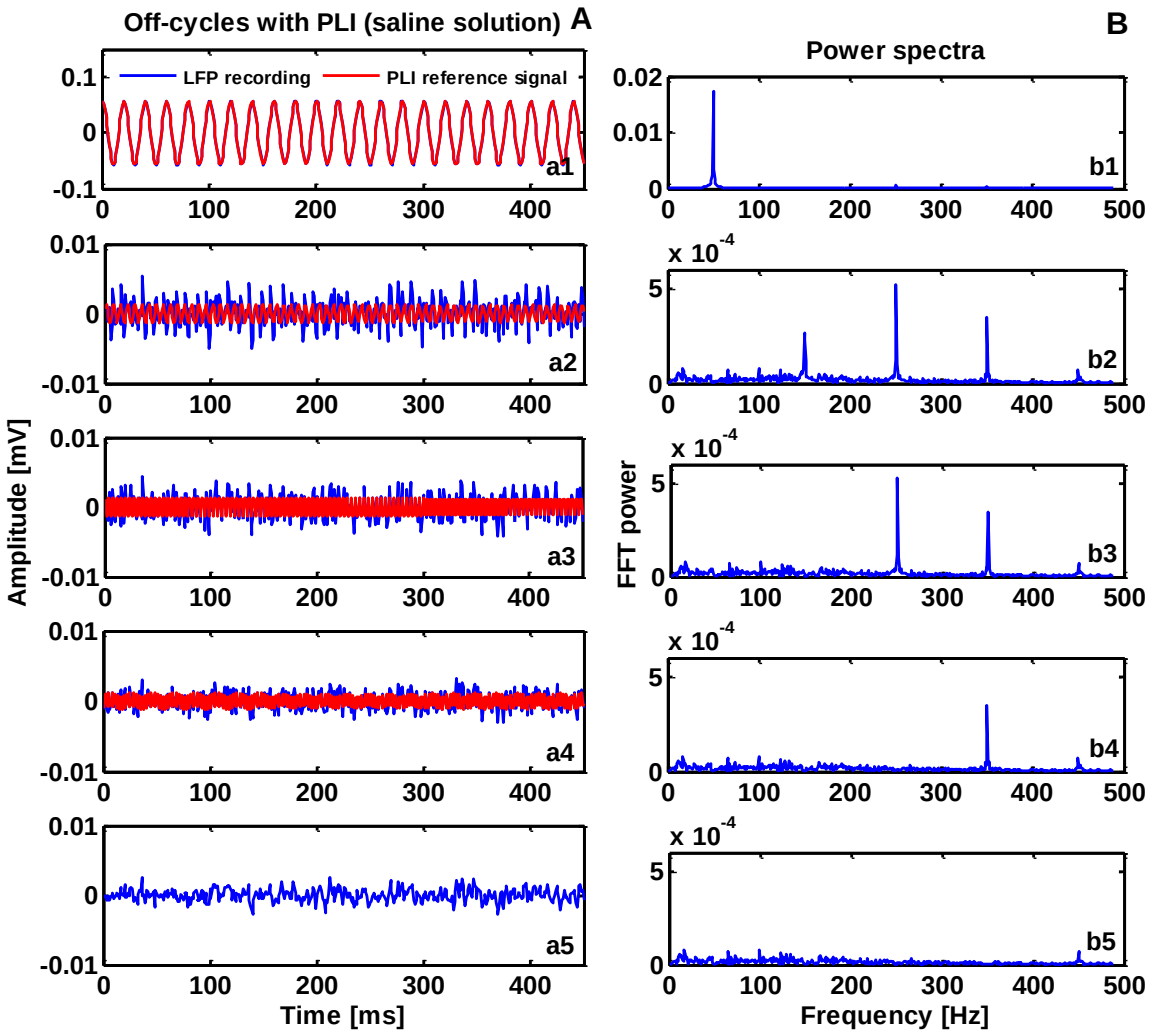

Figure 4.17. Removal of PLI from off-cycles (saline solution). A: Generation of reference signals for the basic PLI, i.e., 150 Hz (a1) and harmonics (a2 – a4). The PLI artifact-free off-cycles are shown in (a5). B: Power spectra of the off-cycles before (b1) and after the removal of basic PLI (b2) and harmonics (b3 – b4). The power spectrum of the PLI artifact-free off-cycles is shown in (b5).

4.1.4 Electrical background noise

Usually, the noise power is assumed to be much smaller than the desired signal power. However, the noise was much higher in the LFP recordings during CR DBS than the recorded neuronal activity. In comparison to the frequency range of interest (i.e., of the neuronal activity), the noise has higher frequency components. Filtering out the noise without affecting the signal is generally impossible (Strang & Nguyen, 1996). Averaging is one of the most commonly used techniques for noise removal. Due to the short duration of the off-cycles and the randomized phase of noise, averaging of off-cycles was the most effective de-noising technique for our LFP recordings, as shown in Figure 4.18. The power of noise can be strongly reduced by averaging, and this could reveal weak neuronal activity

with fixed latency. A large number of off-cycles, triggered by their onset, was mostly required to obtain sufficiently good results.

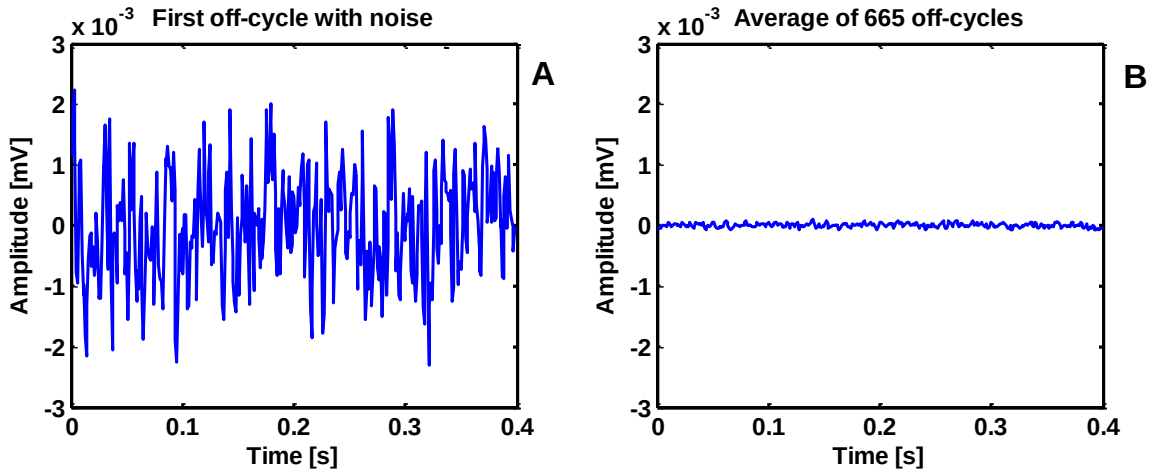

Figure 4.18. Reduction of electrical background noise in the off-cycles (patient data). A: First off-cycles, after the removal of exponential and PLI artifacts, are contaminated by noise. B: Average of 665 off-cycles, results in strong reduction of noise.

4.1.5 Rare movements and technical artifacts

Besides the fore-mentioned principal artifacts in the off-cycles of the LFP recordings from PD patients during CR DBS, some unpredictable and rare artifacts were also observed. These artifacts were irregular in terms of both form and duration. Possible causes for these artifacts include the movements of patients or the stimulation device during recording sessions. In some cases, the PLI amplitude was exponentially modulated and in other cases, the exponential artifact was modulated by low frequencies, as shown in Figure 4.19. Therefore, the reference signal to be generated for PLI artifact rejection must be an

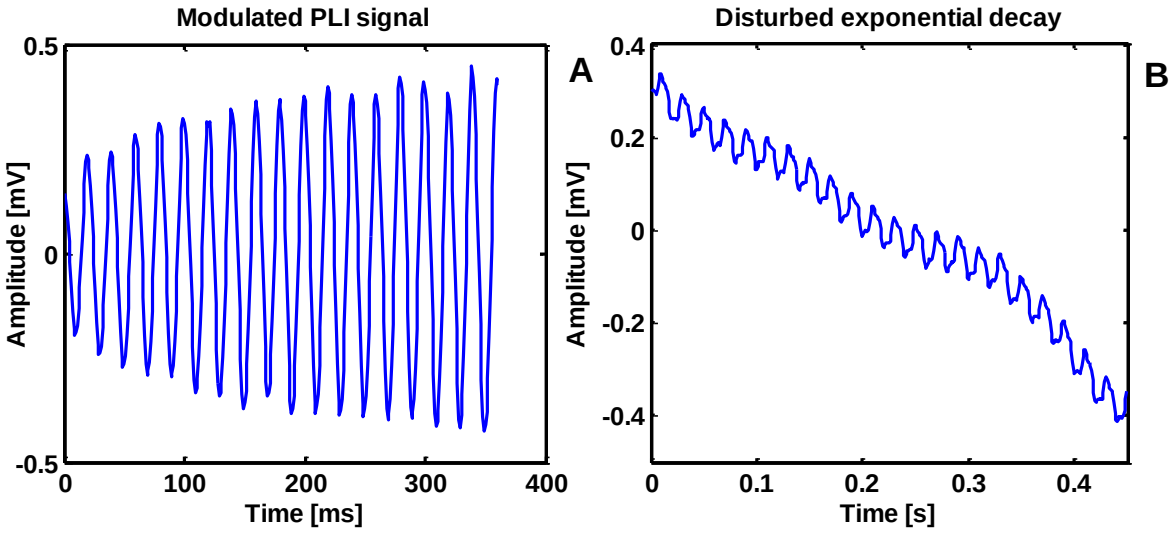

Figure 4.19. Rare movement and technical artifacts in the LFP recordings. A: PLI amplitude is exponentially modulated. B: The exponential artifact is distorted by low frequencies.

exponentially modulated sinusoid at 50 Hz. That is, additional parameters affecting the performance of the DSP should be optimized by the Nelder-Mead algorithm.

The rareness of these artifacts made not worth the implementation of other artifact reduction algorithms. Moreover, in case of averaging many off-cycles, the effect of these artifacts is reduced. However, if these artifacts appear frequently in the LFP recordings, then the analysis of these recordings would be insufficient. Such artifacts cause low frequency activity in the LFP recordings and cannot be classified in real-time whether they belong to neuronal activity or not.

4.1.6 Optimal artifact reduction sequence

Additive low frequencies in the artifact-reduced LFP signal were caused not only by using suboptimal fitting curves for the exponential artifact as discussed in Section 4.1.2, but also by using the wrong sequence when removing the artifacts. These low frequencies have affected the frequency content of interest even after the optimization of the exponential artifact removal technique. We found that the sequence of removing the exponential artifact and PLI was the main source of these low frequencies.

The problem could be resolved by removing the exponential artifact first, since it is the most significant artifact in the off-cycles. However, the large amplitude of the PLI frequency (i.e. the 50 Hz signal) prevented the exponential fitting curve from accurately fitting the off-cycles and inducing in this way low frequency components. Both exponential fitting curves, before and after the removal of PLI are compared and shown

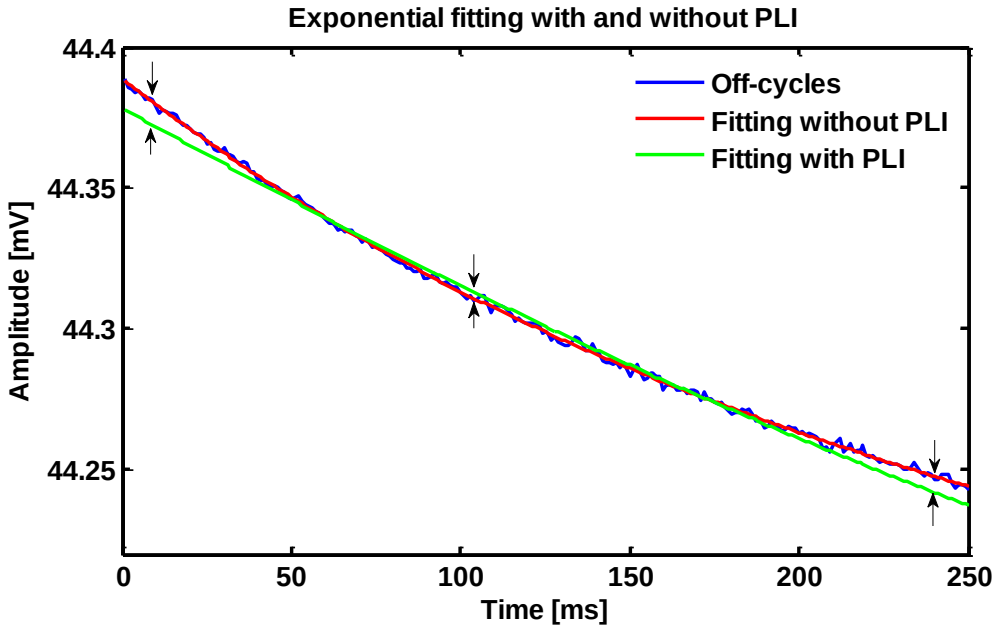

Figure 4.20. Exponential fitting before and after the removal of PLI. The off-cycles (blue) are fitted before (red) and after (green) the removal of PLI. The difference (indicated by the black arrows) between both fitting curves affects the frequency content of the analyzed data.

in Figure 4.20. Additionally, the segmentation approach of the off-cycles (as described in Section 4.1.2) before the removal of PLI components caused discontinuities in the fit residuals. By averaging a large number of off-cycles, these discontinuities could be amplified due to a fixed latency to stimulation misrepresenting in this way the results of spectral analysis.

Hence, we decided to optimize the removal process of PLI and exponential artifacts. The optimization steps were performed as follows:

(i) The off-cycles were transformed from the non-linear to the linear form by deducting an initial exponential fitting curve from the off-cycles, as described at the end of Section 4.1.3, and presented in Figure 4.16. The Nelder-Mead module in Simulink required a small number of iterations to generate the exponential fitting curve, since it is not the primary exponential fit. The purpose of this step is simply to determine the amplitude and phase of PLI and harmonics since they cannot be determined accurately in the non-linear form.

(ii) Reference signals for PLI and harmonics are generated by the Nelder-Mead algorithm for the off-cycles in the linear form and are successively subtracted from the off-cycles in the non-linear form. The objective of removing the harmonics of PLI is to minimize the amplitude of PLI as far as possible in order to accurately fit the exponential artifact.

(iii) After the removal of PLI and harmonics from the off-cycles in the non-linear form, a second primary and more accurate exponential fitting curve is created. The number of iterations of the Nelder-Mead algorithm is increased at this step in order to accurately fit the off-cycles.

(iv) The steps (i) to (ii) were sufficient to remove the exponential artifact. However, we found that the PLI was not completely removed from the off-cycles. This was because the first exponential fitting curve in step (i) could not fit the off-cycles accurately and this resulted in low frequencies that modulated the PLI amplitude. As a result, the accuracy of determining the parameters of the reference signals of PLI, especially the amplitude, was reduced. To overcome this, the second primary exponential fitting curve was subtracted directly from the original off-cycles in the non-linear form, which were still contaminated by PLI. The advantages of these additional steps were (a) exclusion of low frequencies and (b) accurate determination of PLI amplitude.

(v) The reference signals of PLI and harmonics were calculated again and deducted from the off-cycles in the linear form. Therefore, the exponential artifact and PLI were eliminated from the LFP recordings. The steps of the optimal sequence of removing the PLI and exponential artifact are shown in Figure 4.21.

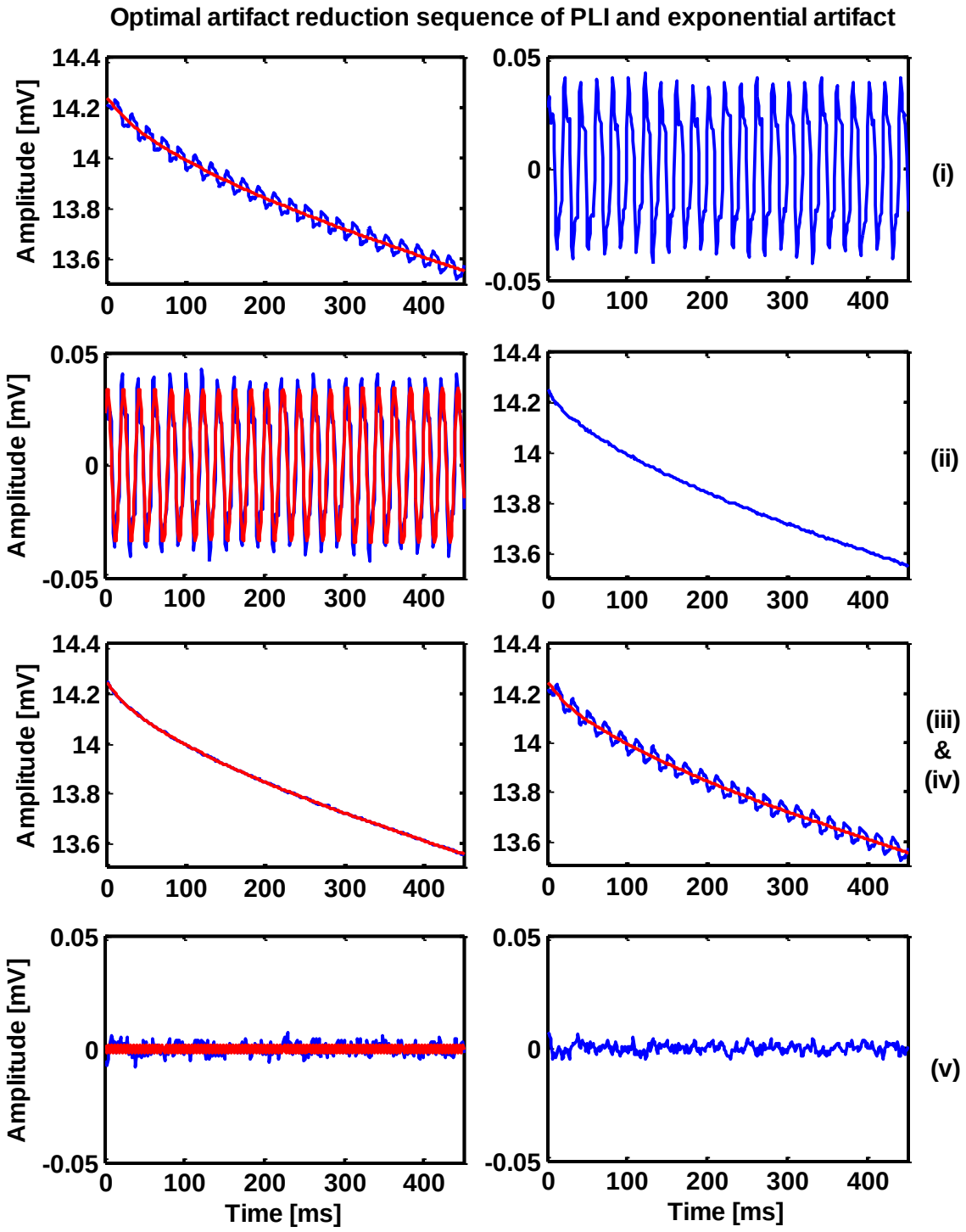

Figure 4.21. Steps of the optimal artifact reduction sequence of PLI and exponential artifact (LFP recording from a PD patient). (i) First exponential fitting curve (red) is generated for the off-cycles (blue) in the non-linear form and the residuals include the PLI in the linear from. (ii) Reference signals of PLI and harmonics (only 50 Hz reference signal is shown here) are generated in the linear form and subtracted from the off-cycles in the original non-linear form. (iii) & (iv) Second primary, and more accurate exponential fitting curve is generated after the removal of PLI. Next, the fitting curve is deducted from the original off-cycles in the non-linear form, which are still contaminated by PLI. (v) Reference signals of PLI and harmonics (the reference signal of the 250 Hz harmonic is shown here) are generated again and deducted from the off-cycles in the linear form.

4.2 Artifact reduction of spontaneous LFP and tremor recordings

Artifact reduction of spontaneous LFP recordings after CR DBS was not as complicated as during stimulation. This is due to: (i) the continuity of input signal, (ii) the absence of superimposed artifacts encountered during CR DBS, particularly the exponential artifact, and (iii) the applicability of typical artifact reduction and data analysis techniques (e.g. digital filters and spectral analysis). The same also applies to the tremor recordings which are contaminated by PLI and electrical background noise. An additional Simulink module was implemented for the real-time artifact reduction of tremor and spontaneous LFP recordings, which includes the following techniques:

4.2.1 Digital filters

Spontaneous LFP and tremor recordings were fed to a set of successive digital filters: (i) A 34 Hz **(**-3dB) low-pass filter with theoretically perfect suppression of PLI and harmonics, which was optimal for data sampled at 1 kHz. As it can be seen in Figure 4.22, the magnitude response of the low-pass filter has zeros at PLI frequency and its harmonics. (ii) A high-pass filter with 0.5 Hz cut-off frequency used to supress the DC and low frequency components. An application of the filters to LFP recording from a non-human

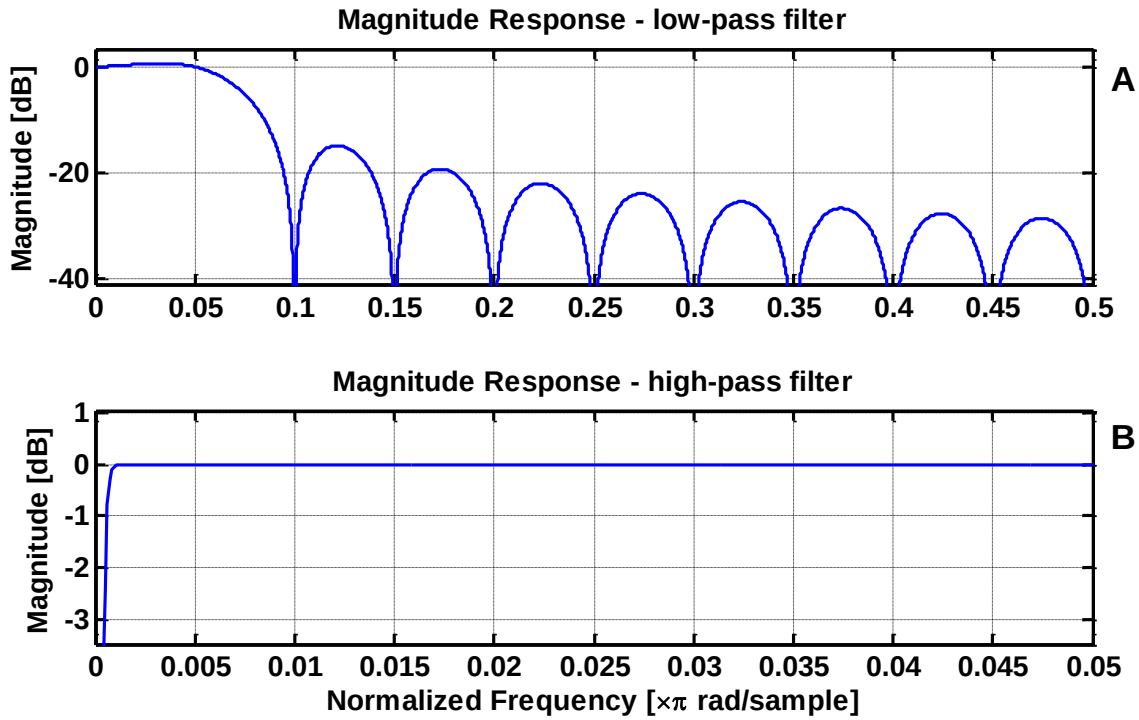

Figure 4.22. Magnitude response of the filters used for artifact reduction of Spontaneous LFP and tremor recordings. A: Discrete-time low-pass filter with cut-off frequency of 34 Hz (-3dB) for optimal suppression of the PLI artifacts. The roots of the filter function are located at PLI and its harmonics. B: Butterworth high-pass filter with cut-off frequency of 0.5 Hz for the removal of DC components and unrelated low frequencies.

primate is shown in Figure 4.23. In Subplot A, the raw data is depicted, in Subplot B, the data after the removal of PLI is presented and in Subplot C, the signal after the removal of DC and low frequency components can be seen. As one can see in this subplot, the signal is still contaminated by electrical background noise.

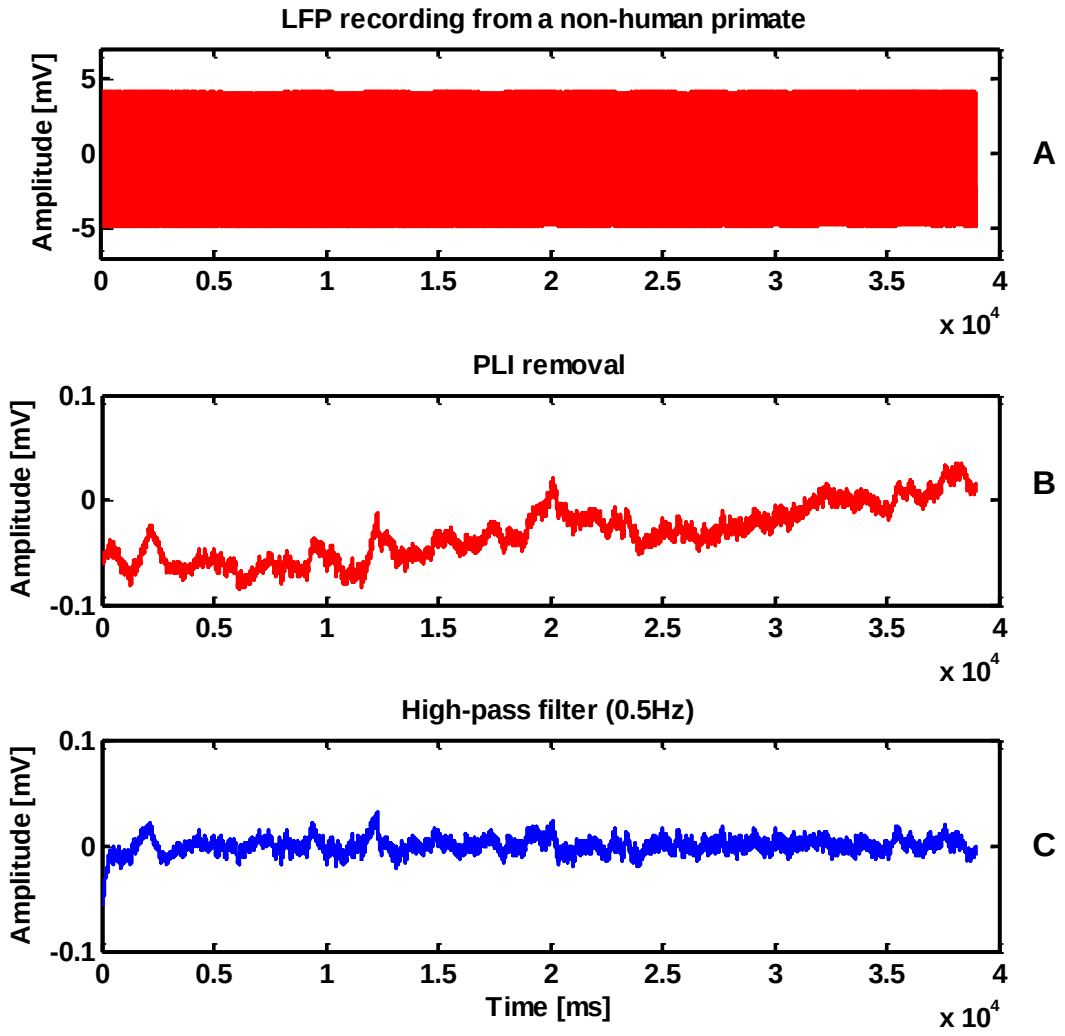

Figure 4.23. Application of the digital filters to a spontaneous LFP recording. A: LFP recording from a non-human primate. B: LFP recording after PLI artifact removal. C: The LFP recording after the removal of DC and low frequency components.

4.2.2 Signal de-noising using wavelets

The wavelet transform is an analysis tool well-suited to perform local analysis (i.e. to analyze changes of localized segment of a larger signal) and reveal signal aspects that other analysis techniques like Fourier transform miss (Strang & Nguyen, 1996). These aspects include discontinuities in higher derivatives, breakdown points and trends. Moreover, wavelet transform can often de-noise a signal without significant distortion. Thus, the

wavelet de-noising technique is used to remove the electrical background noise, and to increase the signal to noise ratio (SNR).

Wavelet transform uses a digital filter bank which consists of a series of high-pass and low-pass FIR filters to decompose a broadband signal into a collection of sub-bands with smaller bandwidths and lower sample rates (Strang & Nguyen, 1996). For real-time de-noising of LFP recordings, we integrated the wavelet de-noising module[12] provided by Simulink with our module. An example of applying the wavelet de-noising to a spontaneous LFP recording is shown in Figure 4.24. In this figure, LFP recording from a non-human primate is shown in Subplot A and the result of signal de-noising using wavelet transform is shown in Subplot B. The wavelet de-noising approach can also be used for the LFP recordings during CR DBS if the number (duration) of off-cycles is large enough (>10 s). For more rigorous treatment of the wavelet transform, we refer to (Strang & Nguyen, 1996).

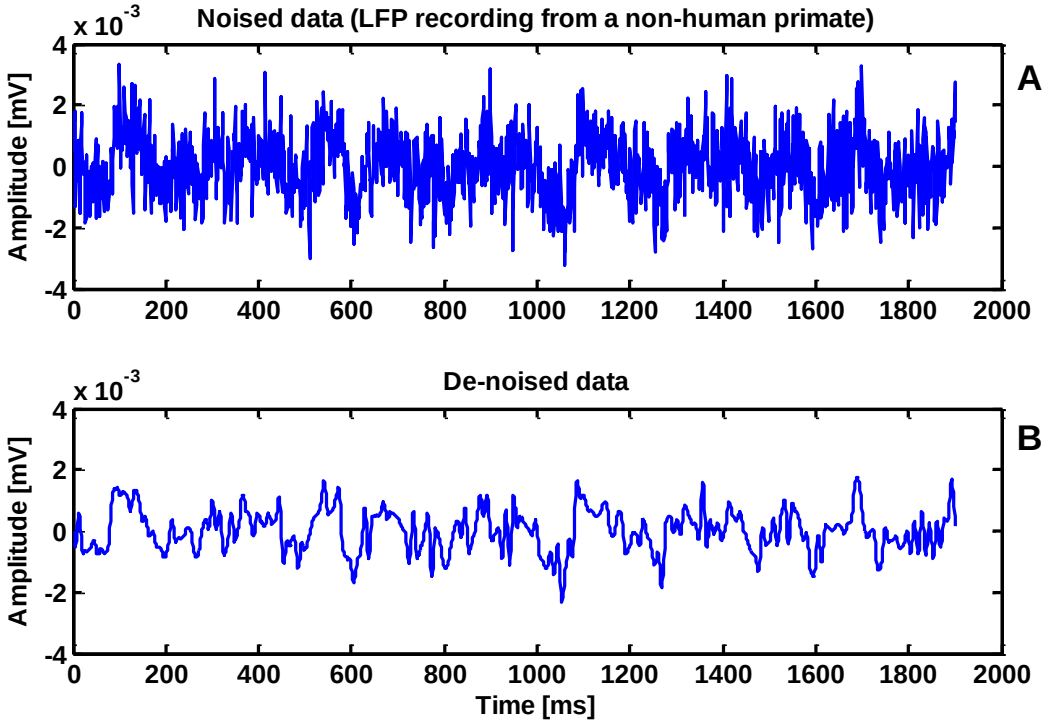

Figure 4.24. Application of wavelet de-noising technique to LFP recordings. A: Noisy LFP recording from a non-human primate. B: The effect of noise removal.

[12] MathWorks, Inc., USA, version 2007a

Chapter 5

Estimation of Demand for Tuning the DBS Parameters

In the previous chapter the developed and implemented technical solutions for real-time artifact reduction of local field potential (LFP) and resting tremor recordings during and after coordinated reset (CR) deep brain stimulation (DBS) were presented. We introduced each type of artifact along with a description of its removal techniques. The optimization of the artifact reduction techniques was important to obtain a reasonable feedback signal for the demand-controlled application of DBS. This chapter's focus is on the development and implementation of technical solutions for: (i) analysis of LFP and tremor recordings, (ii) estimation of a demand for adjusting the stimulation parameters, and (iii) adjustment of the stimulation parameters. The analysis algorithms are dedicated to find the values of relevant biomarkers of pathological activity in the recorded data. Such biomarkers-values can be used for the estimation of demand for further stimulation and subsequently for the tuning of stimulation parameters.

LFP recordings show neuronal oscillations at different frequency ranges as described in Section 2.1. These oscillations are associated with Parkinson's disease (PD) symptoms such as resting tremor which has been shown to be correlated to subcortical oscillations (Tass et al., 2010, Smirnov et al., 2008). Analysis techniques of LFP recordings are typically based on computations in the frequency domain such as power spectral density (PSD) and coherence (Brown et al., 2001, Rossi et al., 2007, Masimore et al., 2004). Additional techniques, e.g., autoregressive modeling have been used to study the temporal dependencies of the signal such as causality and stability (Huberdeau et al., 2011).

For the short off-cycles, in the LFP recordings during CR DBS, we tested several analysis techniques to calculate biomarkers-values of the pathological activity. For spontaneous LFP and tremor recordings, spectral analysis was the main analysis tool. The analysis techniques are based on estimating the strength of pathological synchronized activities. The variation in the strength of such activities is monitored over time to quantify the demand for adjusting the stimulation parameters.

5.1 Data analysis during CR DBS

Since the strength and variability of the stimulation artifacts during CR DBS (on-cycles) together with the subsequent exponential artifacts prevented a real-time analysis, we only analyzed the off-cycles (see Section 4.1.1). Hence, we focused on the short data segments (i.e., off-cycles, max. 500 ms) free of stimulation artifacts and the subsequent exponential artifacts. In order to calculate biomarkers of the pathological activity, the following two analysis methods were utilized: (i) Averaging of off-cycles, and (ii) spectral analysis.

Averaging of off-cycles

In this analysis method, a large number of off-cycles are averaged in order to reveal peaks that describe neuronal response with fixed latency to stimulation. This approach is useful to reveal neuronal activity that has much smaller amplitude than artifacts and electrical background noise (Hashimoto et al., 2002). We tested this method using the off-cycles of LFP recordings from PD patients. These off-cycles, which last 400 ms, were modified by adding a simulated peak with fixed latency of 200 ms prior to the following on-cycles. The peak amplitude was set to 1 mV and was added before processing the data by the artifact reduction algorithms. After the removal of artifacts, a large number of off-cycles were averaged in real-time by the implemented module in Simulink. An example of averaging 100 and 600 off-cycles, triggered by their onset, where the peak was observed to be well-defined, is shown in Figure 5.1. The goal of applying this method to different numbers of off-cycles was to test its robustness and reliability. Out of these results, we conclude that averaging 100 off-cycles in the LFP recordings during CR DBS might be sufficient to detect neuronal activity, time-locked to the stimulation, if present.

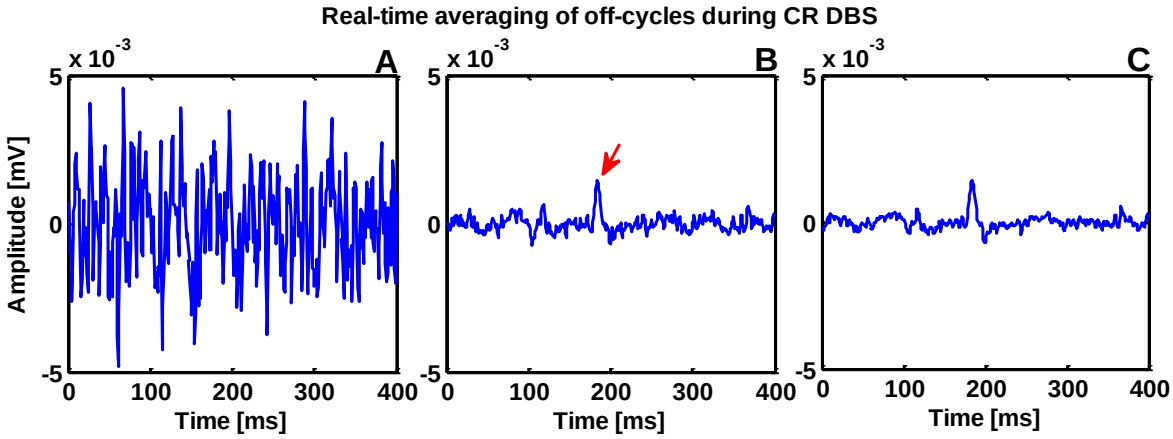

Figure 5.1. Real-time averaging of off-cycles with a simulated peak. A: Single noisy off-cycles period of LFP recording during CR DBS before averaging. The simulated peak was added to all off-cycles of the LFP recording. B: Averaging 100 off-cycles shows reduced noise and the simulated peak in the middle (red arrow). C: Averaging 600 off-cycles shows that an increased number of off-cycles further reduces the noise and makes the peak clearer.

Spectral analysis

Spectral analysis is mainly based on the digital Fourier transformation (DFT) which requires continuity in the data in order to capture the power of dominant frequencies. The delimitation and subsequently concatenation of a large number of off-cycles causes discontinuities, which disturb the coefficients of the DFT and produce a ringing artifact (leakage effect) in the power spectrum. Discontinuities can be smoothed by weighting the data, e.g., with Hanning or Hamming window. However, depending on the length of the off-cycles, the weighting approach may cause low frequencies close to those of resting tremor, i.e. 3 – 10 Hz. The concatenation of off-cycles can be useful if the onset of the off-cycles is a time multiple of the neuronal oscillation period. For instance, if the pathological neuronal activity is at, e.g., 5 Hz and the onset of the off-cycles is at multiples of 200 ms, then the phase information will be preserved. This case was uncommon in our LFP recordings due to the different values of CR stimulation parameters used and the expected variation in the frequency of the pathological activity over time.

To avoid losing the phase information, the spectral analysis was applied to the un-concatenated off-cycles. Here, the off-cycles appear between the on-cycles that are set to zero, as illustrated in Section 4.1.1. The minimum and maximum duration of the off-cycles found in our LFP recordings are 120 ms and 500 ms, respectively. Our tests with simulated sinusoids showed that a frequency can be estimated even with a half of its period in the un-concatenated off-cycles. However, the amplitude was reduced due to the blanking of the on-cycles. In order to estimate the real amplitude, the spectral power was modified as described in the following section.

5.2 Estimation of demand during CR DBS

The method used an averaging of off-cycles intends to find successive peaks that correspond to neuronal activity. The time difference between, at least, two successive peaks can be used to determine their frequency. By monitoring the variation of the amplitude of these peaks, we can determine the strength of the pathological activity. This strength is measured by continuously averaging the amplitudes in real-time and is going to be used to quantify the demand for tuning the stimulation parameters. We applied this approach to our LFP recordings from four PD patients. Figure 5.2 shows two well-defined successive peaks of neuronal activity with fixed latency to stimulation of one patient. These peaks were revealed by averaging 1332 off-cycles. Because of the low amplitude of the peaks, averaging over a larger number of segments was necessary. For the LFP data of other patients, despite of the optimization of the artifact reduction algorithms, no visually clear peaks were found.

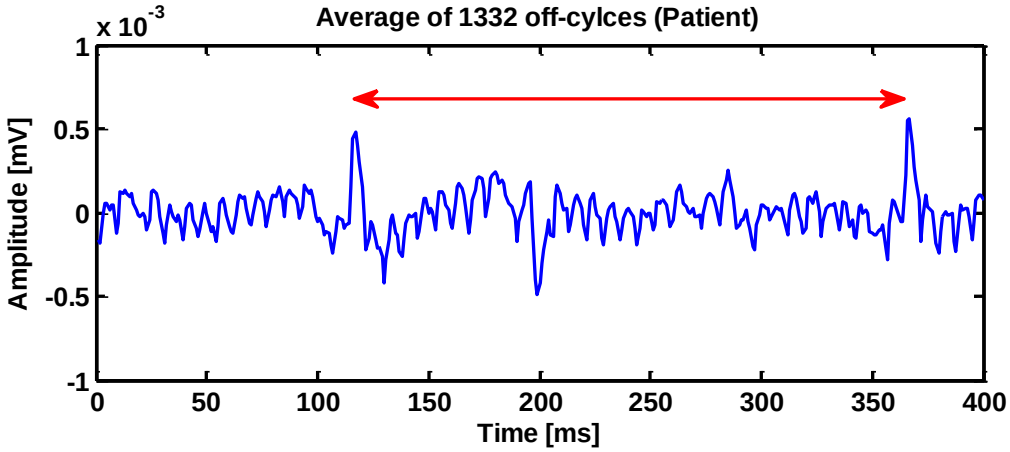

Figure 5.2. Successive peaks revealed by averaging off-cycles of patient's data. The time difference (double red arrow) between the two peaks is 251 ms which corresponds to neuronal activity in the approximate range of 4 Hz. The mean amplitude of the peaks is 0.5 mV. 1332 off-cycles were averaged.

Another approach to estimate the demand value during CR DBS was to rescale the amplitude of the dominant frequency in the power spectrum of the un-concatenated off-cycles. The spectral power was scaled by a factor *k* calculated from the CR stimulation parameters, i.e., the number of off-cycles (N_{off}) and the CR frequency (F_R) of the CR pattern (Section 2.2.2). The scaling factor is defined as shown in Equation 5.1.

$$\boldsymbol{k} = \begin{cases} \dfrac{\boldsymbol{N_{off}} \cdot \boldsymbol{D_{cy}}}{\boldsymbol{f_s}}, & \text{for } \boldsymbol{N_{off}} \cdot \boldsymbol{D_{cy}} < \boldsymbol{f_s}, \\ \boldsymbol{1}, & \text{for } \boldsymbol{N_{off}} \cdot \boldsymbol{D_{cy}} \geq \boldsymbol{f_s}, \end{cases} \qquad 5.1$$

where f_s is the sampling rate (1 kHz) and D_{cy} is $1/F_R$.

This method was tested on a simulated signal, consisting of the sum of two unity-height and white-noised sinusoids of 7 Hz and 23 Hz as shown in Figure 5.3. In this figure, two different sets of CR stimulation parameters are used to test the amplitude dynamics and the scaling factor. Our tests showed that the reduction in the amplitude is proportional to the shortness of the off-cycles (see Figure 5.3.D). The actual amplitude was recovered by the scaling factor as shown in Figure 5.3.E. Application of this method to LFP recordings collected from PD patients under different CR stimulation parameters showed no dominant frequencies. The reason behind this is either, that the pathological synchronized neuronal activity was reduced due to stimulation or simply that such a synchronized activity was not present.

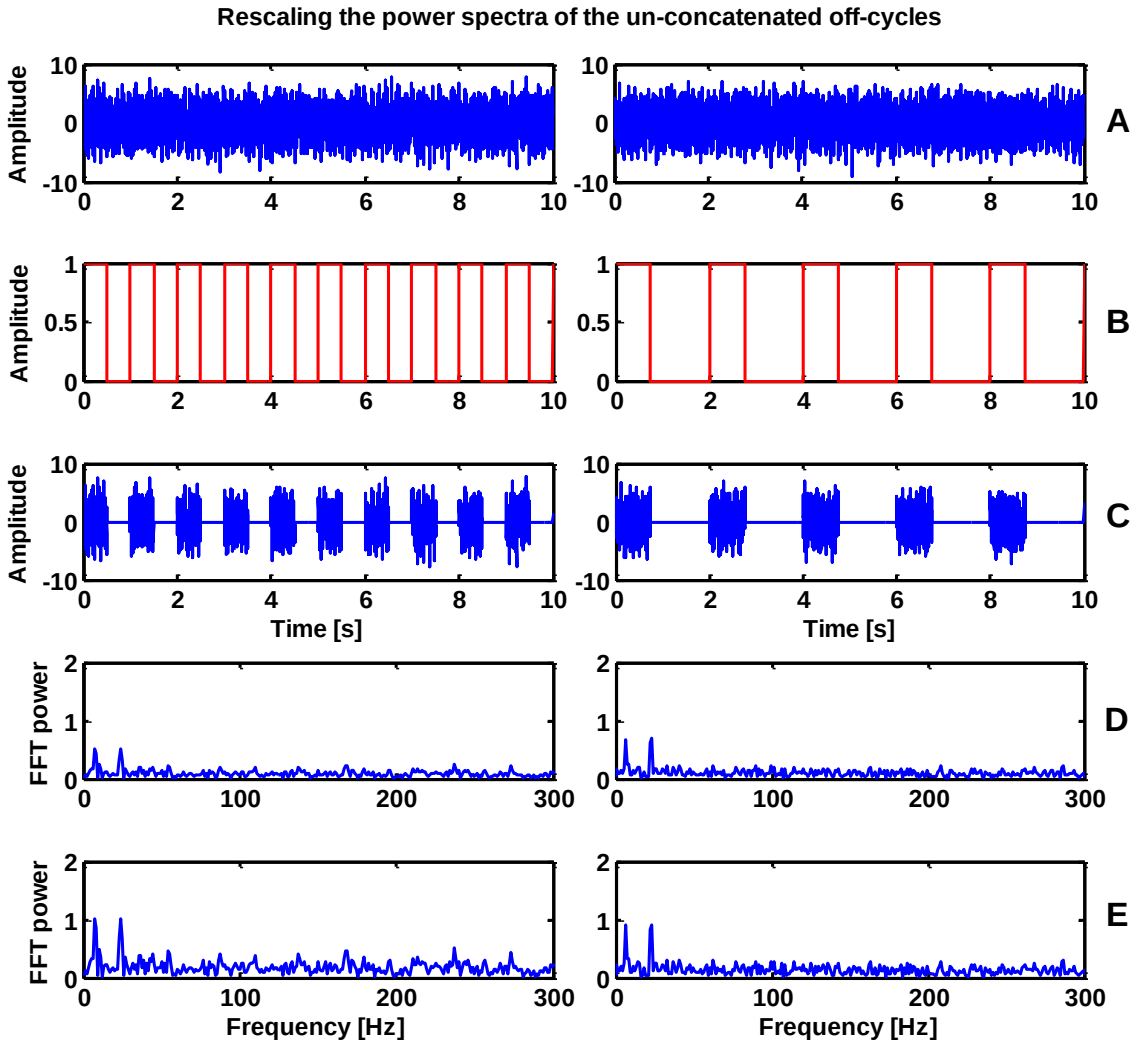

Figure 5.3. Rescaling the power spectra of the un-concatenated off-cycles**.** A: The sum of two simulated, unity-height, and white-noised sinusoids at 7 Hz and 23 Hz. The same signal is shown in both panels. B: Delimitation of off-cycles using unity-height signals generated with two different sets of CR stimulation parameters: (left panel) F_R 4 Hz, N_{off} 2 and N_{on} 2, and (right panel) F_R 4 Hz, N_{off} 3 and N_{on} 5. C: Multiplication of the signals shown in A and B. The off-cycles are delimited, and the on-cycles are set to zero. D: Power spectra with un-scaled amplitude. E: Rescaled amplitude with scaling factor k: 0.5 (left panel) and k: 0.75 (right panel).

5.3 Analysis of spontaneous LFP and tremor recordings

Spontaneous LFP activity was recorded intra- and post-operatively from PD patients and from non-human primates (Macaque monkeys) after CR stimulation (Section 3.2.1). Resting tremor was recorded from PD patients during and after CR DBS. The analysis of these recordings was easier than during stimulation due to continuity of data and absence of stimulus and exponential artifacts. The main analysis tool was the spectral analysis, which aimed at monitoring the variation in the strength of the pathological activity over time. For the off-line tests in MATLAB, we used DFT, periodogram and spectrogram

functions. The last two were applied with additional options like windowing and overlapping of data segments. An example of applying the DFT and the spectrogram to LFP recording of a parkinsonian non-human primate is shown in Figure 5.4. This figure presents 12 s of raw data in Subplot A. The results of spectral analysis are shown in Subplots B and C where an activity at 8 Hz can be seen. DFT was performed on non-overlapping sections of equal length, i.e., 1024 points, giving a frequency resolution of 0.98 Hz. The spectrogram overlapped segments of equal length (i.e., 512 points), overlapping of 500 points, and frequency resolution of 0.1 Hz. Spectrograms were used at first to locate the epochs of the dominant frequencies in the recorded data.

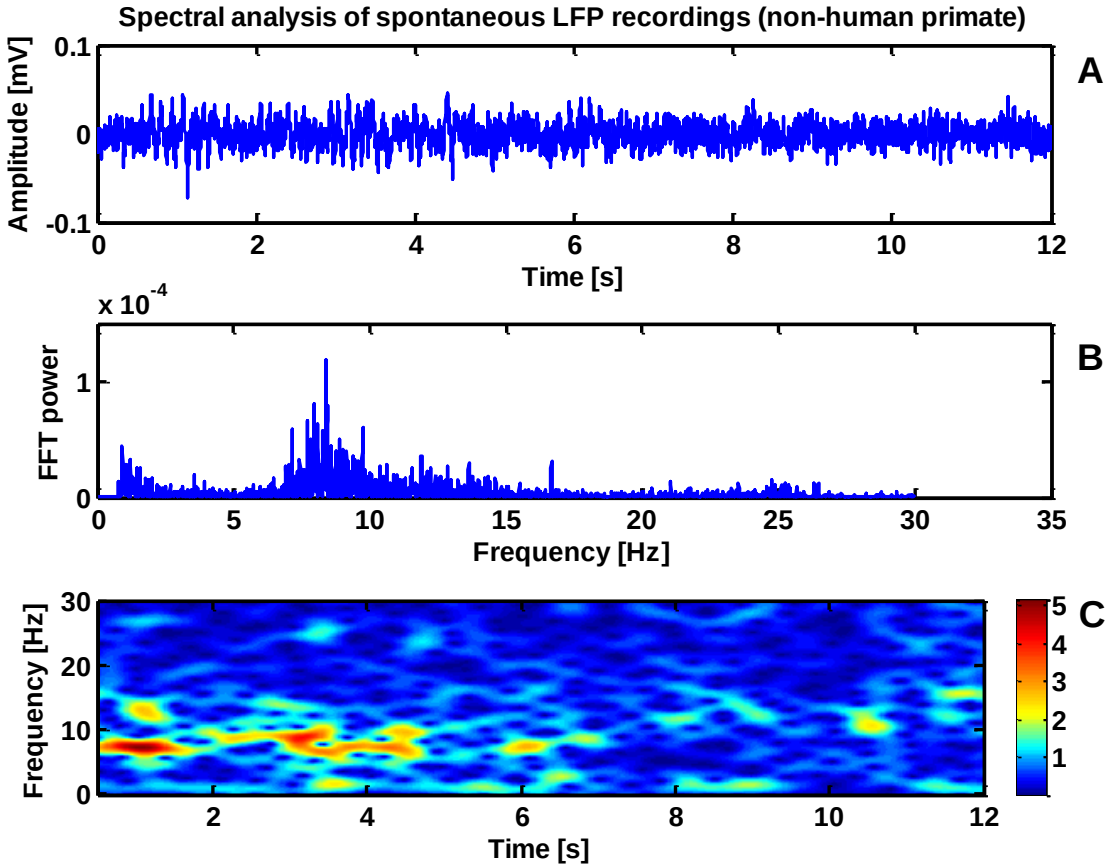

Figure 5.4. Spectral analysis of spontaneous LFP recordings. A: Raw LFP recording from a non-human primate after CR DBS. B: DFT of the recording shows neuronal activity around 8 Hz. C: Spectrogram of the LFP recording shows the same activity as in B as a function of time.

We analyzed the recordings of the three contacts in order to estimate the strength of the pathological activity in the brain layers where the different contacts are placed. An example of two LFP signals, which were recorded by two contacts (i.e., C1 and C2) from a non-human primate are shown in Figure 5.5. The amplitude of the recorded activity is lower on the first contact. Possible reasons for such a difference in amplitude could be dissimilar contact impedances or/and that one contact was closer to the synchronized neuronal population than the other. The variation in the pathological activity in terms of

frequency and amplitude indicates the need for estimating different demand values for the different contacts.

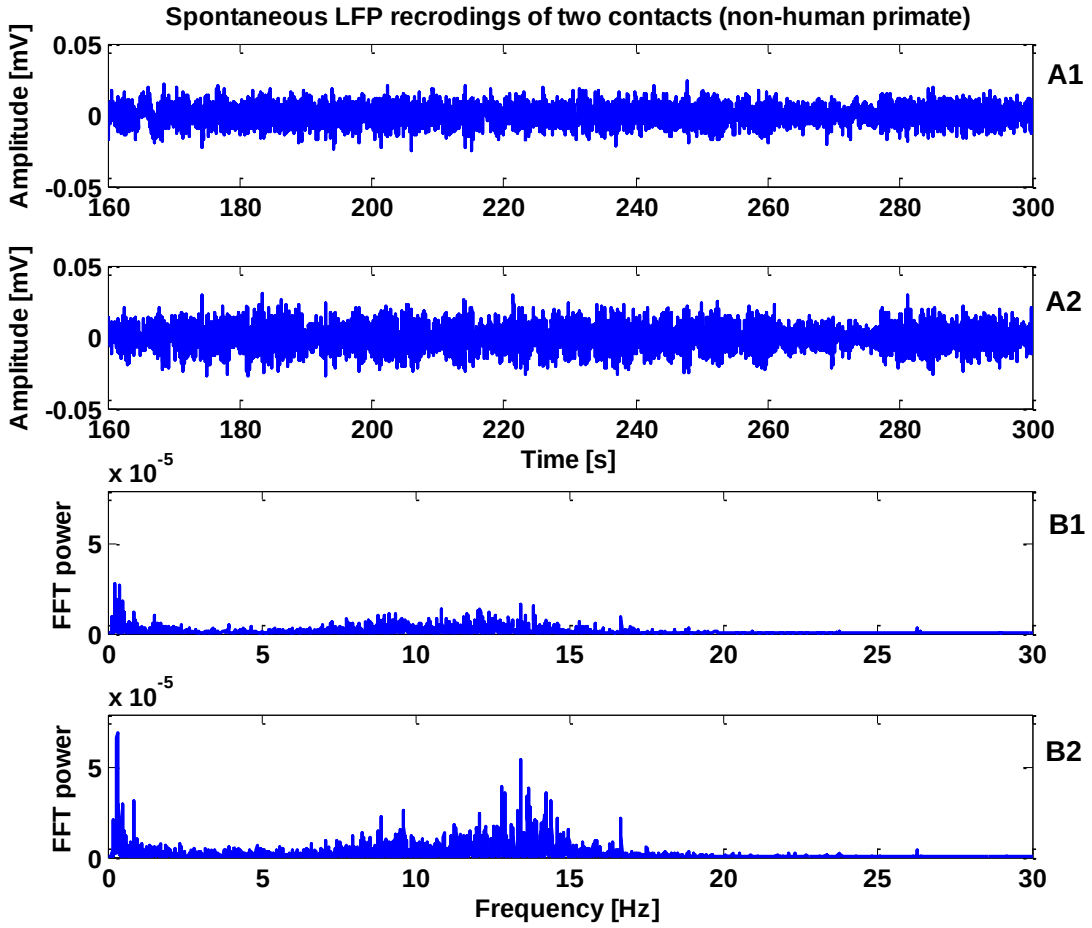

Figure 5.5. Spectral analysis of spontaneous LFP recordings of two contacts from a non-human primate. A1 and A2: LFP activity recorded by two contacts on the implanted electrode, i.e., C1 and C2, respectively. B1: Power spectrum of the recording in A1 shows an activity in the range 8 – 13 Hz. B2: Power spectrum of the recording in A2 shows similar activity as in B1, but with higher amplitude. This difference in the amplitude indicates the need for different demand values.

5.4 Estimation of demand with spontaneous LFP and tremor recordings

In order to calculate the demand value in the spontaneous LFP and tremor recordings, we monitored the variation in the amplitude of the dominant frequencies over time. An example of such a variation is shown in Figure 5.6. In this figure, a section of 30 s LFP recording from a non-human primate after CR stimulation is divided into three segments (each of 10 s). Then, a periodogram (single sided amplitude spectrum) is applied to each segment. The results show that the amplitude of the LFP activity is reduced in the second segment and further reduced in the third one. This variation in the amplitude can be used

to evaluate the strength of the pathological activity and to estimate the demand value in a continuous manner.

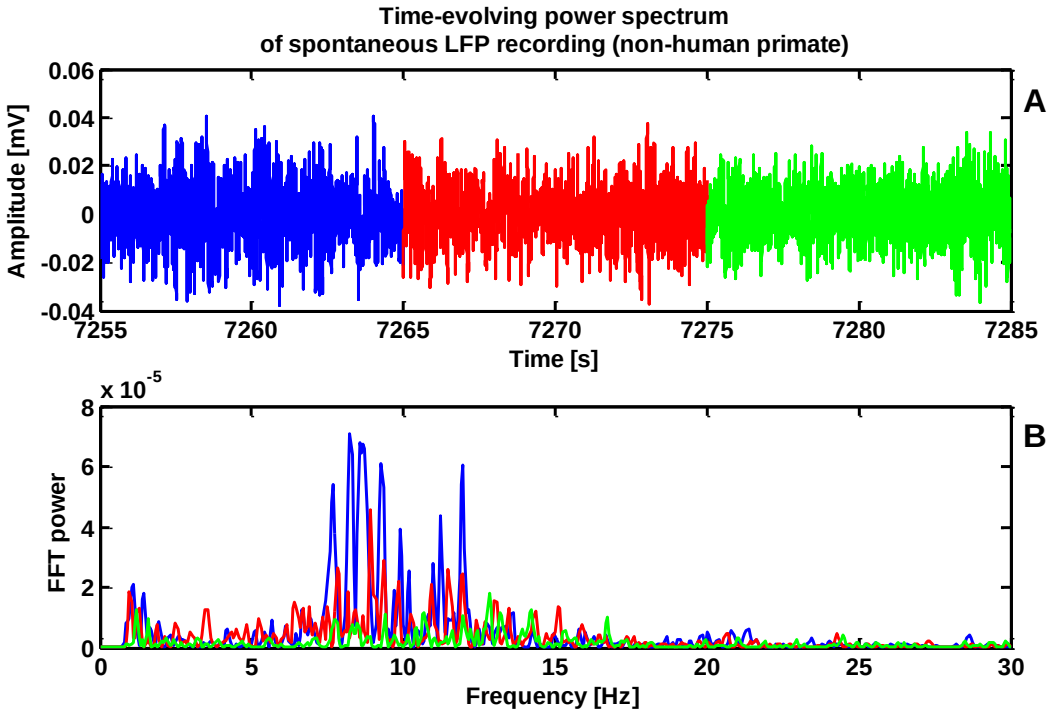

Figure 5.6. Time-evolving power spectrum of a spontaneous LFP recording from a non-human primate. A: LFP recording, which lasts 30 s, is divided into 3 segments each of 10 s (indicated by colors). B: Power spectra of the three segments show a reduction in the amplitude of the recorded activity if time evolves.

The implemented Simulink module for real-time data processing consists of different steps that include artifact reduction (using the methods presented in Section 4.2), data analysis, and estimation of the demand value. The following steps are involved in the data analysis and are explained in detail:

Preprocessing: The aim of this step is to prepare the recorded data for the analysis process. The data is first buffered and divided into data segments. A buffer size of 4096 (2^{12}) samples is used for both wavelet de-noising (explained in Section 4.2.2) and spectral analysis. This buffer size indicates that every 4 seconds a new frequency value is estimated. Furthermore, our tests showed that an overlap of data segments increases the probability of detecting a dominant frequency, but it causes discontinuities in the output signal. We used an overlap of 1024 samples and the discontinuities were reduced by the wavelet de-noising filters without affecting the detected frequencies.

Detection of dominant frequencies: The frequency content of the buffered data is then analyzed using the periodogram function. The latter shows the distribution of the power contained in the signals over a frequency range of 3 – 43 Hz, where each frequency is resolved by 4 bins, i.e., a frequency resolution of 0.24 Hz. The frequency with highest power in the output of the periodogram is marked as a dominant frequency for the current

data segment. This step is repeated for 20 successive segments, i.e., 20 frequency values are detected and buffered. Once a dominant frequency is detected, its power is set to zero in order to detect the next dominant frequency as illustrated in the flow diagram in Figure 5.7. As each frequency in the power spectrum is resolved by 4 bins, the amplitude-bin of the detected frequency ± 1 bins are set to zero. The first dominant frequency is mostly used for the estimation of the demand value. However, if this frequency represents a known artifact (e.g., an interference), it is useful to detect the second highest peak in the power spectrum. A maximum of three frequencies can be detected in each data segment by the Simulink module.

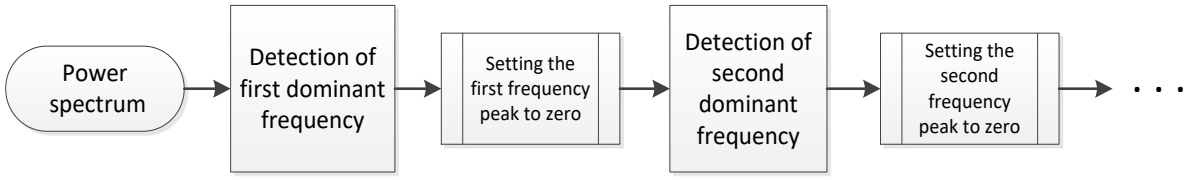

Figure 5.7. Flow diagram for successive detection of dominant frequencies in the power spectrum of spontaneous LFP and tremor recordings.

Histogram: The aim of this step is to evaluate the distribution of the 20 buffered frequency values and to find which frequency is more common in the recorded data. To this end, a histogram is used, in which each detected frequency is represented by 4 bins, giving a frequency resolution of 0.25 Hz. Then, a threshold is set which implies that each frequency should appear at least 12 times in the 20 buffered values. If the distribution of a frequency is below this threshold, this frequency value is discarded. The goal of the threshold and the 20 buffered values is to find reliable and stable pathological oscillations in the LFP and tremor recordings. Examples of the different histograms are shown in Figure 5.8. When a dominant frequency passes the threshold, its index is divided by 4 (i.e., the number of bins in the histogram) to get the frequency value in Hz.

***Estimation of amplitude*:** The corresponding amplitudes of the 20 detected frequencies are estimated from the power spectrum and buffered simultaneously. When a dominant frequency passes the threshold in the histogram, all corresponding amplitudes are extracted and averaged (divided by the distribution value). This step is done to get the instantaneous amplitude of the current pathological activity, as illustrated in Figure 5.9.

After the estimation of the amplitude, the input signal is shifted by one segment. The steps described above are then repeated to evaluate whether the new data segment affects the distribution of frequencies or not. The amplitude value is then either updated or the stimulation continues with the current value. This approach results in an amplitude value every 4 s which can be used to adjust the stimulation parameters.

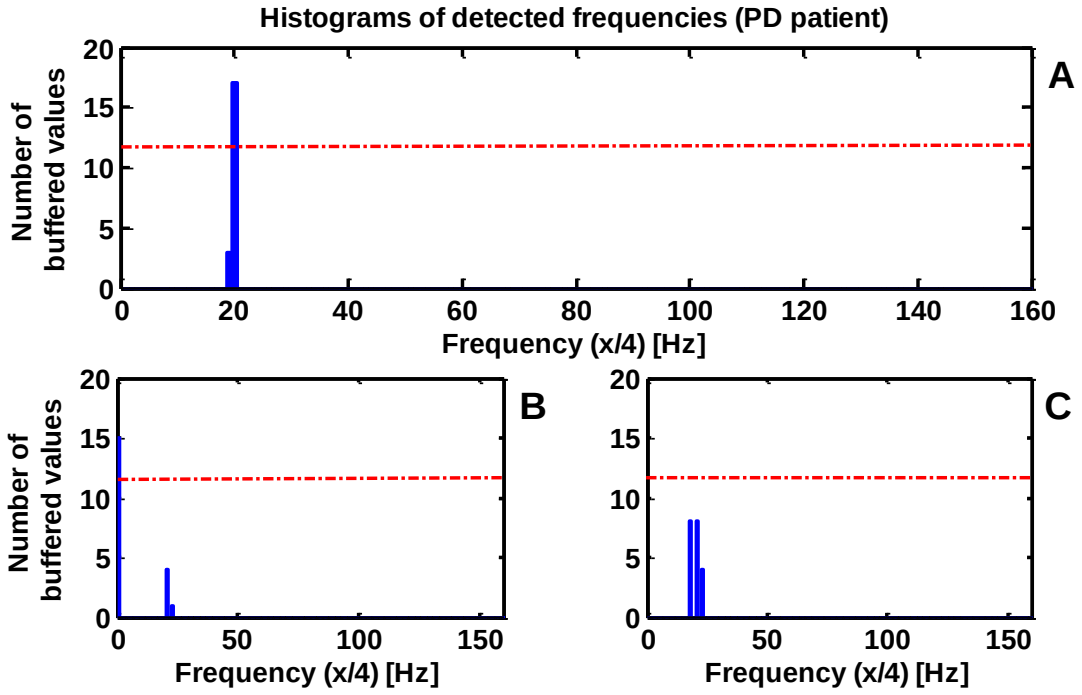

Figure 5.8. Histograms of the 20 detected and buffered frequencies. A: The distribution of a dominant frequency is above the threshold which is set to 12. The frequency is at 5.25 Hz (index 21 divided by 4). B: Case where a low frequency (here at 1 Hz) outside the range of interest is dominant. C: The distribution of a dominant frequency is below the threshold and the variation of this frequency is indicated by the bins next to it.

Buffered frequencies [Hz]		Estimated frequency [Hz]		Flag		Buffered amplitudes [mV]		Extracted amplitudes [mV]		Average of the amplitudes [mV]
4.5		5		0		0.1961		0		
4.5		5		0		0.1811		0		
4.5		5		0		0.1683		0		
4.5		5		0		0.1571		0		
5.5		5		0		0.1474		0		
5.5		5		0		0.1388		0		
5.5		5		0		0.1275		0		
5.5		5		0		0.1162		0		
5	=	5	→	1	X	0.1049	→	0.1049	→	
5		5		1		0.0934		0.0934		0.0459
5		5		1		0.0819		0.0819		
5		5		1		0.0704		0.0704		
5.75		5		0		0.0589		0		
5.75		5		0		0.0474		0		
5.75		5		0		0.0358		0		
5.75		5		0		0.0243		0		
5		5		1		0.0128		0.0128		
5		5		1		0.0012		0.0012		
5		5		1		0.0012		0.0012		
5		5		1		0.0012		0.0012		

Figure 5.9. Real-time averaging of the amplitudes of the detected frequencies. The 20 detected frequencies are compared with respect to the estimated frequency with maximum distribution in the histogram. A logical flag (1/0) indicates the match and mismatch of the values, respectively. The logical flags are multiplied by the corresponding amplitudes to select the related amplitudes, which are averaged to determine the strength of the current pathological activity.

The steps described above are repeated in three phases to detect three dominant frequencies in each data segment as shown in Figure 5.7. The threshold of the frequency distribution is reduced in case of the second dominant frequency. The reason behind this is that the amplitude of the second dominant frequency is often lower than the first one and hence, it has a lower probability to be detected. This situation can be described as throwing a dice that has sides with different areas. At the time of throwing the dice, the maximal probability is given for the side with the largest area which mostly faces the ground. If we set the threshold value to, e.g., 50 % (10 results of 20) for the first frequency, it should be 35 % for the second frequency and even less for the third frequency. However, when the amplitude of the detected frequency could not be distinguished from noise, then it would not reach the threshold. Moreover, by increasing the frequency resolution of the periodogram, it is possible to detect the frequency variations (see Figure 5.8). However, this reduces the probability of detecting the main frequency. In order to use a high-frequency resolution and increase the probability of detecting a dominant frequency, we reduced the threshold value to 7 and 5 for the first and second frequencies, respectively. A flow diagram that summarizes the steps of estimating the amplitude of pathological activity for the demand-controlled application of DBS is shown in Figure 5.10.

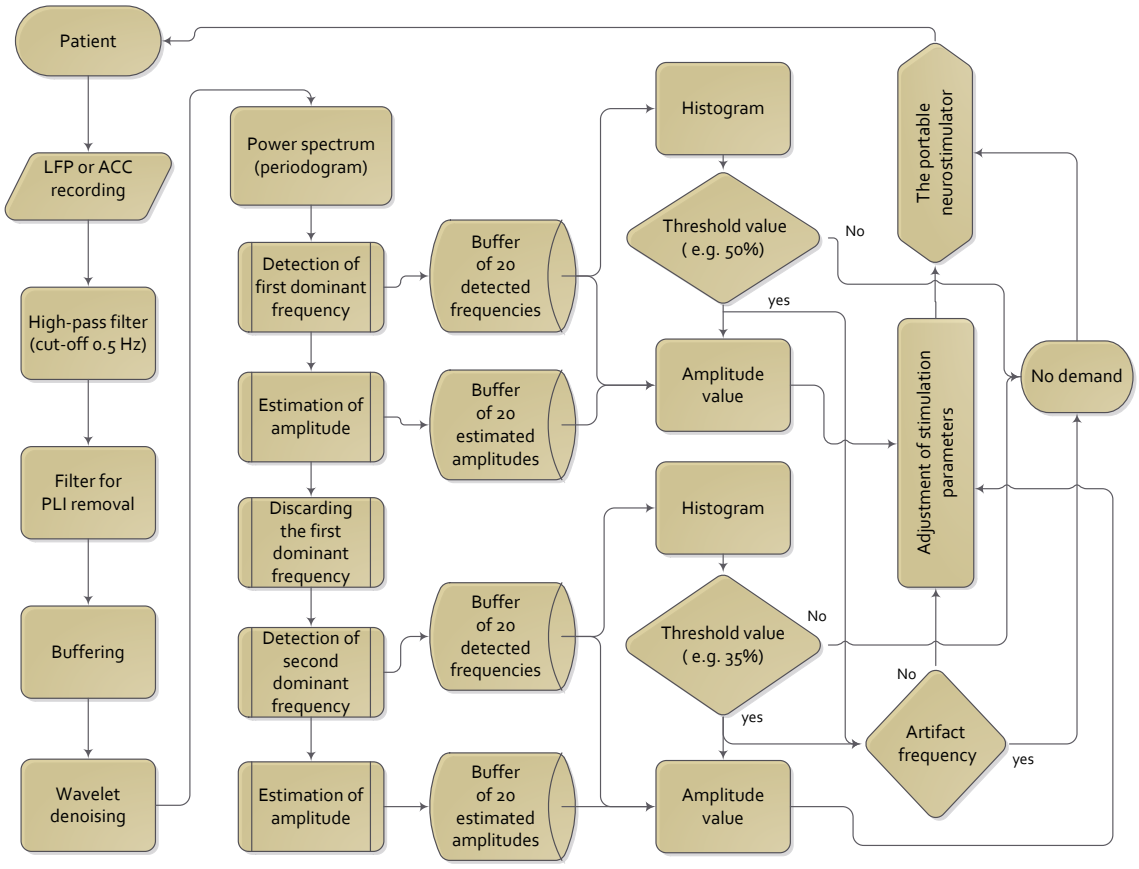

Figure 5.10. Flow diagram for estimating the amplitude of two dominant frequencies.

5.4.1 Tests with LFP and tremor recordings

The implemented module was tested on different data: (i) stimulation signals generated by the portable neurostimulator and recorded from a simple electrical circuit, (ii) LFP recordings from non-human primates, and (iii) spontaneous LFP and tremor recordings from PD patients.

Tests with an electrical circuit

The objective of these tests was to investigate the performance of the implemented module in detecting dominant frequencies. Another objective was to test the possibility of applying this approach to LFP recordings during CR DBS. The four contacts of the stimulation electrode were connected to three resistors each of 1 kΩ and a reference. We set the CR stimulation parameters such that long off-cycles result (N_{on} 1, N_{off} 15, and F_R 1 Hz). For these tests, the off-cycles were concatenated and the length of each off-cycle was 15 s. The stimulation signals were sent to the electrical circuit and recorded simultaneously. Later, we added simulated sinusoids, with low amplitudes (i.e., 100 – 500 µV), to the recorded data before removal of artifacts.

Two tests were performed with two different sets of sinusoids. In the first test, the sum of five sinusoids with the same amplitude and different frequencies were added to the recorded data. In the second test, the same five sinusoids were used but with different amplitudes, as illustrated in Table 5.1. We selected frequencies close to each other to evaluate the ability of the module to detect these frequencies individually. For these tests, we extended our module to make it able to detect five frequencies.

Figure 5.11 shows that all sinusoids were detected. In the first test, the frequencies were detected nearly simultaneously, since all of them have the same probability to be detected, i.e. the same amplitude. In the second test, the detection order of the sinusoids was according to their amplitudes. The sinusoid with maximum amplitude (highest probability) was detected in the first phase, whereas the frequency with lowest amplitude was detected by the last phase.

Table 5.1. Two different sets of sinusoids used to test the implemented module.

Test 1		***Test 2***	
Frequency [Hz]	Amplitude [µV]	Frequency [Hz]	Amplitude [µV]
4	300	4	100
5	300	5	200
7	300	7	300
9	300	9	400
15	300	15	500

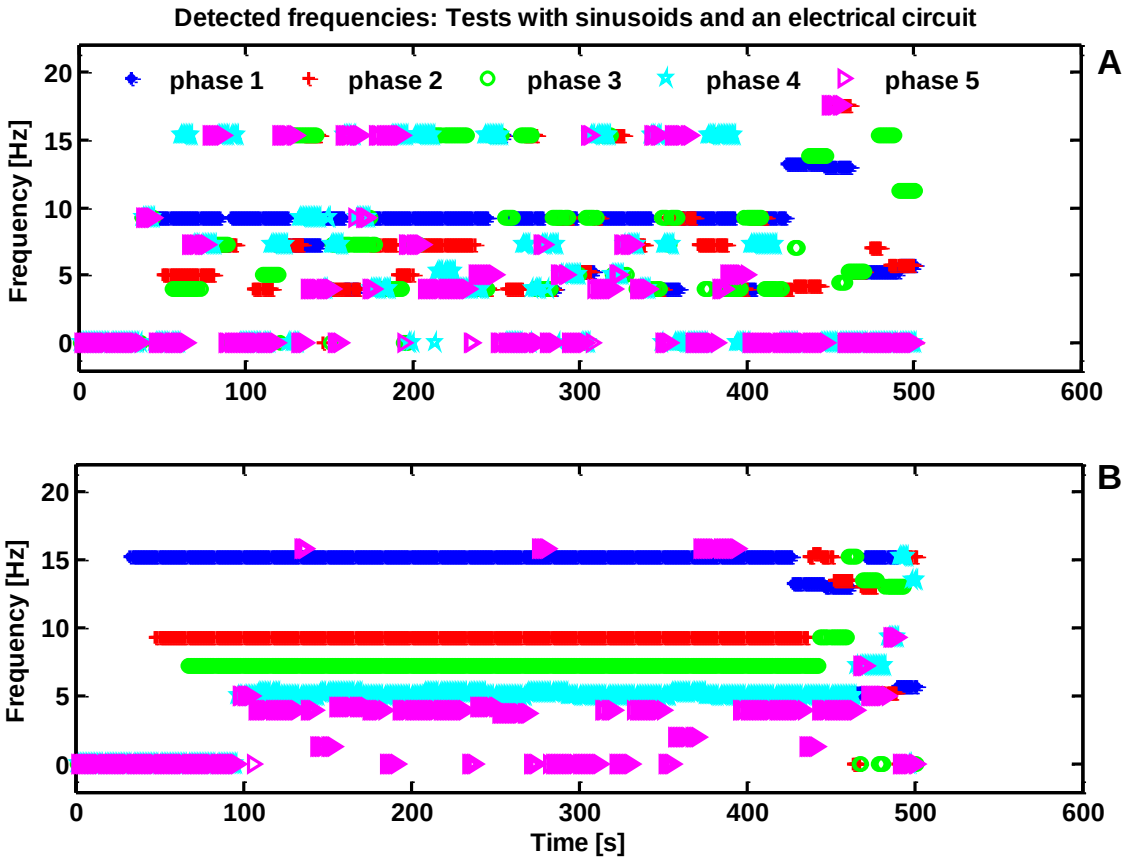

Figure 5.11. Tests with simulated sinusoids and signals recorded from an electrical circuit. A: Results of test 1. Sinusoids with the same amplitude are detected during all phases (indicated by colors) of the implemented module. B: Results of test 2. Sinusoids with different amplitudes are detected according to their amplitudes. Frequency component with highest and lowest amplitudes are detected at first (blue) and last (magenta) phases, respectively. Values at the zero line indicate that no frequency component is detected during this phase.

LFP recordings from non-human primates

We also tested the module retrospectively using LFP recordings collected from parkinsonian non-human primates. Scaled-down version of the human electrode (described in Section 2.2) was implanted in the brain of three Macaque monkeys in order to record LFP activity intra-operatively. More than 20 recordings from each side of the brain were taken over 4 months (for more details see Section 3.2.1). The algorithm was able to detect dominant frequencies within different frequency bands and monitor the changes in the amplitudes of these frequencies. The amplitudes of some of these frequencies were present in a larger number of recordings and were approximately constant over time. We performed later some experiments in the surgery room (in Peking, China), and found that some of the detected frequencies are interferences caused by machines in the background, this holds especially for the peaks at 9.75 Hz and 16.5 Hz (see Figure 5.12). Therefore, these peaks were marked as known artifacts in the implemented module in order to prevent them from

being recognized as neuronal activity during the analysis process. Other peaks were found and might represent synchronized, pathological neuronal activities, i.e., the peak detected at 6 Hz and around 3 Hz.

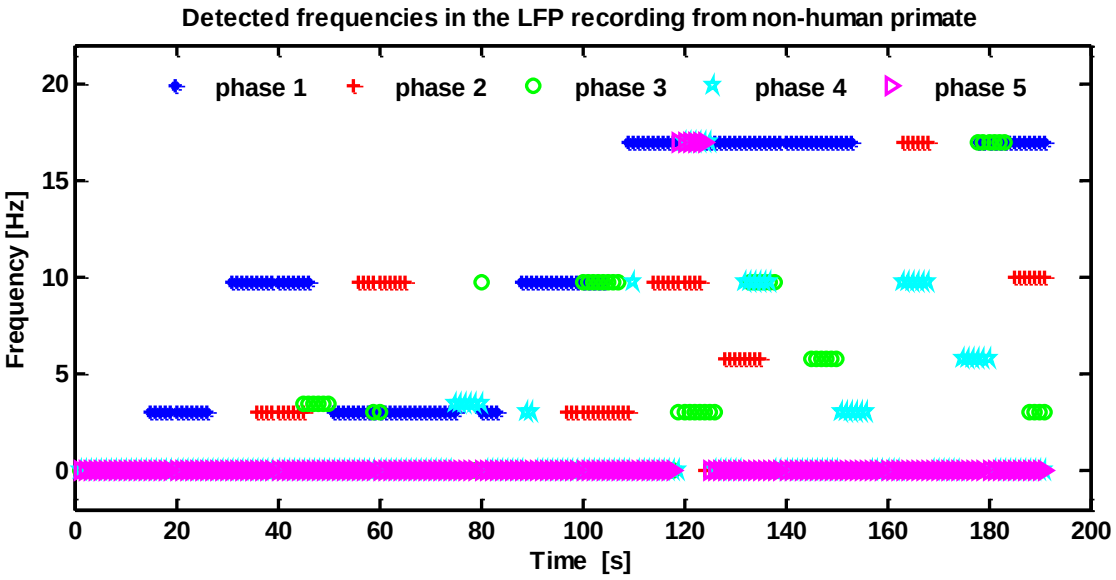

Figure 5.12. Detected frequencies in LFP recording from a non-human primate. The frequencies were detected using the implemented 5-phase module. The peaks at 9.75 Hz and 16.5 Hz are artifacts, whereas the peaks at 6 Hz and around the 3 Hz could reflect neuronal activities.

Spontaneous LFP recordings from PD patients

The implemented module was also tested retrospectively on LFP recordings from a PD patient with bilateral tremor-dominant of both hands. The LFP activity was recorded from the patient over three days using the portable neurostimulator, in an externalized setting, i.e. before leads being connected to the implantable pulse generator (IPG). Similar sets of CR stimulation parameters were used, which differ only in the value of F_R. The latter was chosen to be 16.5 Hz, 20 Hz, and 12 Hz in the three stimulation days. The other CR stimulation parameters had the following values: amplitude (A) was 4 mA, pulse width (PW) 60 µs, balancing pulse width (BPW) 600 µs, number of pulses per burst (N) 6, N_{on} 4, N_{off} 2, and the intra-burst frequency (HF) was 130 Hz. The activation sequence of the stimulation contacts was randomized. LFP activity was recorded bipolarly between three contacts (0, 1 and 2) starting from the tip and uppermost contact (in this experiment, the contact 3 was used as a reference). Therefore, three contact pairs 0-3, 1-3, and 2-3 were used for the LFP recording (for more details on the CR stimulation parameters and patterns see Section 2.2.2).

The implemented module estimated the dominant frequency, the amplitude and the standard deviation of the amplitude over time, as shown in Figure 5.13. This figure displays

the LFP recordings of the contact pairs 0-3 and 1-3 of the left side during the first and the last experimental day. In the first day, data was recorded before first stimulation session and in the last day, after the last stimulation session. The time difference between two stimulation sessions in one day was at least one hour. The change in the synchronicity of the pathological neuronal activity in both channels can be seen between the first and last day. The amplitude of the synchronous activity was remarkably reduced. This could indicate that a fewer number of neurons participated in the synchronized neuronal activity on the last day due to CR stimulation.

Tremor recordings from PD Patients

During and between CR DBS stimulation sessions accelerometers were placed on the limbs of PD patients that manifested resting tremor. Some patients had tremor on both hands such the one whose LFP data was discussed in the previous section. The tremor recordings of both hands of this patient were analyzed using the implemented module and the results are shown in Figure 5.14. In this figure a comparison between the first and last day is displayed. The module has estimated the frequency and amplitude of resting tremor over time around 5 Hz as shown in the middle panel. These results were also corroborated after visualizing the video streams of the patient. Frequency component at 10 Hz might be a harmonic of the detected 5 Hz. The amplitude of tremor was reduced on the last day respect to the first day for both hands. This reduction of amplitude is in accordance with the reduction of activity power measured in the LFP recordings.

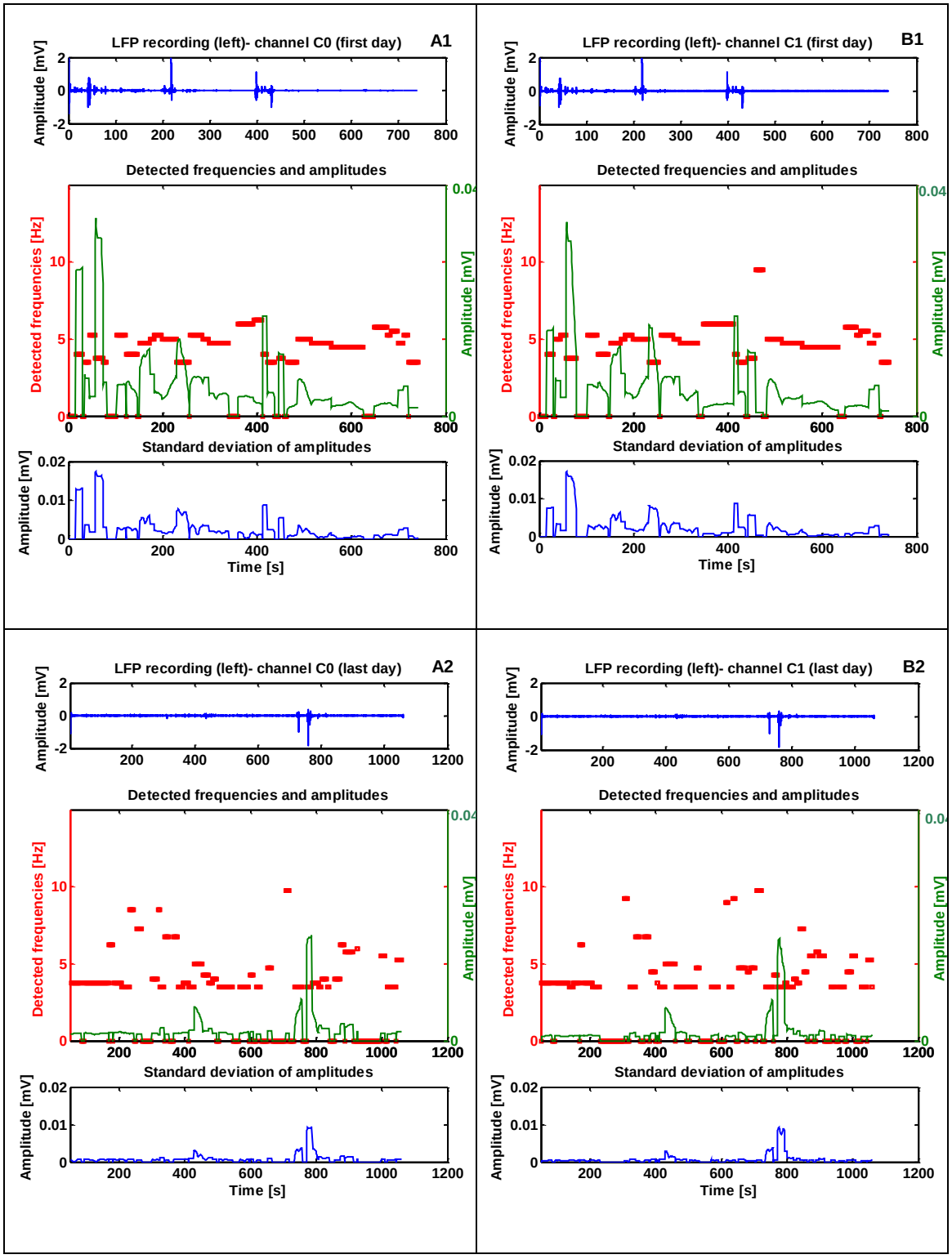

Figure 5.13. Monitoring the dominant activities in the spontaneous LFP recordings. The module estimates the strength (i.e., the amplitude) of dominant frequencies over time in the spontaneous LFP recordings from a PD patient that showed resting tremor. A1 and B1: Raw LFP recordings of two contacts of the implanted electrode on the first day (top panel). A2 and B2: Spontaneous LFP recordings of the same contacts on the last day (i.e., after three days of stimulation). The middle panels show the detected frequencies and the estimated amplitudes over time. One can observe the reduction of amplitude of the detected frequencies on the last day with respect to the first day.

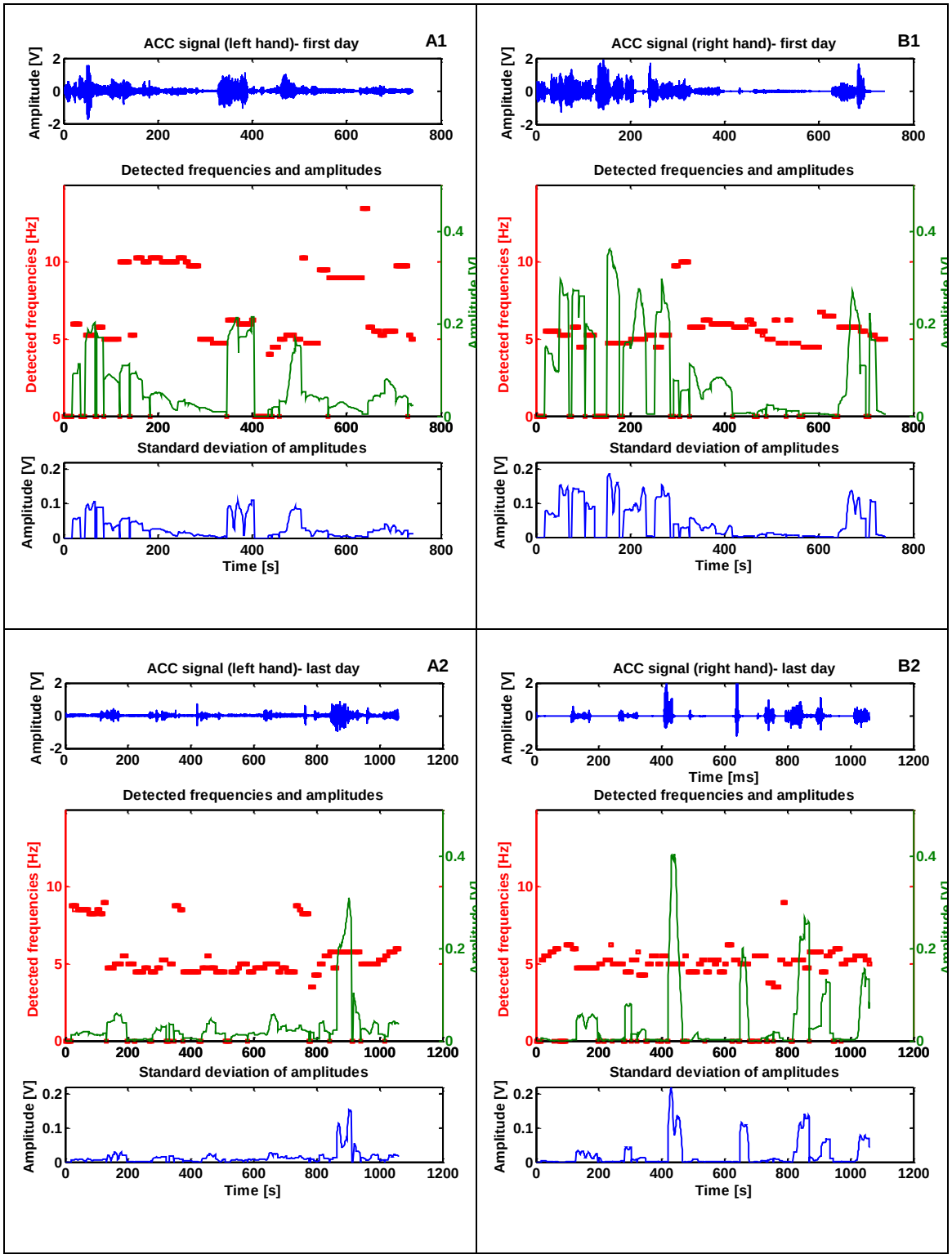

Figure 5.14. Monitoring the strength and frequency of tremor. The module detects the dominant frequencies and estimates their amplitude in the tremor recordings from a PD patient. A1 and B1: Tremor recordings from two accelerometers placed on both hands on the first day (top panel). A2 and B2: Tremor recordings from the same accelerometers on the last day. The middle panels show the detected frequencies and the estimated amplitudes over time. A reduction of tremor amplitude on the last day with respect to the first day can be observed (bottom panels). The reduction in the amplitude is in line with the reduction of LFP activity shown in Figure 5.13.

5.5 Tuning of CR stimulation parameters

The LFP and tremor recordings are analyzed to calculate biomarkers-values that can be used as a criterion to quantify the demand for tuning the stimulation parameters, i.e., for the development of an adaptive DBS system. Such a system aims at continuously adapting the DBS parameters to either the clinical fluctuations typical of advanced PD or to modifications of the physiological activity caused by therapeutic effects. The detected dominant frequencies in thespontaneous LFP and tremor recordings (see Section 5.3 and 5.4) are used to evaluate the strength of the pathological activity. Our proposed concept is to monitor and compare the amplitudes of these frequencies in successive data segments in order to calculate the demand value. If the current amplitude of the pathological activity is higher than the previous one, the value of the stimulation parameter should be increased and vice versa.

Therefore, a module for the adjustment of the CR stimulation parameters is implemented in Simulink. This module uses the tremor recordings as a feedback signal to adjust the CR DBS parameters in real-time. The tremor recordings are first filtered, with Butterworth band-pass filters, in such a way that the magnitude response of the filters includes the pathological activity ±2 Hz. Then, the filtered signal is divided into successive segments of 200 ms. The strength of the pathological activity is estimated in the module by the standard deviation of the signal. The standard deviation value in the first segment is delayed to be compared with the subsequent value. If the current value differs from the previous one, a logical flag (i.e., 1) is raised to indicate the demand for adjusting the stimulation parameter. Otherwise, the stimulation continues with the current value. Both values should be greater than zero. The current value is divided by the delayed one to calculate a scaling factor, which is then multiplied by the selected stimulation parameter. Since the strength of tremor can vary between patients, a calibration is also available in the module to set the maximum values. The initial values of the stimulation parameters can be set by the clinicians, and the maximum and minimum values of the stimulation parameters are restricted.

In order to demonstrate the real-time adjustment of CR DBS parameters, tests were performed with tremor-like signals generated by a healthy subject and recorded by the portable neurostimulator. The signals were analyzed by the above described module. An accelerometer was placed on the right hand of the subject who imitated tremor with different frequencies and amplitudes. Six tests were performed to adjust four CR stimulation parameters during sequential and random CR stimulation, as well as during HF DBS. These parameters are: the amplitude, number of pulses, number of on-cycles, and number of off-cycles. During the tests, the other CR stimulation parameters were set to constant values as follows: F_R 4 Hz, PW 120 µs, BPW 1200 µs, N 10, and HF was 130 Hz.

In each test, which lasts 80 s, only one stimulation parameter was adjusted at a time. The tests include:

(i) Amplitude modulation during standard HF DBS. Figure 5.15 shows a tremor-like recording of a control subject and the corresponding spectrogram. The latter displays the variation in frequency and amplitude of the recording over time. Specifically, the variation in the amplitude is used to modulate the amplitude of the HF stimulation pulses on one contact of the DBS electrode. The amplitude is increased for higher tremor and vice versa. The single charge-balanced stimulation pulses were presented in Figure 2.3. In this test, the maximum amplitude was set to 0.5 mA considering the rebound effect that can cause strong response when stimulation is turned off (Trottenberg et al., 2001, Muta et al., 2001).

(ii) Amplitude modulation during sequential CR DBS. Figure 5.16 shows how the variation in the strength of the imitated tremor is used to tune the amplitude of the CR stimulation pulses. In this case, the amplitude is increased for higher tremor and vice versa. The output signals of the portable neurostimulator shows the amplitude modulation of the sequential bursts of stimulation pulses. These signals were sent to three contacts (C0: blue, C1: red and C2: green) of the DBS electrode, while the fourth contact was used as a reference. The amplitude was restricted to the range 0 – 2 mA during the tests with CR stimulation protocols.

(iii) Amplitude modulation during random CR DBS. Figure 5.17 shows the tuning of the amplitude of the CR stimulation pulses due to the variation in the strength of the imitated tremor. As in (i) and (ii), the amplitude is increased for higher tremor and vice versa. Subplot D shows the sum of the output signals of the portable neurostimulator and the amplitude modulation of the random bursts of stimulation pulses. These signals were sent to the three contacts of the DBS electrode as described previously.

(iv) Adjustment of the number of pulses during random CR DBS. Figure 5.18 shows how the variation in the strength of the imitated tremor is used to adjust the number of pulses in the CR stimulation bursts of the three contacts. Subplot D shows that tremor with higher amplitude results in increased number of stimulation pulses and vice versa. The minimum and maximum number of pulses was set to 1 and 10.

(v) Adjustment of the number of on-cycles during sequential CR DBS. Figure 5.19 shows the adjustment of the number of on-cycles due to the variation in the strength of the imitated tremor. Subplot D shows that high tremor amplitude results in an increased number of on-cycles and vice versa. The minimum and maximum number of on-cycles was set to 1 and 3.

(vi) Adjustment of the number of off-cycles during sequential CR DBS. Figure 5.20 shows how the number of off-cycles is tuned according to the variation in the strength of the imitated tremor. The minimum and maximum number of off-cycles was limited to 0 and 1. In the initial case, the stimulation protocol includes one off-cycle, as can be seen in subplot D, time axis [43 – 47] s. However, the number of off-cycles is reduced to 0 for an increased tremor amplitude as can be seen in time axis [41 – 43] s.

The portable neurostimulator sent the tuned CR stimulation signals to an electrical circuit, where the four contact cables were connected to three resistors, each of 1 kΩ, and a reference. The stimulation signals were then recorded from the electrical circuit by a data acquisition card[13] and monitored using the software LabVIEW SignalExpress[14] on the programing laptop described in Section 3.1. The imitated tremor signals, their spectrograms, and the continuous adjustment of the different CR stimulation parameters (the output signals of the portable neurostimulator) are illustrated from Figure 5.15 to Figure 5.20. All these figures present the real-time adjustment of the stimulation parameters according to the strength of tremor measured by the standard deviation of the amplitude. In order to investigate the changes in amplitude through spectral analysis in real-time, the technical realization requires some hardware modifications and a more powerful processor as it is going to be discussed in the next chapter.

[13] cDAQ-9171 Measuring and Testing Equipment from National instruments, Hungary.
[14] LabVIEW SignalExpress 2012 from National instruments

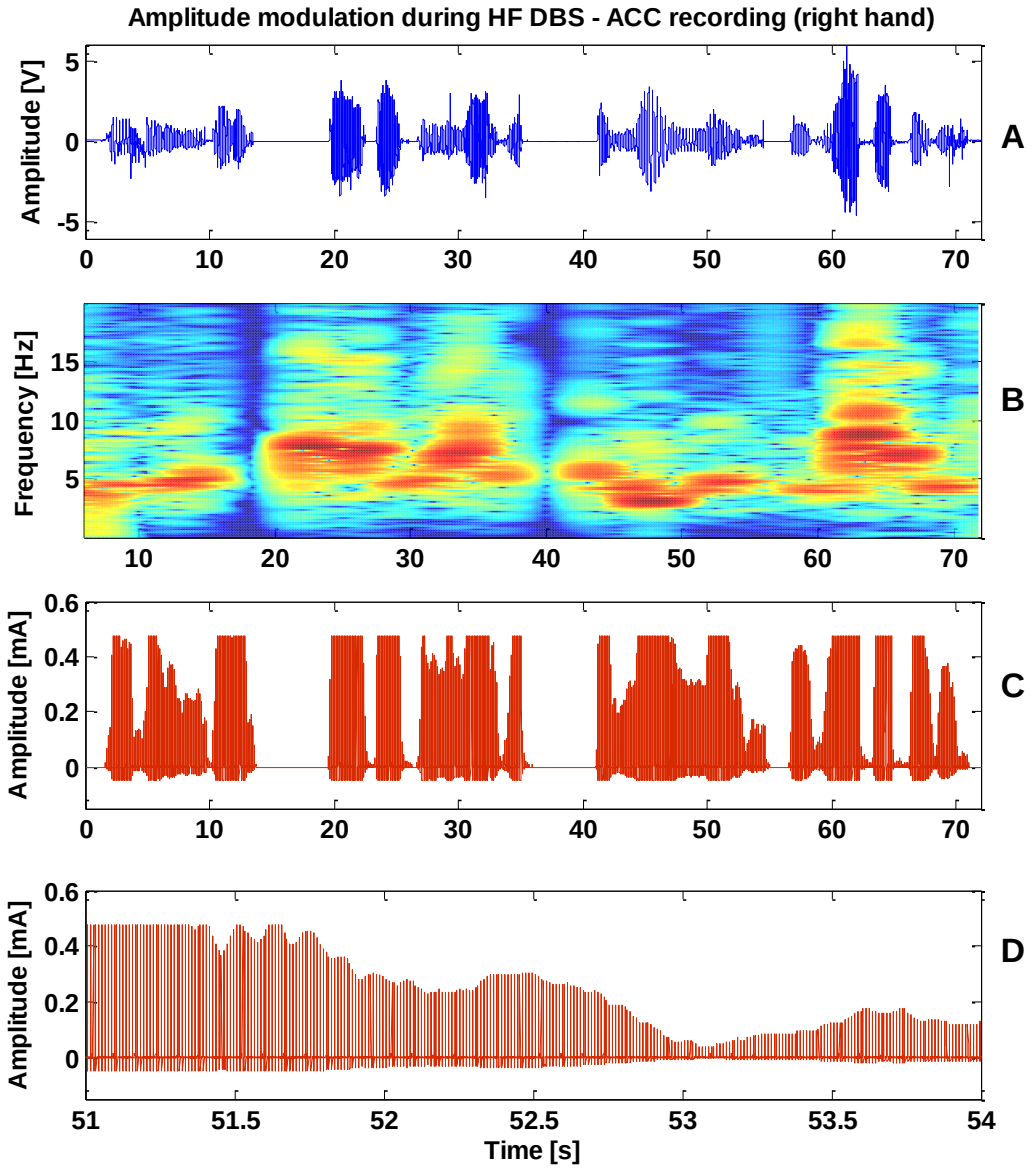

Figure 5.15. Real-time amplitude modulation during HF DBS. A: Tremor-like recording during HF stimulation. B: Spectrogram of the recorded data shows the variation in frequency and amplitude of the tremor-like recording displayed in Subplot A over time. This variation is monitored and used to modulate the amplitude of the HF stimulation pulses. C: Amplitude modulation of the HF stimulation pulses where the maximum amplitude was restricted to 0.5 mA. D: Magnified plot of signal represented in (C) (see time axis). The amplitude of stimulation pulses is increased for higher tremor amplitude and vice versa. The single charge-balanced stimulation pulses were presented in Figure 2.3.

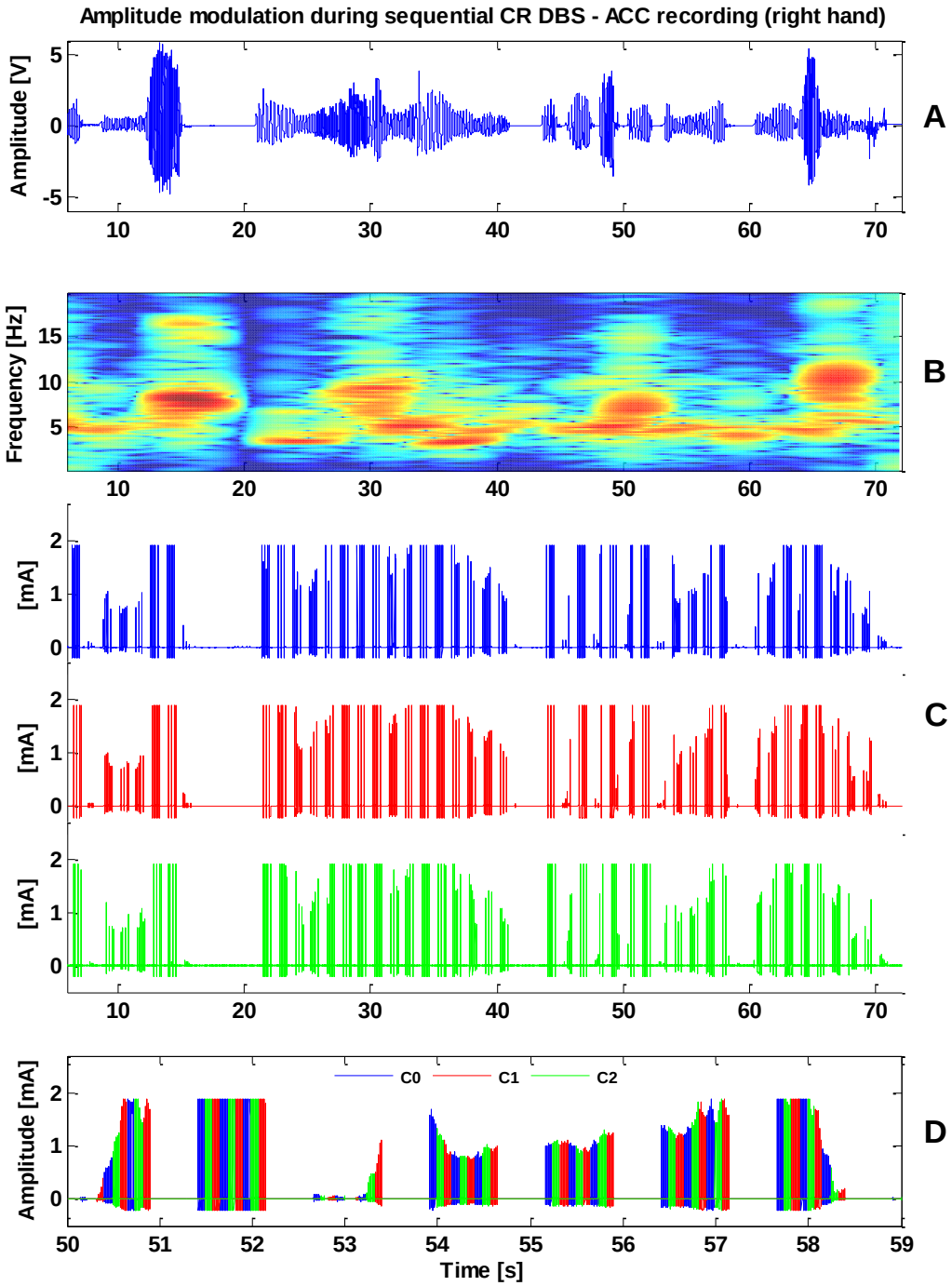

Figure 5.16. Real-time amplitude modulation during sequential CR DBS. A: Tremor-like recording. B: Spectrogram of the recorded data shows the variation in frequency and amplitude of the signal displayed in Subplot A over time. This variation is used to adjust the amplitude of the CR stimulation pulses. C: Output signals (three channels) of the portable neurostimulator show the amplitude modulation of the CR stimulation pulses of the three contacts (C0: blue, C1: red and C2: green). The minimum and maximum amplitude modulation was set to 0 and 2 mA. D: Magnified plot of the sum of the signal presented in (C) (see time axis). The amplitude of stimulation pulses is increased for higher tremor amplitude and vice versa.

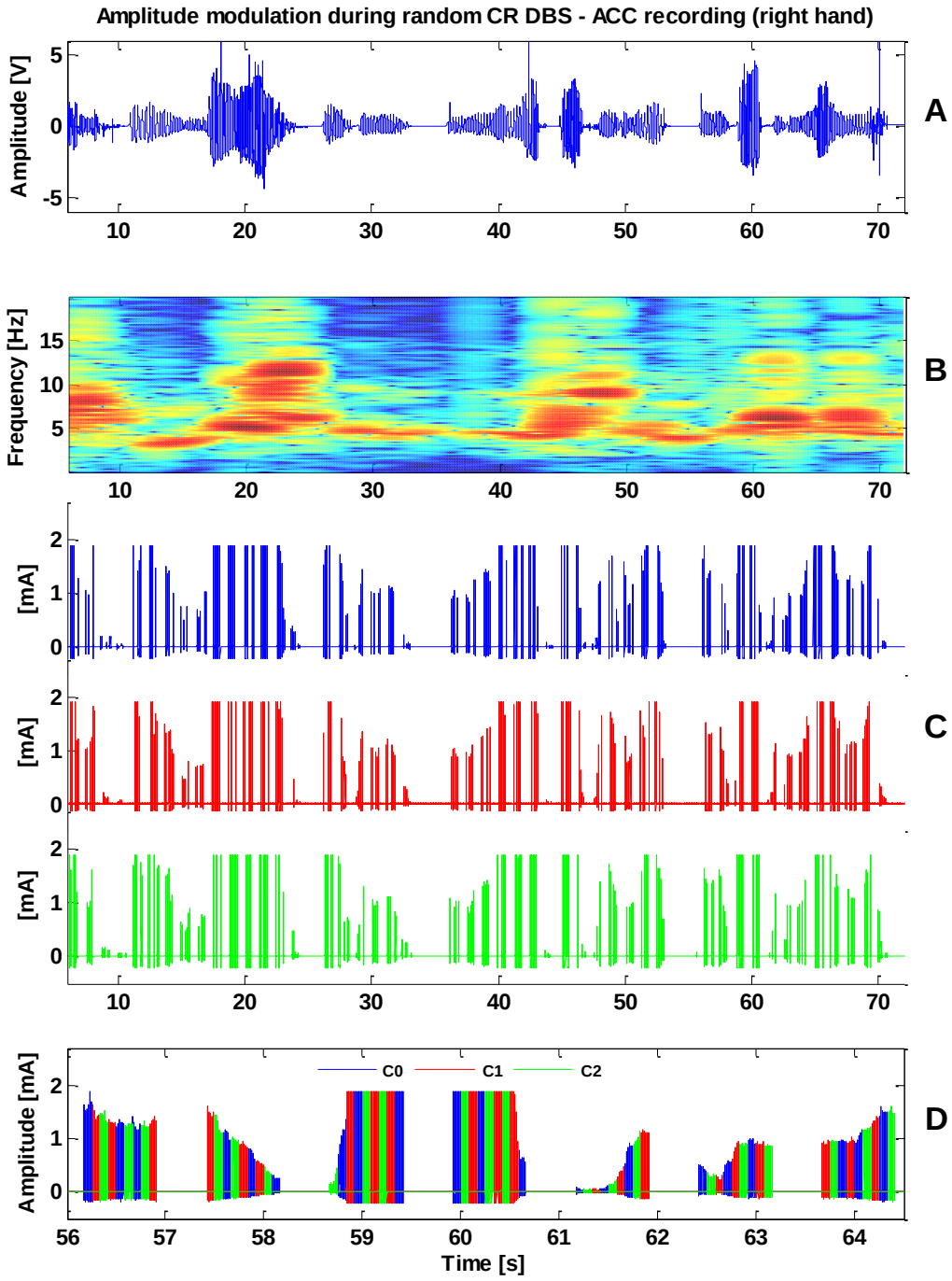

Figure 5.17. Real-time amplitude modulation during random CR DBS. A: Tremor-like recording. B: Spectrogram of the recorded data shows the variation in frequency and amplitude of the tremor-like recording showed in Subplot A over time. This variation is used to adjust the amplitude of the CR stimulation pulses. C: Output signals (three channels) of the portable neurostimulator show the amplitude modulation of the CR stimulation pulses of the three contacts (C0: blue, C1: red and C2: green). The minimum and maximum amplitude modulation was set to 0 and 2 mA. D: Magnified plot of the sum of the signal presented in (C) (see time axis). The amplitude of stimulation pulses is increased for higher tremor amplitude and vice versa.

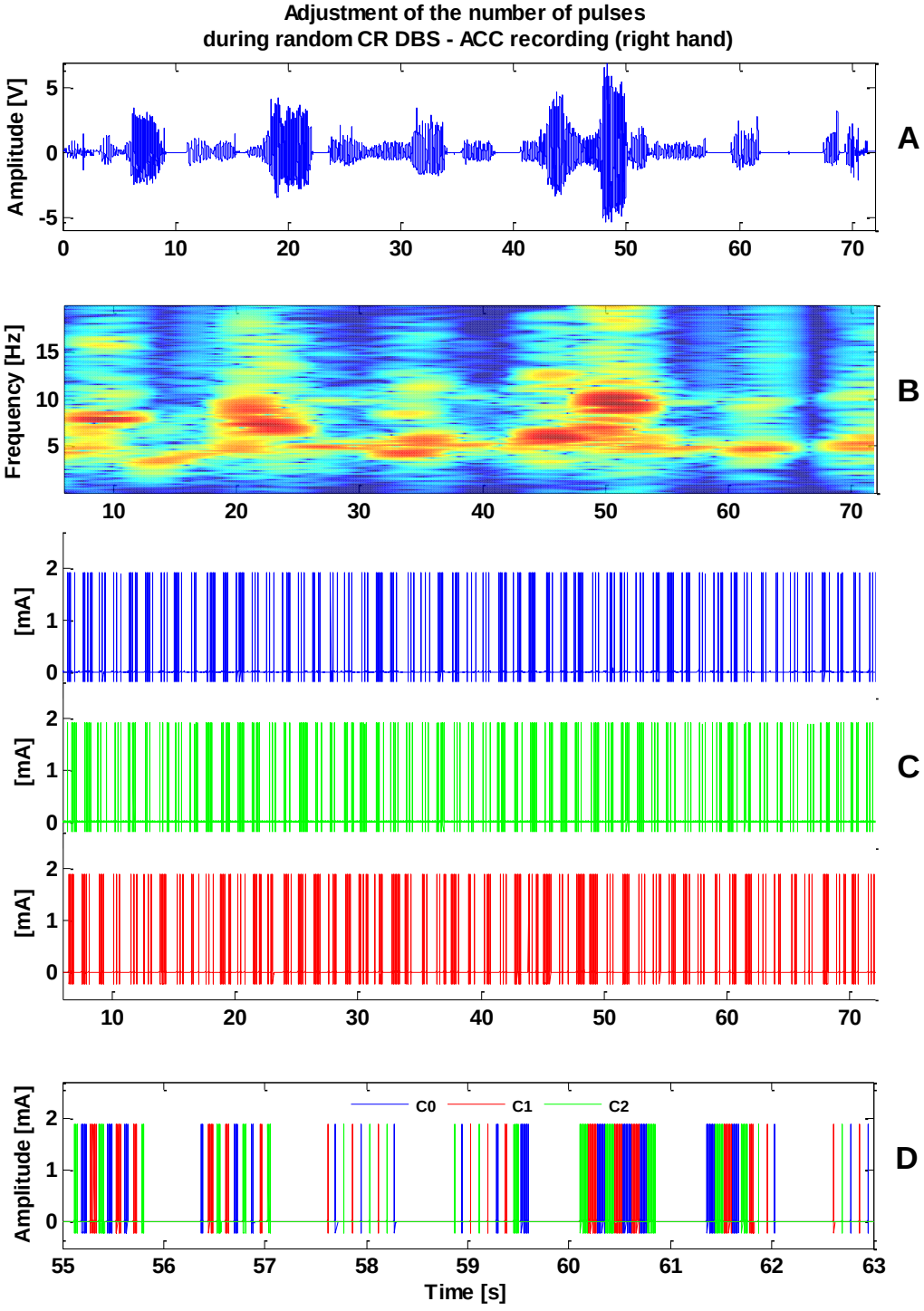

Figure 5.18. Real-time adjustment of the number of pulses during random CR DBS. A: Tremor-like recording. B: Spectrogram of the recorded data displays the variation in frequency and amplitude of the recording shown in Subplot A over time. This variation is used to adjust the number of pulses. C: Output signals (three channels) of the portable neurostimulator show the modification of the number of pulses of the three contacts (C0: blue, C1: red and C2: green). The minimum and maximum number of pulses was set to 1 and 10 pulse(s). D: Magnified plot of the sum of the signals presented in (C) (see time axis). Tremor with higher amplitude results in increased number of stimulation pulses and vice versa.

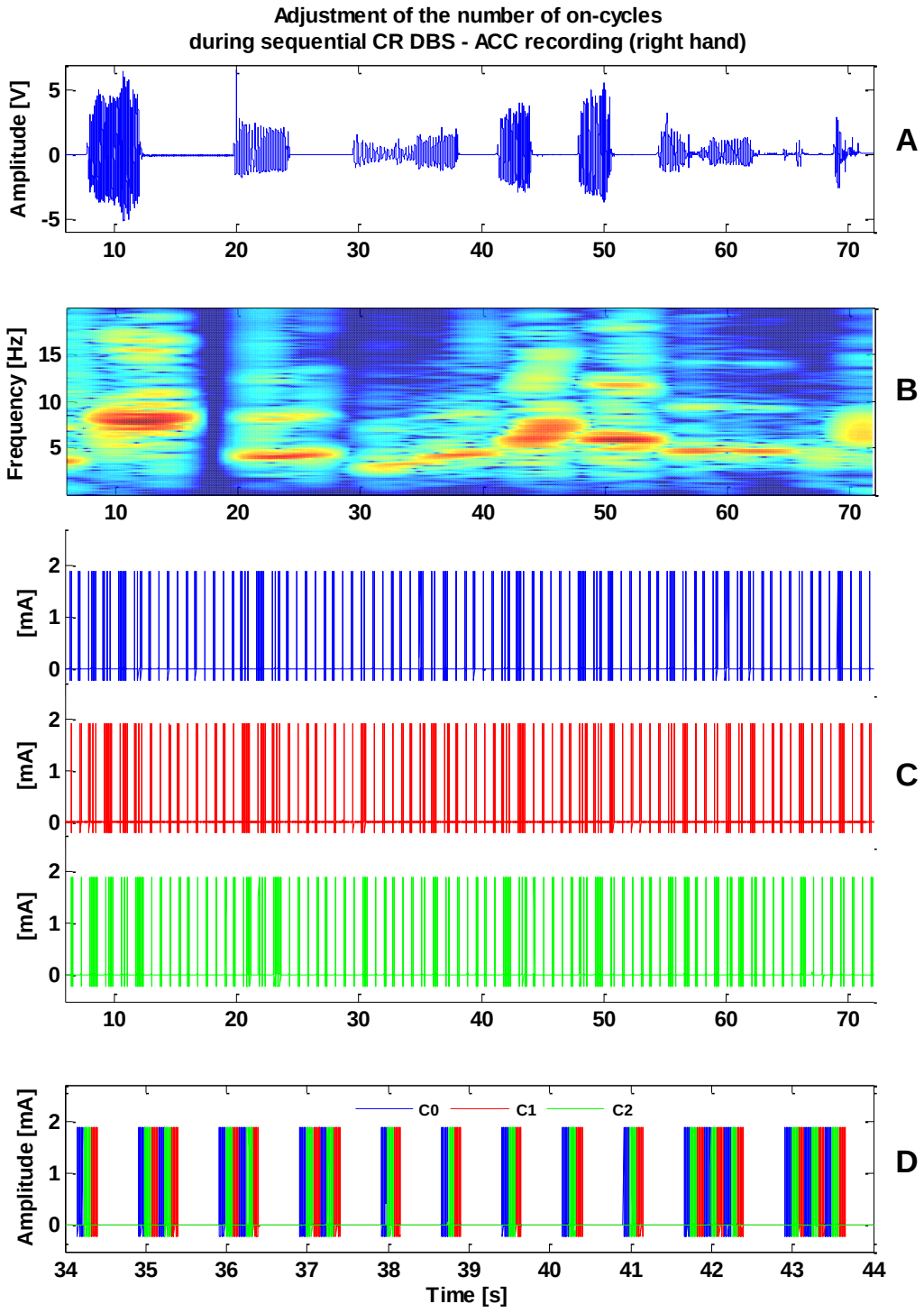

Figure 5.19. Real-time adjustment of the number of on-cycles during sequential CR DBS. A: Tremor-like recording. B: Spectrogram of the recorded data shows the variation in frequency and amplitude of the recorded signal over time. This variation is used to adjust the number of on-cycles. C: Output signals (three channels shown in color C0: blue, C1: red and C2: green) of the portable neurostimulator shows the modification of the number of on-cycles. The minimum and maximum number of on-cycles was set to 1 and 3. D: Magnified plot of sum of signals displayed in (C) shows the variation of the number of on-cycles over time (see time axis). High tremor amplitude results in increased number of on-cycles and vice versa.

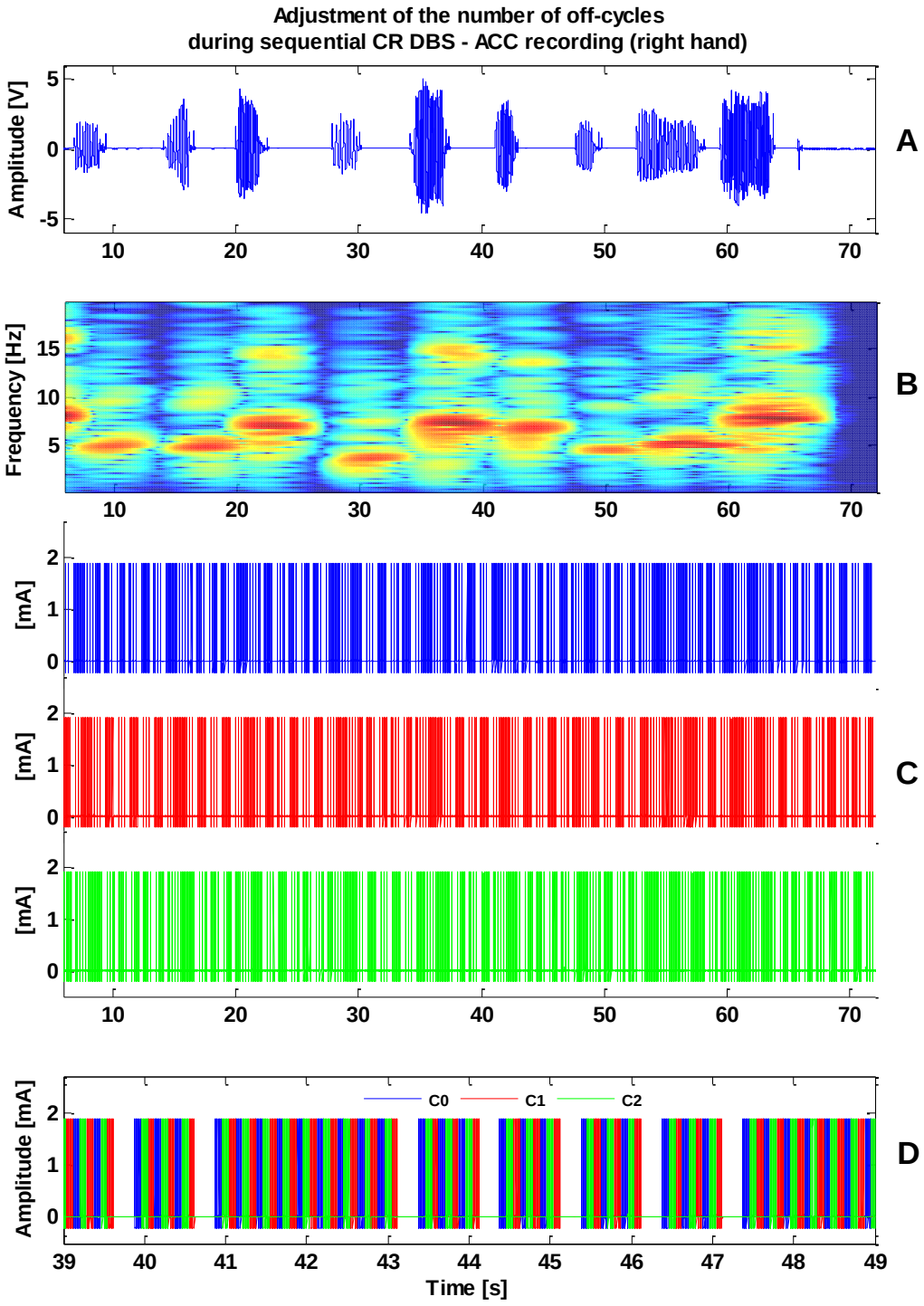

Figure 5.20. Real-time adjustment of the number of off-cycles during sequential CR DBS. A: Tremor recording. B: Spectrogram of the recorded data shows the variation in frequency and amplitude of the recorded signal over time. This variation is used to adjust the number of off-cycles. C: Output signals (three channels shown in color C0: blue, C1: red and C2: green) of the portable neurostimulator shows the modification of the number of off-cycles. The minimum and maximum number of off-cycles was limited to 0 and 1. D: Magnified plot of the sum of the signals displayed in (C) shows the variation of the number of off-cycles over time (see time axis). The number of off-cycles is reduced in the case of large tremor amplitude.

Chapter 6

Summary and Discussion

Feedback control or adaptive techniques for deep brain stimulation (DBS) aim at optimizing the stimulation strategy to further improve the quality of life of the patients, e.g. by minimizing side effects and maximizing the efficiency of therapeutic stimulation. In the last few years, several paradigms have been proposed for delivering adaptive DBS (Santaniello et al., 2011, Rosenblum & Pikovsky, 2004, Popovych et al., 2008, Rosin et al., 2011, Little et al., 2013, Hauptmann et al., 2005, Tass, 2003b, Popovych et al., 2005, Tass, 2003a). Computational and practical adaptive DBS paradigms aim at quantifying the pathological state by analyzing electrophysiological signals in order to vary the stimulation parameters. These electrophysiological signals are either simulated or collected from patients or non-human primates. Some examples of experimental setups of adaptive DBS paradigms are described briefly:

In the experimental setup designed by *Rosin et al.*, two anatomical targets in the brain of non-human primates are selected for the adaptive DBS (Rosin et al., 2011). The first anatomical target is a reference where an electrode detects a trigger signal for stimulation. The trigger is an occurrence of an action potential. The second target is the stimulated structure in the globus pallidus internus (GPi) to which the stimulus at high frequency (HF) is delivered with a predetermined fixed latency of 80 ms to the trigger signal. The stimulus is a single pulse or short train of 7 pulses at 130 Hz. In this setup, a copy of six recorded analog signals is delivered to an external digitial signal processor (DSP) chip which uses one of the signals as a reference for trigger identification (Rosin et al., 2011).

In another experimental setup described by *Little et al.*, local field potentials (LFPs), which are band-pass filtered at beta frequency, are recorded bipolarly directly from the stimulating electrode in the subthalamic nucleus (STN) (Little et al., 2013). Recordings are processed using special external amplification and filtering systems (Eusebio et al., 2011). Filtered recordings are rectified and smoothed to compare the amplitude of the beta activity to a user-defined threshold. The frequency of the beta activity is determined from the power spectrum intra-operatively. The stimulation at HF (i.e., 130 Hz) begins with a latency of 30 – 40 ms after crossing the threshold. The stimulation is delivered starting at 0.5 V and increased by 0.5 V until clinical benefits were seen without side effects. It was demonstrated that an optimization of the stimulation parameters intra-operatively results in

a strong clinical improvement and a reduction of stimulation time and power (Little et al., 2013).

Only few implantable adaptive stimulation hardware have been proposed for clinical use and are dedicated to deliver HF DBS (Jensen et al., 2008). Lately, Medtronic has announced the launch of its first implantable pulse generator (IPG) that enables the sensing and recording of brain activity while simultaneously provide DBS therapy (Medtronic, 2013). Medtronic implantable hardware, which received Conformité Européenne (CE) mark, is dedicated to collect data from patients for research purposes.

In this project, we investigated the realization of a demand-controlled application of desynchronizing coordinated reset (CR) DBS that is adapted according to the variations of the pathological activity of the patients. We studied retrospectively the suitability of two kinds of data for such an application. These include: (i) LFP recordings from Parkinson's disease (PD) patients and parkinsonian non-human primates, and (ii) resting tremor recordings from PD patients. LFP and tremor data was recorded during CR DBS and after the stimulation sessions. The demand-controlled application of desynchronizing CR DBS requires a real-time data processing strategy that incorporates pre-processing and several analysis steps as illustrated in the flow diagram in Figure 6.1.

To this end, we developed, and implemented software-based technical solutions to obtain feedback signals from the recordings and to calculate biomarkers-values of the pathological state. These biomarkers-values are used as a criterion to quantify the demand for tuning the stimulation parameters. The proposed approach aims to monitor, register and analyze the variation in the strength of the recorded activity in order to find reliable and stable pathological oscillations. The implemented technical solutions were tested on the abovementioned recorded data, simulated signals, and measurements in saline solution. Additionally, a demonstration of the tuning of several CR DBS parameters was performed in real-time with a DSP board using tremor-like recordings collected from a healthy subject.

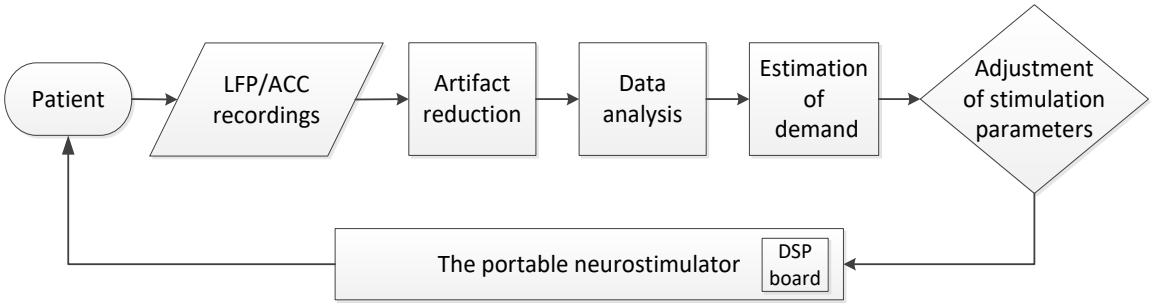

Figure 6.1. Flow diagram of the processing steps used in the demand-controlled application of CR DBS. Technical solutions are developed for each step, tested off-line, implemented for real-time processing, and tested on the DSP board placed in the portable neurostimulator.

The technical solutions were tested on a DSP board within a portable neurostimulator. The latter is an external trial DBS device mainly used for the application of desynchronizing DBS stimulation techniques (Hauptmann et al., 2009). The distinct data processing steps of the implemented module are summarized and discussed in the subsequent sections.

6.1 Artifact reduction

Artifacts are usually found in LFP recordings during DBS. An artifact-reduced signal is important to enable the calculation of the demand value in a continuous way. In order to obtain a feedback signal during CR DBS, we tested several technical solutions for the removal of artifacts. Although many techniques have been introduced in the literature (as described in Section 4.1.1 and Section 4.1.2), our solutions resulted to be more adaptable to deal with considerable signal variability. The latter was noticed in the artifact shapes among electrode channels and even in individual channels among trials of the same type of stimulus. The variability was also found across patients due to, e.g., different stimulation intensities which are set according to the severity of the clinical symptoms, the sensitivity to stimulation and the position of the electrode in the brain. Moreover, the electrical impedance around the contacts of the implanted electrode varies considerably between stimulation sessions (Benabid et al., 1996). Taking into account the abovementioned reasons, it was important to find adaptable and appropriate artifact removal techniques for the LFP recordings collected during CR DBS. The most relevant artifacts are: stimulus artifact, exponential decay/growth after stimulus, power line interference (PLI), and electrical background noise.

LFP activity is recorded during typical CR stimulation patterns, which contain stimulation periods (on-cycles) and large pauses (off-cycles) as can be seen in Figure 6.2. This figure shows LFP recording from a PD patient and illustrates the on- and off-cycles during CR DBS. The technical solutions for artifact reduction during stimulation are developed in such a way that only the signal parts corresponding to the off-cycles are taken into account. This is because the strength and variability of the stimulation artifacts during the on-cycles together with the subsequent exponential artifacts prevented a real-time artifact removal. As a consequence and in order to accurately interpret the neuronal activity, the complete removal of the on-cycles was necessary. Collecting the stimulation artifact-free off-cycles enables the investigation of the recorded neuronal activity on a regular base. To this end, two methods were implemented in order to delimit the off-cycles from the LFP recordings in real-time: *candidate segment of data* and *sawtooth wave* (both methods were introduced in Section 4.1.1).

A key advantage of the *candidate segment of data* method is the ability to automatically detect the onset and end of the stimulation periods (i.e., the on-cycles). One shortcoming of this method is the discarding of some milliseconds after stimulation. This might result in the loss of neuronal activity. The main advantage of the *sawtooth wave* method is that it is based on the selected CR stimulation parameters. One limitation of this method is that the LFP signal has to be synchronized with the *sawtooth wave*. However, this has to be done once at the beginning of the recording process and is performed as long as CR stimulation parameters remain constant. Both methods are implemented in Simulink and presented in Appendix B.

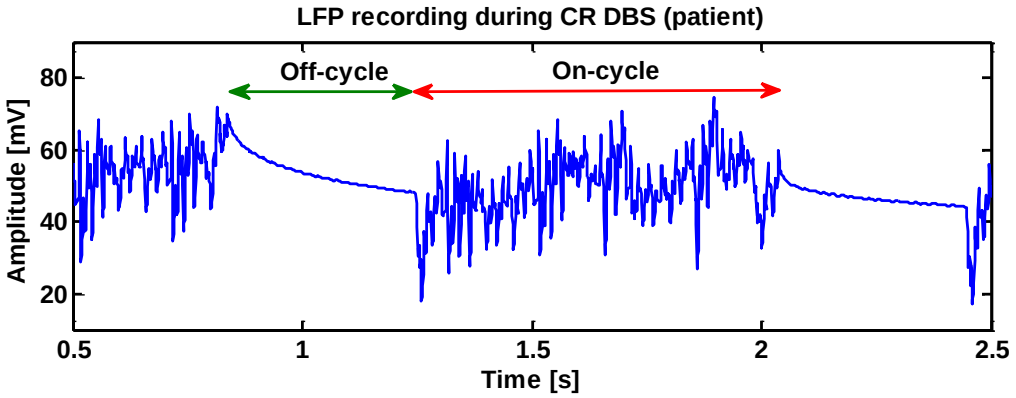

Figure 6.2. LFP recording from a PD patient during CR DBS. The plot illustrates the on-cycles (red double arrow) and off-cycles (green double arrow). The off-cycles are delimited and analyzed for pathological neuronal activity. The CR parameter values used here are: HF 130 Hz, F_R 4 Hz, N_{on} 3, N_{off} 2, N 8, A 2 mA and PW 60 µs.

The exponential artifact, which is caused by the saturation of the amplification system, is the main artifact in the off-cycles as explained in Section 4.1.2. Techniques available for the removal of such artifacts were suboptimal for our application due to the variability of the artifact (Wagenaar & Potter, 2002). The optimal solution was to fit independent functions to each individual artifact. We found that the use of inappropriate fitting techniques generates new artifacts. For instance, we found that polynomial fitting is suboptimal, since the frequency content of the fit residual of the polynomial fitting curve overlaps that of parkinsonian resting tremor, i.e. 3 – 10 Hz. This makes it difficult to classify in the frequency domain whether a peak is caused by the polynomial fitting or by neuronal activity (see Figure 4.7). The use of low polynomial order (e.g., cubic polynomial) has the shortcoming that the curve cannot describe the off-cycle accurately and its residual is not negligible. Hence, other techniques were required to ensure that the frequency response of recorded neuronal activity is not affected.

An efficient solution for the exponential artifact removal is the Nelder-Mead algorithm (Nelder & Mead, 1965). This algorithm is a non-linear and iterative optimization technique based on the least squares method. We implemented the algorithm in Simulink and used it

to fit 2nd (double) and 5th order exponential curves to the off-cycles. Our findings showed that double exponential curves could not fit some of the off-cycles accurately due to, e.g., large PLI amplitude or a high CR frequency of the CR DBS pattern. The 5th order exponential curve was effective in removing the exponential artifact. Since this method is computationally demanding, it will be used as an off-line approach for artifact removal.

In order to overcome the hardware limitations and to calculate more accurate fitting curves, the off-cycles were divided into smaller segments, where each segment was fitted separately with a double exponential curve. The off-cycles are divided into a maximum of three segments and are concatenated again at the end of the artifact removal process. This approach is less expensive from computational perspective and produced more accurate fitting curves. Figure 6.3 shows the result of 10 off-cycles of LFP recording from a PD patient individually fitted. The off-cycles are triggered on the end of the on-cycles, divided into three segments and fitted by double exponential fitting curves after the removal of PLI.

Furthermore, the off-cycles in the LFP recordings during CR DBS include both exponential decays and growths. The use of an exponential fitting curve with adequate exponents (positive or negative) increases the probability of reaching the best fit within a small number of iterations. Thus, both exponential fitting functions were implemented in the Simulink module. The latter can automatically select the fitting curve that describes the exponential artifact the best.

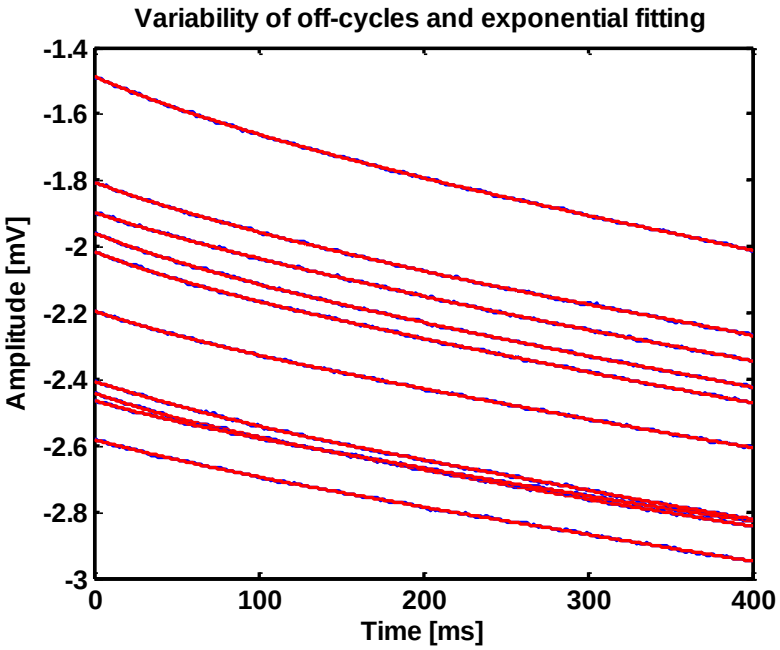

Figure 6.3. Variability of the saturation (exponential) artifact in the off-cycles. Shown are 10 aligned off-cycles (blue lines), of LFP recording from a PD patient during CR DBS, triggered on the end of the on-cycles. The off-cycles are fitted individually by double exponential fitting curves (red lines) after the removal of PLI.

The challenge of removing PLI from the LFP recordings during CR DBS is the short duration of the off-cycles (see Section 4.1.3). Standard filtering approaches are suboptimal here since there is a phase distortion of PLI caused by delimiting the off-cycles. Our tests of some removal techniques of PLI (e.g., subtracting two LFP channels from each other or averaging of off-cycles) showed that the effect of PLI was reduced but not completely eliminated as shown in Section 4.1.3. We found that subtracting an independent reference signal of PLI from the off-cycles is the most effective solution due to the variability of the PLI amplitude and the shortness of the off-cycles. Fortunately, our implemented Nelder-Mead module provided again the solution to remove this artifact and enabled the generation of the reference signals. The module estimates the amplitude and phase of the PLI reference signals within a few number of iterations (<50) (as presented later in Appendix A). The main advantage of this approach is that it copes successfully with changes in amplitude and phase of the PLI and its harmonics. By implementing the Nelder-Mead algorithm in Simulink, we provide a subtraction approach that can dynamically adapt to the variability of the artifacts. The module is used to remove the PLI and the exponential artifacts and provides a practical solution to the complex problem of artifact removal from the short data segments.

For the removal of electrical background noise during CR DBS, real-time averaging of off-cycles was the most effective de-noising technique since the noise was strongly reduced during averaging. Furthermore, other artifacts were found in the LFP recordings, e.g., caused by a movement of the patients during the recording sessions. These artifacts are irregular in terms of form and duration. In case of averaging a large number of off-cycles, the effect of these artifacts was strongly reduced. However, if these artifacts appear frequently, then the averaging method would be not suitable. Such artifacts cause low frequency components in the LFP recordings and one cannot determine in real-time whether they reflect neuronal activity or not.

The tests of our implemented technical solutions for artifact reduction on data recorded in saline solution and from PD patients during CR DBS showed that the abovementioned artifacts were strongly reduced. The objectives of these tests were to give a proof-of-principle and to evaluate the efficiency of the implemented techniques. LFP recordings in saline solution contain no neuronal activity; thus, the artifact-reduced off-cycles of these recordings display no clear peaks or low frequencies, as shown in Figure 6.4.A. In contrary, some peaks, which may represent pathological neuronal activity, were revealed in the LFP recordings collected from a PD patient as shown in Figure 6.4.B.

An additional Simulink module is implemented for the real-time artifact reduction of spontaneous LFP and tremor recordings. Artifact reduction of these recordings is computationally less expensive than the one during CR DBS. This is due to (i) continuity of input signal and (ii) absence of stimulus and exponential artifacts. The artifact reduction solutions are mainly based on digital filters and wavelet de-noising approaches as described

in Section 4.2. The recordings pass through a set of successive digital filters for suppression of PLI and its harmonics as well as the DC and low frequency components. In this thesis, it was shown that our filters are optimal for data sampled at 1 kHz and the wavelet de-noising approach has strongly reduced the electrical background noise without signal distortion (see Section 4.2.1 and 4.2.2).

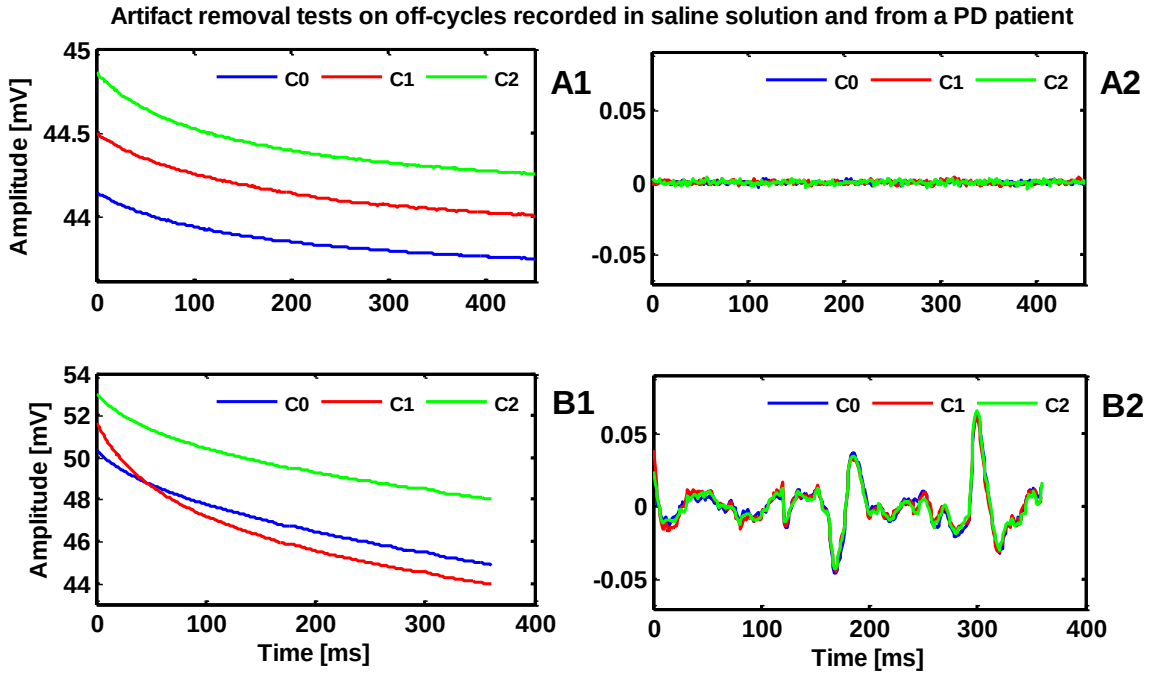

Figure 6.4. Tests of the implemented module using LFP recordings in saline solution and from PD patient. A1: Off-cycles recorded in saline solution through three contacts C0, C1, and C2 (shown in color) of the implanted DBS electrode, where the fourth contact was used as a reference. A2: The same off-cycles shown in A1, after the removal of artifacts, include no peaks or low frequencies. B1: Off-cycles recorded from PD patient through three contacts. B2: The off-cycles displayed in B1 after the removal of artifacts show some clear peaks which might reflect pathological neuronal activity.

Generally, simultaneous DBS and LFP recording through the same electrode make the recording of pathological neuronal activity more difficult due to large stimulation artifacts. One suggested approach to reduce artifacts it to use separate electrodes for stimulation and data acquisition (Al-ani et al., 2011, Hashimoto et al., 2002, Rosin et al., 2011). If the recording site is far away from the stimulation site, the artifacts and the evoked physiological response will not overlap and this approach is even more effective (Harding, 1991). Furthermore, finding a relationship between two anatomical regions in the brain allows the stimulation of one region and data acquisition form another (Rosin et al., 2011). However, the use of separate electrodes may be accompanied with an increase in the technical and surgical complexity, as more electrodes should be chronically implanted for the demand-controlled application of DBS. Nevertheless, using the DBS electrode for the demand-controlled application still has the advantage that it requires no additional electrode

or hardware (Little & Brown, 2012). The accuracy of LFP recordings can also be improved by using more contacts on the implanted electrode for DBS (Buhlmann et al., 2011).

6.2 Data analysis

The technical solutions for data analysis aimed at the calculation of biomarkers-values of the pathological activity in the LFP and tremor recordings. The shortness of the off-cycles is a challenge for the analysis process during CR DBS. In order to find biomarkers of the pathological neuronal activity, we used two analysis methods presented in Section 5.1: (i) off-cycles averaging, and (ii) spectral analysis. A large number of off-cycles are averaged in order to reveal peaks that describe neuronal response with fixed latency to stimulation. We tested this method on LFP recordings from a PD patient by adding a simulated peak to the off-cycles with fixed latency of 200 ms prior to the following on-cycles. The off-cycles last 400 ms. Once the artifacts are removed, a large number of off-cycles were averaged in real-time and the peak was observed to be well-defined. We found that averaging 100 off-cycles might be sufficient to detect neuronal activity, time-locked to the stimulation.

Spectral analysis of individual off-cycles in the LFP recordings is impractical due to the short duration of off-cycles (i.e., 120 ms – 500 ms). Additionally, the concatenation of a large number of off-cycles causes discontinuities which produce a ringing artifact (leakage effect) in the power spectrum. Smoothing these discontinuities by weighting the data, e.g. with a Hamming window, causes the presence of low frequencies close to those of resting tremor, i.e. 3 – 10 Hz. The main problem by the concatenation approach is the partial loss of phase information. In order to solve this problem and estimate the demand value during CR DBS, the spectral analysis was applied to the un-concatenated off-cycles as discussed in the next section.

For the spontaneous LFP and tremor recordings, spectral analysis was the main analysis tool (see Section 5.3). We used DFT, periodogram, and spectrogram functions for the off-line analysis. Spectrograms were used at first to locate the epochs of the dominant frequencies in the recorded data. The results show synchronized activity of the spontaneous LFP recordings from PD patients and from non-human primates (Macaque monkeys) in the range from 3 – 15 Hz. An additional module is implemented in Simulink for real-time analysis based on the periodogram function. We analyzed the LFP recordings of the three contacts in order to estimate the strength of the pathological activity in the brain layers where the different contacts are placed. We found different characteristics of the pathological activity in terms of frequency and amplitude. This variation in the pathological activity on the different contacts indicates the need for estimating different demand values for the different stimulated brain layers.

6.3 Proposed approach for tuning the DBS parameters

The method used for averaging the off-cycles during CR DBS intends to find successive peaks that correspond to neuronal activity. The time difference between, at least, two successive peaks can be used to determine their frequency. The strength of the pathological activity, measured by averaging the amplitudes of these peaks, can be used to adjust the stimulation parameters. We applied this approach to the LFP recordings from different PD patients and found some well-defined successive peaks of neuronal activity with fixed latency to stimulation as shown in Figure 6.5.

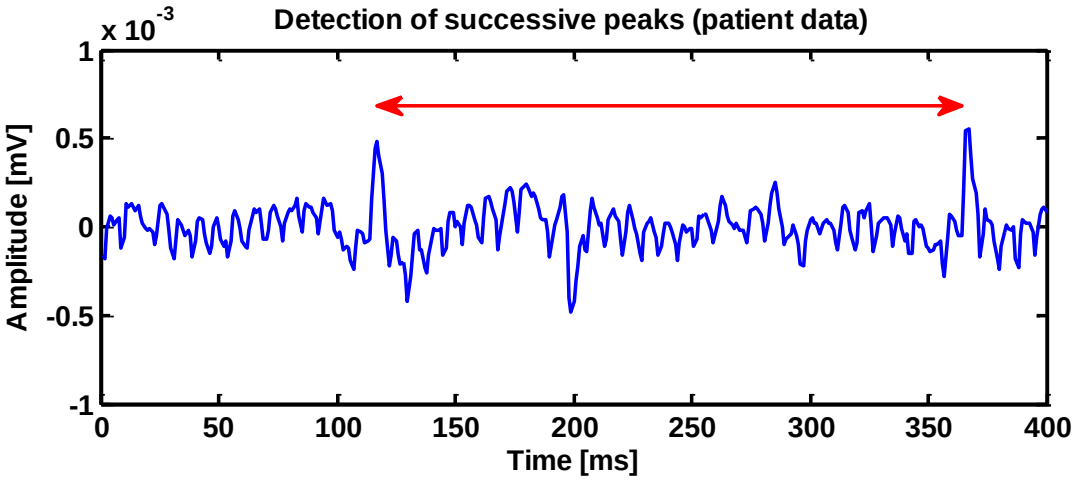

Figure 6.5. Detection of successive peaks in the averaged off-cycles of a PD patient. The time difference between such peaks and their amplitudes can be useful to determine the frequency and the strength of the pathological activity, respectively.

Another approach to estimate the demand value during CR DBS was to rescale the amplitude of dominant frequencies in the power spectrum of the un-concatenated off-cycles. Our tests with simulated sinusoids and different sets of CR stimulation parameters showed that a frequency can be estimated even with half of its period in the un-concatenated off-cycles. However, the amplitude was reduced due to the blanking of the on-cycles. We found that the reduction in the amplitude is proportional to the shortness of the off-cycles. In order to recover the amplitude, we modified the spectral power by a scaling factor k calculated from the CR DBS parameters (as shown in Section 2.2.2 and Equation 5.1). The tests with sinusoids showed that the actual amplitude was recovered by the scaling factor (Section 5.2). Applications of this method to LFP recordings collected from PD patients for different CR stimulation parameters showed no dominant frequencies. The reason behind this is either, that the pathological synchronized neuronal activity was reduced due to stimulation or simply that such a synchronized activity was not present.

In order to calculate the demand value from the spontaneous LFP and tremor recordings, we focused on the variation of dominant frequencies in the power spectra of these recordings (see Section 5.4). The signals are divided into successive segments, where

a periodogram function analyzes the frequency content of each segment. The dominant frequencies in 20 successive segments, together with their amplitudes, are buffered. Subsequently, a histogram function evaluates the distribution of the 20 buffered frequencies in the range from 3 – 43 Hz. Then, a threshold is set which implies that each frequency should appear at least 12 times in the 20 buffered values. The goal of the threshold and the 20 buffered values is to find reliable and stable pathological oscillations in the LFP or tremor recordings. When a dominant frequency exceeds the threshold in the histogram, all corresponding amplitudes are extracted and averaged (divided by the distribution value). This is done in order to get the instantaneous amplitude of the current pathological activity. This approach results in an amplitude value every 4 s which can be used to adjust the stimulation parameters. We found that increasing the frequency resolution of the periodogram enables the detection of frequency variations, but it reduces the probability of detecting the main frequency. In case of using a high-frequency resolution, the threshold can be reduced.

The tests on different data showed the efficiency of our implemented module for the detection of dominant frequencies and the estimation of their amplitudes. The tests were performed on tremor and spontaneous LFP recordings from PD patients and LFP recordings from non-human primates. We also tested the module with simulated sinusoids and stimulation signals generated by the portable neurostimulator and acquired from a simple electrical circuit. An example of monitoring the variation in the amplitude of the dominant frequencies is shown in Figure 6.6. This figure shows the time-evolving power spectrum of LFP recording from a PD patient, with an activity around the 5 Hz.

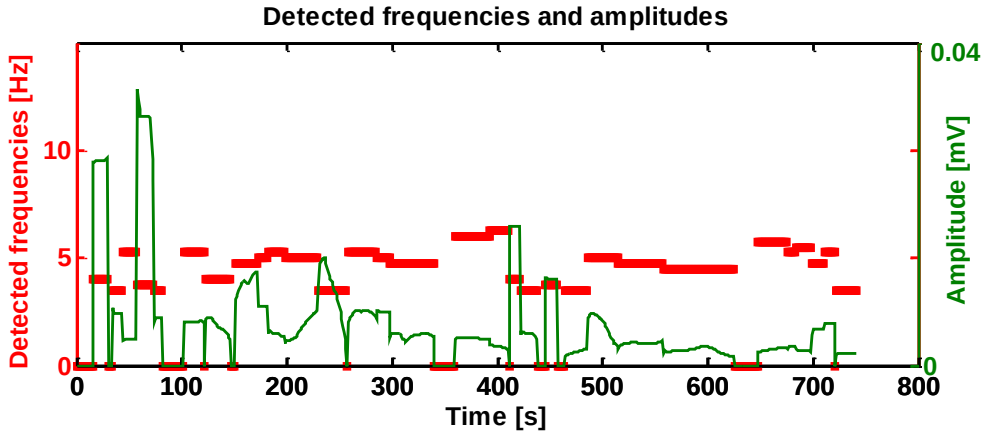

Figure 6.6. Monitoring the variation of the dominant frequency in an LFP recording from a PD patient. This variation is analyzed to quantify the demand for adjusting the stimulation parameters.

The portable neurostimulator system allows the adjustment of five CR DBS parameters: the amplitude (A), number of off-cycles (N_{off}), number of on-cycles (N_{on}), the number of pulses (N), and the pulse width (PW) (Section 2.2.2 and Section 5.5). Each parameter can be adjusted independently by an algorithm based on the estimated demand

value in real-time. The concept is to monitor and compare the strength of the pathological activity in successive data segments. If the amplitude of the pathological activity in the current data segment differs from the previous one, a flag is raised to indicate the demand for updating the stimulation parameter. The current value is divided by the stored value to define a scaling factor that is then multiplied by the value of current stimulation parameter. Otherwise, the stimulation proceeds with the current value. The initial values of the stimulation parameters can be set by the clinicians, and the maximum and minimum values of the stimulation parameters are restricted.

A module is implemented in Simulink, which currently uses the tremor recordings as a feedback signal, to adjust the CR DBS parameters in real-time. The module can also be calibrated to the individual clinical state as the strength of tremor varies between patients. Demonstrations of the simulated adjustment process of four CR stimulation parameters through tremor-like recordings from a healthy subject were performed with the module. The strength of tremor was measured by the standard deviation of the amplitude in the successive data segments. This demand-controlled approach is tested successfully in real-time on the DSP board and the results are presented from the Figure 5.15 to Figure 5.20 in Section 5.5.

6.4 Limitations and future directions

Deploying real-time applications with limited resources in terms of processing speed and memory is challenging. In this case, feedback signals for the demand-controlled applications of DBS are managed with the lowest computational requirements to reduce the processing time and the battery consumption. In this thesis, the implementation of complex algorithms for artifact reduction and data analysis, particularly during CR DBS, results in a complex source code. Hence, the implemented algorithms were improved iteratively to meet the hardware requirements imposed by the DSP board (Section 3.1.1 and Appendix B). The complexity of the source code can be reduced by discarding some processing steps which will yield in less accurate results, e.g., artifacts might not be eliminated. Considering this and for implantable pulse generators (IPGs), a compromise between the size of algorithms and accuracy of results versus processing time and battery consumption must be taken into consideration and proposed as a future work. Besides the software solutions, hardware modifications can improve the artifact reduction process, e.g., the integration of a dedicated amplification system may reduce the artifacts in the early recording stage and increase the data quality (Little et al., 2013, Rossi et al., 2007).

Biomarkers of the pathological activity should be specific, sensitive, and should provide an instantaneous measure of the clinical state (Little & Brown, 2012). LFP recordings are still the most suitable biomarkers for the pathological neuronal activity than other signals like electroencephalogram (EEG) or single-unit recordings. This is the reason

why they result to be the most attractive option for the design and development of demand-controlled DBS systems (Priori et al., 2013). Clinical tests, e.g. using the external stimulator can answer the question if the dynamic of LFP recordings can be used to characterize the different clinical conditions of the disease and whether there is a need to establish multiple biomarkers for each different symptoms (Little & Brown, 2012). Furthermore, during these first retrospective clinical tests the analysis algorithms must still be optimized in order to enable the calculation of reliable neurophysiological biomarkers-values that provide information regarding to the current patients' clinical state. Recent results, where a simple spectral analysis and the division of the pathological activity into different frequency bands were used, support the assumption of a linear relationship between the recorded data and the clinical feature. Nevertheless, more complex algorithms might be required to uncover other complex relationships among brain areas and disease symptoms (Little & Brown, 2012). These critical issues were not addressed in this work since the main focus was the development of technical solutions for the individual processing of the recorded data.

The work presented in this thesis has set the necessary conditions for the implementation of a demand-controlled application of DBS as well as shown that the adaptation of the stimulation parameters using LFP data is possible. In this work, the demand for DBS is adaptable to the clinical characteristics of each patient through the adjustment of the stimulation parameters according to the strength of the on-going pathological activity. The results presented here can be used in future studies and experiments as groundwork for the development of an autonomic DBS system implanted in PD patients. Such a system is expected to open new doors for the deeper understanding of the disease causes and providing new insights about the mechanism of the electrical DBS.

Appendix A

Implementation of the Nelder-Mead Algorithm in Simulink

The Nelder-Mead algorithm or simply the simplex-algorithm is a commonly used non-linear optimization technique proposed by John Nelder and Roger Mead (Nelder & Mead, 1965). This algorithm is one of the direct, iterative and unconstrained search methods that are easy to program and do not require derivatives (Mckinnon, 1998). Based on the least squares problem, the algorithm is used to solve parameter estimation, e.g. data fitting. In this appendix we introduce the Nelder-Mead algorithm briefly and present the results of its implementation in Simulink.

A.1 Algorithm

The Nelder-Mead algorithm uses the concept of a simplex, which is a polytope of $n + 1$ vertices v_i in n dimensions (Nelder & Mead, 1965). The vertices are associated with function values $f_i = f(v_i)$ which are sorted in such a way that the functions with minimal (i.e., best vertex) and maximal (i.e., worst vertex) values have index 1 and $n + 1$, respectively (Baudin, 2010). A function with n parameters requires a simplex with $n + 1$ vertices. In this section, we use the same definitions of the equations as in the algorithmic implementation of the *fminsearch*[15] function in MATLAB. The method approximates a local optimum of a problem with n variables where the objective function f is described as

$$\min f(x), \text{ for } x \in \mathbb{R}^n.$$

Through iterative comparisons of function values in the parameter space, the method controls the tendency towards the minimum value.

The algorithm, as explained by *Lagarias et al.*, makes use of four scalar parameters: coefficients of reflection ρ, expansion χ, contraction ψ, and shrinkage σ (Lagarias et al., 1998). According to the original Nelder-Mead method, these parameters should satisfy:

[15] MathWorks, Inc., USA, version 2007a

$$\rho > 0, \qquad \chi > 1, \qquad 0 < \psi < 1, \qquad \text{and} \quad 0 < \sigma < 1$$

The almost standard choices used in the Nelder-Mead algorithm are $\rho = 1$, $\chi = 2$, ψ = 0.5, and σ = 0.5.

The algorithm replaces the worst vertex v_{n+1} at each step in the iteration by a new one. In order to do this, the centroid $\bar{x}$ of the *n* best vertices should be computed as follows:

$$\bar{x} = \frac{1}{n}\sum_{i=1}^{n} v_i.$$

The centroid is used for the reflection step, which is performed with respect to the worst vertex v_{n+1} to generate the reflected point x_r as follows:

$$x_r = (1 + \rho) \cdot \bar{x}(n + 1) - \rho \cdot v_{n+1}.$$

Then, the reflection point x_r (i.e., a new vertex) is used to evaluate the function:

$$f_r = f(x_r).$$

This function is compared with the function values of the other vertices to find the worst vertex and to replace it, i.e., if $f_1 \leq f_r < f_n$, replace x_{n+1} with x_r.

If $f_r < f_1$, i.e., the new reflected point x_r is better than the best point x_1, then calculate the expansion point x_e

$$x_e = (1 + \rho \cdot \chi) \cdot \bar{x}(n + 1) - \rho \cdot \chi \cdot v_{n+1},$$

and evaluate the function:

$$f_e = f(x_e).$$

This function is further compared with the function values of the other vertices to replace again the worst vertex.

If $f_e < f_r$, the worst vertex $v_{n+1}$is replaced by x_e, otherwise it is replaced by x_r.

If $f_r < f_n$, the worst vertex $v_{n+1}$is replaced by x_r, otherwise a contraction between $\bar{x}$ and the better of v_{n+1} and x_r is required. The contraction step considers two cases: outside contraction and inside contraction.

If $f_r < f_{n+1}$, i.e., x_r is strictly better than v_{n+1}, then an outside contraction is computed as follows:

$$x_{oc} = (1 + \psi \cdot \rho) \cdot \bar{x}(n+1) - \psi \cdot \rho \cdot v_{n+1}.$$

The outside construction point x_{oc} is then used to evaluate the function:

$$f_{oc} = f(x_{oc}) .$$

If $f_{oc} \leq f_r$, the worst vertex $v_{n+1}$is replaced by x_{oc}, otherwise a shrink step is required.

If $f_{oc} > f_r$, compute the inside contraction point x_{ic} from

$$x_{ic} = (1 - \psi) \cdot \bar{x}(n+1) + \psi \cdot v_{n+1},$$

and evaluate the function:

$$f_{ic} = f(x_{ic}) .$$

If $f_{ic} < f_{n+1}$, the worst vertex $v_{n+1}$is replaced by x_{ic}, otherwise a shrink step is required.

The shrink step is used to form a new simplex and is defined for all vertices as

$$v_i = v_1 + \sigma \cdot v_i - v_1,$$

where the function values $f_i = f(v_i)$ should be computed again and the steps described above should be repeated until the minimum is found. The minimization process of a simplex with 11 vertices by our Simulink module is shown in Figure A.1.

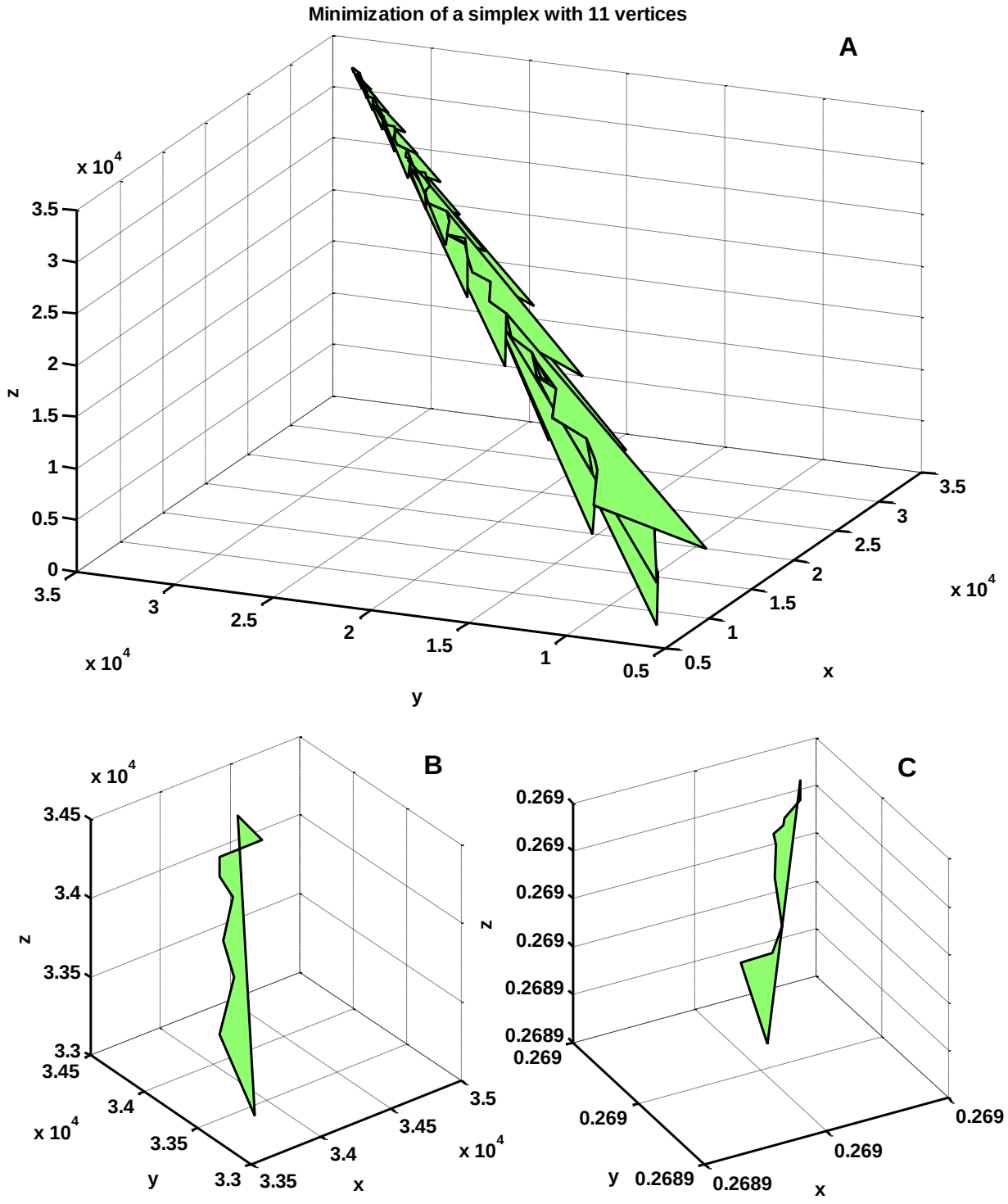

Figure A.1. Iterative minimization of a simplex with 11 vertices in Simulink. A: First 50 iterations show the convergence process of the simplex towards the minimum. The simplex varies in shape from iteration to iteration. The axes x, y, and z show the function *f(x)* of the vertices. B: Initial simplex with large function values (scale 10^4). C: the minimized simplex with a very small function value (scale 0.27) in comparison with the one shown in (B).

A.2 Applications

In this thesis, the Nelder-Mead module is used to fit a double- or 5th order exponential function to the input data in order to remove the exponential artifact from the off-cycles of the LFP recordings. Another application of the algorithm is to remove PLI and its harmonics from very short signals. For the reference signal of PLI, which is a sinusoid with two parameters, amplitude and phase (n=2), a simplex with three vertices (i.e., n+1=3) is formed. Double exponential fitting has four parameters and thus a simplex with 5 vertices is required and for the 5th order exponential fitting a simplex with 11 vertices is used. An example of the applications of the module is shown in Figure A.2.

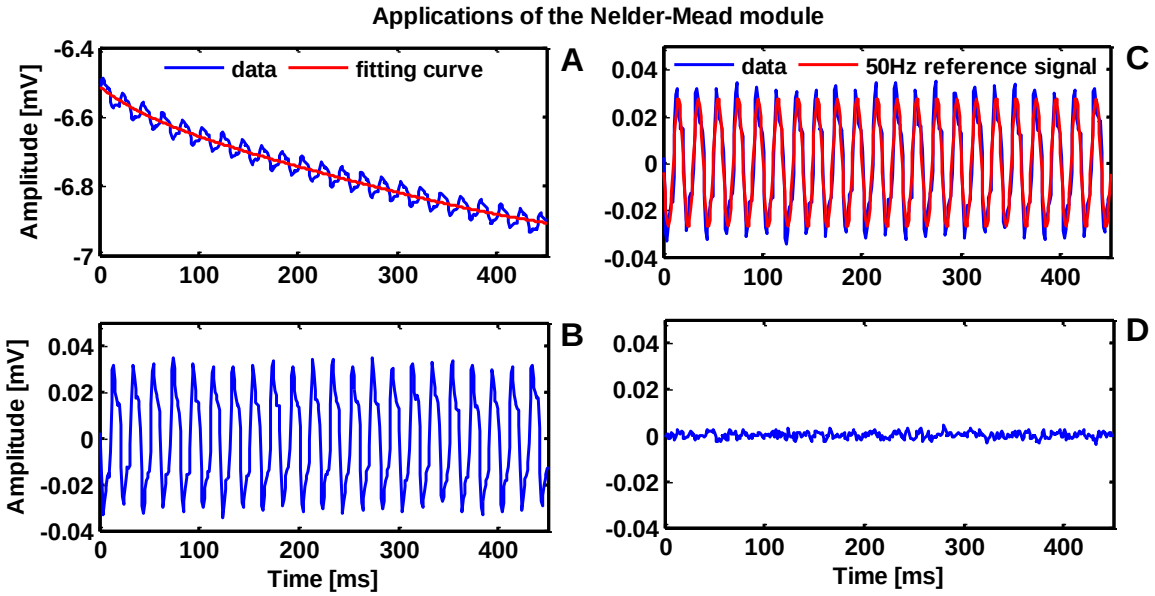

Figure A.2. Applications of the Nelder-Mead module to LFP recordings during CR DBS. A: 5th order exponential curve is calculated by the module to remove the exponential artifact. B: Fit residuals after the removal of the exponential artifact shown in (A). C: Generation of reference signal for PLI shown in (B). D: Fit residuals after the removal of PLI show the artifact-reduced LFP recording.

A.3 Implementation

The algorithm is implemented in several ways in different programming languages such as MATLAB, Scilab, Fortran, and C. For more details about the distinct implementations of the algorithm we refer to (Baudin, 2010). In our Simulink module, we implemented the algorithm using Simulink blocks (Appendix B). One of the main differences between the various implementations lies in the construction of the initial simplex and in the selection of the termination condition that is used to end the optimization process. Starting values are used to calculate the vertices that form the initial simplex. These values were calculated as it was done in the *fminsearch* function.

$$C = (1 + \delta) \cdot C_i,$$

where C_i is the initial guess given as a vector of ones and δ = 0.05. The initial values C are computed and given as constant matrices in the Simulink module.

$$C_{PLI} = \begin{bmatrix} 1 & 1 \\ 1.05 & 1 \\ 1 & 1.05 \end{bmatrix}, \qquad C_{exp} = \begin{bmatrix} 1 & 1 & 1 & 1 \\ 1.05 & 1 & 1 & 1 \\ 1 & 1.05 & 1 & 1 \\ 1 & 1 & 1.05 & 1 \\ 1 & 1 & 1 & 1.05 \end{bmatrix},$$

where C_{PLI} and C_{exp} are the start values for the reference signal of PLI and double exponential fitting curves, respectively. In order to terminate the minimization process, the function *f(x)* of the vertices is compared at each iteration to test the convergence of the simplex. This approach is also used in the *fminsearch* function of MATLAB. If the function values of the vertices become similar (Figure A.1.D), the iterative for-loop is terminated even when the maximum number of iterations has not been reached.

The implementation of the Nelder-Mead algorithm should take some special cases into consideration. For instance, the maximum number of iterations is reached before finding a minimum or a shrink step is started at the last iterations. In such cases, a restart of the algorithm is usually performed using modified starting values.

In our module, the maximum number of iterations is restricted, since it should process successive segments of data in a limited amount of time. Thus, we implemented the optimization process in several successive modules. If the first module could not converge to the minimum within a given amount of time, a second module of parameter optimization is performed. Not more than three successive modules are used. The number of iterations was also reduced during the second and the third phases, since the estimated parameters of the first phase are given as starting values for the next phase. In this way, the parameters can be further optimized using smaller number of iterations, as shown in Figure A.4. A further optimization of parameters is also useful when shrinkage of the simplex is required. Although the shrink step was programmed in the module, it was not required in our application. Furthermore, the number of iterations was set according to the number of parameters to be optimized. For a function with 10 parameters (e.g., the 5^{th} order exponential fit), the number of iterations was three times the number of iterations required for a function with 4 parameters (e.g., the double exponential fit).

The rate of convergence was tested using data segments (i.e., off-cycles of LFP recordings) that were contaminated with PLI and electrical background noise. The rate of convergence for double exponential fitting and the reference signal of the PLI are shown in Figure A.3. As can be seen in this figure, the module uses a smaller number of iterations for the PLI reference signal to converge in comparison to the double exponential fitting.

The rate of convergence for the 5th order exponential fitting before and after the removal of PLI from the off-cycles is shown in Figure A.4. In this figure, the optimal parameters calculated by the algorithm before the removal of PLI (Subplot A) were used for the optimization process after removing the PLI (Subplot B). This explains the low function values in the y-axis and the low number of iterations required in Subplot B.

The processing steps of the algorithm are included in a Simulink for-loop block that is incorporated in an enabled subsystem. Our module accepts the input data as a frame (buffered samples) and gives two outputs: the fitting curve and the residuals. This module was converted successfully into C code by the Embedded Coder of MATLAB. The module can also be used to fit arbitrary functions to input data for many scientific applications developed on Simulink. These functions should be included in a Simulink subsystem than can be integrated into the module in a straightforward manner. The number of iterations can also be changed arbitrary. Some block diagrams of the implemented Simulink module are shown in Appendix B.

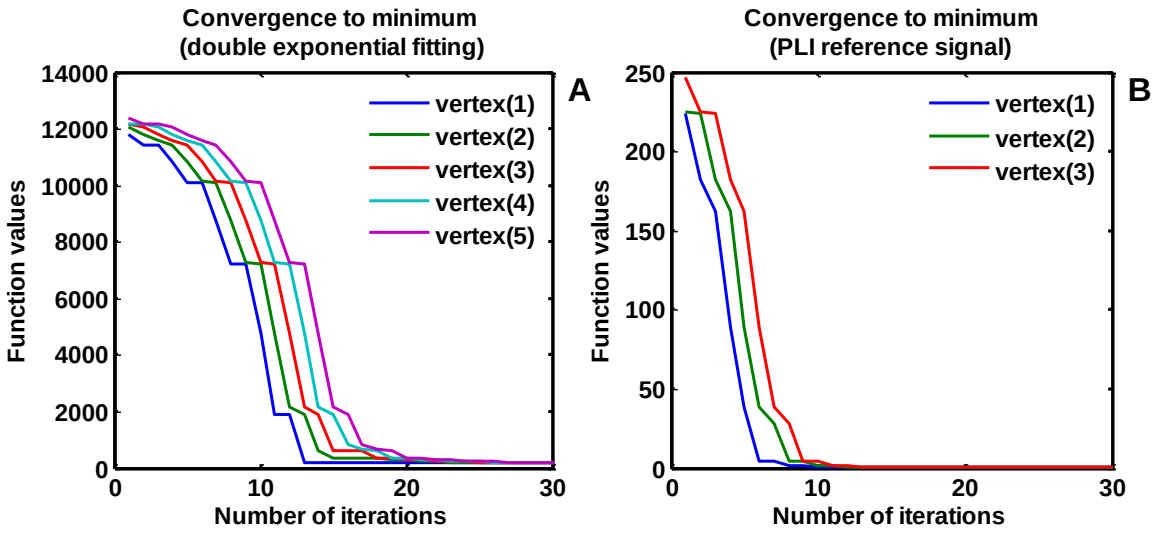

Figure A.3. Rate of convergence of the double exponential and the reference signal of PLI. A: Double exponential simplex converges towards the minimum within 25 iterations. B: The simplex of PLI reference signal converges in less than 15 iterations towards the minimum. The rate of convergence depends on the number of parameters (vertices).

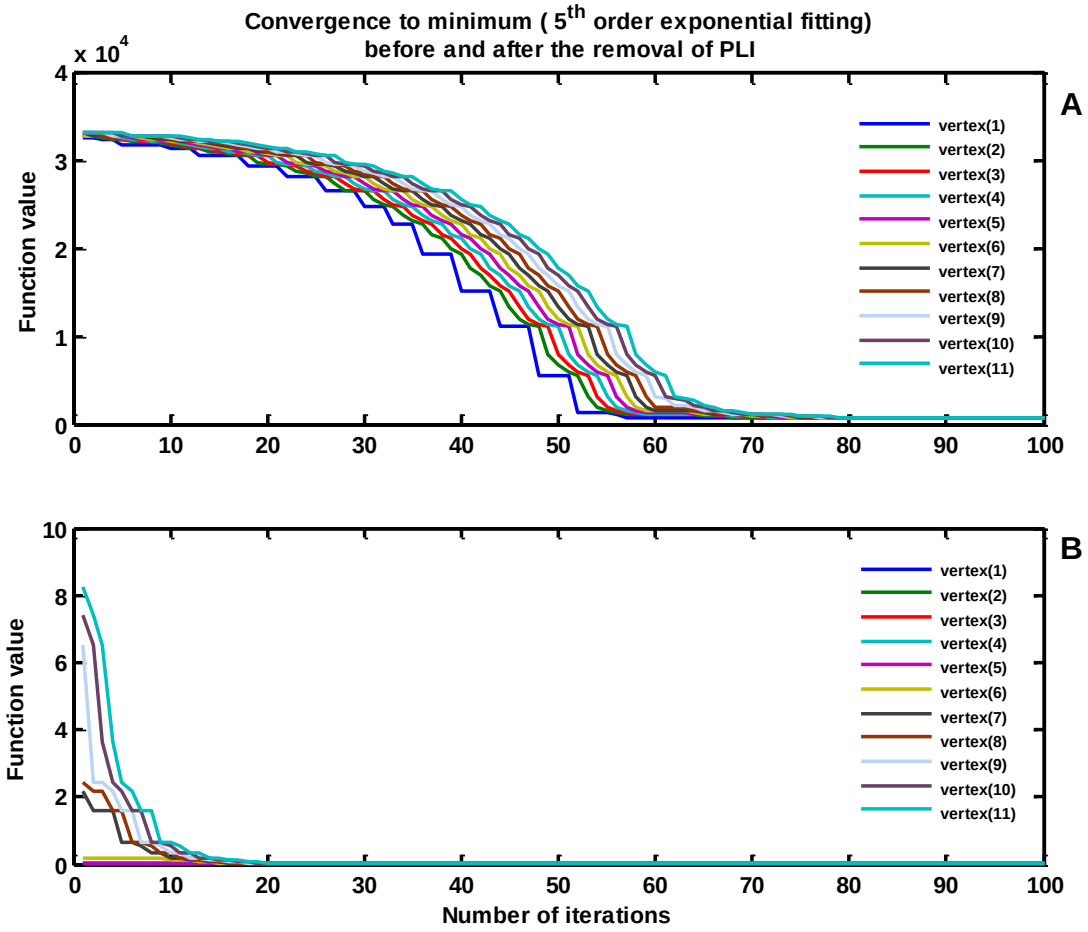

Figure A.4. Rate of convergence of the 5th order exponenital fitting . A: Rate of convergence of the function values before the removal of PLI. B: Rate of convergence after the removal of PLI. Less number of iteration is used in B. This is because the optimal parameters calculated in (A) were used as starting values for the simplex in (B).

Appendix B

Simulink Modules

In this Appendix we present the Simulink modules of the developed and implemented technical solutions for the demand-controlled application of desynchronizing CR DBS. In order to give a better idea of the multiple layers of complexity, we presented the most representative modules. The modules comprise interlinked blocks that perform several calculations. Very complex calculation blocks can be condensed into a modular block set, called subsystem, to be viewed in a more intuitive way. A subsystem may also include further subsystems and several MATLAB routines. This approach allowed the creation of independent subsystems outside of the main Simulink module. After testing and functional verification, these subsystems can be easily integrated into the primary module. The latter includes the independent modules for (i) artifact reduction, (ii) data analysis, (iii) estimation of demand, and (iv) adjustment of the stimulation parameters. The advantage of testing a module outside of the main module is that the time required for testing and processing can be decreased significantly. The Simulink modules were tested with the digital signal processor (DSP) board. The content of the Simulink modules shown along this appendix are highlighted using colored backgrounds and explained in sections as follows:

B.1 Data processing modules during CR DBS

The main module for artifact reduction during CR DBS is shown in Figure B.1. The reference signal, which is generated by the portable neurostimulator and used to build the delimiting signal, is preprocessed in the blocks colored magenta. The subsystem with a cyan background builds the delimiting signal by using the *candidate segment of data* method (Section 4.1.1). The subsystem with a green background imports the local field potential (LFP) signal which is still contaminated with artifacts. The subsystem with a blue background is an enabled subsystem that includes the artifact reduction algorithm and the implemented Nelder-Mead algorithm. An enabled subsystem contains an enable port which acts like an In-Port. If the subsystem receives a positive signal (trigger) on this port, it is activated. The counter subsystem with an orange background is dedicated to estimate and count the duration and the number of the detected off-cycles, respectively. Figure B.2 shows the block diagram corresponding to the *candidate segment of data* method. In this figure, the subsystems with blue backgrounds take into consideration the different window

sizes used to detect the off-cycles. A graphical example of the content of these subsystems is shown in Figure B.3.

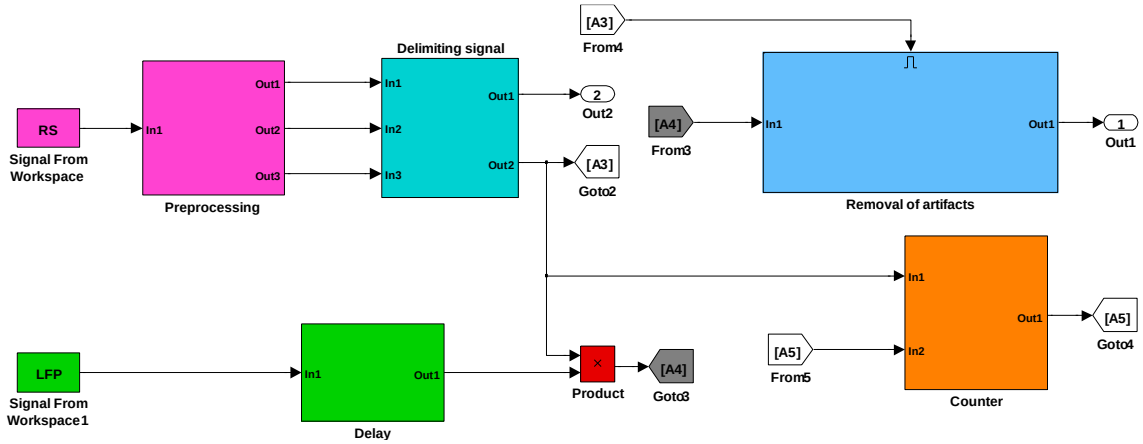

Figure B.1. Simulink block diagram of the main module used to process the data during CR DBS.

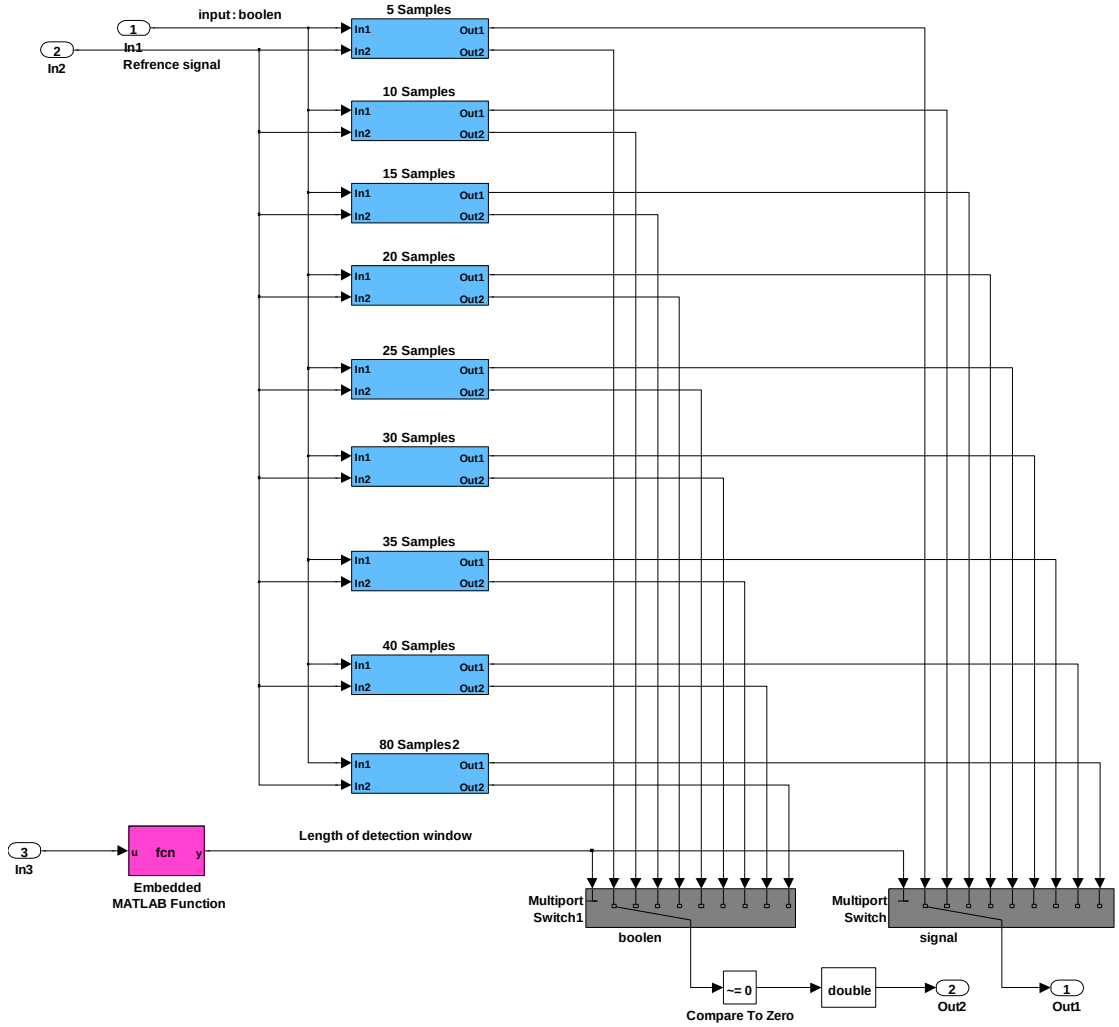

Figure B.2. Simulink block diagram of the *candidate segment of data* method.

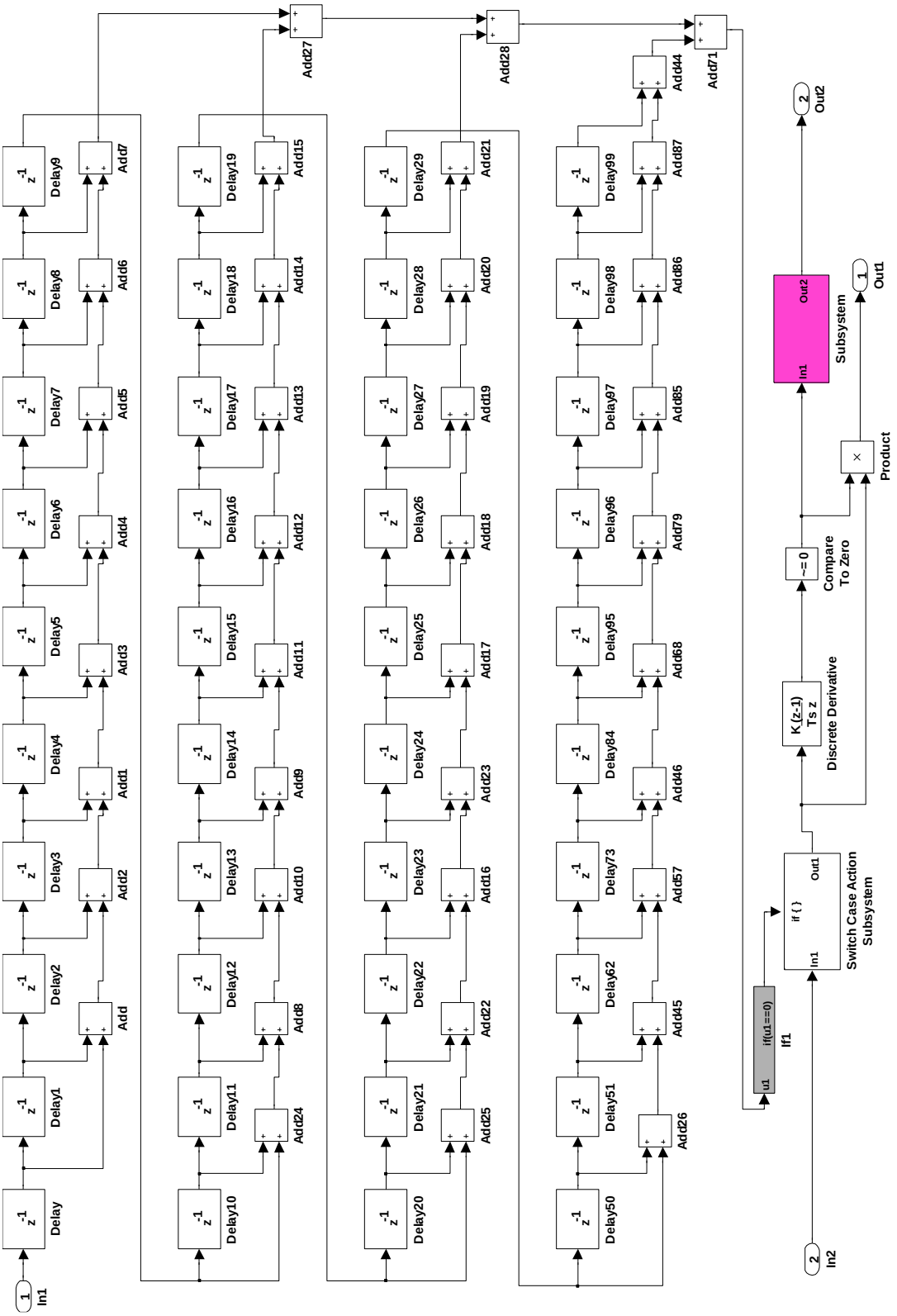

Figure B.3. A subsystem used for the implementation of the *candidate segment of data* method. In this particular case, a window size of 40 is used to detect the off-cycles**.**

Figure B.4 shows the content of the artifact removal module (see Figure B.1). The red blocks determine the length of the off-cycles which is an important step in the process of dividing the off-cycles into segments. When a specific number of samples is reached, a MATLAB routine (green block) activates the enabled subsystem of the artifact reduction module (blue background). The detail of this subsystem is shown from Figure B.5 to Figure B.19.

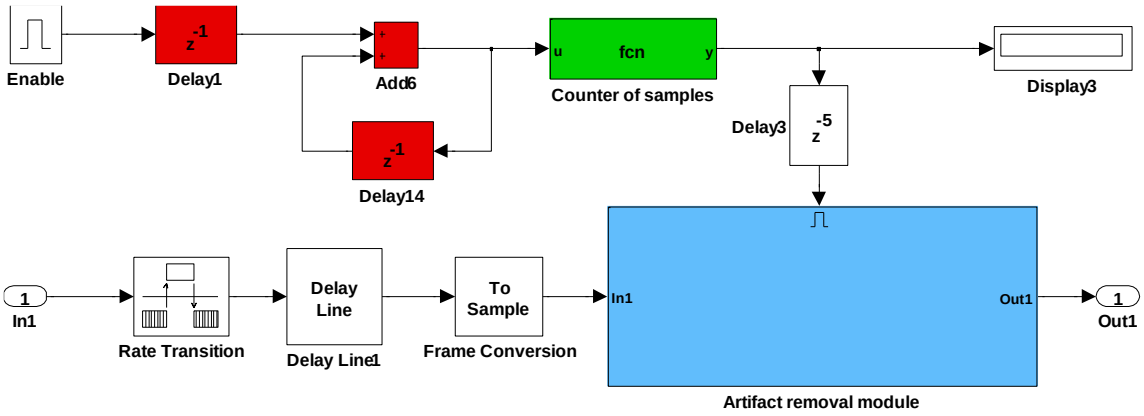

Figure B.4. Block diagram of the artifact removal subsystem

Figure B.5 includes the subsystems used to remove the exponential artifact and power line interference (PLI), as detailed in Section 4.1.2. In this figure, the subsystems depicted in blue include the first and second phases of the procedure for the exponential artifact removal. These two phases are implemented before and after the removal of PLI. The subsystems with a magenta background are used as part of the PLI removal approach (for the first and second phases). In these subsystems, reference signals are generated for the 50 Hz PLI and its harmonics. All these subsystems include the implemented Nelder-Mead algorithm explained in Appendix A. In the subsystems that correspond to the exponential artifact removal, either double or 5^{th} order exponential fitting functions can be calculated. A mixture of both is also possible. An example of the block diagram that implements the second phase of PLI removal is shown in Figure B.6. In this phase, the generated reference signals for PLI and harmonics are subtracted one after the other from the input signal (i.e., the off-cycles of the LFP recordings) and before the removal of the exponential artifact.

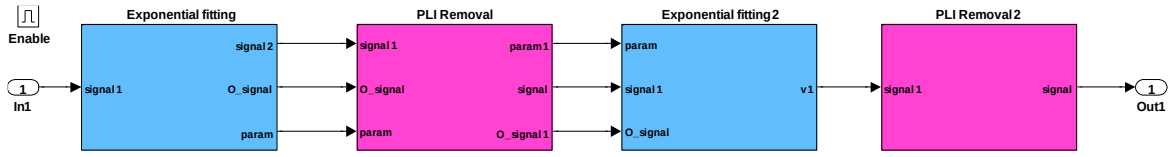

Figure B.5. Simulink block diagram that correspond to the removal of exponential artifact and PLI approaches .

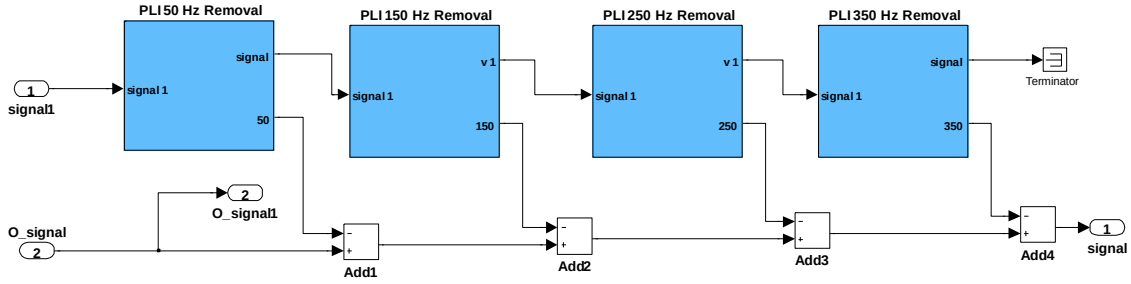

Figure B.6. Simulink block diagram of PLI removal after the removal of the exponential artifact. The removal of PLI and harmonics is performed here using subsystems connected in series. This module was optimized and replaced by only one subsystem as shown later in Figure B.20.

The two phases for the exponential artifact removal are shown in Figure B.7 and Figure B.8. Each phase includes the exponential fitting functions with positive and negative exponents where each exponential fitting curve is optimized three times using three subsystems (blue background): exponential fitting functions with positive exponents are located at the top row and negative exponents are placed at the bottom row. The parameters of the fitting curve calculated in the first subsystem are sent to the next subsystem to be further optimized. The subsystem with a magenta background is used to build the initial step of the simplex (Nelder-Mead algorithm described in Appendix A). The selection of the best fitting function is performed in the blocks with an orange background which compares the outputs of both fitting functions (with positive and negative exponents). Then, using the estimated parameters, the exponential fitting curve is generated in the subsystems with a green background. At the end, the exponential artifact is removed by subtracting the fitting function from the input signal (red blocks).

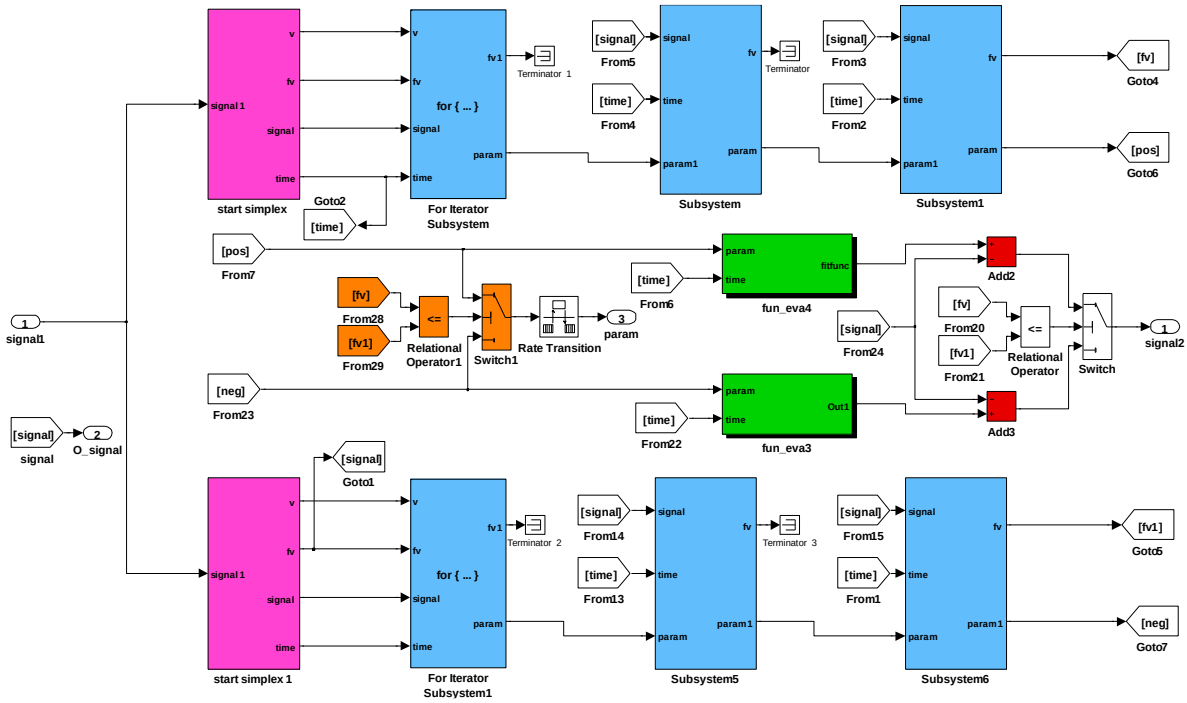

Figure B.7. Module where it is implemented the first phase of the exponential artifact removal approach before removing the PLI.

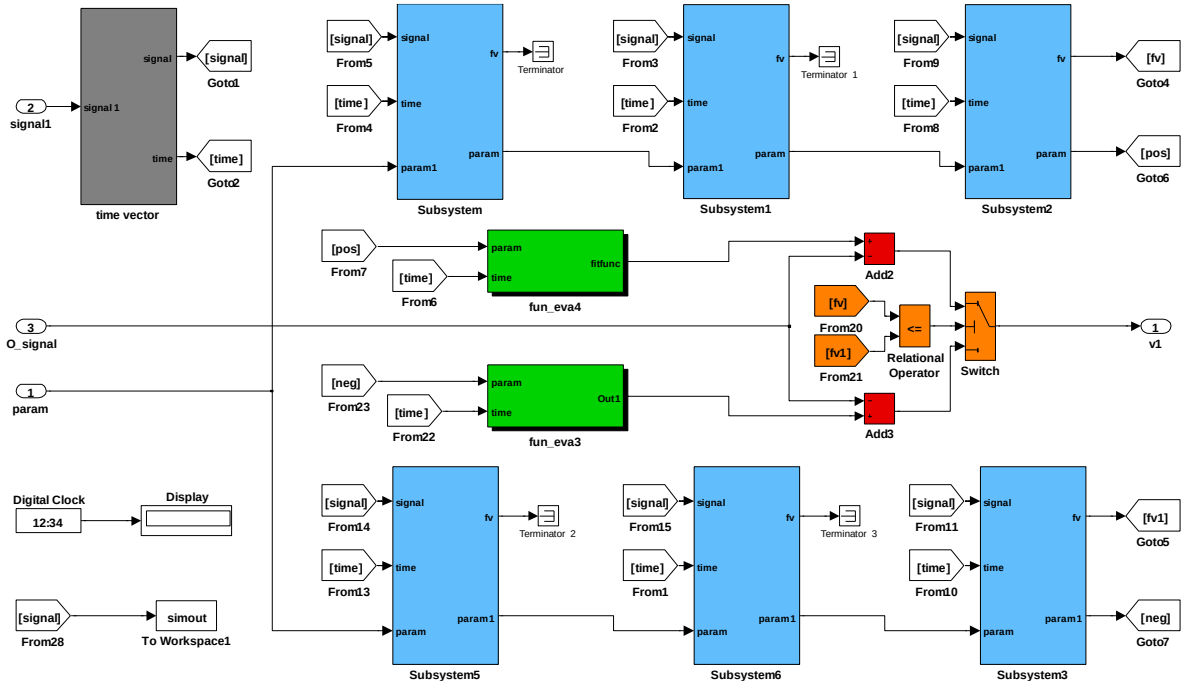

Figure B.8. Module where it is implemented the second phase of the exponential artifact removal approach after removing the PLI.

The main block diagram for the Nelder-Mead module is shown in Figure B.9. The module consists of two subsystems for (i) building the initial simplex (blue background) and (ii) optimizing the parameters in a for-iterator (magenta background). The block diagrams for the initial phase in the simplexes for double and 5th order exponential fitting are shown in Figure B.10 and Figure B.11, respectively. For the first simplex (both for the exponential artifact and for the PLI removal), a constant matrix is used as starting values; whereas for the second phase, the simplex is rebuilt taking as initial values the parameters that were optimized in the first phase. This process increases the accuracy of the fitting process and reduces the number of iterations significantly. The block diagrams for rebuilding the simplexes for the double and 5th order exponential fitting functions are shown in Figure B.12 and B.13, respectively. The content of the for-iterator subsystem is shown from Figure B.14 to Figure B.19.

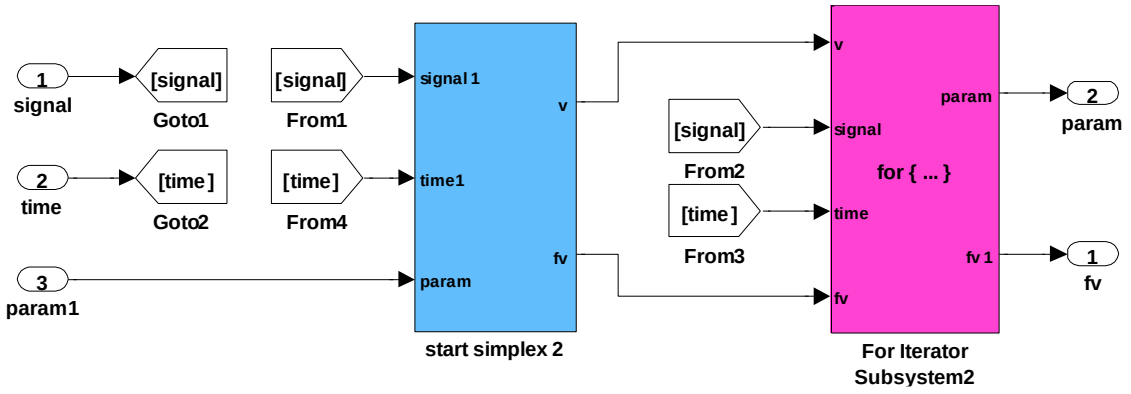

Figure B.9. Main module of the Nelder-Mead algorithm.

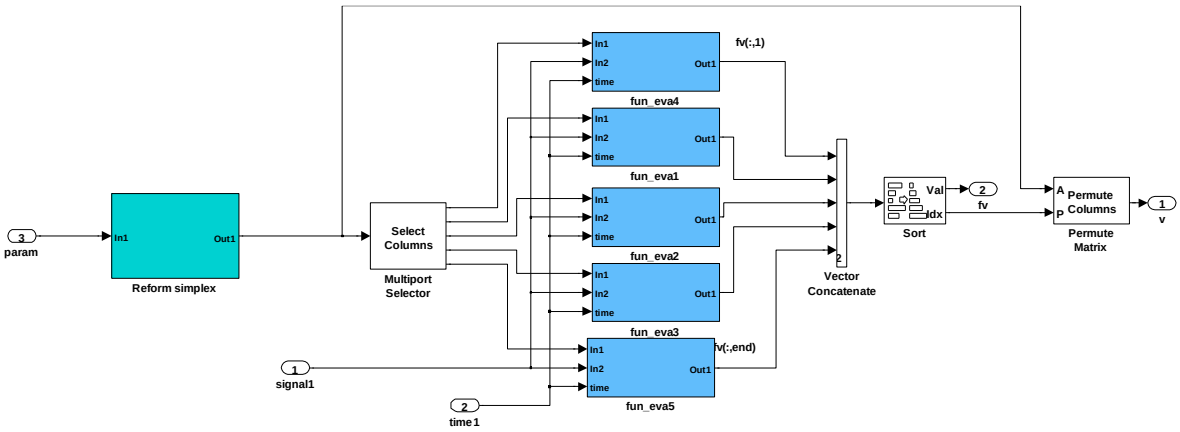

Figure B.10. Block diagram used in the second phase for building the simplex of the double exponential fitting.

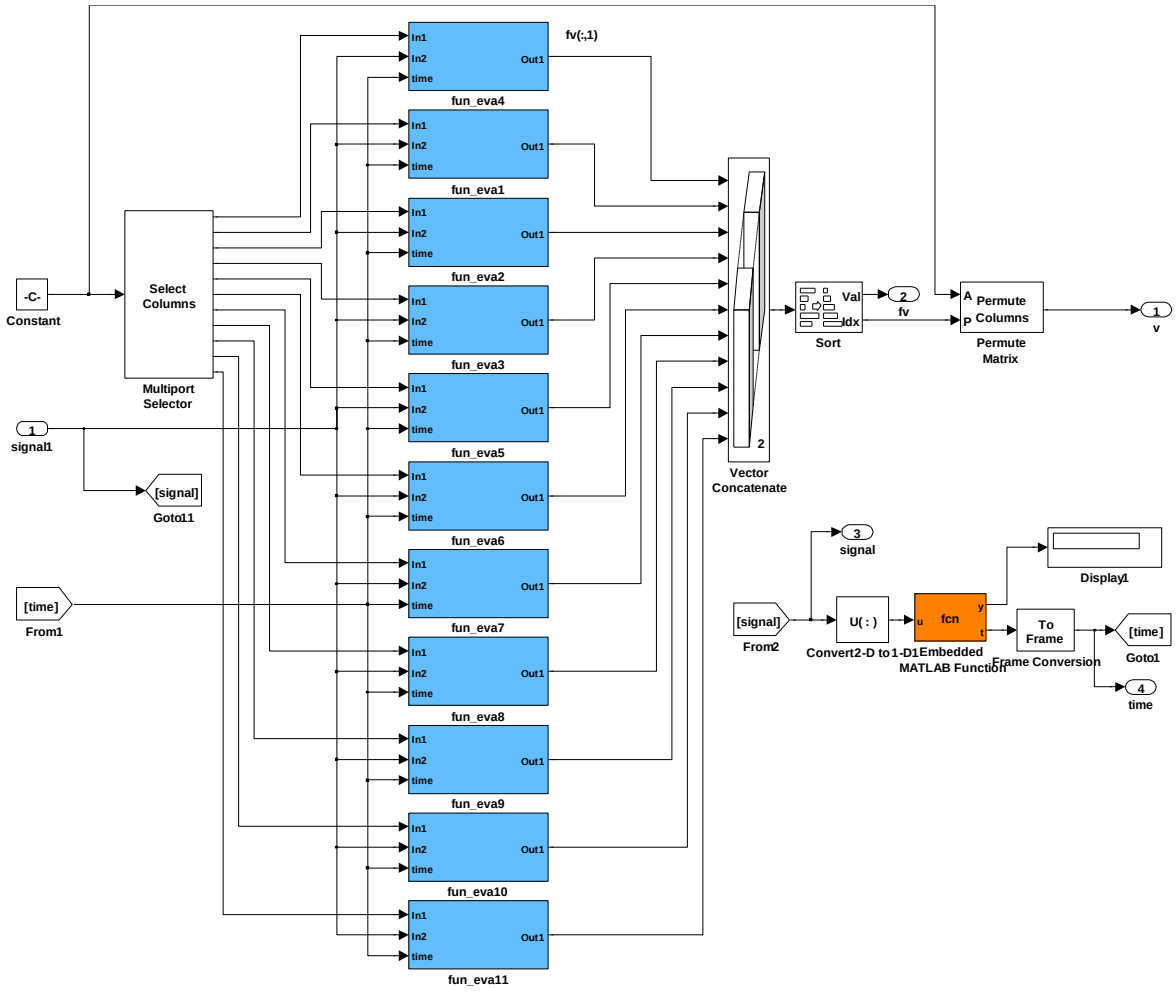

Figure B.11. Block diagram used in the first phase for building the simplex of the 5th exponential fitting.

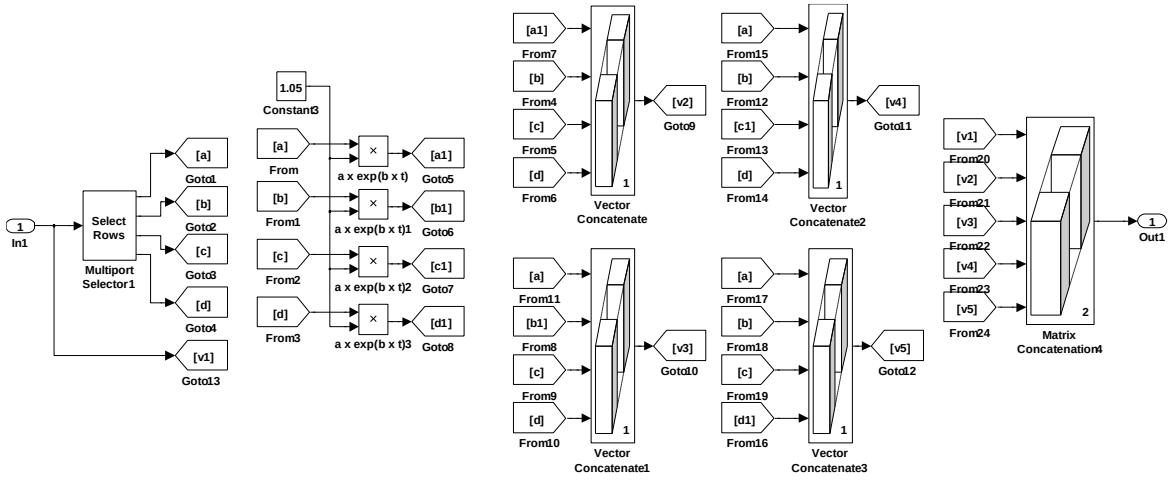

Figure B.12. Rebuilding the simplex to optimize the double exponential fitting function.

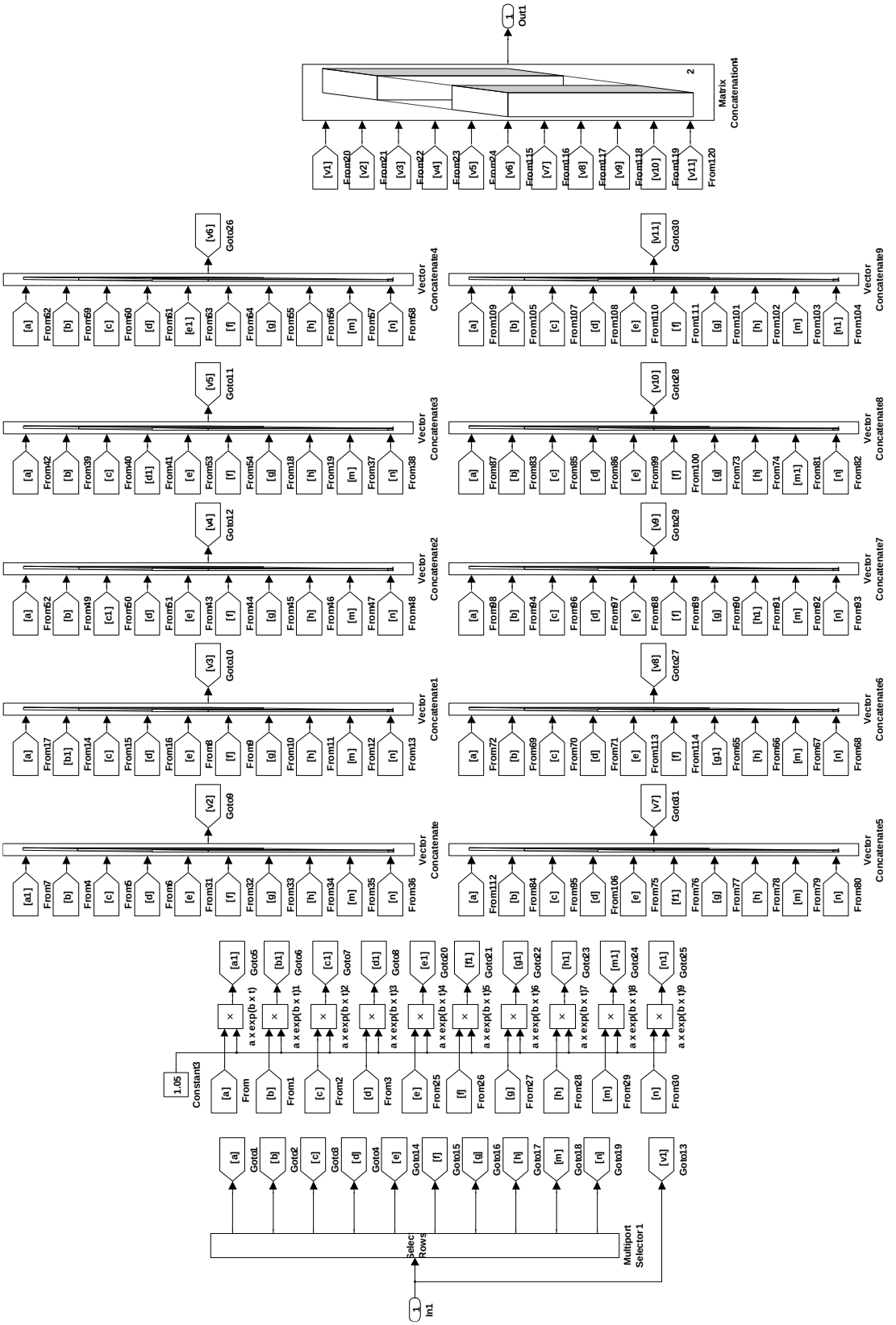

Figure B.13. Rebuilding the simplex to optimize the 5th order exponential fitting function.

The for-iterator module of the Nelder-Mead algorithm is presented in Figure B.14. The subsystem colored magenta includes the internal processing steps of the algorithm that optimize the parameters of the objective function. The number of iterations is limited taking into account the restrictions coming from the real-time implementation. Examples of the block diagrams of some internal processing steps performed within the for-iterator loop are shown from Figure B.15 to Figure B.19. The mean value of the vertices of the simplex (see Appendix A) is calculated with the block diagram shown in Figure B.15. The reflection step in which the worst vertex is reflected with respect to the mean value is implemented using the block diagram shown in Figure B.16.

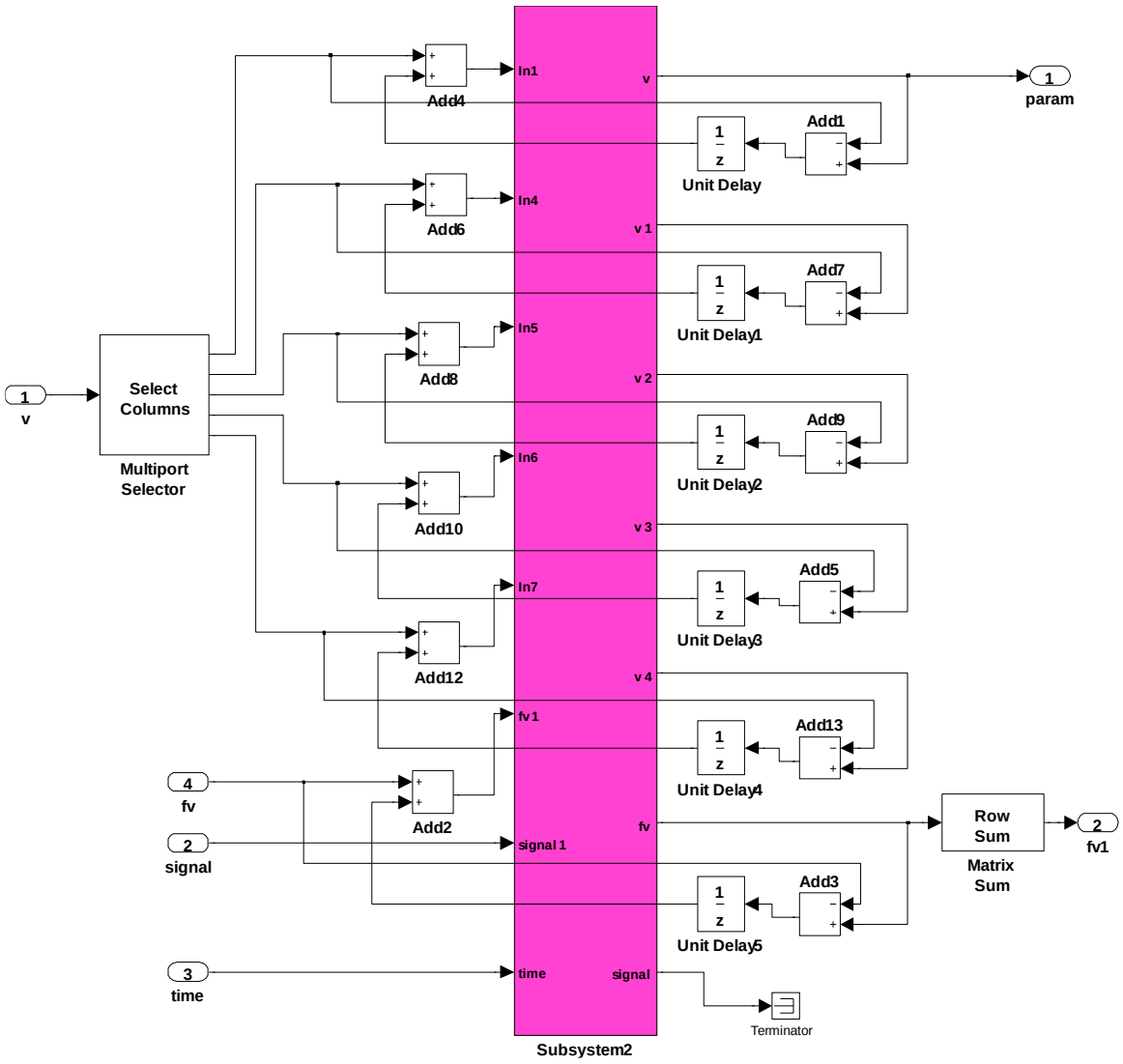

Figure B.14. Simulink block diagram of the for-iterator of the Nelder-Mead algorithm.

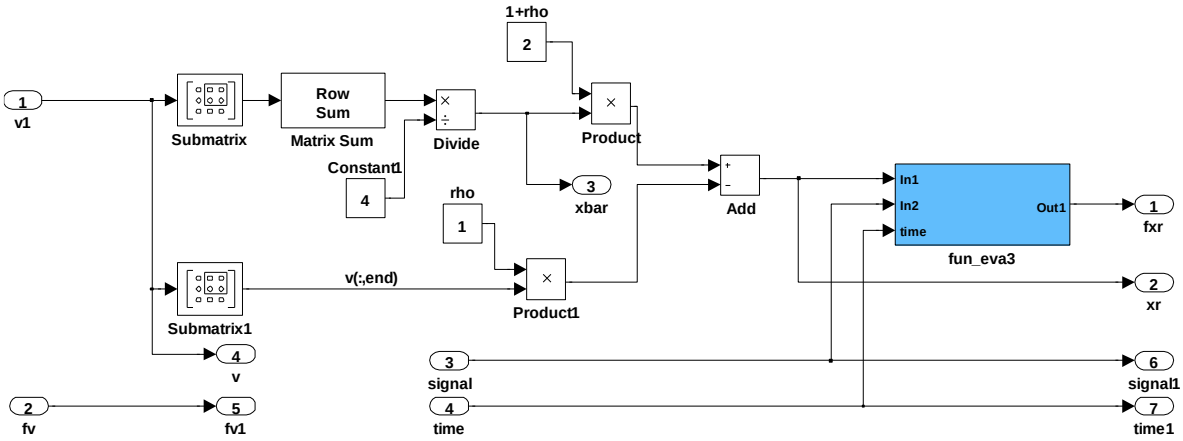

Figure B.15. Block diagram to calculate the mean value of three vertices, e.g., the reference signal of the PLI.

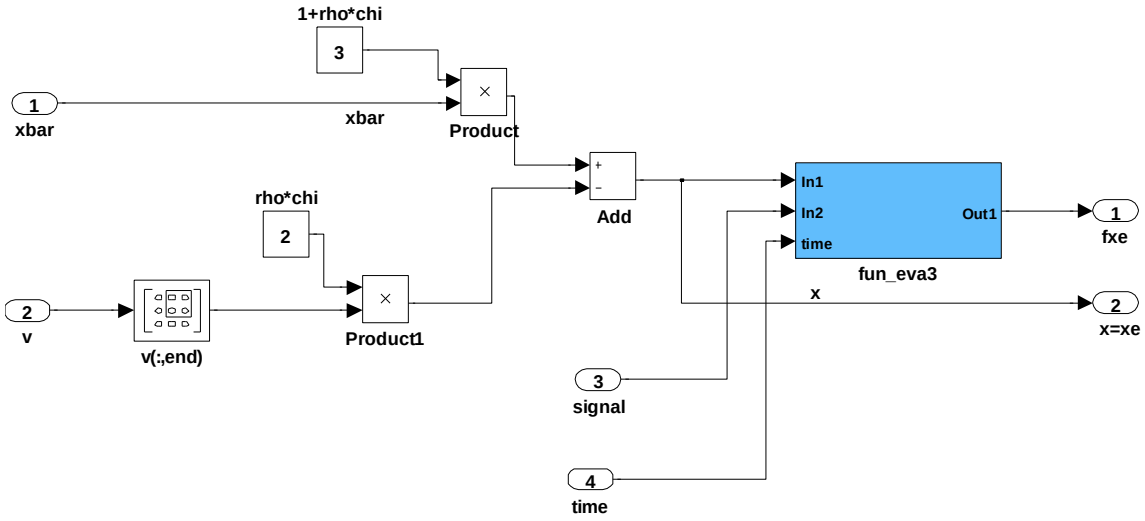

Figure B.16. Block diagram to calculate the reflection point of the simplex.

The most critical step in the Nelder-Mead algorithm is the shrink step, in which the entire simplex should be reconstructed. This is a critical step, since the input data are processed in real-time. If the parameters could not be optimized in the given number of iterations, there will not be enough time to start again since the next off-cycle is buffered to be analyzed in this subsystem. Although the shrink step was not reached during the processing of our data, the block diagram of this step was implemented. In case that a shrink step is required, the parameters can be optimized in the next subsystems (see Figure B.7 and Figure B.8). The block diagrams for the shirk step of the double and 5^{th} exponential fitting functions are shown in Figure B.17 and Figure B.18, respectively. The block diagram for calculating the 5^{th} order exponential fitting function (Equations 4.11 and 4.12) is shown in Figure B.19.

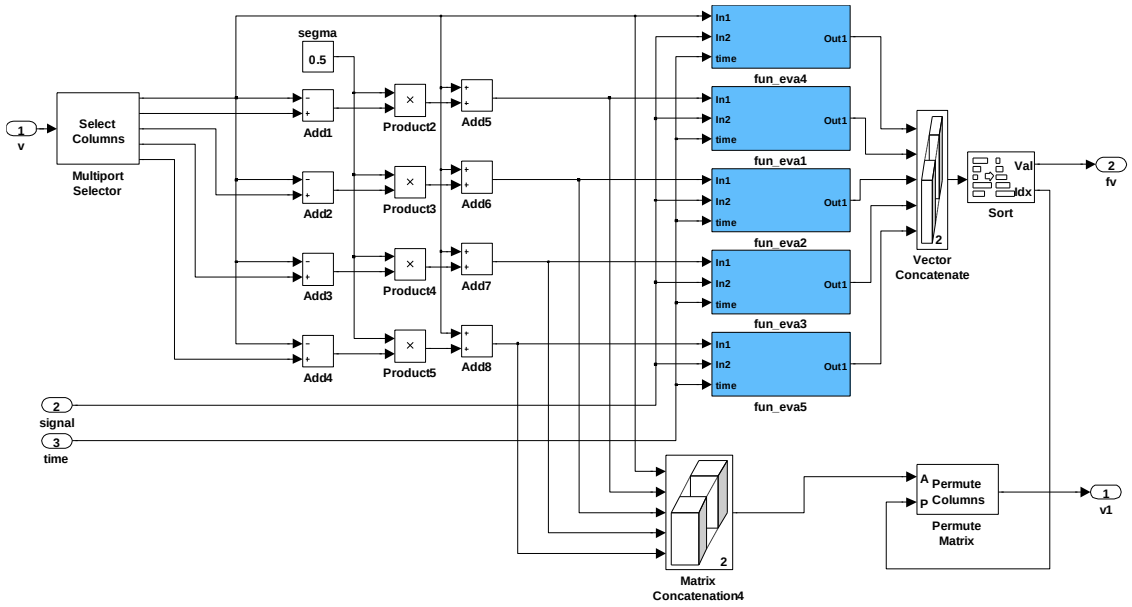

Figure B.17. Block diagram of the shrink step of the double exponential fitting.

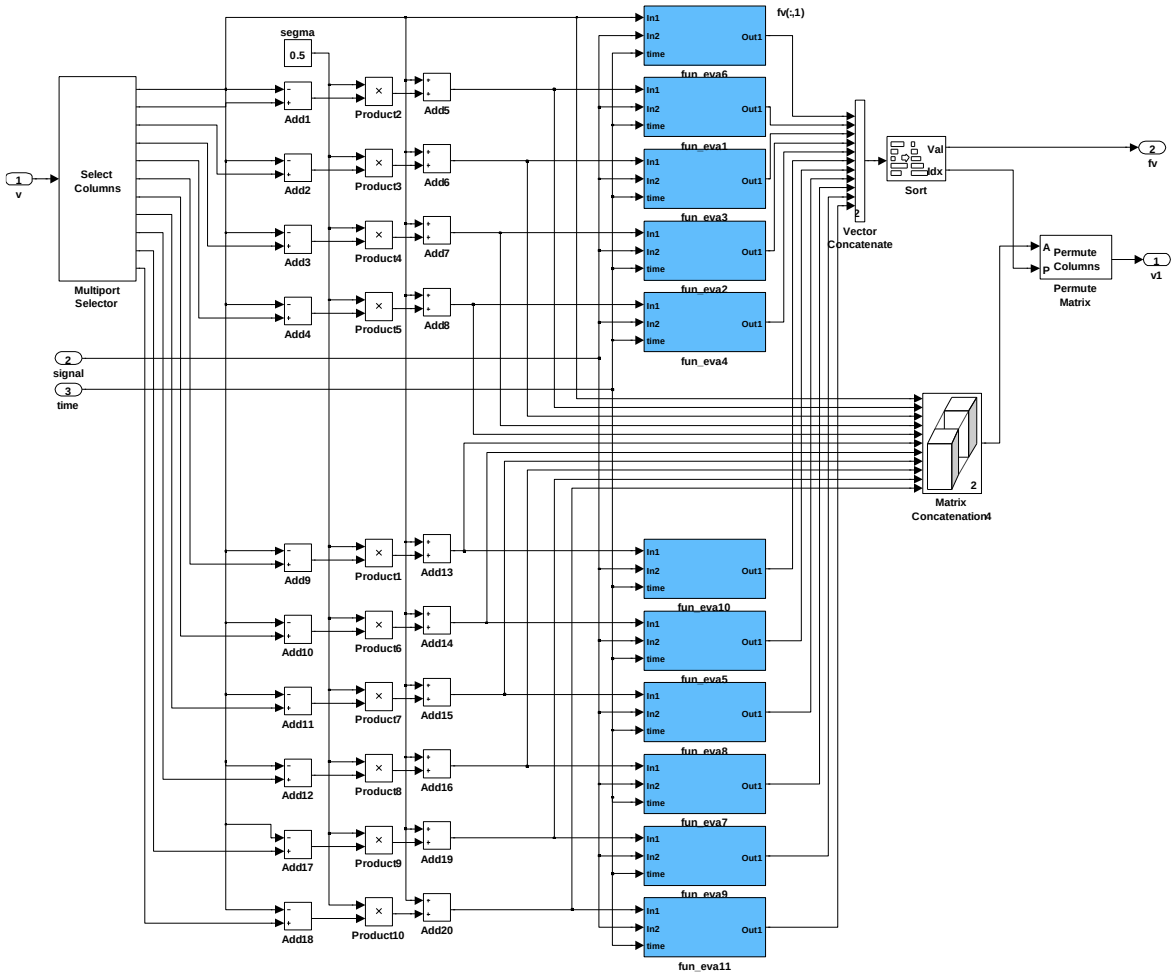

Figure B.18. Block diagram of the shrink step for the 5th order exponential fitting.

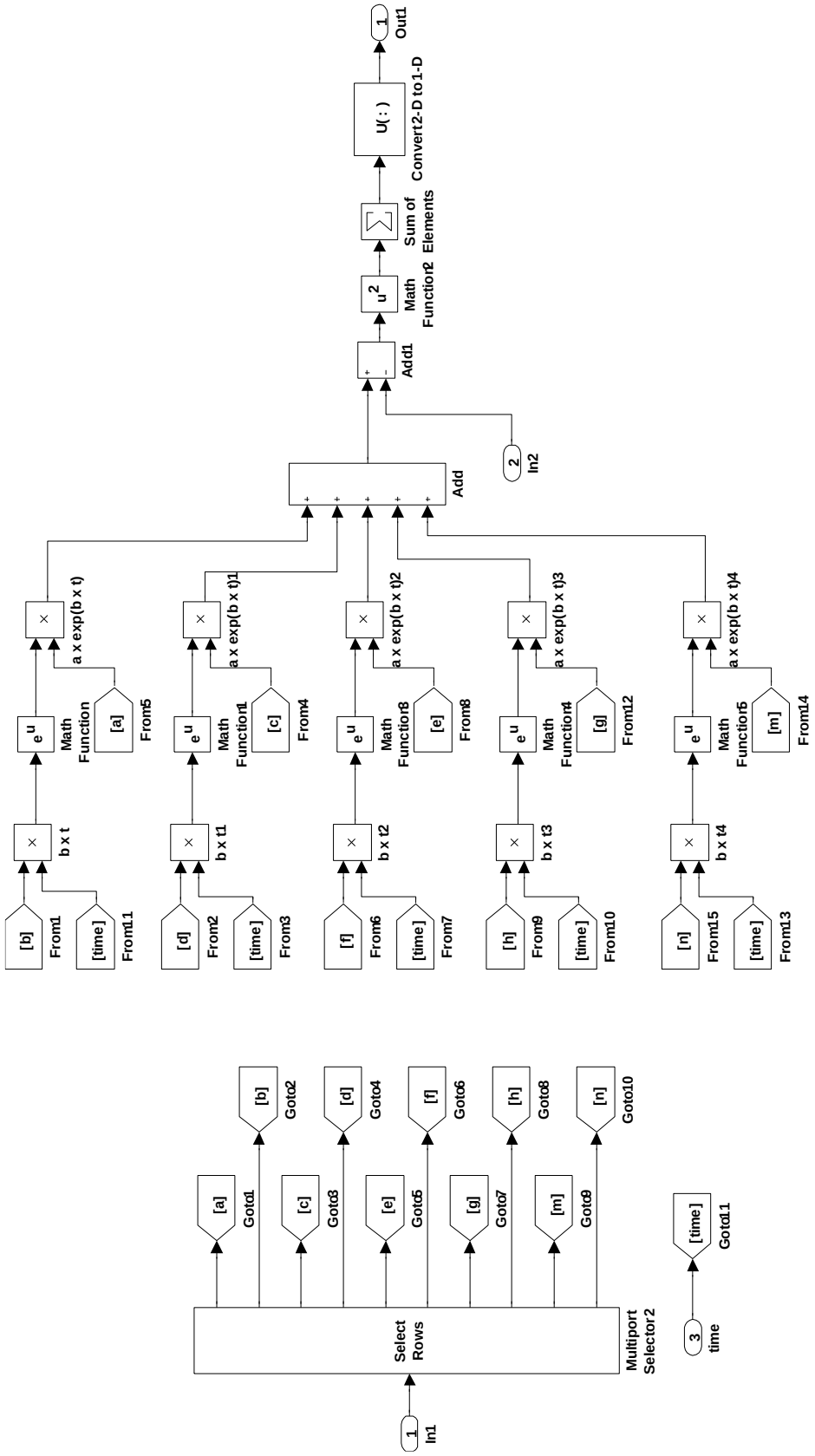

Figure B.19. Calculation of the 5th exponential fitting function

B.2 Optimization of the artifact reduction module

In order to increase the performance of the processing module during CR DBS and to reduce the size of the C files (Section 3.3), the module was optimized. Instead of using multiple subsystems that include the Nelder-Mead algorithm (as shown in Figure B.5 and Figure B.6), only one subsystem (orange background) is used for generating the reference signals of the PLI and harmonics as shown in Figure B.20. After subtracting the reference signal of PLI from the input signal, they were feedback to the same subsystem in order to remove the other harmonics. Careful timing was required to trigger the entire module. The triggering was performed by the controlling subsystem, colored green, in which the data can also be divided into smaller segments. This subsystem is also used to generate time series of the input data.

The second method, i.e., the *sawtooth* method (Section 4.1.1), used to delimit the off-cycles is included as a MATLAB routine in the subsystem with a magenta background. This subsystem generates the *sawtooth* signal using the stimulation parameters. Real-time averaging of off-cycles to reveal neuronal activity with fixed latency to stimulation (Section 5.2) is performed in the subsystem colored cyan.

The optimized module to remove PLI is shown in Figure B.21. In this figure, the subsystems with cyan and orange backgrounds include the implemented Nelder-Mead algorithm. Three switchers select the frequency of PLI and harmonics (multiplied by a factor of 2) and determine whether the signal should be processed before or after the removal of the exponential artifact. The switchers are triggered by the controlling subsystem.

In the optimized module we also tested the polynomial fitting functions to remove the exponential artifact. They are implemented in the subsystem with a blue background (see Figure B.20). The two phases of polynomial fitting are illustrated in Figure B.22. In this figure, a MATALB routine implemented in the magenta block determines the order of the polynomial function. A trigger signal determines which polynomial function should be used before and after the PLI removal. Both polynomials can have different orders. In order to generate the parameters of the polynomial fitting function, we used either the Simulink function *Polyfit* (Figure B.22) or our built module for polynomial fitting (Figure B.23). It is worth to mention that polynomial fitting is used as a secondary fitting technique for the exponential artifact removal. The main technique was the exponential fitting with the Nelder-Mead algorithm as shown in the previous section.

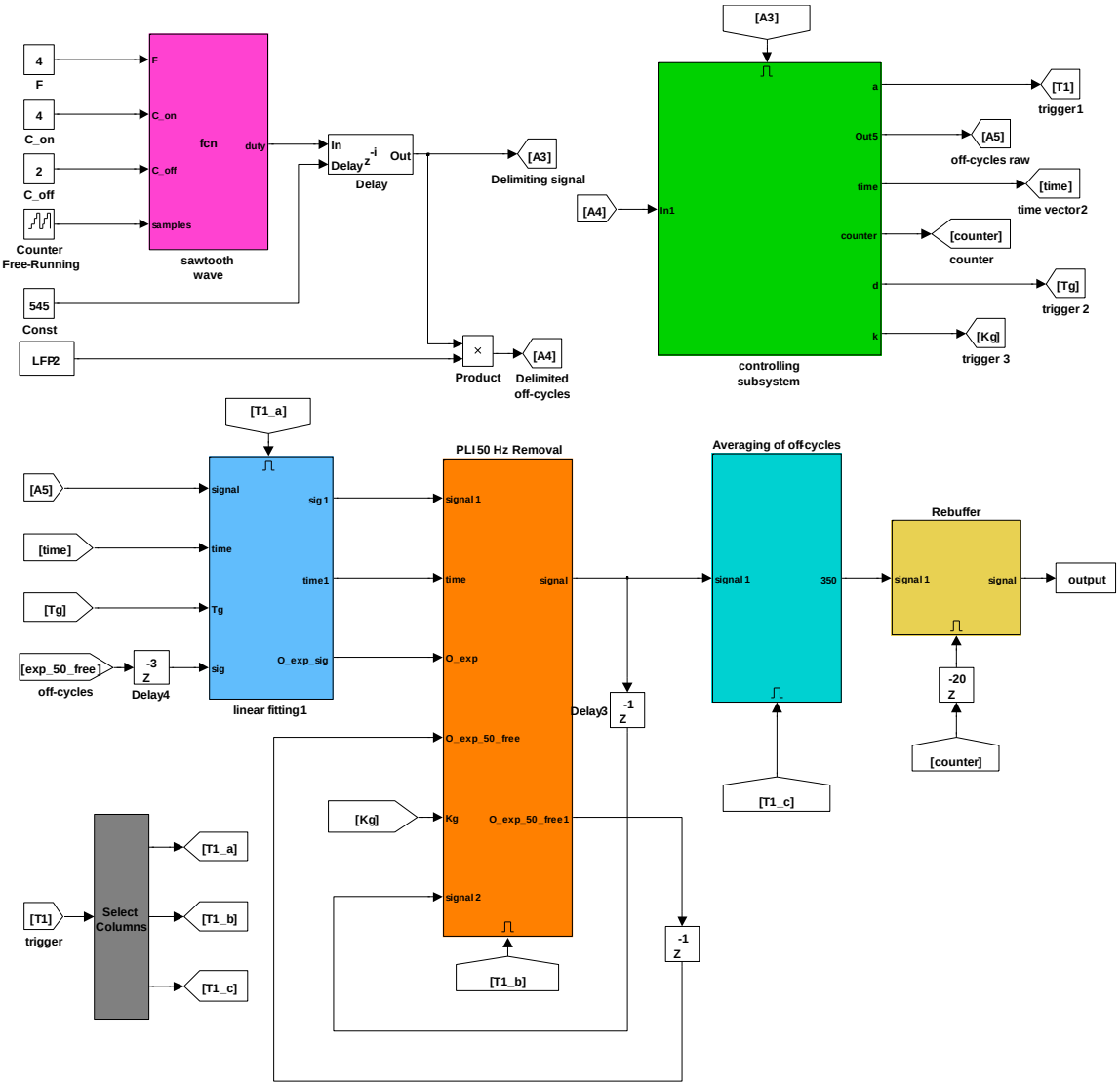

Figure B.20. Optimization of the data processing module during CR DBS

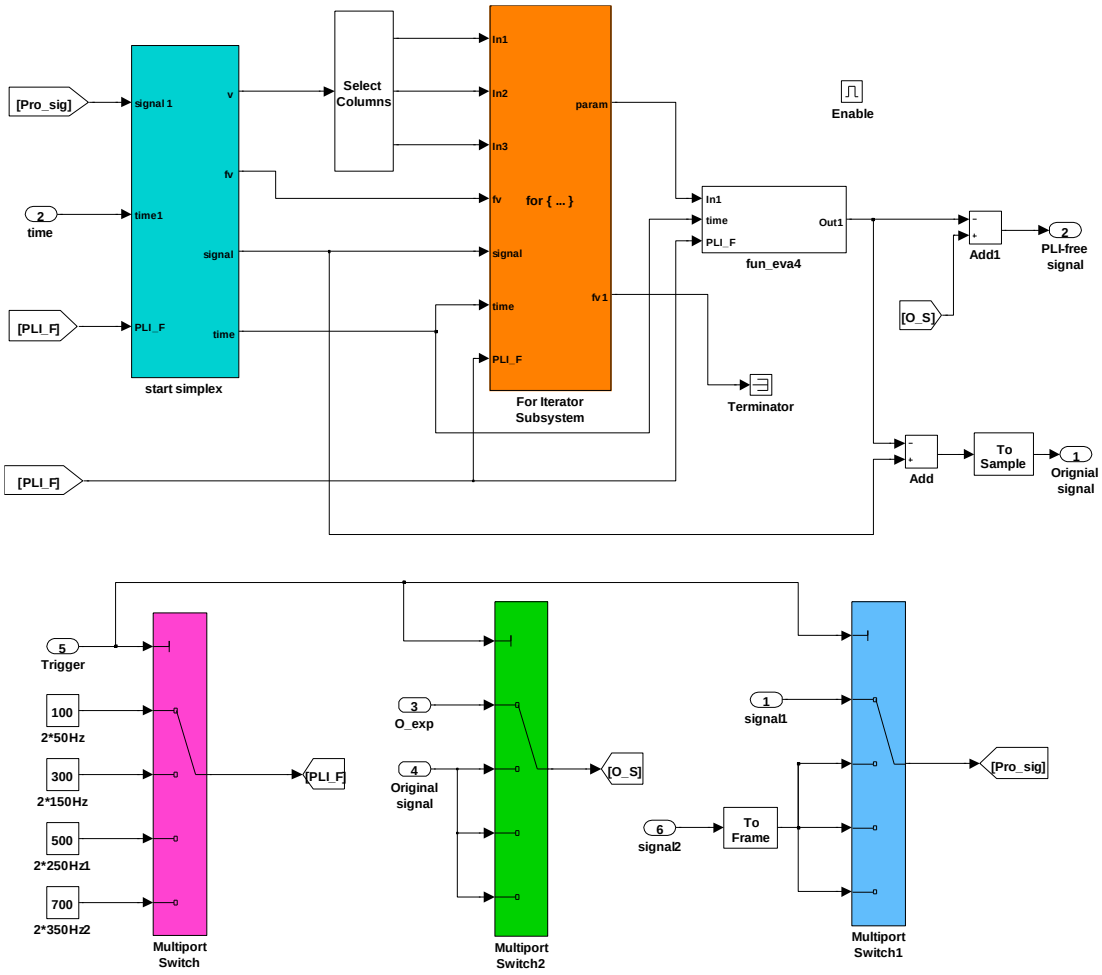

Figure B.21. Single subsystem for the PLI removal.

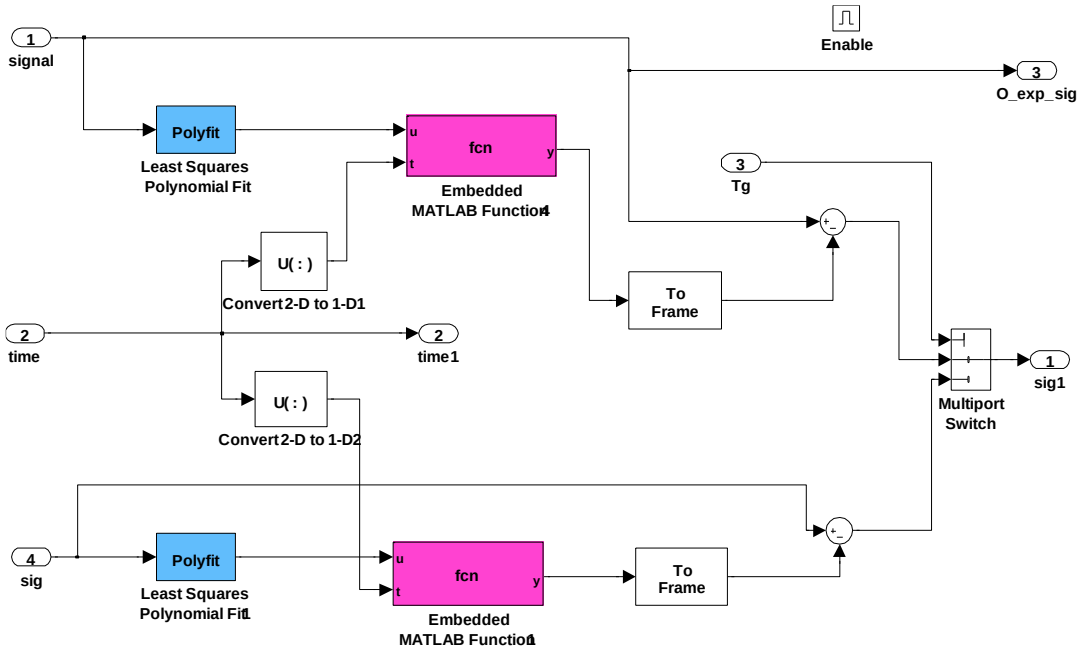

Figure B.22. Two phases of polynomial fitting using the Simulink block *polyfit*.

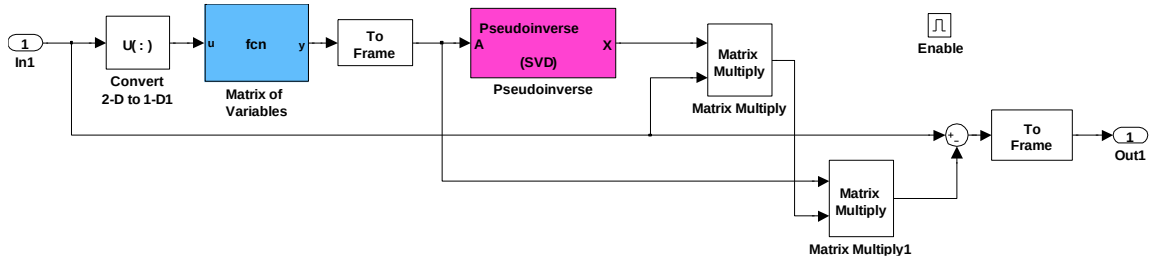

Figure B.23. Block diagram of the implemented module for polynomial fitting.

B.3 Data processing modules of spontaneous recordings

The main module for artifact reduction and analysis of spontaneous LFP and tremor recordings is shown in Figure B.23. The subsystem with a magenta background has the same function as the one shown in Figure B.20; where it is used for delimiting the off-cycles. Particularly, this module is dedicated for delimiting long off-cycles, i.e., > 5 s. The subsystem with a blue background comprises three subsystems: (i) digital filters to remove PLI and low frequency components, (ii) signal de-noising algorithm using wavelet filters, and (iii) a periodogram block for spectral analysis. These three subsystems are shown in Figure B.25. The subsystems colored orange have the same block set and include the three phases used for detecting three dominant frequencies in the spontaneous LFP or tremor recordings (see Section 5.4). The detail of these subsystems is presented in Figure B.26 and Figure B.27.

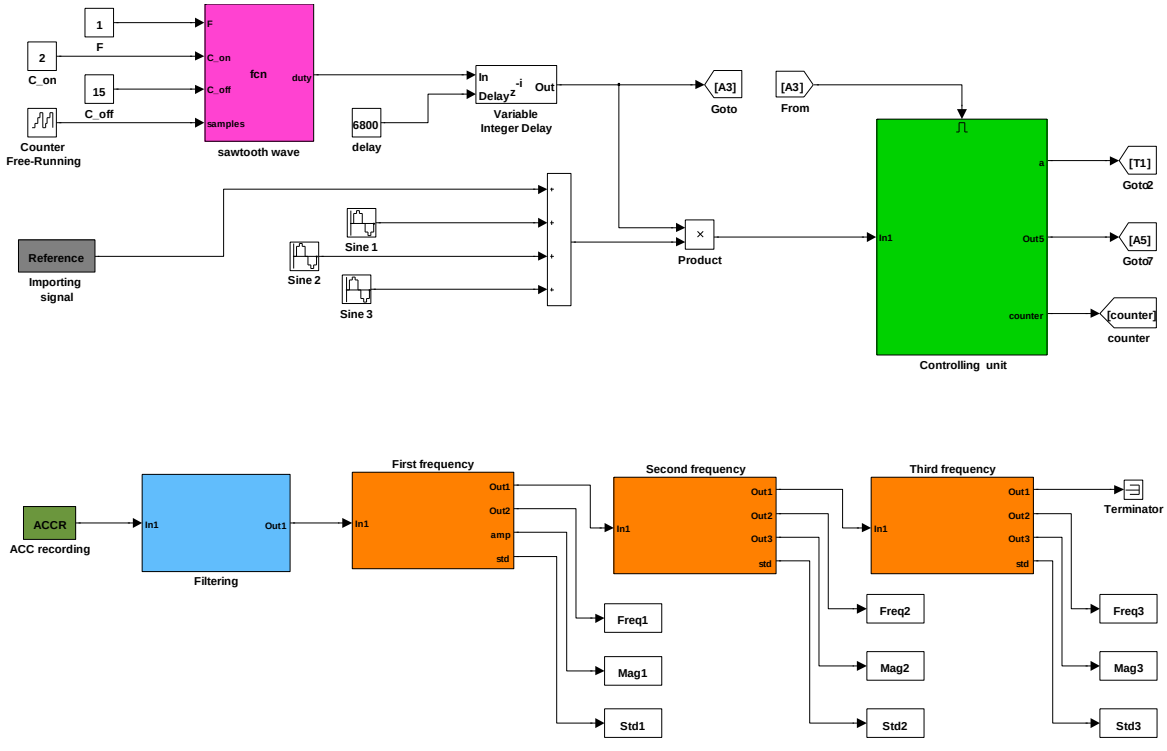

Figure B.24. Main module for artifact reduction and analysis of spontaneous LFP and tremor recordings.

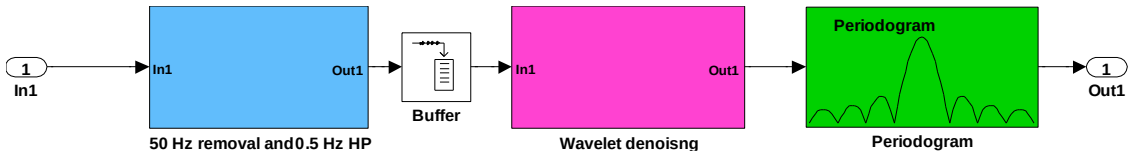

Figure B.25. Block diagram of the subsystems used for the removal of PLI and electrical background noise as well as for spectral analysis.

Figure B.26 shows the subsystem used for detecting a dominant frequency in the recorded data. The cyan block includes a MATLAB routine to restrict the frequency content to the range of 3 – 43 Hz. The subsystems with blue and yellow backgrounds buffer the detected values of dominant frequencies and their amplitudes, respectively. The histogram block (red) calculates the distribution of the detected frequencies. A MATLAB routine implemented in the magenta block: (i) compares the distribution of each frequency with a threshold value and (ii) decides whether the buffered values should be sent to the next subsystem (colored green). The latter determines the amplitude of the most common frequency and its content is shown in Figure B.27. This Simulink module extracts and averages the amplitudes of the most common frequency (moving-average) and estimates the strength of the on-going pathological activity.

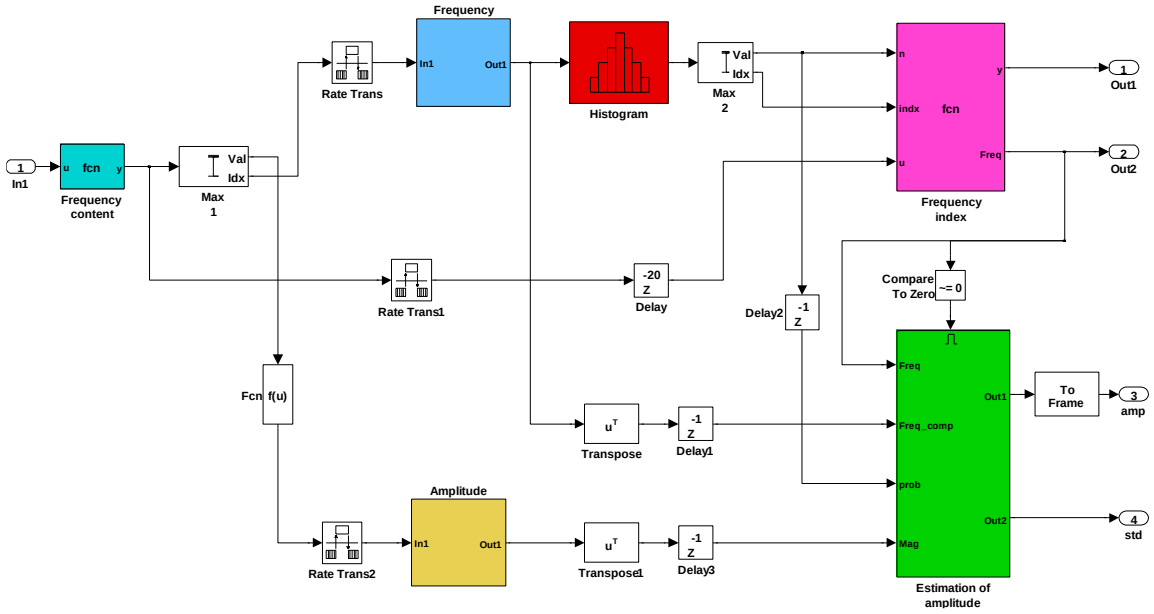

Figure B- 26. Analysis module of spontaneous LFP and tremor recordings.

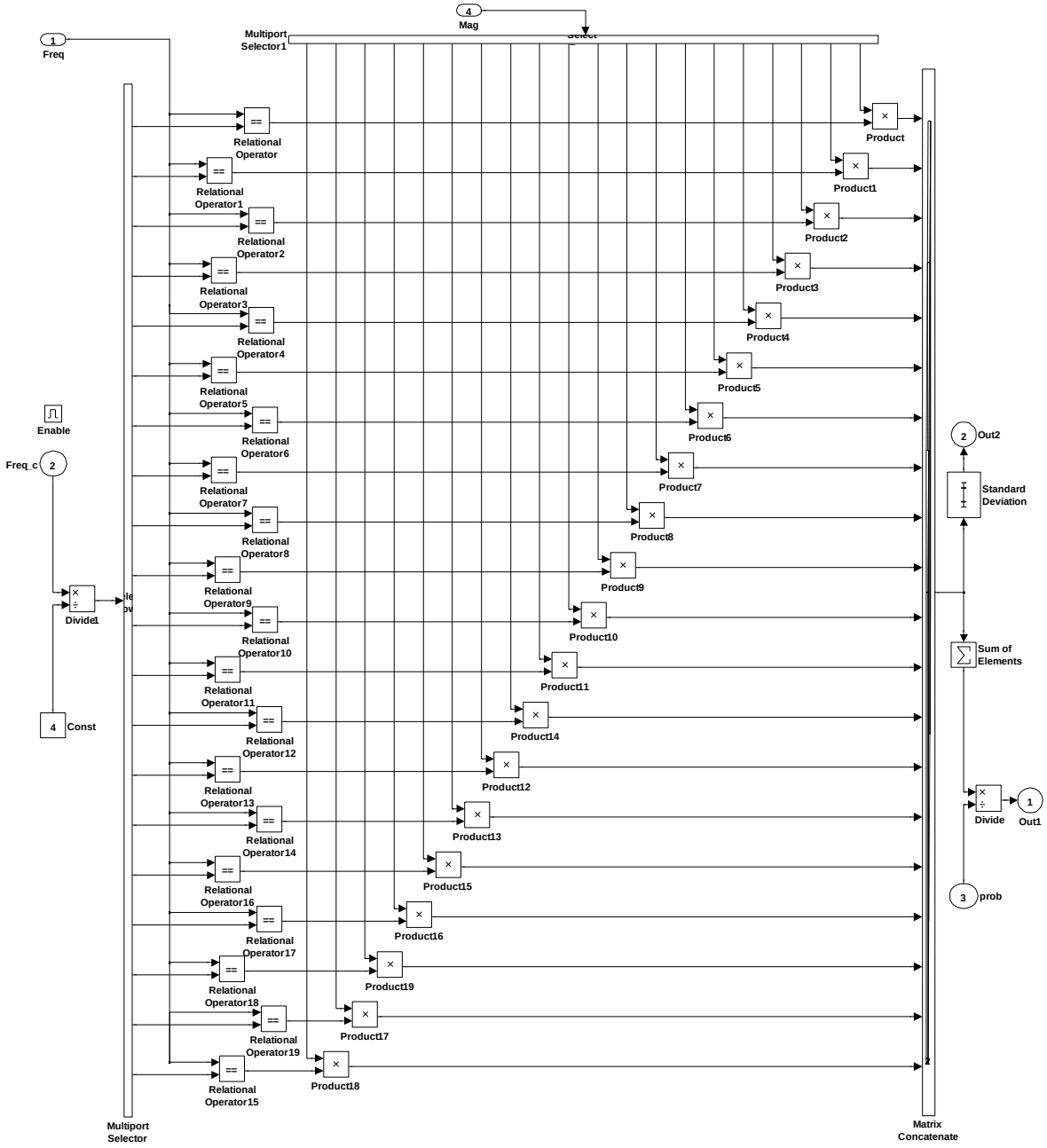

Figure B.27. Simulink block diagram for estimating the amplitude of the dominant frequencies in the spontaneous LFP and tremor recordings.

B.4 Adjustment of stimulation parameters module

The main module used for tuning the stimulation parameters in real-time is shown in Figure B.28. This module is used mainly for the tremor recordings. The subsystem with a blue background transports the stimulation parameters and the tremor signals to the analysis subsystems (with orange background) which process two signals simultaneously. These two signals could be the tremor recordings from two limbs of a tremor patient, e.g., the hands. MATLAB routines are included in the green and magenta blocks to analyze both

signals and sent the tuned stimulation signals to the outputs of the portable neurostimulator (Section 3.1).

Figure B.29 shows the content of the analysis subsystem. The recorded signals are first filtered (Section 5.5) within the subsystem colored green. The strength of the pathological activity is measured by the standard deviation of the filtered signal in the blue subsystem. Then, the stimulation signal is scaled by a MATLAB routine implemented in the orange block before being sent as outputs of the portable neurostimulator. The filters block diagram is shown in Figure B.30.

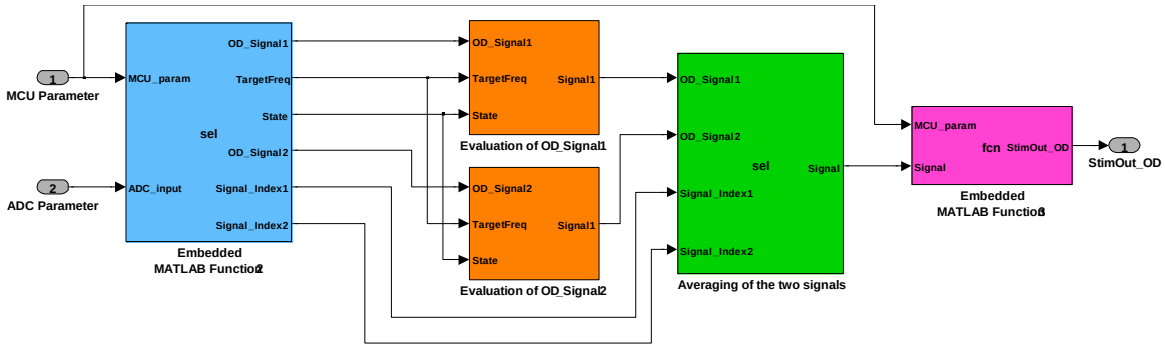

Figure B.28. Block diagram of the module used for tuning the stimulation parameters.

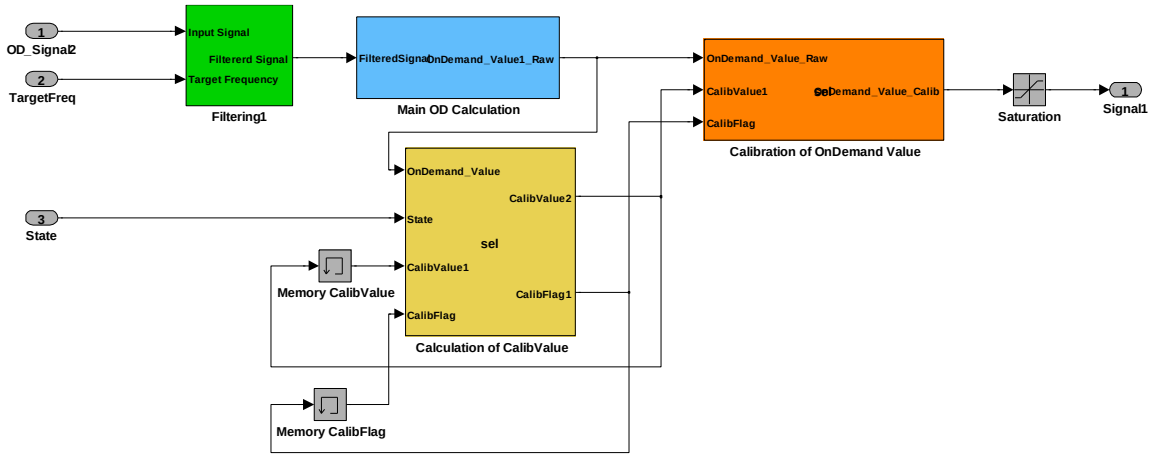

Figure B.29. Block diagram of the module used for filtering, analyzing and scaling the stimulation signals.

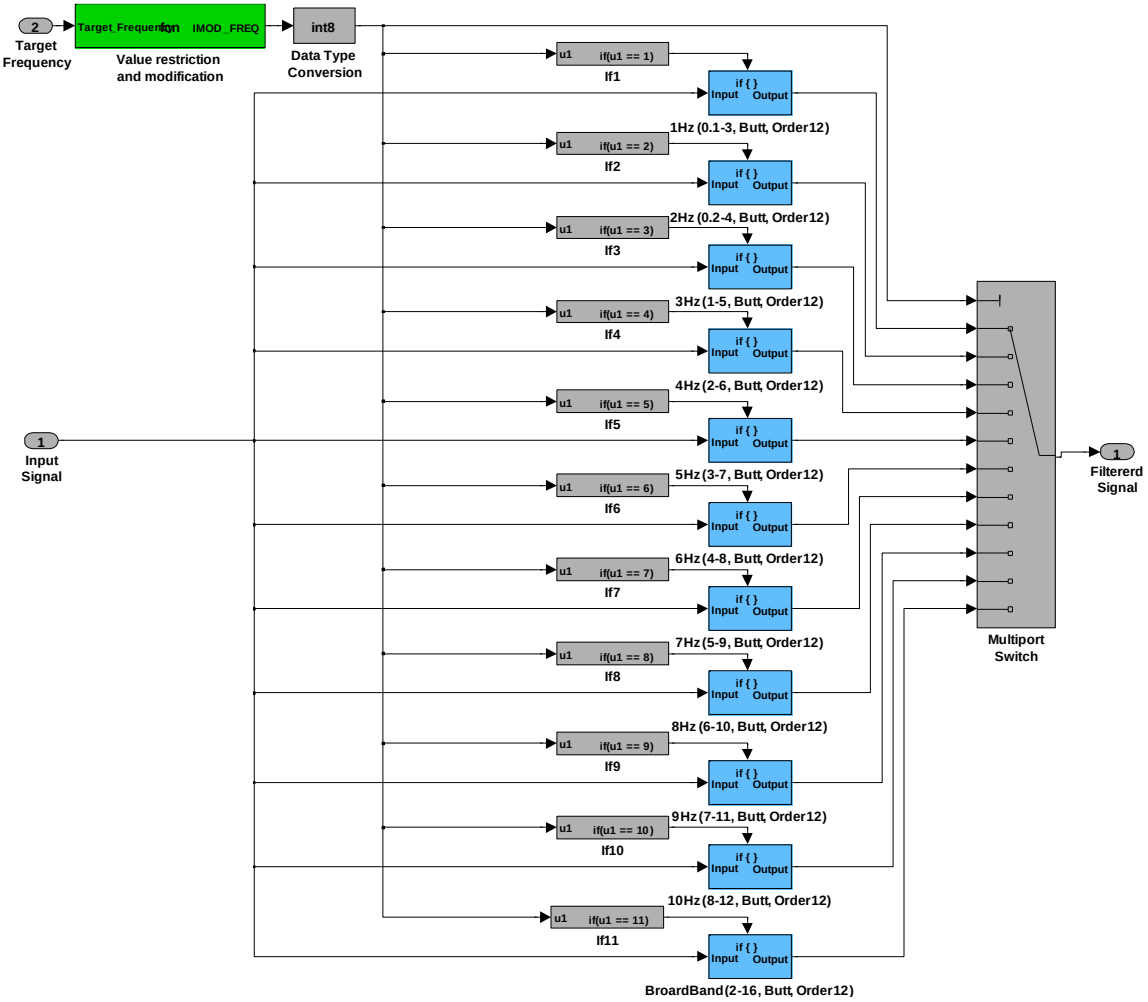

Figure B.30. Block diagram of the filtering module.

Bibliography

Abosch, A., Lanctin, D., Onaran, I., Eberly, L., Spaniol, M. & Ince, N. F. 2012. Long-term Recordings of Local Field Potentials From Implanted Deep Brain Stimulation Electrodes. *Neurosurgery,* 71**,** 804-814.

Al-Ani, T., Cazettes, F., Palfi, S. & Lefaucheur, J. P. 2011. Automatic removal of high-amplitude stimulus artefact from neuronal signal recorded in the subthalamic nucleus. *J Neurosci Methods,* 198**,** 135-146.

Albin, R. L., Young, A. B. & Penney, J. B. 1989. The Functional-Anatomy of Basal Ganglia Disorders. *Trends in Neurosciences,* 12**,** 366-375.

Alexander, G. E. & Crutcher, M. D. 1990. Functional Architecture of Basal Ganglia Circuits - Neural Substrates of Parallel Processing. *Trends in Neurosciences,* 13**,** 266-271.

Angermann, A., Beuschel, M., Rau, M. & Wohlfarth., U. 2007. *MATLAB-Simulink-Stateflow,* München, Germany Oldenburg Wissenschaftsverlag GmbH.

Babb, T. L., Mariani, E., Strain, G. M., Lieb, J. P., Soper, H. V. & Crandall, P. H. 1978. A sample and hold amplifier system for stimulus artifact suppression. *Electroencephalogr Clin Neurophysiol,* 44**,** 528-531.

Baudin, M. 2010. Nelder-Mead User's Manual.

Benabid, A. L. 2007. What the future holds for deep brain stimulation. *Expert Rev Med Devices,* 4**,** 895-903.

Benabid, A. L., Chabardes, S., Mitrofanis, J. & Pollak, P. 2009. Deep brain stimulation of the subthalamic nucleus for the treatment of Parkinson's disease. *Lancet Neurol,* 8**,** 67-81.

Benabid, A. L., Costecalde, T., Torres, N., Moro, C., Aksenova, T., Eliseyev, A., Charvet, G., Sauter, F., Ratel, D., Mestais, C., Pollak, P. & Chabardes, S. 2011. Deep brain stimulation: BCI at large, where are we going to? *Brain Machine Interfaces: Implications for Science, Clinical Practice and Society,* 194**,** 71-82.

Benabid, A. L., Pollak, P., Gao, D., Hoffmann, D., Limousin, P., Gay, E., Payen, I. & Benazzouz, A. 1996. Chronic electrical stimulation of the ventralis intermedius nucleus of the thalamus as a treatment of movement disorders. *J Neurosurg,* 84**,** 203-214.

Benabid, A. L., Pollak, P., Gervason, C., Hoffmann, D., Gao, D. M., Hommel, M., Perret, J. E. & De Rougemont, J. 1991. Long-term suppression of tremor by chronic stimulation of the ventral intermediate thalamic nucleus. *Lancet,* 337**,** 403-406.

Benabid, A. L., Pollak, P., Louveau, A., Henry, S. & Derougemont, J. 1987. Combined (Thalamotomy and Stimulation) Stereotactic Surgery of the Vim Thalamic Nucleus for Bilateral Parkinson Disease. *Applied Neurophysiology,* 50**,** 344-346.

Benabid, A. L., Pollak, P., Seigneuret, E., Hoffmann, D., Gay, E. & Perret, J. 1993. Chronic VIM thalamic stimulation in Parkinson's disease, essential tremor and extra-pyramidal dyskinesias. *Acta Neurochir Suppl (Wien),* 58**,** 39-44.

Bergman, H. & Deuschl, G. 2002. Pathophysiology of Parkinson's disease: from clinical neurology to basic neuroscience and back. *Mov Disord,* 17 Suppl 3**,** S28-40.

Bevan, M. D., Magill, P. J., Terman, D., Bolam, J. P. & Wilson, C. J. 2002. Move to the rhythm: oscillations in the subthalamic nucleus-external globus pallidus network. *Trends in Neurosciences,* 25**,** 525-531.

Black, R. C., Clark, G. M., O'leary, S. J. & Walters, C. 1983. Intracochlear electrical stimulation of normal and deaf cats investigated using brainstem response audiometry. *Acta Otolaryngol Suppl,* 399**,** 5-17.

Blogg, T. & Reid, W. D. 1990. A digital technique for stimulus artifact reduction. *Electroencephalogr Clin Neurophysiol,* 76**,** 557-561.

Brown, P. 2003. Oscillatory nature of human basal ganglia activity: relationship to the pathophysiology of Parkinson's disease. *Mov Disord,* 18**,** 357-363.

Brown, P., Oliviero, A., Mazzone, P., Insola, A., Tonali, P. & Di Lazzaro, V. 2001. Dopamine dependency of oscillations between subthalamic nucleus and pallidum in Parkinson's disease. *Journal of Neuroscience,* 21**,** 1033-1038.

Brown, P. & Williams, D. 2005. Basal ganglia local field potential activity: character and functional significance in the human. *Clinical Neurophysiology,* 116**,** 2510-2519.

Buhlmann, J., Hofmann, L., Tass, P. A. & Hauptmann, C. 2011. Modeling of a segmented electrode for desynchronizing deep brain stimulation. *Front Neuroeng,* 4**,** 15.

Carron, R., Chabardes, S. & Hammond, C. 2012. [Mechanisms of action of high-frequency deep brain stimulation. A review of the literature and current concepts]. *Neurochirurgie,* 58**,** 209-217.

Cassidy, M., Mazzone, P., Oliviero, A., Insola, A., Tonali, P., Di Lazzaro, V. & Brown, P. 2002. Movement-related changes in synchronization in the human basal ganglia. *Brain,* 125**,** 1235-1246.

Chaudhuri, K. R. & Schapira, A. H. 2009. Non-motor symptoms of Parkinson's disease: dopaminergic pathophysiology and treatment. *Lancet Neurol,* 8**,** 464-74.

Coffey, R. J. 2009. Deep brain stimulation devices: a brief technical history and review. *Artif Organs,* 33**,** 208-220.

Costa, M. H. & Tavares, M. C. 2009. Removing harmonic power line interference from biopotential signals in low cost acquisition systems. *Comput Biol Med,* 39**,** 519-526.

Deuschl, G., Herzog, J., Kleiner-Fisman, G., Kubu, C., Lozano, A. M., Lyons, K. E., Rodriguez-Oroz, M. C., Tamma, F., Troster, A. I., Vitek, J. L., Volkmann, J. & Voon, V. 2006a. Deep brain stimulation: postoperative issues. *Mov Disord,* 21 Suppl 14**,** S219-237.

Deuschl, G., Raethjen, J., Baron, R., Lindemann, M., Wilms, H. & Krack, P. 2000. The pathophysiology of parkinsonian tremor: a review. *J Neurol,* 247 Suppl 5**,** V33-48.

Deuschl, G., Schade-Brittinger, C., Krack, P., Volkmann, J., Schafer, H., Botzel, K., Daniels, C., Deutschlander, A., Dillmann, U., Eisner, W., Gruber, D., Hamel, W., Herzog, J., Hilker, R., Klebe, S., Kloss, M., Koy, J., Krause, M., Kupsch, A., Lorenz, D., Lorenzl, S., Mehdorn, H. M., Moringlane, J. R., Oertel, W., Pinsker, M. O., Reichmann, H., Reuss, A., Schneider, G. H., Schnitzler, A., Steude, U., Sturm, V., Timmermann, L., Tronnier, V., Trottenberg, T., Wojtecki, L., Wolf, E., Poewe, W. & Voges, J. 2006b. A randomized trial of deep-brain stimulation for Parkinson's disease. *N Engl J Med,* 355**,** 896-908.

Eusebio, A., Thevathasan, W., Doyle Gaynor, L., Pogosyan, A., Bye, E., Foltynie, T., Zrinzo, L., Ashkan, K., Aziz, T. & Brown, P. 2011. Deep brain stimulation can suppress pathological synchronisation in parkinsonian patients. *J Neurol Neurosurg Psychiatry,* 82**,** 569-573.

Feng, X., Greenwald, B., Rabitz, H., Shea-Brown, E. & Kosut, R. 2007. Toward closed-loop optimization of deep brain stimulation for Parkinson's disease: concepts and lessons from a computational model. *J Neural Eng,* 4**,** L14-L21.

Fletcher, R. & Powell, M. J. D. 1963. A Rapidly Convergent Descent Method for Minimization. *Computer Journal,* 6**,** 163-&.

Foffani, G., Ardolino, G., Meda, B., Egidi, M., Rampini, P., Caputo, E., Baselli, G. & Priori, A. 2005a. Altered subthalamo-pallidal synchronisation in parkinsonian dyskinesias. *J Neurol Neurosurg Psychiatry,* 76**,** 426-8.

Foutz, T. J. & Mcintyre, C. C. 2010. Evaluation of novel stimulus waveforms for deep brain stimulation. *J Neural Eng,* 7**,** 066008.

Freeman, J. A. 1971. An electronic stimulus artifact suppressor. *Electroencephalogr Clin Neurophysiol,* 31**,** 170-2.

Giannicola, G., Rosa, M., Servello, D., Menghetti, C., Carrabba, G., Pacchetti, C., Zangaglia, R., Cogiamanian, F., Scelzo, E., Marceglia, S., Rossi, L. & Priori, A. 2012. Subthalamic local field potentials after seven-year deep brain stimulation in Parkinson's disease. *Exp Neurol,* 237**,** 312-317.

Grant & Lowery 2013. Simulation of cortico-Basal Ganglia oscillations and their suppression by closed loop deep brain stimulation. *IEEE Trans Neural Syst Rehabil Eng,* 21**,** 584-94.

Harding, G. W. 1991. A method for eliminating the stimulus artifact from digital recordings of the direct cortical response. *Comput Biomed Res,* 24**,** 183-95.

Hariz, M. 2012. Twenty-five years of deep brain stimulation: celebrations and apprehensions. *Mov Disord,* 27**,** 930-3.

Harnack, D., Winter, C., Meissner, W., Reum, T., Kupsch, A. & Morgenstern, R. 2004. The effects of electrode material, charge density and stimulation duration on the safety of high-frequency stimulation of the subthalamic nucleus in rats. *J Neurosci Methods,* 138**,** 207-16.

Hartley, H. O. 1960. A Modified Gauss-Newton Method for the Solution of Non-Linear Squares Problems. *Journal of the American Statistical Association,* 55**,** 361-361.

Hashimoto, T., Elder, C. M. & Vitek, J. L. 2002. A template subtraction method for stimulus artifact removal in high-frequency deep brain stimulation. *J Neurosci Methods,* 113**,** 181-186.

Hauptmann, C., Popovych, O. & Tass, P. A. 2005. Effectively desynchronizing deep brain stimulation based on a coordinated delayed feedback stimulation via several sites: a computational study. *Biol Cybern,* 93**,** 463-70.

Hauptmann, C., Roulet, J. C., Niederhauser, J. J., Doll, W., Kirlangic, M. E., Lysyansky, B., Krachkovskyi, V., Bhatti, M. A., Barnikol, U. B., Sasse, L., Buhrle, C. P., Speckmann, E. J., Gotz, M., Sturm, V., Freund, H. J., Schnell, U. & Tass, P. A. 2009. External trial deep brain stimulation device for the application of desynchronizing stimulation techniques. *J Neural Eng,* 6**,** 066003.

Hauptmann, C. & Tass, P. A. 2007. Therapeutic rewiring by means of desynchronizing brain stimulation. *Biosystems,* 89**,** 173-181.

Hauptmann, C. & Tass, P. A. 2009. Cumulative and after-effects of short and weak coordinated reset stimulation: a modeling study. *J Neural Eng,* 6**,** 016004.

Huberdeau, D., Walker, H., Huang, H., Montgomery, E. & Sarma, S. V. 2011. Analysis of local field potential signals: a systems approach. *Conf Proc IEEE Eng Med Biol Soc,* 2011**,** 814-7.

Huhta, J. C. & Webster, J. G. 1973. 60-HZ interference in electrocardiography. *IEEE Trans Biomed Eng,* 20**,** 91-101.

Jensen, S., Molnar, G., Giftakis, J., Santa, W., Jensen, R., Carlson, D., Lent, M. & Denison, T. 2008. Information, Energy, and Entropy: Design Principles for Adaptive, Therapeutic Modulation of Neural Circuits. *Esscirc 2008: Proceedings of the 34th European Solid-State Circuits Conference***,** 32-39.

Kent, A. R. & Grill, W. M. 2012. Recording evoked potentials during deep brain stimulation: development and validation of instrumentation to suppress the stimulus artefact. *J Neural Eng,* 9**,** 036004.

Knaflitz, M. & Merletti, R. 1988. Suppression of simulation artifacts from myoelectric-evoked potential recordings. *IEEE Trans Biomed Eng,* 35**,** 758-63.

Kumar, R., Lozano, A. M., Sime, E. & Lang, A. E. 2003. Long-term follow-up of thalamic deep brain stimulation for essential and parkinsonian tremor. *Neurology,* 61**,** 1601-4.

Kuncel, A. M. & Grill, W. M. 2004. Selection of stimulus parameters for deep brain stimulation. *Clinical Neurophysiology,* 115**,** 2431-2441.

Kuo, S. M. & Gan, W.-S. S. 2004. *DIGITAL SIGNAL PROCESSING Architecture, Implementation, and Applications.*, Pareson Education, Inc., New Jersey,.282-287

Lagarias, J. C., Reeds, J. A., Wright, M. H. & Wright, P. E. 1998. Convergence properties of the Nelder-Mead simplex method in low dimensions. *Siam Journal on Optimization,* 9**,** 112-147.

Latteri, A., Arena, P. & Mazzone, P. 2011. Characterizing Deep Brain Stimulation effects in computationally efficient neural network models. *Nonlinear Biomed Phys,* 5**,** 2.

Lenz, F. A., Kwan, H. C., Martin, R. L., Tasker, R. R., Dostrovsky, J. O. & Lenz, Y. E. 1994. Single unit analysis of the human ventral thalamic nuclear group. Tremor-related activity in functionally identified cells. *Brain,* 117 (Pt 3)**,** 531-43.

Levkov, C., Mihov, G., Ivanov, R., Daskalov, I., Christov, I. & Dotsinsky, I. 2005. Removal of power-line interference from the ECG: a review of the subtraction procedure. *Biomed Eng Online,* 4**,** 50.

Levy, R., Hutchison, W. D., Lozano, A. M. & Dostrovsky, J. O. 2002. Synchronized neuronal discharge in the basal ganglia of parkinsonian patients is limited to oscillatory activity. *Journal of Neuroscience,* 22**,** 2855-2861.

Lilly, J. C. 1961. *Injury and excitation by electric currents: a. The balanced pulse-pair waveform Electrical Stimulation of the Brain.* , Univ. of Texas Press for Hogg Foundation for Mental Health, Austin, Texas.

Limousin, P., Pollak, P., Benazzouz, A., Hoffmann, D., Le Bas, J. F., Broussolle, E., Perret, J. E. & Benabid, A. L. 1995. Effect of parkinsonian signs and symptoms of bilateral subthalamic nucleus stimulation. *Lancet,* 345**,** 91-5.

Little, S. & Brown, P. 2012. What brain signals are suitable for feedback control of deep brain stimulation in Parkinson's disease? *Brain Stimulation in Neurology and Psychiatry,* 1265**,** 9-24.

Little, S., Pogosyan, A., Neal, S., Zavala, B., Zrinzo, L., Hariz, M., Foltynie, T., Limousin, P., Ashkan, K., Fitzgerald, J., Green, A. L., Aziz, T. Z. & Brown, P. 2013. Adaptive deep brain stimulation in advanced Parkinson disease. *Ann Neurol*.

Lucht, P. 2013. *Boston Scientific Receives CE Mark Approval For GUIDE™ DBS System* [Online]. Boston Scientific Corporation. Available: http://boston scientific.mediaroom.com/2013-05-27-Boston-Scientific-Receives-CE-Mark-Approval-For-GUIDE-DBS-System [Accessed July 28, 03:00 p.m. 2013].

Lumsden, D. E., Ashmore, J., Charles-Edwards, G., Lin, J. P., Ashkan, K. & Selway, R. 2013. Accuracy of stimulating electrode placement in paediatric pallidal deep brain stimulation for primary and secondary dystonia. *Acta Neurochir (Wien),* 155**,** 823-36.

Lysyansky, B., Popovych, O. V. & Tass, P. A. 2011. Desynchronizing anti-resonance effect of m: n ON-OFF coordinated reset stimulation. *J Neural Eng,* 8.

Magill, P. J., Bolam, J. P. & Bevan, M. D. 2001. Dopamine regulates the impact of the cerebral cortex on the subthalamic nucleus-globus pallidus network. *Neuroscience,* 106**,** 313-30.

Marquardt, D. W. 1963. An Algorithm for Least-Squares Estimation of Nonlinear Parameters. *Journal of the Society for Industrial and Applied Mathematics,* 11**,** 431-441.

Masimore, B., Kakalios, J. & Redish, A. D. 2004. Measuring fundamental frequencies in local field potentials. *J Neurosci Methods,* 138**,** 97-105.

Mcgill, K. C., Cummins, K. L., Dorfman, L. J., Berlizot, B. B., Leutkemeyer, K., Nishimura, D. G. & Widrow, B. 1982. On the nature and elimination of stimulus artifact in nerve signals evoked and recorded using surface electrodes. *IEEE Trans Biomed Eng,* 29**,** 129-37.

Mckinnon, K. I. M. 1998. Convergence of the Nelder-Mead simplex method to a nonstationary point. *Siam Journal on Optimization,* 9**,** 148-158.

Medtronic, Inc. 2013. *New Medtronic Deep Brain Stimulation System The First To Sense And Record Brain Activity While Delivering Therapy* [Online]. Available: http://multimediacapsule.thomsonone.com/medtronic/new-medtronic-deep-brain-stimulation-system-the-first-to--sense-and-record-brain-activity [Accessed September 8, 06:00 p.m. 2013].

Meissner, W., Leblois, A., Hansel, D., Bioulac, B., Gross, C. E., Benazzouz, A. & Boraud, T. 2005. Subthalamic high frequency stimulation resets subthalamic firing and reduces abnormal oscillations. *Brain,* 128**,** 2372-82.

Minzly, J., Mizrahi, J., Hakim, N. & Liberson, A. 1993. Stimulus artefact suppressor for EMG recording during FES by a constant-current stimulator. *Med Biol Eng Comput,* 31**,** 72-5.

Miocinovic, S., Somayajula, S., Chitnis, S. & Vitek, J. L. 2013. History, applications, and mechanisms of deep brain stimulation. *JAMA Neurol,* 70**,** 163-71.

Muta, D., Goto, S., Nishikawa, S., Hamasaki, T., Ushio, Y., Inoue, N. & Mita, S. 2001. Bilateral pallidal stimulation for idiopathic segmental axial dystonia advanced from Meige syndrome refractory to bilateral thalamotomy. *Mov Disord,* 16**,** 774-7.

Nelder, J. A. & Mead, R. 1965. A Simplex-Method for Function Minimization. *Computer Journal,* 7**,** 308-313.

Nguyen, T. K., Musa, S., Eberle, W., Bartic, C. & Gielen, G. 2013. Mixed-signal template-based reduction scheme for stimulus artifact removal in electrical stimulation. *Med Biol Eng Comput,* 51**,** 449-58.

Nini, A., Feingold, A., Slovin, H. & Bergman, H. 1995. Neurons in the Globus-Pallidus Do Not Show Correlated Activity in the Normal Monkey, but Phase-Locked Oscillations Appear in the Mptp Model of Parkinsonism. *Journal of Neurophysiology,* 74**,** 1800-1805.

Nishio, M., Korematsu, K., Yoshioka, S., Nagai, Y., Maruo, T., Ushio, Y., Kaji, R. & Goto, S. 2009. Long-term suppression of tremor by deep brain stimulation of the ventral intermediate nucleus of the thalamus combined with pallidotomy in hemiparkinsonian patients. *J Clin Neurosci,* 16**,** 1489-91.

O'keeffe, D. T., Lyons, G. M., Donnelly, A. E. & Byrne, C. A. 2001. Stimulus artifact removal using a software-based two-stage peak detection algorithm. *J Neurosci Methods,* 109**,** 137-45.

Obeso, J. A., Rodriguez-Oroz, M. C., Rodriguez, M., Lanciego, J. L., Artieda, J., Gonzalo, N. & Olanow, C. W. 2000. Pathophysiology of the basal ganglia in Parkinson's disease. *Trends in Neurosciences,* 23**,** S8-S19.

Ortmanns, M. 2007. Charge balancing in functional electrical stimulators: A comparative study. *2007 Ieee International Symposium on Circuits and Systems, Vols 1-11*, 573-576.

Popovych, O., Hauptmann, C. & Tass, P. 2005. Demand-controlled desynchronization of brain rhythms by means of nonlinear delayed feedback. *Conf Proc IEEE Eng Med Biol Soc*, 7, 7656-9.

Popovych, O., Hauptmann, C. & Tass, P. A. 2008. Impact of nonlinear delayed feedback on synchronized oscillators. *J Biol Phys*, 34, 267-79.

Priebe, J. A., Rieckmann, P. & Lautenbacher, S. 2012. [Central pain processing and Parkinson's disease. Epidemiology, physiology, and experimental results issuing pain processing]. *Schmerz*, 26, 647-54.

Priori, A., Foffani, G., Rossi, L. & Marceglia, S. 2013. Adaptive deep brain stimulation (aDBS) controlled by local field potential oscillations. *Exp Neurol*, 245, 77-86.

Roby, R. J. & Lettich, E. 1975. Proceedings: A simplified circuit for stimulus artifact suppression. *Electroencephalogr Clin Neurophysiol*, 39, 435.

Rodriguez-Oroz, M. C., Obeso, J. A., Lang, A. E., Houeto, J. L., Pollak, P., Rehncrona, S., Kulisevsky, J., Albanese, A., Volkmann, J., Hariz, M. I., Quinn, N. P., Speelman, J. D., Guridi, J., Zamarbide, I., Gironell, A., Molet, J., Pascual-Sedano, B., Pidoux, B., Bonnet, A. M., Agid, Y., Xie, J., Benabid, A. L., Lozano, A. M., Saint-Cyr, J., Romito, L., Contarino, M. F., Scerrati, M., Fraix, V. & Van Blercom, N. 2005. Bilateral deep brain stimulation in Parkinson's disease: a multicentre study with 4 years follow-up. *Brain*, 128, 2240-2249.

Rosenblum, M. & Pikovsky, A. 2004. Delayed feedback control of collective synchrony: an approach to suppression of pathological brain rhythms. *Phys Rev E Stat Nonlin Soft Matter Phys*, 70, 041904.

Roshan, G., Philip, B. & Nat, S. 2003. TMS320C6713 Digital Signal Processor Optimized for High Performance Multichannel Audio Systems.

Rosin, B., Slovik, M., Mitelman, R., Rivlin-Etzion, M., Haber, S. N., Israel, Z., Vaadia, E. & Bergman, H. 2011. Closed-loop deep brain stimulation is superior in ameliorating parkinsonism. *Neuron*, 72, 370-84.

Rossi, L., Foffani, G., Marceglia, S., Bracchi, F., Barbieri, S. & Priori, A. 2007. An electronic device for artefact suppression in human local field potential recordings during deep brain stimulation. *J Neural Eng*, 4, 96-106.

Rulph, C. 2004. *Digital Signal Processing and Applications with the C6713 C6416 DSK*, John Wiley & Sons, USA, .

Santaniello, S., Fiengo, G., Glielmo, L. & Grill, W. M. 2011. Closed-Loop Control of Deep Brain Stimulation: A Simulation Study. *Ieee Transactions on Neural Systems and Rehabilitation Engineering*, 19, 15-24.

Scheiner, A., Mortimer, J. T. & Roessmann, U. 1990. Imbalanced biphasic electrical stimulation: muscle tissue damage. *Ann Biomed Eng*, 18, 407-25.

Smirnov, D. A., Barnikol, U. B., Barnikol, T. T., Bezruchko, B. P., Hauptmann, C., Buhrle, C., Maarouf, M., Sturm, V., Freund, H. J. & Tass, P. A. 2008. The generation of Parkinsonian tremor as revealed by directional coupling analysis. *Epl*, 83.

Sooksood, K., Stieglitz, T. & Ortmanns, M. 2009. An experimental study on passive charge balancing. *Copernicus Publications*.

Spectrum Digital, Inc. 2003. Technical Reference Review TMS320C6713 DSK, . Texas Instruments

Spectrum Digital, Inc. 2004. Reference Guide of Two-Level Internal Memory TMS320C621x/C671x DSP, . Texas Instruments.

Spectrum Digital, Inc. 2006. Set Reference Guide of TMS320C67x/C67x+ DSP CPU and Instruction,. Texas Instruments.

Spectrum Digital, Inc. 2007. Reference Set of TMS320C54 x DSP, Volume 5: Enhanced Peripherals,. Texas Instruments

Starr, P. A., Turner, R. S., Rau, G., Lindsey, N., Heath, S., Volz, M., Ostrem, J. L. & Marks, W. J., Jr. 2004. Microelectrode-guided implantation of deep brain stimulators into the globus pallidus internus for dystonia: techniques, electrode locations, and outcomes. *Neurosurg Focus,* 17**,** E4.

Strang, G. & Nguyen, T. 1996. *Wavelet and Filter Banks,* Wellesley, USA, Wellesley-Cambridge Press, 86-388

Tasker, R. R. 1998. Deep brain stimulation is preferable to thalamotomy for tremor suppression. *Surg Neurol,* 49**,** 145-53; discussion 153-4.

Tass, P. A. 2003a. A model of desynchronizing deep brain stimulation with a demand-controlled coordinated reset of neural subpopulations. *Biol Cybern,* 89**,** 81-8.

Tass, P. A. 2003b. Desynchronization by means of a coordinated reset of neural sub-populations - A novel technique for demand-controlled deep brain stimulation. *Progress of Theoretical Physics Supplement***,** 281-296.

Tass, P. A. & Hauptmann, C. 2007. Therapeutic modulation of synaptic connectivity with desynchronizing brain stimulation. *International Journal of Psychophysiology,* 64**,** 53-61.

Tass, P. A. & Hauptmann, C. 2009. Anti-kindling achieved by stimulation targeting slow synaptic dynamics. *Restor Neurol Neurosci,* 27**,** 589-609.

Tass, P. A. & Majtanik, M. 2006. Long-term anti-kindling effects of desynchronizing brain stimulation: a theoretical study. *Biol Cybern,* 94**,** 58-66.

Tass, P. A., Qin, L., Hauptmann, C., Dovero, S., Bezard, E., Boraud, T. & Meissner, W. 2012. Coordinated Reset has sustained after-effects in parkinsonian monkeys. *Annals of Neurology*.

Tass, P. A., Smirnov, D., Karavaev, A., Barnikol, U., Barnikol, T., Adamchic, I., Hauptmann, C., Pawelcyzk, N., Maarouf, M., Sturm, V., Freund, H. J. & Bezruchko, B. 2010. The causal relationship between subcortical local field potential oscillations and Parkinsonian resting tremor. *J Neural Eng,* 7**,** 16009.

Thakor, N. V. & Webster, J. G. 1980. Ground-free ECG recording with two electrodes. *IEEE Trans Biomed Eng,* 27**,** 699-704.

Trottenberg, T., Meissner, W., Kabus, C., Arnold, G., Funk, T., Einhaupl, K. M. & Kupsch, A. 2001. Neurostimulation of the ventral intermediate thalamic nucleus in inherited myoclonus-dystonia syndrome. *Mov Disord,* 16**,** 769-71.

Van Someren, E. J., Pticek, M. D., Speelman, J. D., Schuurman, P. R., Esselink, R. & Swaab, D. F. 2006. New actigraph for long-term tremor recording. *Mov Disord,* 21**,** 1136-43.

Volkmann, J. 2004. Deep brain stimulation for the treatment of Parkinson's disease. *Journal of Clinical Neurophysiology,* 21**,** 6-17.

Volkmann, J. 2007. Deep brain stimulation for Parkinson's disease. *Parkinsonism Relat Disord,* 13 Suppl 3**,** S462-5.

Waddell, C., Pratt, J. A., Porr, B. & Ewing, S. 2009. Deep Brain Stimulation Artifact Removal Through Under-Sampling and Cubic-Spline Interpolation. *Proceedings of the 2009 2nd International Congress on Image and Signal Processing, Vols 1-9***,** 3953-3957.

Wagenaar, D. A. & Potter, S. M. 2002. Real-time multi-channel stimulus artifact suppression by local curve fitting. *J Neurosci Methods,* 120**,** 113-20.

Weigelt, J. C. 2013. *St. Jude Medical First to Receive CE Mark Approval of Deep Brain Stimulation Systems for Both Primary and Secondary Dystonia.* [Online]. St. Jude Medical, Inc. Available: http://investors.sjm.com/phoenix.zhtml?c=73836&p=irol-newsArticle&ID=1805195&highlight=DBS [Accessed July 28, 04:00 p.m. 2013].

Wichmann, T. 2000. A digital averaging method for removal of stimulus artifacts in neurophysiologic experiments. *J Neurosci Methods,* 98**,** 57-62.

Wichmann, T. & Delong, M. R. 1996. Functional and pathophysiological models of the basal ganglia. *Curr Opin Neurobiol,* 6**,** 751-8.

Wolf, J. P., Bouhaddi, M., Louisy, F., Mikehiev, A., Mourot, L., Cappelle, S., Vuillier, F., Andre, P., Rumbach, L. & Regnard, J. 2006. Side-effects of L-dopa on venous tone in Parkinson's disease: a leg-weighing assessment. *Clin Sci (Lond),* 110**,** 369-77.

Yacoup, S. & Raoof, K. 2008. Noise Removal from Surface Respiratory EMG Signal. *International Journal of Computer, Information, and Systems science, and Engineering,* 2:4.

Erklärung

Ich versichere, dass ich die von mir vorgelegte Dissertation selbstständig angefertigt, die benutzten Quellen und Hilfsmittel vollständig angegeben und die Stellen der Arbeit - einschließlich Tabellen, Karten und Abbildungen -, die anderen Werken im Wortlaut oder dem Sinn nach entnommen sind, in jedem Einzelfall als Entlehnung kenntlich gemacht habe; dass diese Dissertation noch keiner anderen Fakultät oder Universität zur Prüfung vorgelegen hat; dass sie noch nicht veröffentlicht worden ist sowie, dass ich eine solche Veröffentlichung vor Abschluss des Promotionsverfahrens nicht vornehmen werde. Die Bestimmungen dieser Promotionsordnung sind mir bekannt. Die von mir vorgelegte Dissertation ist von Priv.- Doz. Dr. Christian Hauptmann betreut worden.

Ich versichere, dass ich alle Angaben wahrheitsgemäß nach bestem Wissen und Gewissen gemacht habe und verpflichte mich, jedmögliche, die obigen Angaben betreffenden Veränderungen, dem Promotionsausschuss unverzüglich mitzuteilen.

---------- ----------

Datum Unterschrift